Title
Atmospheric gas isotopes preserved in groundwater, seawater, and ice cores as climatic tracers

Permalink
https://escholarship.org/uc/item/2q25f4hj

Author
Seltzer, Alan M

Publication Date
2019

Peer reviewed|Thesis/dissertation

UNIVERSITY OF CALIFORNIA SAN DIEGO

Atmospheric gas isotopes preserved in groundwater, seawater, and ice cores as climatic tracers

A dissertation submitted in partial satisfaction of the
requirements for the degree
Doctor of Philosophy

in

Earth Sciences

by

Alan Myland Seltzer

Committee in charge:

Jeff Severinghaus, Chair
Ralph Keeling
Justin Kulongoski
Mark Thiemens
Ray Weiss

2019

The dissertation of Alan Myland Seltzer is approved, and it is acceptable in quality and form for publication on microfilm and electronically:

Chair

University of California, San Diego

2019

EPIGRAPH

When you come to a fork in the road, take it.

Lawrence Peter “Yogi” Berra

TABLE OF CONTENTS

LIST OF FIGURES

LIST OF TABLES

ACKNOWLEDGEMENTS

It has been a true privilege to spend these past five years at Scripps Institution of Oceanography. I am grateful to have had the opportunity to grow as a scientist together with my talented, supportive, and inspiring graduate student peers. To my 2014-cohort colleagues – Stephen, Reuben, Bia, Dillon, Olavo, Isa, Matt, Effie, Osi, Charlotte, Jon, Derek, and Paul – thank you for your camaraderie, which has brightened my time in graduate school. To my lab mates – Sarah, Ross, Jessica, Jacob, Christy, Benni, Berni, and Daniel – thank you for creating such a supportive community; I admire you all and would have achieved far less without your kind help. To my committee – Ralph, Justin, Ray, Mark, Jeff, and the late Dave Hilton – your advice and mentorship have been indispensable, and it has been a pleasure getting to know each of you these past few years. To my parents and brother, please know that your unwavering support, especially in the difficult times, has carried me through my doctoral studies. To Kate, I am deeply indebted to you for your ability and willingness to patiently listen and thoughtfully advise; you have made me a better scientist and a better person. To the fine folks in the SIO administration, especially Gilbert and Maureen, who help us students navigate the bureaucratic mazes of our doctoral studies, thank you for your caring support. To my other wonderful friends from SIO and beyond – Frankie, Gui, JD, Mike, Rishi, Catherine, Alfredo, Tiago, Momme, Art and Jenny, the members of the Na casino, JG and Catherine, and anyone else I’ve surely forgotten – thank you for your friendship; it has meant more to me these past five years than I can adequately describe. Finally, to Jeff – thank you for taking a risk by accepting me to work with dirty groundwater samples in your clean ice core lab and thereby enabling my hopeful pursuit of an idea that you and Martin Stute (whom I also thank) first proposed 25 years ago. Your deep appreciation of Nature and love of science are

contagious. I have learned a great deal from your careful yet creative approach to research, and I look forward to continuing to learn from you as we work together in the coming years.

Chapter 2, in full, is a reproduction of material as it appears in Seltzer, A., Severinghaus, J., Andraski, B., and D. Stonestrom, Steady State Fractionation of Heavy Noble Gas Isotopes in a Deep Unsaturated Zone, *Water Resources Research*, 2017. The dissertation author was the primary investigator and author of this work.

Chapter 3, in full, is a reproduction of material as it appears in Seltzer, A., Ng, J. and J. Severinghaus. Precise Determination of Ar, Kr, and Xe isotopic fractionation due to diffusion and dissolution in fresh water, *Earth and Planetary Science Letters*, 2019. The dissertation author was the primary investigator and author of this work.

Chapter 4, in full, has been submitted for publication in *Nature Communications*: Seltzer, A., Ng, J., Danskin, W., Kulongoski, J., Gannon, R., Stute, M., and J. Severinghaus, Dissolved Kr and Xe Isotope Ratios in Groundwater Preserve Gravitational Signals of Past Water-Table Depth, *Science*, 2019. The dissertation author was the primary investigator and author of this work.

Chapter 5, in full, is a reproduction of material as it appears in Seltzer, A., Pavia, F., Ng, J., and J. Severinghaus, Heavy Noble Gas Isotopes as New Constraints on the Ventilation of the Deep Ocean, *Geophysical Research Letters*, 2019. The dissertation author was the primary investigator and author of this work.

Chapter 6, in full, is a reproduction of material as it appears in Seltzer, A., Buizert, C., Baggenstos, D., Brook, E., Ahn, J., Woong, J.-W., and Severinghaus, J. Does δ^{18}O of O_2 record meridional shifts in tropical rainfall? *Climate of the Past*, 2017. The dissertation author was the primary investigator and author of this work.

VITA

2010-2014	Bachelor of Arts in Earth Science, Columbia University
2014-2019	Graduate Student Researcher, Scripps Institution of Oceanography
2016	Master of Science in Earth Sciences, University of California San Diego
2019	Doctor of Philosophy in Earth Sciences, University of California San Diego

PUBLICATIONS

Gannon, R. S., Seltzer, A. M., Amaya, D. J., and Danskin, W. R. Southwestern United States climate variability assessment through groundwater stable isotopes, 40 kyr BP to present. In preparation for submission to *Geophysical Research Letters*.

Seltzer, A. M., Ng, J., Kulongoski, J. T., Danskin, W. R., Gannon, R. S., Stute, M., and Severinghaus, J. P. Dissolved Kr and Xe Isotopes in Groundwater Preserve Gravitational Signals of Past Water-Table Depth. In review at *Nature Communications*.

Seltzer, A. M., Pavia, F. J., Ng, J., and Severinghaus, J. P. (2019), Heavy noble gas isotopes as new constraints on the ventilation of the deep ocean. *Geophysical Research Letters*. Accepted. doi: 10.1029/2019GL084089

Seltzer, A. M., Ng. J., and Severinghaus, J. P. (2019), Precise determination of Ar, Kr and Xe isotopic fractionation due to diffusion and dissolution in fresh water. *Earth and Planetary Science Letters*. 514, 156-165, doi: 10.1016/j.epsl.2019.03.008.

Seltzer, A. M., Buizert, C., Baggenstos, D., Brook, E. J., Ahn, J., Yang, J.-W., and Severinghaus, J. P. (2017), Does $\delta^{18}O$ of O_2 record meridional shifts in tropical rainfall?, *Climate of the Past.* 13, 1323-1338, doi: 10.5194/cp-2017-83.

Seltzer, A. M., Severinghaus, J. P., Andraski, B. J., and Stonestrom, D. A. (2017), Steady-state fractionation of heavy noble gas isotopes in a deep unsaturated zone, *Water Resources Research* 53(4), 2716–2732, doi:10.1002/2016WR019655.

Seltzer, A. M., Stute, M., Morgenstern, U., Stewart, M., Schaefer, J. (2015), Mean annual temperature in New Zealand during the last glacial maximum derived from dissolved noble gases in groundwater. *Earth and Planetary Science Letters.* 431, 206-216, doi: 10.1016/j.epsl.2015.09.032.

ABSTRACT OF THE DISSERTATION

Atmospheric gas isotopes preserved in groundwater, seawater, and ice cores as climatic tracers

by

Alan Myland Seltzer

Doctor of Philosophy in Earth Sciences

University of California San Diego, 2019

Jeffrey P. Severinghaus, Chair

Observations are key to our ability to understand present climate and predict future change. However, for many climatic variables of interest, direct observations are not possible. Well-mixed atmospheric gas tracers preserved in groundwater, seawater, and ice cores provide a crucial lens into past climate and contemporary large-scale signals that cannot be resolved by modern observations. This work is predominantly concerned with dissolved noble gas isotope tracers in groundwater, which are here shown to record mean water-table depths at the time of recharge.

Noble gases are ideal tracers of geophysical processes due to their inertness and constant atmospheric concentrations on glacial-interglacial timescales. The foremost goal of this work has been to develop a quantitative tool for past water-table depth reconstruction by measuring the stable isotope ratios of Kr and Xe dissolved in groundwater at high precision. This approach relies on the dominance of depth-dependent gravitational settling fractionation in unsaturated zone (UZ) air prior to its dissolution at the water table, which is predicted by theory and consistent with observations in a deep UZ. Because this gravitational signal, in which heavy-to-light Kr and Xe isotope ratios increase nearly linearly with depth, is transferred to groundwater during dissolution, the isotopic composition of noble gases in groundwater records information about water-table depth at the time of recharge.

To fully employ these isotopic tracers of water-table depth, a complete geochemical model for fractionation between the well-mixed atmosphere and groundwater was developed, and constrained by laboratory determinations of relevant isotopic solubility and diffusivity ratios. In measurements from 58 groundwater samples across California, the expected dominance of gravitational settling was confirmed, modern water table depths were reproduced, and a mean decrease in regional San Diego water-table depth of ~20 meters during the last deglaciation was discovered, consistent with prior work that broadly indicates of the prevalence of wetter conditions during the late glacial period.

In two additional studies, noble gas isotopes in the deep north Pacific were measured to explore air-sea disequilibrium signals of rapid cooling and gas uptake during deep-water formation, and a composite record of $\delta^{18}O$ of O_2 from two ice cores was compiled to explore the sensitivity of this ratio to shifts in tropical rainfall.

Chapter 1

Introduction

Our fundamental understanding of climate variability on global and regional scales hinges on precise, long-term observations. In many cases, however, observational records are too short or sparse to sufficiently shed light on questions of societal relevance. For instance, to gain insight into regional hydrological-cycle sensitivity to large-scale climate forcing, decades of high-quality observations often do not capture signals equivalent in magnitude to those seen over millennial timescales or longer. Similarly, robust quantification of large-scale processes, such as the ventilation of the deep ocean, are frequently hindered by the low spatial resolution of observations.

This thesis explores the potential of well-mixed atmospheric gas tracers to resolve regional and large-scale climate signals both in the present and over the last glacial-interglacial cycle. The primary goal of this work is to reconstruct precise regional hydrological changes over one to ten thousand-year timescales from atmospheric noble gas isotopes dissolved in ancient groundwater. Noble gases are ideal tools for this purpose because their atmospheric mixing ratios are temporally and spatially constant and they are chemically and biologically unreactive. Therefore, observed changes in dissolved noble gas isotope ratios from modern atmospheric composition reflect important physics at the time of groundwater recharge. Two additional studies included in this thesis address large-scale signals recorded by atmospheric gas tracers. Using trapped air in ice, oxygen isotopes of O_2 are employed to investigate past shifts in the tropical rain belts. In the deep North Pacific, noble gas isotope ratios are measured to study the influences of various physical mechanisms of air-sea gas exchange during deep-water formation.

The principal aim of this thesis - the development of a noble gas isotope tool for past water-table depth reconstruction - builds upon several decades of noble gas studies in groundwater. Some of the most reliable reconstructions of terrestrial surface temperatures during the last glacial period have come from groundwater noble gas paleothermometry (GNGP). GNGP is a geochemical tool that exploits the different sensitivities of noble gas solubilities to temperature by assuming that dissolved concentrations of neon, argon, krypton, and xenon in groundwater reflect solubility equilibrium at the water table at the time of recharge, with an additional contribution from the dissolution of entrapped air bubbles (Aeschbach-Hertig et al., 2000; Aeschbach-Hertig & Solomon, 2013; Heaton et al., 1986; Heaton & Vogel, 1981; Mazor, 1972; Stute & Schlosser, 1993). By measuring these inert gases in ^{14}C-dated groundwater, an inverse model can be constrained to estimate mean-annual temperature at the water table at the time of recharge. For water tables that lie below the ~10-15 meter depth range of seasonal soil temperature fluctuations but are shallow enough to be largely unaffected by geothermal heat, water-table temperature (WTT) closely resembles mean annual surface temperature (MAST; Stute & Schlosser, 1993). However, without knowledge of past water-table depth at the time of recharge, the correspondence of WTT and MAST must be assumed. Additionally, GNGP assumes that the inert gas composition of soil air above the water table is identical to that of the well mixed atmosphere. However, diffusive processes in porous air-containing region above the water table (known as the unsaturated zone) are known to fractionate gases as a function of depth. Therefore, knowledge of past water-table depth is of great utility in assessing and correcting for the underlying assumptions of GNGP. This work was jointly motivated by the potential to resolve these longstanding concerns regarding GNGP and the possibility that past water-table depth information might provide insight into regional-scale hydrological change.

Theory predicts that noble gas isotopes in groundwater should record information about past water table depth because of gravitational settling in the unsaturated zone (Seltzer et al., 2017; Severinghaus et al., 1996). Gravitational settling is a well understood physical process by which heavy-to-light gas ratios increase nearly linearly with depth in diffusive media (Schwander, 1989). Whereas other processes, such as thermal diffusion (Grew & Ibbs, 1953) and diffusion against a steady-state flux of water vapor (Severinghaus et al., 1996), substantially counteract the influence of gravity on isotope ratios of light gases, the isotopes of Kr and Xe are largely insensitive to non-gravitational processes (Seltzer et al., 2017). Because groundwater inherits its dissolved gas composition from the unsaturated zone at the water-table, this depth-proportional gravitational signal in unsaturated zone air is transferred to dissolved Kr and Xe isotopes. Isotopic solubility differences and dissolution of entrapped air further fractionate Kr and Xe isotopes in groundwater from their atmospheric ratios (Seltzer et al., 2019).

At the outset of this work, the theory that Kr and Xe isotopes in soil air primarily reflect gravitational settling had not been tested, the solubility and diffusivity ratios of these isotopes in water were unknown, and the conventional analytical precision of dissolved Kr and Xe isotope ratios was roughly one hundred times too low to resolve meter-scale gravitational settling signals. This thesis represents a step towards the development of a noble gas isotope water-table depth tool by making progress on each of the three above issues. Chapter 2 presents results from noble gas isotopic analyses of soil air in a deep unsaturated zone, confirming the expected strong influence of gravitational settling fractionation on Kr and Xe isotopes. Chapter 3 introduces a new measurement technique for analyses of Ar, Kr and Xe isotope ratios in water samples at ±5 per meg amu^{-1} precision. This chapter contains results of laboratory experiments to determine the solubility and kinetic fractionation factors for these isotope ratios in water. Chapter 4 is a comprehensive study of groundwater Kr and Xe isotope ratios from 58 samples collected from 36 wells throughout the State of California. In this chapter, the observed relationship between Kr and Xe isotopes is found to closely follow the gravitational expectation. Isotopic measurements are used to reconstruct known modern water-table depths near Fresno, California and changes in water-table depth since the late Pleistocene in the San Diego regional aquifer system.

Chapters 5 and 6 concern large-scale climate signals recorded by atmospheric gas isotopes in seawater and ice core air bubbles, respectively. Chapter 5 applies the high-precision noble gas isotopic analytical technique (presented in Chapter 3) to seawater samples to consider the influence of air-sea gas exchange processes during deep-water formation on heavy noble gas isotopic disequilibria in the deep ocean. In Chapter 6, the sensitivity of the oxygen isotopic composition of O_2 to meridional shifts in rainfall on millennial timescales is investigated, drawing inferences from the modern seasonal cycles of terrestrial productivity and oxygen isotopes in precipitation.

References

Aeschbach-Hertig, W., & Solomon, D. K. (2013). Noble Gas Thermometry in Groundwater Hydrology. In *The Noble Gases as Geochemical Tracers* (pp. 81–122). Berlin, Heidelberg: Springer Berlin Heidelberg. https://doi.org/10.1007/978-3-642-28836-4_5

Aeschbach-Hertig, W., Peeters, F., Beyerle, U., & Kipfer, R. (2000). Palaeotemperature reconstruction from noble gases in ground water taking into account equilibration with entrapped air. *Nature*, *405*(6790), 1040–4. https://doi.org/10.1038/35016542

Grew, K. E., & Ibbs, T. L. (1953). Thermal diffusion in gases. *Quarterly Journal of the Royal Meteorological Society*, *79*(341), 458–458. https://doi.org/10.1002/qj.49707934127

Heaton, T. H. E., & Vogel, J. C. (1981). “Excess air” in groundwater. *Journal of Hydrology*. https://doi.org/10.1016/0022-1694(81)90070-6

Heaton, T. H. E., Talma, A. S., & Vogel, J. C. (1986). Dissolved gas paleotemperatures and 18O variations derived from groundwater near Uitenhage, South Africa. *Quaternary Research*, *25*(1), 79–88. https://doi.org/10.1016/0033-5894(86)90045-1

Mazor, E. (1972). Paleotemperatures and other hydrological parameters deduced from noble gases dissolved in groundwaters; Jordan Rift Valley, Israel. *Geochimica et Cosmochimica Acta*, *36*(12), 1321–1336. https://doi.org/10.1016/0016-7037(72)90065-8

Schwander, J. (1989). The transformation of snow to ice and the occlusion of gases. In H. Oeschger & C. C. Langway (Eds.), *The Environmental Record in Glaciers and Ice Sheets* (pp. 53–67). New York: Wiley.

Seltzer, A. M., Severinghaus, J. P., Andraski, B. J., & Stonestrom, D. A. (2017). Steady state fractionation of heavy noble gas isotopes in a deep unsaturated zone. *Water Resources Research*, *53*(4), 2716–2732. https://doi.org/10.1002/2016WR019655

Seltzer, A. M., Ng, J., & Severinghaus, J. P. (2019). Precise determination of Ar, Kr and Xe isotopic fractionation due to diffusion and dissolution in fresh water. *Earth and Planetary Science Letters*, *514*, 156–165. https://doi.org/10.1016/J.EPSL.2019.03.008

Severinghaus, J. P., Bender, M. L., Keeling, R. F., & Broecker, W. S. (1996). Fractionation of soil gases by diffusion of water vapor, gravitational settling, and thermal diffusion. *Geochimica et Cosmochimica Acta*, *60*(6), 1005–1018. https://doi.org/10.1016/0016-7037(96)00011-7

Stute, M., & Schlosser, P. (1993). Principles and Applications of the Noble Gas Paleothermometer. In P. K. Savin, S. K. C., L. J., & M. S. (Eds.), *Climate Change in Continental Isotopic Records, Volume 78* (pp. 89–100). American Geophysical Union (AGU). https://doi.org/10.1029/gm078p0089

Chapter 2

Steady-State Fractionation of Heavy Noble Gas Isotopes in a Deep Unsaturated Zone

Abstract

To explore steady-state fractionation processes in the unsaturated zone (UZ), we measured argon, krypton and xenon isotope ratios throughout a ∼110-m deep UZ at the United States Geological Survey (USGS) Amargosa Desert Research Site (ADRS) in Nevada, USA. Prior work has suggested that gravitational settling should create a nearly linear increase in heavy-to-light isotope ratios toward the bottom of stagnant air columns in porous media. Our high-precision measurements revealed a binary mixture between 1) expected steady-state isotopic compositions, and 2) unfractionated atmospheric air. We hypothesize that the presence of an unsealed pipe connecting the surface to the water table allowed for direct inflow of surface air in response to extensive UZ gas sampling prior to our first (2015) measurements. Observed isotopic resettling in deep UZ samples collected a year later, after sealing the pipe, supports this interpretation. Data and modeling each suggest that the strong influence of gravitational settling and weaker influences of thermal diffusion and fluxes of CO_2 and water vapor accurately describe steady-state isotopic fractionation of argon, krypton and xenon within the UZ. The data confirm that heavy noble gas isotopes are sensitive indicators of UZ depth. Based on this finding, we outline a potential inverse

approach to quantify past water-table depths from noble gas isotope measurements in paleogroundwater, after accounting for fractionation during dissolution of UZ air and bubbles.

2.1. Introduction

Noble gases in nature have widespread applications as conservative tracers of physical processes. Because of their inertness in chemical and biological processes, and approximately constant atmospheric abundance over long timescales (Phillips, 1981), noble gases and their isotopes in groundwater (Mazor, 1972; Stute et al., 1995), lakes (Kipfer et al., 2002; Tomonaga et al., 2012), seawater (Hamme & Severinghaus, 2007; Stanley & Jenkins, 2013), polar ice bubbles (Severinghaus et al., 1998), sand dunes (Severinghaus et al., 1996), and firn (Kawamura et al., 2013; Severinghaus & Battle, 2006), among other substrates, have been used as quantitative tools to estimate physical properties and explore processes in natural systems. This study evaluates heavy noble gas isotopes in a deep unsaturated zone (UZ) as possible indicators of depth. Although noble gas isotopes in the UZ have been measured in several recent studies (Freundt et al., 2013; Guillon et al., 2016), this study is the first to our knowledge to resolve UZ fractionation at a precision of <0.01‰ per isotopic mass difference (amu). We compare depth profiles of argon, xenon and krypton isotope ratios measured above a ~110-m deep water table to profiles predicted by a theoretical fractionation model based on Severinghaus et al. (1996).

This study is motivated by the potential for future measurements of dissolved noble gas isotopes in paleogroundwater to quantify water-table depth at the time of recharge. Because dissolved gases in groundwater are inherited from the UZ, quantitative information about past water-table depth may be retained in paleogroundwater sequestered from the atmosphere since the time of recharge. Paleotemperature estimation from dissolved bulk Ne, Ar, Kr and Xe concentrations, a common application of atmospheric noble gases in the subsurface, assumes that soil gas of atmospheric composition dissolves into groundwater (Stute & Schlosser, 1993). Noble gas temperature (NGT) models neglect fractionation in the UZ between the free atmosphere and water table because its thickness (i.e. water-table depth at the time of recharge) is usually unknown. NGTs are typically assumed to represent mean annual surface temperature (MAST) for water tables around 10 meters (in mid-latitudes), because the amplitude of the seasonal temperature cycle is nearly completely damped in soil below this depth (Werner Aeschbach-Hertig & Solomon, 2013; Stute & Schlosser, 1993). However, the lack of past water-table depth information introduces a potential bias in the conversion of NGTs to past MAST due to the contribution of geothermal heat. For example, NGTs of paleogroundwater that equilibrated at water tables much deeper than 10 m would be warmer than MAST at the time of recharge, because temperature generally increases with depth in the shallow lithosphere. With knowledge of past water-table depth, measurement of current geothermal gradient, and the assumption that geothermal gradients in the subsurface are constant on timescales of at least 10 kyr, this bias could be removed from NGT-based MAST reconstructions as follows:

$$MAST = NGT - \Gamma(z_{WT} - z_{MAST}) \tag{2.1}$$

where Γ is the mean geothermal gradient (°C m^{-1}), z_{WT} is mean water-table depth (m) at the time of recharge and z_{MAST} is the depth (m) at which MAST applies. The opportunities to implement this paleotemperature correction and to gain quantitative past hydroclimatic constraints from reconstructions of past water-table depths are both key motivations of our study to quantify the actual steady-state noble gas isotopic fractionation in the UZ.

We begin by presenting a model for steady-state isotopic profiles in UZ air (Figure 2.2.1). We then test this model in a deep UZ at the US Geological Survey (USGS) Amargosa Desert

Research Site (ADRS) near Beatty, Nevada, USA. The ADRS is located adjacent to a closed, low-level radioactive waste (LLRW) disposal site and presents a unique challenge due to its perturbed thermal structure (Mayers et al., 2005), elevated CO_2 (Stonestrom et al., 2004) and volatile organic compound (VOC) concentrations (Baker et al., 2012), and capacity for atmospheric contamination of deep soil air. Finally, we present two inverse model applications for a suite of heavy noble gas isotope measurements: 1) quantifying atmospheric contamination of steady-state UZ air at ADRS, and 2) estimating past UZ thickness from reconstructed past steady-state UZ noble gas isotope ratios (e.g. from dissolved gas measurements in paleogroundwater).

2.1.1 Isotopic Fractionation in the Unsaturated Zone

Noble gases in the unsaturated zone are effective physical tracers of advection and diffusion in porous media, as confirmed by both field (Weeks et al., 1982) and laboratory (Ding et al., 2016) studies. In an idealized one-dimensional UZ, atmospheric noble gases diffuse to reach steady-state concentrations. The ratio of steady-state concentrations of two inert gas species can be described as the sum of three fractionation processes: gravitational settling, thermal diffusion, and diffusion against constant fluxes of other gases (typically water vapor) as suggested by measurements of O_2 and N_2 isotope ratios in a sand dune (Severinghaus et al., 1996). Formally, the idealized steady-state ratio of any two gas species (e.g. two noble gas isotopes), δ_{NET}, in a one-dimensional unsaturated zone is given by:

$$\delta_{NET} = \delta_{\mathrm{grav}} + \delta_{\mathrm{therm}} + \delta_{\mathrm{diff}} \tag{2.2}$$

where δ_{grav}, δ_{therm}, and δ_{diff} are the magnitudes of fractionation due to gravitational settling, thermal diffusion, and diffusion against vertical fluxes. δ_i is defined for any isotope ratio, i, as:

$$\delta_i = \delta^{a}/_{b}X = \left(\frac{\left(\frac{a}{b}\right)_{smp}}{\left(\frac{a}{b}\right)_{atm}} - 1\right) \times\ 10^3‰ \tag{2.3}$$

where a and b, respectively, are mass numbers of heavy and light isotopes of gas X. The fractions $\left(\frac{a}{b}\right)_{smp}$ and $\left(\frac{a}{b}\right)_{atm}$ are concentration ratios measured in sample gas and dry atmospheric air, respectively. We define in more detail the three main components of δ_{NET} throughout this section. Figure 2.1 shows expected steady-state δ_i profiles (section 2.2.2.1) for each of the isotope ratios measured in this study.

2.1.1.1. Gravitational Settling

In a column of gas in hydrostatic balance, total pressure increases exponentially with depth. Individual gas partial pressures are governed by the same balance, such that denser gas species increase in concentration (pressure) more than light species with depth. This enrichment of heavy versus light gas species is known as gravitational settling and has been observed in nature in porous media such as firn (Craig et al., 1988) and sand dunes (Severinghaus et al., 1996). Its steady-state effect, expressed in delta notation, for any gas ratio, i, is given (in ‰) by:

$$\delta_{grav}(i,z) = \left[\exp\left(\frac{\Delta m_i g z}{RT(z)}\right) - 1\right] \times 10^3‰ \tag{2.4}$$

where Δm_i is the mass difference in kg mol^{-1} between the heavy and light isotopes in ratio i, g is gravitational acceleration (9.8 m s^{-2}), z is depth in m (with z positive downwards), R is the ideal gas constant (8.314 J K^{-1} mol^{-1}), and $T(z)$ is mean temperature in K at depth z.

2.1.1.2. Thermal Diffusion

In the presence of a temperature gradient in a column of gas, individual species diffuse preferentially according to their molecular mass, with low-mass species generally moving toward the warm end (Grew & Ibbs, 1953). This effect, called thermal diffusion fractionation, has been observed in firn (Severinghaus et al., 2001) and sand dunes (Severinghaus et al., 1996) as well as measured extensively in laboratory experiments (Grachev & Severinghaus, 2003; Kawamura et al., 2013). At UZ depths below the influence of the seasonal cycle, the vertical temperature difference between the surface and a depth z, is given by the geothermal gradient, Γ, multiplied by z. This temperature difference leads to thermal diffusion fractionation of a magnitude (in ‰) given by:

$$\delta_{\text{therm}}(i,z) = -\Omega_i \, \Gamma \, z \tag{2.5}$$

where Ω_i is the thermal diffusion sensitivity of ratio i in ‰ K^{-1}, Γ is the geothermal gradient in K m^{-1}, and z is depth in m.

2.1.1.3. Diffusion Against Vertical Fluxes

The deep UZ (relative humidity →100%) diffusively transports water vapor upward to the drier lower atmosphere at steady state. From observations of O_2 and N_2 isotope ratios in a sand dune, (Severinghaus et al., 1996) first discovered that this upward flux of water vapor induces kinetic fractionation of "stagnant" UZ gases, leading to a depletion of heavy relative to light isotopes within the moist UZ. This phenomenon, known as the "water vapor flux fractionation effect," results because of the lower binary diffusivities of heavy isotopologues relative to light isotopologues diffusing against water vapor (Fuller et al., 1966). In other words, the upward flux of water vapor advects stagnant UZ gases (e.g. noble gases) upward, and at steady state this advective transport is balanced by downward diffusive transport, as required by mass conservation. This diffusive transport is faster for light isotopologues, leading to their steady-state enrichment vs. heavy isotopologues, relative to the free atmosphere. As derived in Severinghaus et al.(1996), the magnitude of this effect on a gas ratio, i, is approximated (in ‰) by:

$$\delta_{\text{diff}}(\text{i}, \text{z}) \approx \left[\left(\frac{1\text{-}\chi_{\text{k}}(\text{z})}{1\text{-}\chi_{\text{k}}(0)} \right)^{\frac{D_{\text{b-k}}}{D_{\text{a-k}}}\text{-}1} \text{-}1 \right] \times \, 10^3 ‰ \tag{2.6}$$

where *a* and *b* are the heavy and light species, respectively, of ratio *i*, *k* is the steady-state diffusing gas (e.g. water vapor), $\chi_k(z)$ is the mole fraction of gas *k* at depth *z* in the UZ (in m), and D_{a-k} and D_{b-k} are the binary diffusivities (Fuller et al., 1966) of gas species *a* and *b* against gas *k*, respectively, in m^2 s^{-1}. This approximation is valid to within ~0.001‰ (Severinghaus et al., 1996). At ADRS, a substantial deep source of CO_2 similarly leads to steady-state upward diffusion of CO_2 (Walvoord et al., 2005). In our steady-state fractionation model at ADRS, δ_{diff} is composed of fractionation due to upward diffusion of both H_2O and CO_2. In Figure 2.1, the resulting two components of δ_{diff} are shown independently as δ_{H2O} and δ_{CO2}.

Because the UZ depth range considered this study (below 20 m) is saturated with respect to water vapor, changes in χ_{H20} with depth are slight and purely a function of temperature. Because temperature increases with depth along the geothermal gradient, χ_{H20} also increases because warmer UZ air has a higher saturation vapor pressure via the Clausius-Clapeyron relation. Water vapor flux fractionation, therefore, is relatively insensitive to depth (Figure 2.1).

2.1.2 Study Area: ADRS

The ADRS is located adjacent to a closed, state-managed, LLRW disposal site in the Amargosa Desert in Nye County, Nevada (Figure 2.2). The UZ at ADRS, composed mostly of sand and gravel, is about 110 m thick at the locations of the two bores sampled in this study: UZB-2 and UZB-3. Sedimentary layering at ADRS leads to higher lateral than vertical diffusivity, as inferred from a gas tracer study carried out from 2005–06 (Green et al., 2015). Mean annual surface temperature, relative humidity, and ambient air pressure at the site are 21.4 °C, 29.2%, and 91.8 kPa, respectively, according to hourly measurements made over an eight-year span (Johnson et al. 2002, 2007). The geothermal gradient at bores UZB-2 and UZB-3 is 0.046 K m^{-1} (Walvoord et al., 2004). Bores UZB-2 and UZB-3 contain ports spaced irregularly between the surface and depths of 108.8 m and 103.9 m, respectively. These ports consist of nylon tubing connected to 30 cm vertical screens in gravel sealed at the top and bottom by bentonite. The nylon tubing at each sampling port extends up to stations at the surface of each bore where each gas line is kept closed to the atmosphere while not in use. CO_2 concentration profiles at UZB-2 and UZB-3 below ∼50 m similarly increase monotonically to ∼1% by volume above the water table (Walvoord et al., 2005). Because a mid-depth CO_2 peak at UZB-3 is likely due to waste-induced microbial activity (Stonestrom et al., 2004), we take the UZB-2 CO_2 profile as indicative of steady-state in both bores (Appendix 2.B).

UZB-3 is located nearer than UZB-2 to the waste site and as a result, any thermal or chemical anomalies in the UZ below the waste affect UZB-3 samples more than UZB-2. Although persistent horizontal temperature differences are unlikely in most UZs, heat production within the buried waste next to ADRS is possible due to high microbial activity (Mayers et al., 2005). The effect of this potential lateral temperature structure on measured isotope ratios is discussed in Section 2.4.1. Unlike UZB-2, in addition to the nylon sampling tubes, UZB-3 contains a ~5 cm diameter PVC pipe extending to a 1.5-m tall screened interval straddling the water table. Prior to the April 2015 sampling this pipe was fitted with a PVC cap (Figure 2.S1a). Extensive UZ gas sampling to characterize contaminants was done prior to noble gas sampling in April 2015, potentially inducing a downward pressure gradient and drawing atmospheric air to the water table through this unsealed cap. In January 2016, an adjustable rubber-sealed cap (Figure 2.S1b) was installed to prevent the UZB-3 pipe from being a potential conduit to the atmosphere.

2.2. Methods

2.2.1. Steady-state fractionation model

Expected values of δ_{NET} in the ADRS UZ are time invariant. We model the individual components δ_{NET} (Figure 2.1) using equation 2, evaluated via equations 4-6. The model is constructed using mean site parameters at ADRS (pressure, temperature, geothermal gradient, surface humidity, and CO_2) and their estimated uncertainties. The 2σ uncertainty of the model is estimated by 1000 Monte Carlo simulations with assumed Gaussian variance of site parameters.

In this steady-state model, $T(z)$ (equation 4) is given by $T_{surf} + \Gamma z$, where T_{surf} is mean annual surface temperature. In the model, T_{surf} is 21.4 ± 0.4 °C (Johnson et al. 2002, 2007), Γ is 0.046 ± 0.005 K m^{-1} (Walvoord et al., 2004), and z ranges from 20-110 m below the surface with uncertainty assumed to be ± 93 cm (1σ). The uncertainty in sample depth results from the vertical extent of the UZ pore space from which samples were drawn. We estimated this value to be the radius of a sphere with volume equal to the ~2 L min^{-1} pumping rate (Section 2.2.2) multiplied by the average pumping time elapsed after flushing and sample collection (~40 min) divided by the mean ADRS porosity of 0.24 (Andraski, 1996). Thermal diffusion sensitivities (equation 5) are based on published values for isotopes of Ar (Grachev & Severinghaus, 2003), Kr (Kawamura et al., 2013) and Xe (Kawamura et al., 2013). Binary diffusivities (equation 6) are calculated according to the method of (Fuller et al., 1966) as described in (Reid et al., 1977).

At ADRS, we assume water-vapor saturated air throughout the entire modeled UZ (20–110 m) and 0.005 ± 0.001 mole fraction of water vapor at the surface (Johnson et al. 2002, 2007). ADRS also has a constant upward flux of CO_2 driven by a mole fraction of ∼0.01 at the water table. We parameterize the CO_2 profile at ADRS based on past UZB-2 measurements and their uncertainties (Appendix 2.B, Walvoord et al., 2005).

2.2.2. Unsaturated Zone Gas Sampling

Gas samples were collected from seven depths at UZB-2 and six depths at UZB-3 in April 2015 (Figure 2.2). Because the focus of this study is steady-state fractionation, we limited the influence of the seasonal temperature and moisture changes, which affect only the top few meters of the unsaturated zone, by exclusively sampling below 20 m. Two replicate 2-L glass flasks were filled from each depth. Each flask was filled by purging the 4 mm (internal diameter) tubing 20 times before pumping UZ gas through thermally insulated fluorocarbon tubing (Dekoron®) at ~2 L min^{-1} for 10 min. A magnesium perchlorate trap was used to remove moisture upstream of the tubing. The tubing included ~1-m long coils both upstream and downstream of the flask to prevent ambient air from entering the flask during the 10 seconds between turning off the pump and closing the valves. Figure 2.S5 contains a diagram of the sample collection setup. At UZB-2, samples were collected at depths of 24.1, 34.1, 47.9, 57.6, 94.2, 106.4, and 108.8 m. At UZB-3, sample were collected at depths of 23.8, 48.6, 72.1, 82.4, 94.1, and 103.9 m.

In May 2016, four deep ports were resampled to test the hypothesis of atmospheric contamination during the 2015 sampling. Samples were collected from 106.4 m and 108.8 m at UZB-2 and 82.4 m and 103.9 m at UZB-3. One 2-L glass flask was filled from each of these four depths following the same procedure used in the prior year.

2.2.3. Sample Preparation and Analysis

Stable isotope ratios of argon ($\delta^{40}/_{36}$Ar, $\delta^{40}/_{38}$Ar), krypton ($\delta^{86}/_{82}$Kr, $\delta^{86}/_{83}$Kr and $\delta^{86}/_{84}$Kr) and xenon ($\delta^{136}/_{129}$Xe, $\delta^{134}/_{129}$Xe and $\delta^{132}/_{129}$Xe) were measured in the Noble Gas Isotope Laboratory at Scripps Institution of Oceanography, broadly following techniques of Kawamura et al. (2013). Each measured aliquot was extracted from the sampling flask into a ∼100 cm^3

evacuated volume before being transferred through a water trap (–80 to –100 °C) into a dip tube immersed in liquid helium.

The dip tube was then connected to a secondary vacuum line and gettered at 900 °C with SAES Zr/Al getter sheets before being transferred to a secondary dip tube immersed in liquid helium. This dip tube was then analyzed on a Thermo-Finnigan MAT 253 dual inlet mass spectrometer after allowing a minimum of three hours of equilibration.

Sample analysis was completed in two phases: one main campaign from September 2015 to January 2016 (campaign A) and a subsequent minor campaign from May to June 2016 (campaign B). Campaign A included measurement of six to seven replicate aliquots from each depth sampled in April 2015. Campaign B included three replicate aliquot measurements from each of the four depths sampled in May 2016 as well as reanalysis of two replicate aliquots (collected in April 2015) from the deepest ports of both UZB-2 and UZB-3 (see Appendix 2.A). The run sequence on the mass spectrometer was modified for campaign B in order to avoid an artifact in Ar isotopic measurements caused by low measurement pressures and validate an apparent pressure sensitivity correction to previous Ar isotopic measurements (see Appendix 2.A).

Measured isotope ratios were normalized to the mean of dry atmospheric air replicates collected off the Scripps pier in La Jolla, CA. These replicate aliquots were collected, prepared, and analyzed throughout each measurement campaign in the same manner as other sample aliquots (11 replicates during campaign A and 6 during campaign B). During campaign A, three aliquots from a flask of air collected from the surface at ADRS were measured, using the same equipment used for UZ sampling. All mean isotope ratios measured in ADRS surface samples agreed (within $2\sigma_{pooled}$) with the mean pier air values, confirming that our sampling technique does not fractionate noble gas isotopes.

During campaign A, five blocks (25 integration cycles per block, 26 s integration time) of xenon and krypton isotopes each were measured at 350 mV (mass 132) and 800 mV (mass 82) respectively. Four blocks of argon isotopes (16 integration cycles per block, 16 s integration time) were measured at 5500 mV for mass 36 (actual intensities dropped to 3000 mV, see Appendix 2.A). Inlet gas pressures were >40 mbar during Kr and Xe analysis, but as low as 20 mbar during Ar measurements due to consumption of the aliquot during the ~10-hr run. During campaign B, xenon and krypton isotopes were measured in the same manner, except two 25-cycle Kr isotope blocks were removed to accommodate higher pressure (11000 mV, ~45 mbar inlet pressure) argon measurements. Incomplete gettering of several campaign B aliquots resulted in isobaric interference with Xe isotopes. Mass spectrum comparisons between ungettered UZ and standard gases revealed a non-Xe peak in UZ gas centered near mass 134. We surmise that this contaminant was from known abundant chlorofluorocarbon species in the Xe mass range in ADRS UZ air [*Baker et al.*, 2012]. In campaign B, we observed large disagreement among replicate aliquots (e.g. ~ 1‰ for $\delta^{136}/_{129}$Xe) which also showed characteristically high $\delta^{134}/_{129}$Xe, implying isobaric interference in these measurements. We concluded that getter sheet manufacturing inconsistencies led to incomplete gettering. In response, we increased the number of getter sheets used in campaign B to 56 (from 36 in campaign A) to ensure complete gettering. Measurements of aliquots affected by isobaric interference have been excluded and aliquots gettered with additional sheets showed improved Xe isotope agreement, with pooled standard deviations (σ_{pooled}) comparable to those of campaign A (Table 2.1). Measured isotope ratios were corrected for pressure imbalances between the pressure-adjusting bellows containing sample and standard gases via pressure imbalance sensitivity tests run every one to two weeks throughout each campaign. The pooled standard deviations of isotope ratios measured in each campaign are given in Table 2.1.

2.2.4. Inverse model applications

At ADRS, known UZ parameters such as vertical gradients of temperature, water vapor, and CO_2 were used to directly estimate the magnitude of steady-state noble gas isotope fractionation using a forward model (Section 2.1.1). In principle, however, measured noble gas isotope ratios could be used to solve an inverse problem in order to estimate one or more UZ parameters. Here we introduce an inverse approach for two applications: 1) to resolve the extent of mixing with atmospheric air introduced at depth (specific to ADRS, Section 2.3.2) and 2) to estimate the past depth of a gas parcel within a UZ from reconstructed steady-state UZ noble gas isotope ratios (e.g. from paleorecharge sequestered as deep groundwater, a potential future application discussed in Section 2.4.2).

For the first application, determining atmospheric admixture extent of each sample, $f_{atm}(z,b)$, a cost function, $C(z,b)$ is defined as follows:

$$C(z,b) = \sum_{i=1}^{N} \left(\frac{\delta(i,z,b)_{meas} - (1 - f_{atm}(z,b))\delta(i,z,b)_{model}}{\sigma(i,z,b)} \right)^2 \tag{2.7}$$

for a sample collected at depth, z, in bore, b, where i is one of $N=8$ independent isotope ratios measured in this study, $\delta_{meas}(i,z,b)$ and $\delta_{model}(i,z,b)$ are replicate-mean measured and steady-state modeled (Equation 2.2) isotope ratios (in ‰), respectively, and $\sigma(i,z,b)$ is the quadrature sum of measurement and model standard deviations of isotope ratio i (in ‰). Because $\delta_{model}(i,z,b)$ is fully determined based on known ADRS UZ parameters, the eight $\delta_{meas}(i,z,b)$ values at each bore-depth pair comprise an overdetermined system of equations with one unknown: $f_{atm}(i,z,b)$. For 1000 Monte Carlo simulations, in which each $\delta_{meas}(i,z,b)$ is perturbed with Gaussian random noise with zero-mean and standard deviation equal to $\sigma(i,z,b)$, $f_{atm}(i,z,b)$ is solved for by minimizing Equation 2.7, which amounts to a linear least squares approach.

For the second application, estimating depth from a suite of measured or inferred UZ noble gas isotope ratios, we define an alternate cost function that weights individual isotope ratios based on their relative sensitivity to gravitational settling. In this case, depth is treated an unknown variable and is estimated through cost-function minimization (nonlinear least squares). For each sample, *C(z,b)* is defined similarly to Equation 2.7:

$$C(z,b) = \sum_{i=1}^{N} W_i \left(\frac{\delta(i,z,b)_{meas} - \delta(i,z,b)_{model}}{\sigma(i,z,b)}\right)^2 \tag{2.8}$$

where W_i is the weighting factor (defined below), $\sigma(i,z,b)$ is the measurement standard deviation, and $\delta(i,z,b)_{model}$ is calculated (Equations 2, 4-6) using a modern value for Γ, prescribing or neglecting a vertical CO_2 gradient (as described in Section 2.4.2), and leaving the other two variables in the model (depth and water vapor gradient) as free parameters. Equation 2.8, therefore, comprises a system of eight equations and two unknowns. While the steady-state vertical CO_2 gradient at ADRS is substantial, we note that UZ depth estimation would be most applicable in settings without high deep CO_2 concentrations (and without correspondingly strong CO_2-flux fractionation). In Section 2.4.2, we examine the sensitivity of UZ depth estimates (via Equation 2.8) to prescription of a steady-state UZ CO_2 profile or omission of CO_2-induced fractionation altogether.

Because the relative contribution of water vapor flux fractionation is small for each measured isotope ratio, we do not expect to accurately resolve past UZ water vapor mole fraction differences between the water table and surface using heavy noble gas isotopes. Instead, this inverse model only roughly estimates the small magnitude of water vapor flux fractionation in order to isolate the contribution of gravitational settling fractionation and therefore resolve depth. Indeed, our decision to measure Ar, Kr and Xe isotopes was motivated by the expected high sensitivity of these isotope ratios to gravitational settling fractionation. To further increase the composite sensitivity of a suite of Ar, Kr and Xe isotopes to depth within the UZ, we define a weighting W_i in the following manner:

$$W_i = \frac{Q_i}{Q_{40/36}} \tag{2.9}$$

where Q_i represents the ratio of gravitational settling fractionation per meter to thermal diffusion fraction per Kelvin for isotope ratio i, such that weights are calculated relative to this ratio for $\delta^{40}/_{36}$Ar. Formally, Q_i is defined:

$$Q_i = \frac{\partial\delta_{grav,i}/\partial z}{\Omega_i} \tag{2.10}$$

where $\delta_{grav,i}$ and Ω_i are calculated at 293 K. $\partial\delta_{grav,i}/\partial z$ is given by its first Taylor approximation:

$$\partial\delta_{grav,i}/\partial z = \frac{\Delta m_i g}{RT} \tag{2.11}$$

where Δm_i is the mass difference between heavy and light isotopes for isotope ratio, i, in amu, R is the ideal gas constant in J K^{-1} mol^{-1}, and T is temperature in K.

Table 2.1 contains the weights, mass differences, and measurement precision of isotope ratios measured in this study. Because δ_{grav} is independent of atomic mass (equation 4) and $|\delta_{\mathrm{diff}}| / |\delta_{net}|$ decreases with atomic mass, $|\delta_{\mathrm{grav}}| / |\delta_{net}|$ increases with atomic mass. Therefore, isotope ratios of heavy gases are weighted more than those of light gases. Specifically, Xe and Kr isotope ratios are respectively weighted roughly five and four times more than Ar isotope ratios. $|\delta_{\mathrm{diff}}| / |\delta_{net}|$ decreases with atomic mass because D_{a-k} / D_{b-k} approaches unity. In other words, the depth signal of interest is strongest in the xenon isotopes.

2.3 Results

2.3.1. Measured Isotope Ratios in April 2015 Samples

Replicate-mean δ values of all eight isotope ratios measured at all depths below 60 meters fell below modeled values (i.e. ratios were depleted in the heavier isotope, Figure 2.3). Additionally, replicate-mean δ measurements across all depths and both bores were always greater than or equal to atmospheric air (δ =0), within 1σ. The degree to which measured values deviated from the model below 60 meters was substantially higher at UZB-3 than UZB-2. Figure 2.3 shows replicate-mean measured δ values (open markers) at each of the 13 sampled depths alongside the modeled steady-state isotopic profiles (δ_{NET}) described in Section 2.1.1.

The UZB-3 sample nearest to the water table (103.9 m depth) was effectively atmospheric with respect to the eight measured isotope ratios. Normalizing each ratio by its isotopic mass difference (e.g. 4 for $\delta^{40}/_{36}Ar$), the replicate-mean, ratio-mean, per-mass-unit δ value was 0.004 ± 0.009 ‰ amu^{-1} at this depth. Above this depth, the next three sampled UZB-3 depths (94.1 m, 82.4 m, and 72.1 m) monotonically decreased in deviation from the model (increased in δ value) in all eight measured isotope ratios. Though less extreme, a similar decrease in deviation from the model with height above the water table was apparent in UZB-2.

We hypothesize that extensive sampling from the UZ in the week before our April 2015 field study induced bulk flow of atmospheric air through an unsealed PVC pipe (Figure 2.S1) directly into the deep UZ above the water table at UZB-3. Pumping at shallower UZB-3 depths prior to our sampling would have spread this unfractionated atmospheric air upward from ~110 m depth, where it would have diluted the preexisting UZ air, until ~50m depth, where contamination was effectively undetectable (Section 2.3.2). This volume of atmospheric air between 50-110 m would also have spread laterally outwards and affected the deeper portion of UZB-2. We tested this hypothesis in two ways. First, we ran the inverse model (Section 2.2.4) with measured δ values and prescribed ADRS conditions (surface pressure, temperature, absolute humidity, geothermal gradient, and CO_2 profiles) to solve for the fraction of atmospheric contamination at each depth. We tested for model convergence around a narrow range of likely atmospheric contamination percentages at each depth (Section 2.3.2, Appendix 2.C). Second, we returned to ADRS in May 2016 after installation of a gas-tight seal in the UZB-3 PVC pipe and collected samples from two deep ports in UZB-2 (106.4 m and 108.8 m) and UZB-3 (82.4 m and 103.9 m) to determine if isotope ratios had progressed toward the steady-state modeled δ values.

2.3.2. Atmospheric Contaminant Determination and Correction

The percentage of atmospheric contamination was estimated at each depth using 1000 Monte Carlo simulations of the inverse model described by Equation 2.7. Replicate-mean δ values were perturbed with normally distributed measurement uncertainties as described in Section 2.2.4 in order to estimate the mean and uncertainty of atmospheric contaminant fractions in each sample, $f_{atm}(z,b)$. Figure 2.4 shows the results of atmospheric contamination estimation in April 2015 samples. The atmospheric contaminant percentage in each bore decreased between the water table and ~50m depth. At UZB-3, the deepest sample (103.9 m) was estimated to be 98 ± 1% pure atmospheric air.

To qualitatively evaluate the goodness of fit among the eight measured isotope ratios, we corrected the replicate-mean δ values at each depth for mixing with the estimated concentration of atmospheric air. Figure 2.3 (filled markers) shows these air contamination-corrected profiles and their good general agreement with the steady-state model. Due to large atmospheric contamination in the two deepest UZB-3 samples, the remaining non-atmospheric signal is too small to meaningfully estimate and these samples are therefore excluded from Figure 2.3.

We more quantitatively assessed the least-squares estimation of atmospheric contamination by independently calculating alternate contamination estimates based on individual isotope ratios measured in each sample. The details of the analysis are presented in Appendix 2.C. The 95% confidence intervals of individual atmospheric contaminant fraction estimates overlap for the six Xe and Kr isotope ratio-based estimates for all samples collected at ADRS (Figure 2.S6). In six of thirteen total samples, atmospheric contaminant fractions estimated independently by Ar isotope ratios diverge slightly from estimates derived independently from Kr and Xe isotope ratios. Given that Ar is substantially more sensitive to thermal diffusion and CO_2-flux fractionation, uncertain and potentially large horizontal thermal gradients as well as uncertainty concerning the steady-state CO_2 profile may explain why Ar isotopes sometimes yield differing atmospheric contaminant estimates. We further discuss these complications for modeling Ar isotope fractionation at ADRS in Section 2.4.1.

2.3.3. Measured Isotope Ratios in May 2016 Samples

The mean δ values measured in three replicate aliquots from four deep samples collected in May 2016 (UZB-2: 106.4 m and 108.8 m; UZB-3: 82.4 m and 103.9 m) are shown in Figure 2.5. Whereas isotope ratios were relatively unchanged from April 2015 in three of these four samples, all eight replicate-mean δ values at 103.9m in UZB-3 increased substantially toward the steady-state model. We interpret these results as evidence of partial diffusive resettling after the atmospheric contamination event in April 2015 and suggest that the sealed cap on the UZB-3 PVC pipe (Figure 2.S1) had prevented further atmospheric contamination.

We note that relative to their April 2015 deviation from the steady-state model, δ values of Ar isotopes (faster diffusivity) increased more than those of Kr and Xe isotopes (slower diffusivity) in the UZB-3 103.9m sample. With incomplete knowledge of the three-dimensional structure of effective diffusivity at ADRS and the initial amount and location of atmospheric air contamination, we cannot quantify the degree of diffusive resettling. Nonetheless, we note generally that the pattern of isotopic changes from April 2015 to May 2016 is consistent with our hypothesized contamination event and steady-state model.

The smaller April 2015-May 2016 changes in UZB-2 and at 82.4m in UZB-3 may be explained by less initial atmospheric contamination (below 50% at each of these depths, Figure 2.4). The driver of isotopic rebound after the contamination, as hypothesized, is equivalent to the model-measurement discrepancy, $\Delta\delta(i,z,b) = \delta(i,z,b)_{2015} - \delta(i,z,b)_{model}$. Because $\Delta\delta(i,z,b)$ decreases in magnitude above and laterally away from the bottom of UZB-3, the steeper spatial gradient, $\nabla\cdot(\Delta\delta(i,z,b))$ in the deepest portion of UZB-3 versus the overlying depths would lead to higher diffusive transport according to Fick's law. As a result, there is less isotopic change from April 2015-May 2016 at the considered.

2.4. Discussion

2.4.1. Noble gas isotopes as tracers at ADRS

Measured isotope ratios of Ar, Kr and Xe in UZ samples collected at the ADRS deviated from expected steady-state values in a systematic way. All April 2015 measured isotope ratios (δ values) at all depths below 60 m were lower than expected, especially at UZB-3 where the deepest sample (103.9 m) closely approximated atmospheric noble gas isotopic composition (Figure 2.3). We applied a weighted inverse model (section 2.2.4) to estimate the fraction of atmospheric contaminant at each depth, which showed a monotonic decrease in contaminant fraction with height above the water table until ~50 m (Figure 2.4). Subsequent analysis on a subset of deep ports resampled in May 2016 showed substantial development of isotope ratios in the deepest

UZB-3 sample towards the expected steady-state concentration (Figure 2.5). We interpret deviations of deep UZ samples from the expected steady-state profile as evidence of an atmospheric contamination event at the UZB-3 water table prior to sampling in April 2015.

Above 60 m, measured δ values were much nearer to the steady-state model, except for Ar isotopes at both UZB-2 and UZB-3. Ar isotope δ values in UZB-3 especially were higher than expected, consistent with unexpected thermal diffusion fractionation, possibly associated with heat produced by microbial activity within the buried waste at the neighboring waste disposal facility (Stonestrom et al., 2004). A waste-generated heat source could lead to a horizontal temperature gradient, driving thermal diffusion fractionation. Because lighter isotopes diffuse preferentially toward warmer temperatures (Grew & Ibbs, 1953), δ values would increase at UZB-3 and, to a lesser extent, at UZB-2, which is farther from the waste. Because the thermal diffusion sensitivities (per mass unit) are more than four times greater for isotopes of Ar (Grachev & Severinghaus, 2003) than Kr and Xe (Kawamura et al., 2013), we suggest that the poorer fit of corrected Ar δ values to the model is a consequence of a two-dimensional horizontal thermal structure, plausibly due to the heat generated by decomposition in the horizontally-adjacent waste dump. Uncertainty in the steady-state upward CO_2 flux may also explain why independent Ar isotope-derived estimates of atmospheric contamination in some cases diverge from those of Kr and Xe isotopes (Appendix 2.C), since Ar isotopes are more sensitive to CO_2 flux fractionation (high $|\delta_{\mathrm{CO2}}| / |\delta_{NET}|$). A more complete correction would estimate and remove the influence of horizontal temperature gradients as well as atmospheric contamination. However, due to the low sensitivity to thermal diffusion fractionation (small $|\delta_{\mathrm{therm}}| / |\delta_{NET}|$) among the isotope ratios measured in this study, the inverse model (described in Section 2.2.4) could not reasonably resolve horizontal temperature gradients. The sensitivity of Ar isotopes to processes other than gravitational fractionation justify its relative downweighting in the inverse model we propose for depth estimation.

2.4.2. Potential applications of noble gas isotopes in paleogroundwater

Preferential-flow features that provide direct conduits between the water table and atmosphere will limit the proposed application to unfissured unsaturated zones, like that present at the ADRS (Green et al., 2015; cf. Weisbrod et al., 2009; Mourzenko et al., 2014). In the absence of these uncommon disruptions, we expect noble gas isotopes to follow the steady-state model outlined in section 2.1.1. The good agreement of atmospheric contaminant-corrected ADRS measurements with the steady-state model adds confidence to this expectation.

One potential application of this suite of eight noble gas isotope ratios, measured in paleogroundwater, is its capacity to estimate past water-table depth. Over long timescales, groundwater with dissolved UZ gases is sequestered from the atmosphere in confined aquifers. Because the heavy noble gas isotopes in these paleogroundwaters were inherited from a past UZ, they contain information about gravitational settling fractionation and therefore past UZ thickness (i.e. water-table depth).

The reconstruction of steady-state UZ Ar, Kr and Xe isotope ratios from measurement of dissolved gases in groundwater would be complicated by fractionation during dissolution (Tempest & Emerson, 2013). This additional fractionation influences measured isotope ratios in two ways: 1) the slightly different isotopic solubilities induces “solubility fractionation” at equilibrium, and 2) the partial dissolution and potential reequilibration of so-called “excess air” may induce further fractionation. At present, solubility fractionation factors for isotopes of Xe and Kr are unknown and would need to be empirically determined prior to the application of this proposed paleo water-table depth estimation tool. The solubility fractionation factor for $\delta^{40}/_{36}$Ar is

~1.07‰ [*Tempest and Emerson*, 2013]. To constrain the fractionation due to excess air, a noble gas groundwater excess air model would need to be extended to Ar, Kr and Xe isotopes. The closed-system equilibration (CE) model (W Aeschbach-Hertig et al., 2000), which has been widely used for paleotemperature reconstruction, assumes partial dissolution of persistent entrapped air in solubility equilibrium with groundwater. This model would be applicable to isotopes and only requires knowledge of solubility fractionation factors for all measured isotope ratios. Another common excess air model, the partial reequilibration (PR) model (Stute et al., 1995), assumes diffusive reequilibration after complete dissolution of entrapped air. The extension of this model to isotopic measurements would require empirical determination of kinetic fractionation factors for each isotope ratio across the air-groundwater interface. This kinetic fractionation factor has been measured for $\delta^{40}/_{36}$Ar, but with wide disagreement between two independent studies (Tempest & Emerson, 2013; Tyroller et al., 2014). We suggest that future attempts to quantify past water-table depths from measurement of dissolved noble gas isotopes in paleogroundwater begin with samples of known low excess air concentrations and good fit of bulk noble gas concentrations using the CE model, to reduce potential sources of uncertainty.

By accounting for fractionation due to dissolution, measured dissolved noble gas isotope ratios could be converted to paleo-UZ noble gas ratios. Paleo water-table depth could then be estimated by using the weighted inverse model described in Section 2.2.4 (Equation 2.8). Ar isotope measurements at ADRS displayed poorer agreement with the model than did Kr and Xe isotopes, likely due in part to uncertainty about the magnitude of the steady-state CO_2 flux. Because the proposed water table depth estimation method would be most successful at sites with known weak UZ CO_2 fluxes, we investigated the sensitivity of the inverse model to the inclusion/exclusion of Ar isotopes and CO_2-flux fractionation.

This sensitivity test was carried out using synthetic data produced by the forward UZ fractionation model (Section 2.1) run at ADRS environmental conditions (geothermal gradient, temperature, pressure, humidity, and CO_2). As outlined in the method section, we ran 1000 Monte Carlo simulations at each depth from 20 to 110 meters perturbing the modeled isotopic values with normally distributed random values of zero mean and standard deviation equal to pooled measurement standard deviations (campaign A). For each simulation, we estimated depth under four configurations of the inverse model: 1) using all eight isotope ratios and accounting for CO_2 flux fractionation, 2) using all eight isotope ratios but neglecting CO_2 flux fractionation, 3) using only Kr and Xe isotopes and accounting for CO_2 flux fractionation, and 4) using only Kr and Xe isotopes and neglecting CO_2 flux fractionation. Figure 2.6 shows the ability of the inverse model to estimate true depths under each scenario.

Under all scenarios, root mean squared deviations (RMSD) between synthetic measurements and the steady-state model are less than 6 m. Scenario 2, which includes Ar isotopes and neglects CO_2-flux fractionation, exhibits the largest deviations from true depths. However, in the shallower UZ (above ~95 m), the scenarios that include Ar isotopes (1 and 2) display better agreement with true values than the scenarios that ignore Ar isotopes (3 and 4). We suggest that including Ar isotopes and neglecting CO_2-flux fractionation in future UZ applications (scenario 2) is justifiable for carefully selected sites with negligible deep CO_2 sources. However, for applications in sites where substantial deep sources of CO_2 in the past cannot be ruled out, the bias from excluding CO_2-flux fractionation would be significantly reduced by excluding Ar isotope measurements as inverse model constraints. Based the RMSD of scenarios 1 and 2, we suggest that the ±1σ uncertainty of past water-table depth estimation for carefully selected sites without strong CO_2 fluxes would be around 1 m, plus an additional contribution to total uncertainty from the conversion of dissolved gas to steady-state UZ air isotope ratios.

2.5. Conclusions

Measured Ar, Kr and Xe isotope profiles at ADRS are consistent with the hypothesis that steady-state UZ fractionation is governed by gravitational settling, thermal diffusion, and diffusion against vertical fluxes of gases, after accounting for binary mixing with atmospheric air. Gravitational settling is the dominant fractionation process, leading to δ_i-depth profiles that are strongly dependent, nearly linear functions of depth for isotopes of these heavy noble gases. This is expected, as the magnitude of gravitational settling fractionation is independent of atomic mass (equation 4) while the magnitudes of the water vapor and CO_2 flux fractionations decrease with atomic mass. By weighting isotope ratios by their sensitivity to gravitational settling, we demonstrate that an inverse model (section 2.2.4) can accurately estimate depth from a suite of high-precision Ar, Kr and Xe isotope measurements.

The ability to estimate depth from UZ gas measurements has important applications for quantitative reconstructions of past climate change. Because dissolved gases in groundwater are inherited from the UZ air at the water table, we suggest that noble gas isotope measurements in paleogroundwater may enable accurate resolution of mean water-table depth at the time of recharge. Laboratory determination of kinetic and solubility fractionation factors for noble gas isotope dissolution in water will be essential for this potential future application. With knowledge of past water-table depth and geothermal gradient, NGTs may be used to reconstruct MAST with greater confidence by removing a bias associated with geothermal heat. Together, accurate estimates of both water-table depth and MAST may place important quantitative constraints helpful in understanding and modelling past hydroclimatic change.

Appendix 2.A: Argon isotope correction

Due to erroneously low inlet pressures during the measurement of argon isotopes in the April 2015 samples, a small correction was made to the measured δ values. This correction was on average –.023‰ and –.009‰, and at most –.050‰ and –.020‰ for measurements of $\delta^{40}/_{36}$Ar and $\delta^{40}/_{38}$Ar, respectively. At low pressure, viscous flow of gas from the inlet to the source of the mass spectrometer begins to transition to molecular flow. This transition induces a small kinetic fractionation, such that the light isotope travels faster than the heavy one and is thus preferentially analyzed. At low Knudsen numbers (high pressure, low mean free path), this fractionation is negligible. However, because the April 2015 samples were analyzed at the end of a long sequence, there was insufficient gas remaining to reach a suitably high pressure. Although both sample and standard inlet pressures were lower than the set point of 5500 mV (expressed in terms of ^{36}Ar voltage), they were balanced. Despite approximately equal pressures between sample and standard gas, there was an apparent systematic trend among argon isotope measurement blocks of the same sample toward lower delta values with lower pressure. This trend was reproduced in subsequent lab experiments by intentionally varying the argon isotope measurement pressure from 3000 to 11000 mV (~15–45 mbar) and examining the response in $\delta^{40}/_{36}$Ar and $\delta^{40}/_{38}$Ar. Because sample and standard inlet pressures were balanced, the mean free paths of argon molecules must have been similar. Thus, we hypothesize that at low pressures (high Knudsen numbers), small differences in the capillary diameters on the standard and sample sides of the inlet lead to differences in the degree of kinetic fractionation due to a reduction in viscous flow. Specifically, we suggest that a slightly narrower capillary on the standard side leads to more kinetic fractionation than the sample side at low total pressure. This would lead measured $\delta^{40}/_{36}$Ar and $\delta^{40}/_{38}$Ar to increase with a decrease in total pressure.

To remove this fractionation from our measurements, we determined apparent pressure sensitivities for $\delta^{40}/_{36}$Ar, $\delta^{40}/_{38}$Ar, and $\delta^{38}/_{36}$Ar from the 368 argon measurement blocks in the April 2015 data set. Apparent pressure sensitivity, *APS*, is defined as the slope of the geometric mean regression of measurement block delta anomalies, δ'_{block}, onto total pressure anomalies, V'_{36}.

$$APS = -\frac{\sigma(\delta'_{block})}{\sigma(V'_{36})} \tag{2.A1}$$

Block delta anomalies (in ‰) are defined as $\delta'_{block} = \delta_{block} - \bar{\delta}_{\text{sample}}$, where δ_{block} is the mean pressure-imbalance corrected delta value of a 16-cycle block and $\bar{\delta}_{\text{sample}}$ is the mean of δ_{block} among all measured aliquots of a given sample (typically 4 blocks/aliquot and six aliquots/sample). Pressure anomalies (in mV) are defined as $V'_{36} = V_{36,block} - 5500\ mV$, where $V_{36,block}$ is the mean standard side intensity at mass 36 over the course of a block. Figure 2.S2 plots δ'_{block} against V'_{36} for all 368 argon isotope measurement blocks. The *APS* determined from these regressions are –0.00010 ‰ mV^{-1}, -0.00008 ‰ mV^{-1} and –0.00004 ‰ mV^{-1} for $\delta^{40}/_{36}$Ar and $\delta^{40}/_{38}$Ar, respectively.

Original argon isotope δ_{block} measurements were then corrected using these *APS* values:

$$\delta_{block,corr} = \delta_{block} - V'_{36} \times APS \tag{2.A2}$$

For the deepest samples of each bore (108.8 m at UZB-2 and 103.9 m at UZB-3), two aliquots from each archived April 2015 sample were re-measured in May 2016 at higher argon pressure (11000 mV). The mean correction among six UZB-2 108.8 m aliquots was rather small: –.006‰ and –.002‰ for $\delta^{40}/_{36}$Ar and $\delta^{40}/_{38}$Ar, respectively. However, the mean correction among six UZB-3 103.9 m aliquots was more substantial: –.049‰ and –.020‰ for $\delta^{40}/_{36}$Ar and $\delta^{40}/_{38}$Ar, respectively. The two sets of re-measured aliquots from each sample agreed well with the corrected values, as shown in Figure 2.S3.

Appendix 2.B: Prescribed steady-state CO_2 profile

The CO_2 depth profile used in our steady-state model was prescribed based on measurements compiled by *Walvoord et al.*, 2005. At ADRS, a persistent, deep CO_2 source is thought to govern steady-state CO_2 concentrations, which increase with depth from atmospheric concentrations near the surface to as high as ~1% mole fraction at depth. Precipitation of calcite from groundwater supersaturated in bicarbonate and microbial activity in the saturated zone are the presumed sources of this deep CO_2 (Walvoord et al., 2005). For our model, we use the measured UZB-2 CO_2 profile instead of UZB-3, because UZB-3 CO_2 concentrations are likely elevated between 0–60 m due to non-steady-state microbial source. High CO_2 concentrations at mid-UZ depths in UZB-3 (up to 2% mole fraction) coincide with high ^{14}C activity of CO_2 (up to 600,000% modern carbon), suggesting microbial respiration of a radioactive carbon source below the waste site (Stonestrom et al., 2004). For our model, we approximated UZB-2 CO_2 as an exponential profile from 42 Pa at the surface to 960 ± 225 Pa at 108.8m. The profile and its 1σ uncertainty are presented in Figure 2.S4.

Appendix 2.C: Agreement of independent versus least-square contamination estimates

Least-squares estimates of atmospheric contamination (Sections 2.2.4 and 2.3.2) are weighted by the measurement and model uncertainties of the eight isotope ratios used as constraints. Here we formally assess the degree to which estimates of atmospheric contamination inferred by individual isotope ratios agree with the least-squares estimates. To start, we formally state our hypothesis of atmospheric contamination:

$$\delta_{meas} = (1 - f_{atm})\, \delta_{model} + f_{atm}\, \delta_{atm} \tag{2.C1}$$

where δ_{meas} and δ_{model} represent measurement and model isotope ratios, respectively, in a given sample.

Noting that δ_{atm} = 0 (by definition), we can rewrite (C1) and solve for f_{atm}.

$$f_{atm} = 1 - \frac{\delta_{meas}}{\delta_{model}} \tag{2.C2}$$

We can then rewrite an independent version of (C2) for any isotope ratio, i, with measurement and model means $\overline{\delta_{meas,i}}$ and $\overline{\delta_{model,i}}$, and uncertainties, $\delta'_{meas,i}$ and $\delta'_{model,i}$, respectively:

$$\overline{f_{atm,i}} \pm f'_{atm,i} = 1 - \frac{\overline{\delta_{meas,i}} \pm \delta'_{meas,i}}{\overline{\delta_{model,i}} \pm \delta'_{model,i}} \tag{2.C3}$$

We note that based on (C3) the individual atmospheric contaminant estimate uncertainties, $f'_{atm,i}$, are large for isotope ratios with high $\frac{\delta'_{meas,i}}{\overline{\delta_{meas,i}}}$ and $\frac{\delta'_{model,i}}{\overline{\delta_{model,i}}}$. For this reason, an unweighted average of all $\overline{f_{atm,i}}$ for *N* isotope ratio measurements (8 in our study) would not be a reasonable approach to estimate f_{atm}. Specifically, argon isotope ratios must be down-weighted relative to other measured isotope ratios, because of their high model uncertainty. The heteroscedasticity of model and measurement uncertainties across the different isotope ratios is our justification for applying weighed least-squares to estimate f_{atm} (Section 2.2.4).

However, evaluating agreement between independent estimates $\overline{f_{atm,i}}$ and our least-squares f_{atm} is a means to assess the validity of our atmospheric contamination hypothesis and subsequent correction. To carry out this evaluation, we estimate $\overline{f_{atm,i}}$ and $f'_{atm,i}$ via 1000 Monte

Carlo simulations for each measured ratio i in each sample across both UZB-2 and UZB-3 (13 sample depths in total). We then compare the 95% confidence ranges of individual $f_{atm,i}$ estimates to the least-squares estimate for each sample. Figure 2.S6 shows this comparison.

The 95% confidence intervals for all six krypton and xenon isotope ratios generally overlap with the least-squared estimates. In roughly half of the sampled depths (6 of 13), argon isotope 95% confidence intervals do not agree with the least-squares estimate. As discussed in the text, uncertainty about both horizontal thermal gradients and the background, steady-state CO_2 profile limit our confidence in the applicability of the model for Ar isotopes at ADRS, given their high sensitivity to thermal diffusion and vertical gas fluxes. We interpret “negative” atmospheric contaminant fractions inferred by Ar isotopes in the shallower UZ to be consistent with thermal diffusion fractionation in response to a waste-related heat source, which would cause Ar isotope ratios at UZB-2 and UZB-3 to be isotopically heavier. The good agreement of the atmospheric contaminant fractions estimated independently by the six Kr and Xe isotope ratios add confidence to the hypothesis of atmospheric contamination, since these isotope ratios are less sensitive to steady-state gas fluxes and to thermal diffusion.

Acknowledgments

We thank the landowner State of Nevada, the site operator U.S. Ecology, and geologist Charles Feast for access to the site and assistance and advice with the field component of this study. USGS reviewer William C. Evans provided helpful feedback, as did 3 anonymous reviewers. Major funding was provided by the National Science Foundation’s Graduate Research Fellowship Program and through NSF grant OPP05-21642. USGS funding was provided through the Toxic Substances Hydrology Program and the National Research Program. All individual

aliquot measurements of Ar, Kr and Xe isotope ratios during campaigns A and B are included in the supplemental data file. Trade names are used for identification purposes only and do not imply product endorsement.

This chapter, in full, is a reproduction of material as it appears in Seltzer, A., Severinghaus, J., Andraski, B., and D. Stonestrom, Steady State Fractionation of Heavy Noble Gas Isotopes in a Deep Unsaturated Zone, *Water Resources Research*, 2017. The dissertation author was the primary investigator and author of this work.

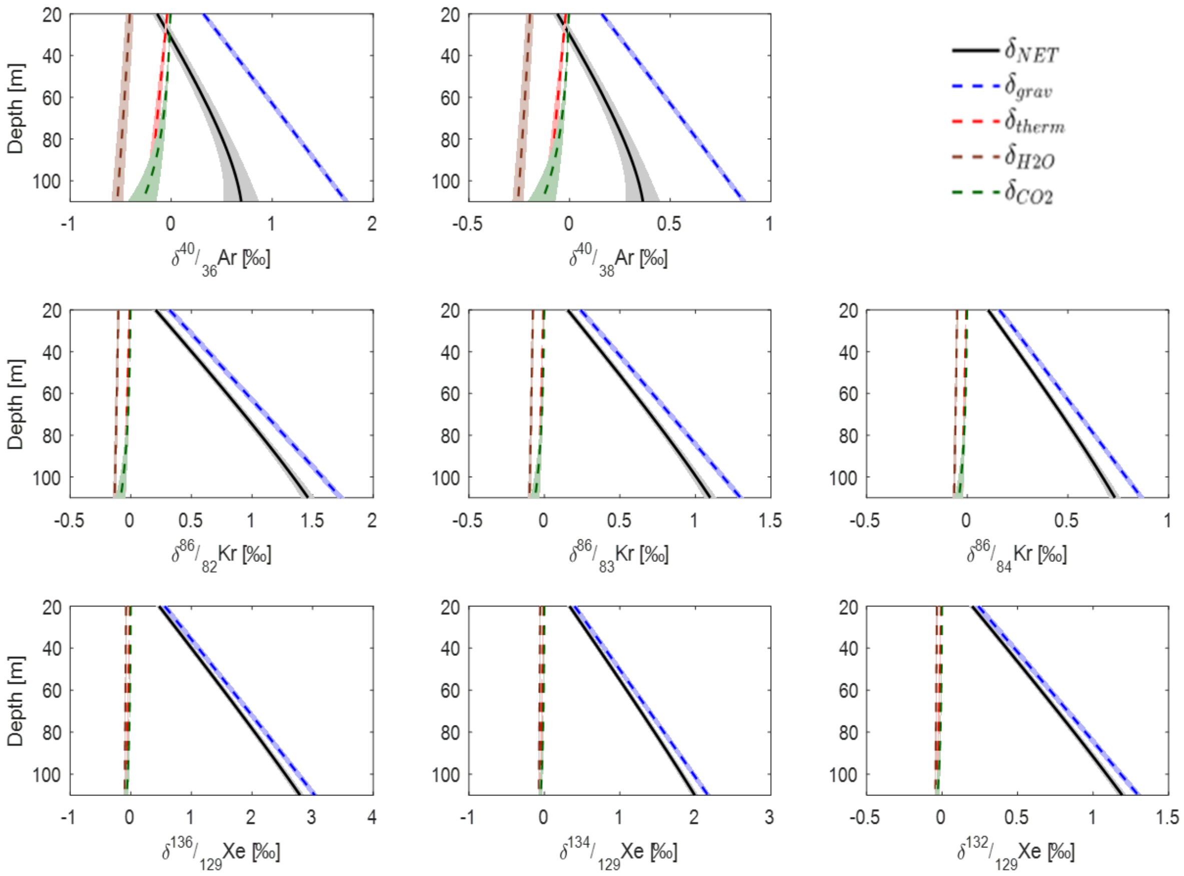

Figure 2.1: Modeled steady-state isotopic fractionation (net and individual components) at ADRS. Inputs to the model include the mean values and uncertainties of eight years of micrometeorolical data from ADRS [*Johnson et al.*, 2002, 2007], measurement-based CO_2 profiles [Figure 2.S4, *Walvoord et al.*, 2005], and the assumption of water vapor saturation below 20 m. Shaded regions indicate 2σ uncertainties of each fractionation component from 1000 Monte Carlo simulations.

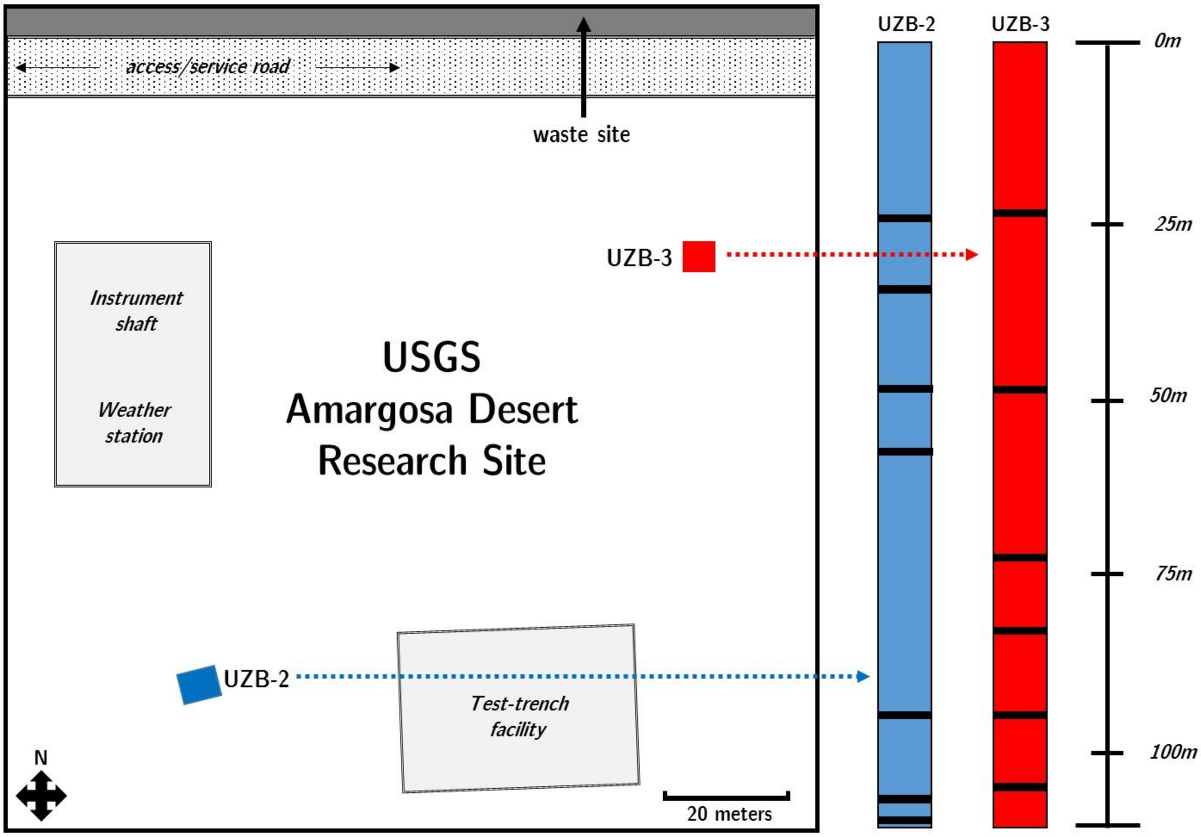

Figure 2.2: Amargosa Desert Research Site (ADRS) map showing locations of unsaturated zone sampling bores UZB-2 and UZB-3, weather station, edge of the closed, low-level waste site, and sampling depths.

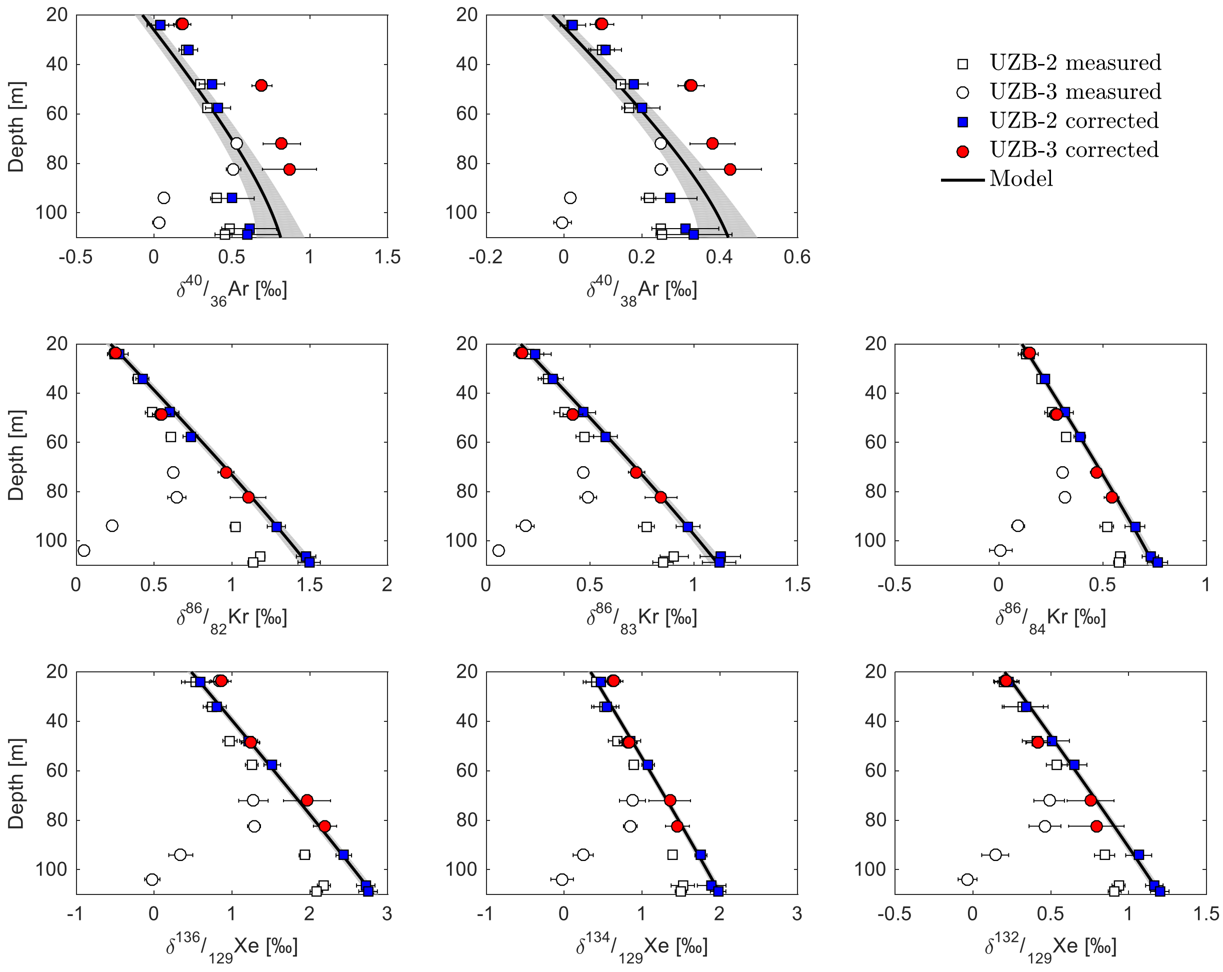

Figure 2.3: Measured and atmospheric contamination-corrected Ar, Kr and Xe isotope ratios in April 2015 ADRS unsaturated zone samples. Corrected values are plotted for all depths except for the two deepest ports at UZB-3, at which the atmospheric contamination fraction is too large (> 80%) to meaningfully remove it and estimate uncontaminated values. Error bars on corrected values indicate 2σ uncertainty based on atmospheric contamination percentage estimated by 1000 Monte Carlo simulations. Error bars on uncorrected measurements indicate 2σ uncertainty based on six to seven replicate aliquot measurements at each depth. Shaded gray region around mean modeled profiles indicates 2σ model uncertainty from 1000 Monte Carlo simulations.

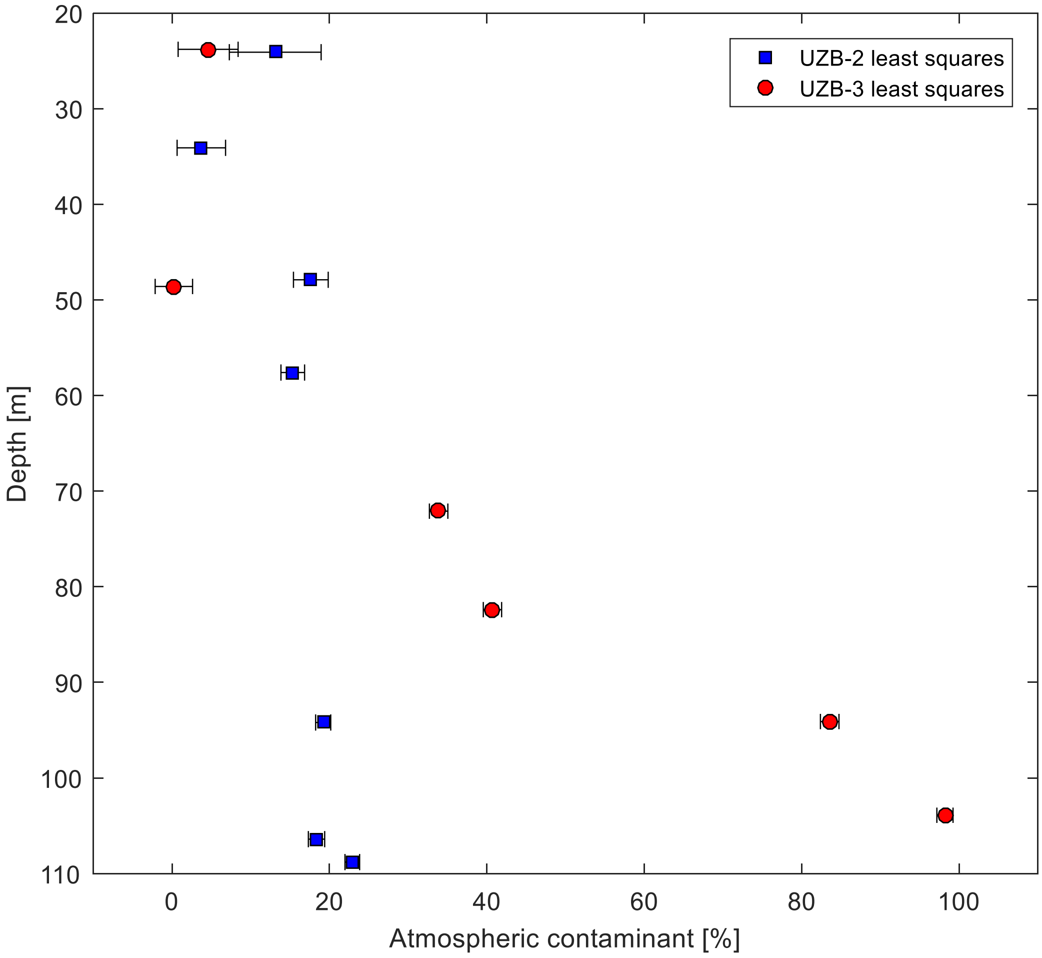

Figure 2.4: Inferred atmospheric contamination percentage at measured sample depths. Atmospheric contamination is determined by weighted least squares based on the deviations between the eight measured and modeled noble gas isotope ratios at each depth. Error bars indicate 1σ uncertainty based on 1000 Monte Carlo simulations with variance prescribed by measurement and model uncertainties.

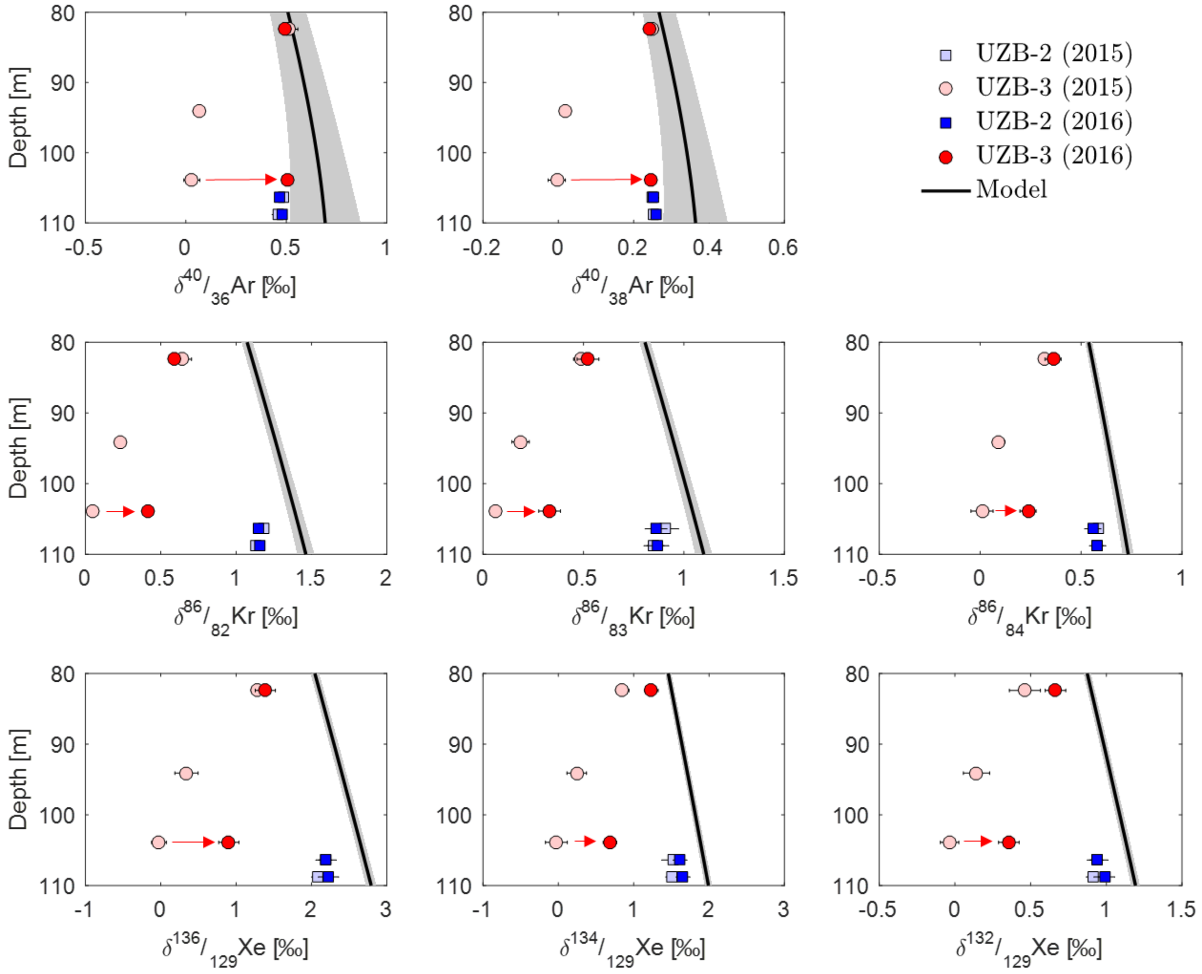

Figure 2.5: Measured Ar, Kr and Xe isotope ratios in April 2015 (light colors) and May 2016 (dark colors) ADRS unsaturated zone samples. May 2016 measurements were made on samples collected at 106.4 m and 108.8 m in UZB-2 and 82.4 m and 103.9 m in UZB-3. Red arrows highlight the development of the deepest UZB-3 sample toward the expected modeled values between the 2015 and 2016 measurements. Error bars on April 2015 samples indicate 2σ uncertainty based on six to seven replicate aliquot measurements at each depth. Error bars on May 2016 samples indicate 2σ uncertainty from pooled variance of measurement campaign B (N=22). Shaded gray region around mean modeled profiles indicate 2σ model uncertainty from 1000 Monte Carlo simulations.

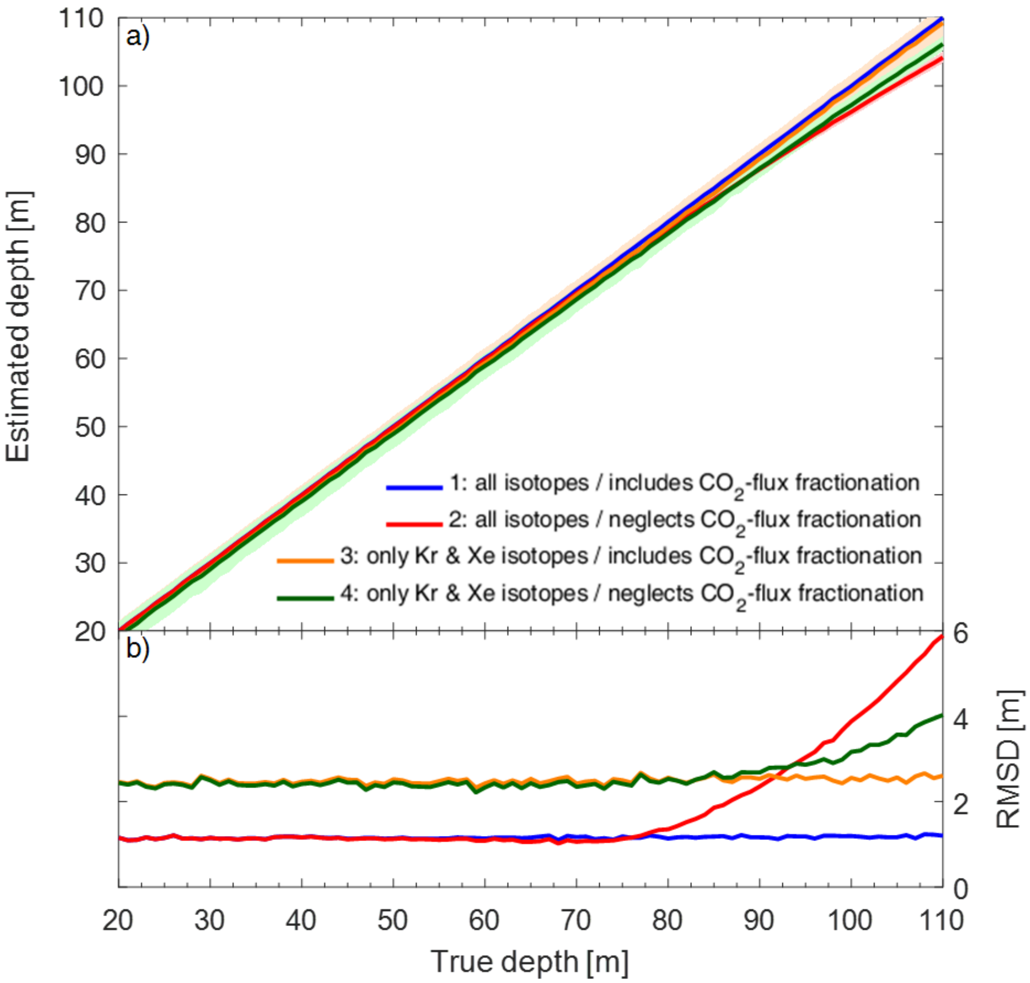

Figure 2.6: Comparison of actual to estimated sample depths in sensitivity test of inverse model run under four scenarios at ADRS environmental conditions (temperature, pressure, humidity, CO_2, geothermal gradient). Scenarios 1 and 2 utilize all eight noble gas isotope ratios considered in this study as constraints for the inverse model. Scenarios 3 and 4 exclude argon isotope ratios. Scenarios 2 and 4 exclude CO_2-flux fractionation to assess the potential bias for neglecting CO_2 fractionation in a paleo UZ for which CO_2 profiles would not be known a priori.

Table 2.1: Isotope ratio weights in inverse model, mass differences, thermal diffusion sensitivities, and measurement uncertainties (σ_{pooled}) for measurement campaigns A and B. [a] Thermal diffusion sensitivities for argon [*Grachev and Severinghaus*, 2003], krypton [*Kawamura et al.*, 2013], and xenon [*Kawamura et al.*, 2013] isotopes.

	$\delta^{40}/_{36}$	$\delta^{40}/_{38}$	$\delta^{86}/_{82}$	$\delta^{86}/_{83}$	$\delta^{86}/_{84}$	$\delta^{136}/_{129}$	$\delta^{134}/_{129}$	$\delta^{132}/_{129}$
Gas	Ar	Ar	Kr	Kr	Kr	Xe	Xe	Xe
W_i	1	1.03	4.10	4.13	4.15	5.19	5.15	5.11
Δm_i (g mol^{-1})	4	2	4	3	2	7	5	3
Ωi (‰K-1) a	0.043	0.021	0.010	0.008	0.005	0.014	0.010	0.006
σ_{pooled} A (‰)	0.017	0.009	0.021	0.027	0.017	0.067	0.065	0.042
σ_{pooled} B (‰)	0.004	0.006	0.028	0.022	0.021	0.069	0.047	0.035

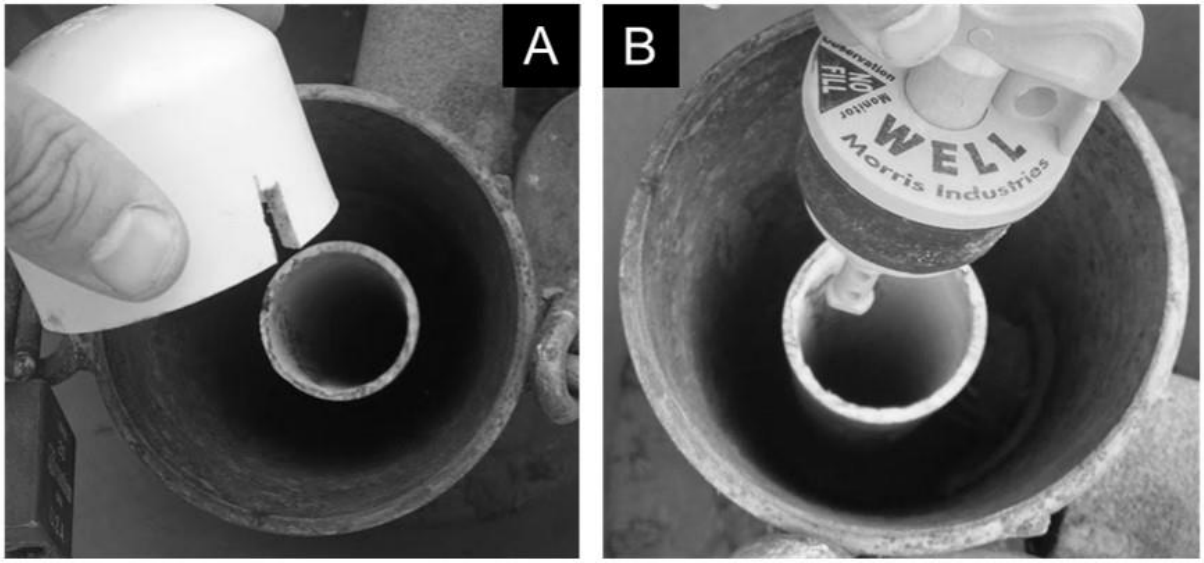

Figure 2.S1: PVC pipe at UZB-3 in background below original PVC cap installed at time of April 2015 sampling (A) and adjustable rubber-sealed cap installed in January 2016 (B).

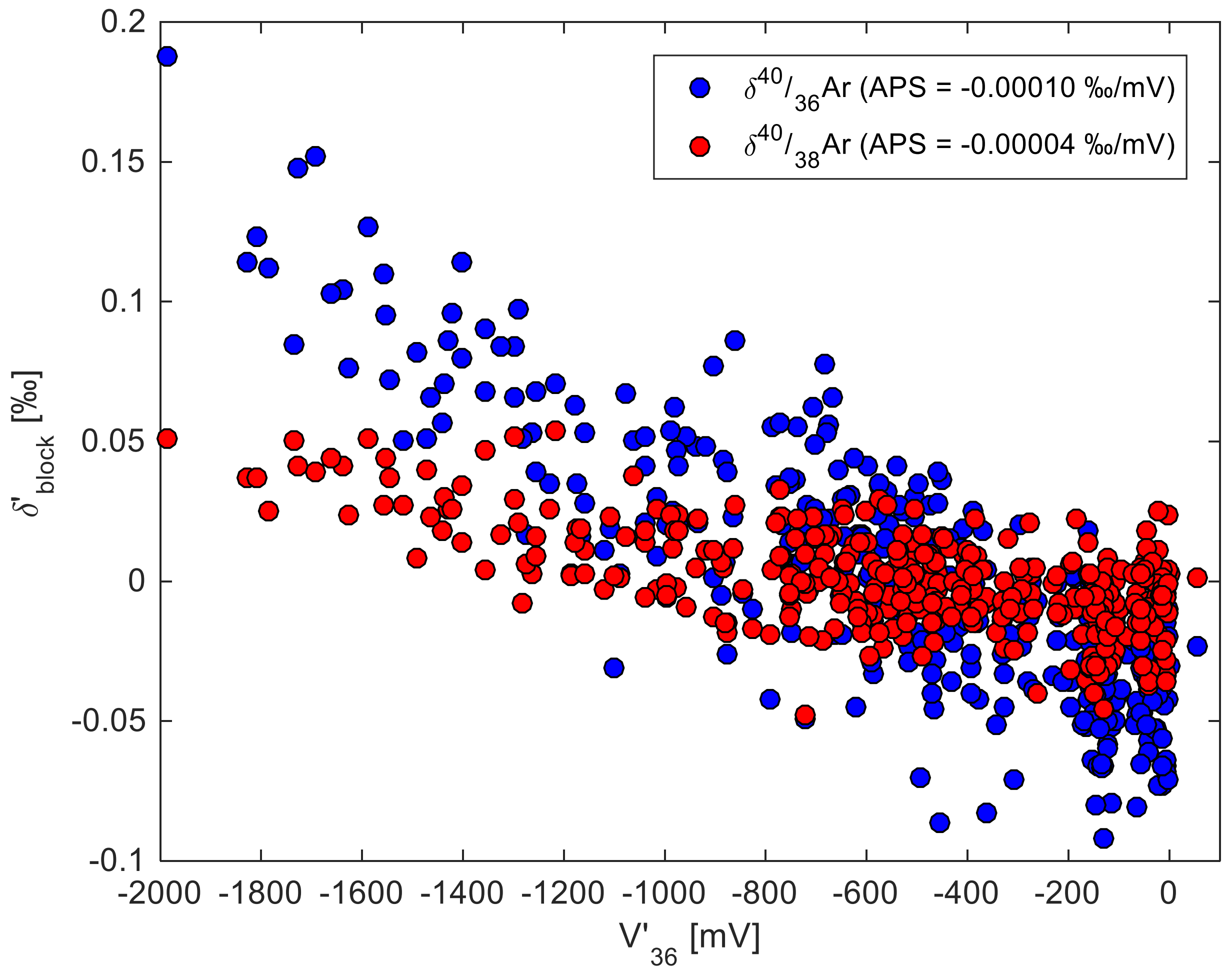

Figure 2.S2: Block delta anomalies versus block pressure anomalies for all 368 Ar measurement blocks measured in April 2015 sample analysis. The apparent pressure sensitivity used to remove these trends from the original data is calculated from the geometric mean regressions for each of these three isotope ratios.

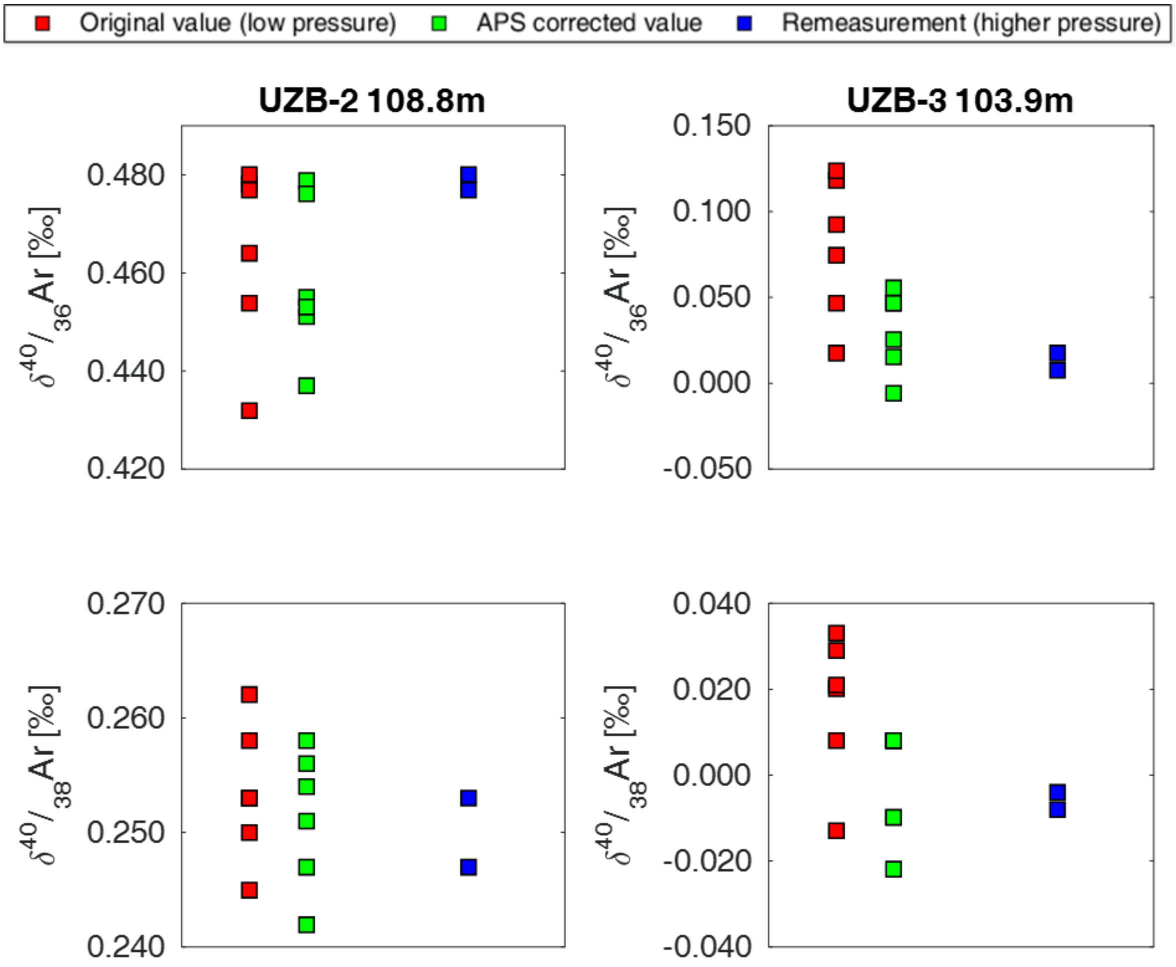

Figure 2.S3: Aliquot-mean argon isotope ratios in the deepest samples at bores UZB2 and UZB-3. Red markers indicate original aliquot mean measurements (mean of 4 argon blocks/measurement at or below 5500 mV). Green markers indicate pressure corrected aliquot mean measurements. Blue markers indicate re-measured aliquots in May 2016 (2 blocks/aliquot) at a higher pressure (11000 mV intensity at mass 36).

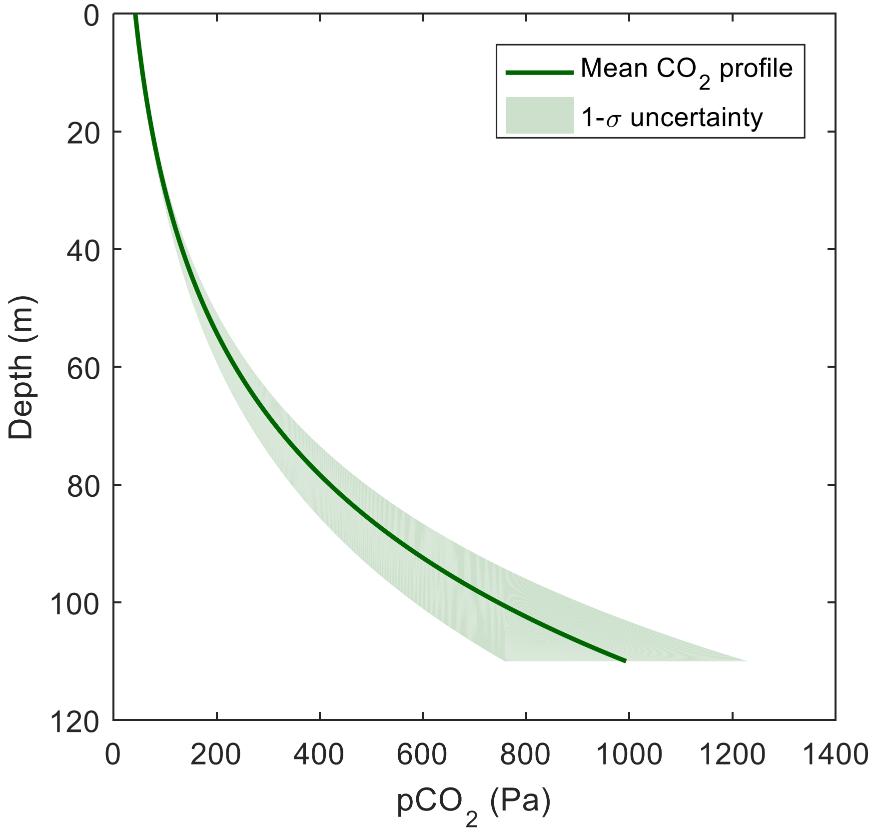

Figure 2.S4: Prescribed CO_2 concentrations and 1σ uncertainties used in steady-state model to calculate fractionation due to upward diffusive flux of CO_2. Mean profile and its uncertainty based on measurements of CO_2 in UZB-2 at ADRS (Walvoord et al., 2005).

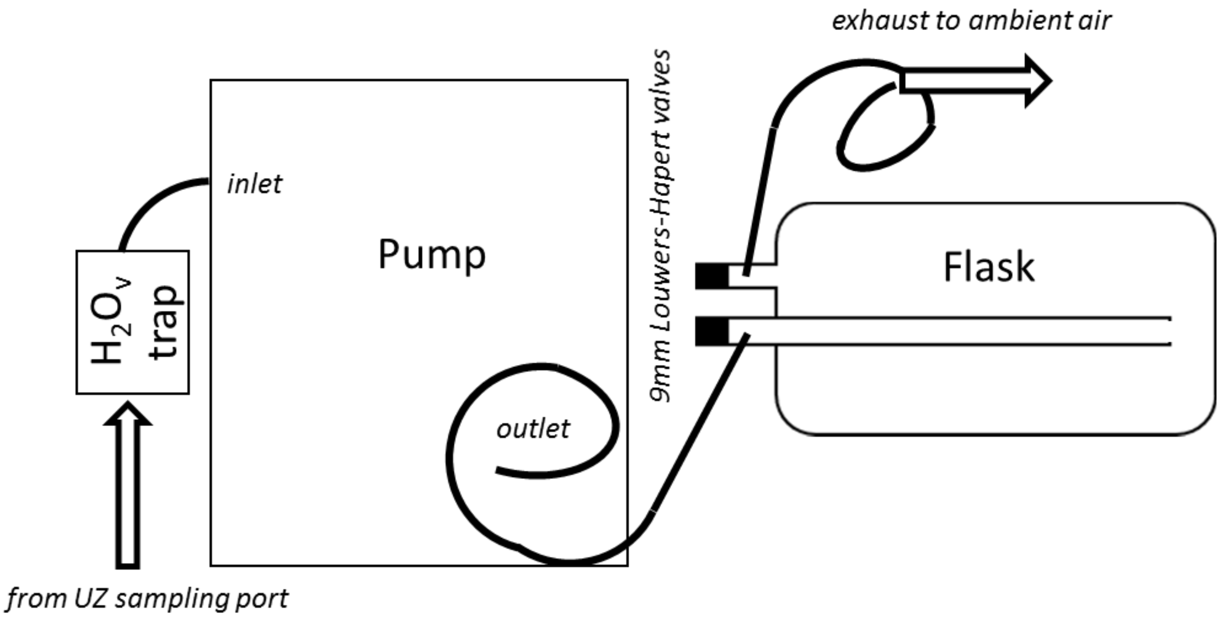

Figure 2.S5: Schematic of system used to collect dried UZ gas samples at ADRS.

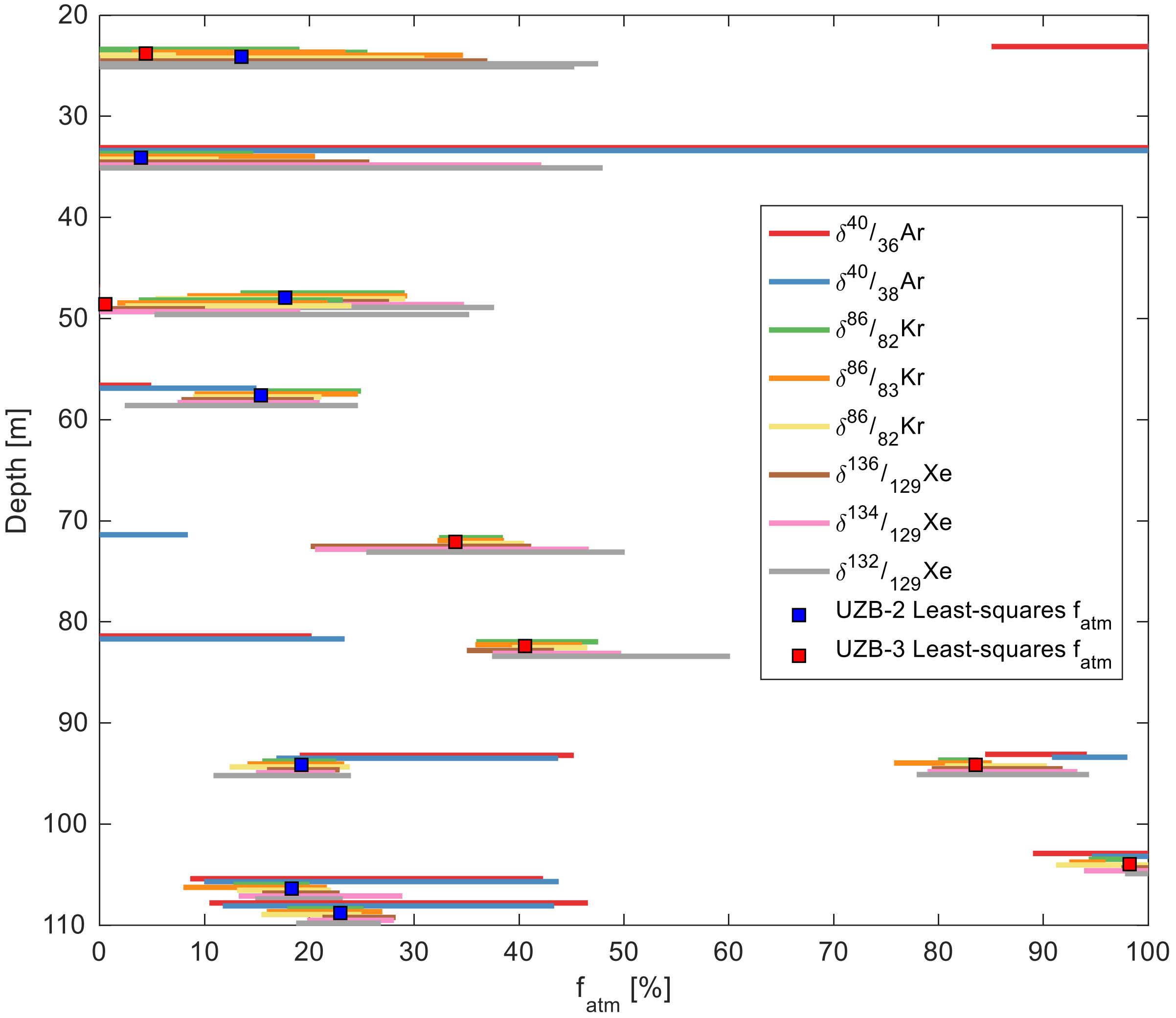

Figure 2.S6: 95% confidence intervals for independent estimates of atmospheric contaminant fraction by individual isotope ratios (colored bars). Independent estimates are accomplished by 1000 Monte Carlo simulations per isotope ratio per sample. Least-squares estimates of atmospheric contamination are shown as filled squares. Note that bars are staggered throughout ±1 m range surrounding sampled depth.

References

Aeschbach-Hertig, W., & Solomon, D. K. (2013). Noble Gas Thermometry in Groundwater Hydrology. In *The Noble Gases as Geochemical Tracers* (pp. 81–122). Berlin, Heidelberg: Springer Berlin Heidelberg. https://doi.org/10.1007/978-3-642-28836-4_5

Aeschbach-Hertig, W., Peeters, F., Beyerle, U., & Kipfer, R. (2000). Palaeotemperature reconstruction from noble gases in ground water taking into account equilibration with entrapped air. *Nature*, *405*(6790), 1040–4. https://doi.org/10.1038/35016542

Baker, R. J., Andraski, B. J., Stonestrom, D. a., & Luo, W. (2012). Volatile Organic Compounds in the Unsaturated Zone from Radioactive Wastes. *Journal of Environment Quality*, *41*(4), 1324. https://doi.org/10.2134/jeq2011.0480

Craig, H., Horibe, Y., & Sowers, T. (1988). Gravitational separation of gases and isotopes in polar ice caps. *Science*, *242*(4886), 1675–8. https://doi.org/10.1126/science.242.4886.1675

Ding, X., Kennedy, B. M., Evans, W. C., & Stonestrom, D. A. (2016). Experimental Studies and Model Analysis of Noble Gas Fractionation in Porous Media. *Vadose Zone Journal*, *15*(2). https://doi.org/10.2136/vzj2015.06.0095

Freundt, F., Schneider, T., & Aeschbach-Hertig, W. (2013). Response of noble gas partial pressures in soil air to oxygen depletion. *Chemical Geology*, *339*, 283–290. https://doi.org/10.1016/j.chemgeo.2012.07.026

Fuller, E. N., Schettler, P. D., & Giddings, J. C. (1966). A new method for prediction of binary gas-phase diffusion coefficients. *Industrial and Engineering Chemistry*, *16*(10), 551. https://doi.org/10.1016/0042-207X(66)90400-3

Grachev, A. M., & Severinghaus, J. P. (2003). Determining the thermal diffusion factor for 40Ar/36Ar in air to aid paleoreconstruction of abrupt climate change. *Journal of Physical Chemistry A*, *107*(23), 4636–4642. https://doi.org/10.1021/jp027817u

Green, C. T., Walvoord, M. A., Andraski, B. J., Striegl, R. G., & Stonestrom, D. A. (2015). Multimodel analysis of anisotropic diffusive tracer-gas transport in a deep arid unsaturated zone. *Water Resources Research*, *51*(8), 6052–6073. https://doi.org/10.1002/2014WR016055

Grew, K. E., & Ibbs, T. L. (1953). Thermal diffusion in gases. *Quarterly Journal of the Royal Meteorological Society*, *79*(341), 458–458. https://doi.org/10.1002/qj.49707934127

Guillon, S., Gréau, C., & Pili, E. (2016). Continuous Monitoring of the Vadose Zone Gas Phase by Mass Spectrometry. *Vadose Zone Journal*, *15*(8), 0. https://doi.org/10.2136/vzj2015.12.0168

Hamme, R. C., & Severinghaus, J. P. (2007). Trace gas disequilibria during deep-water formation. *Deep-Sea Research Part I: Oceanographic Research Papers*, *54*(6), 939–950. https://doi.org/10.1016/j.dsr.2007.03.008

Johnson, M. J., C. J. Mayers, and B. J. Andraski (2002), Selected Micrometeorological and Soil-Moisture Data at Amargosa Desert Research Site in Nye County Near Beatty, Nevada, 1998–2000, *USGS Open-File Report 2002–348*.

Johnson, M. J., C. J. Mayers, and B. J. Andraski. (2007). Selected Micrometeorological and Soil-Moisture Data at Amargosa Desert Research Site in Nye County Near Beatty, Nevada, 2001–2005, *USGS Open-File Report 2007–284*.

Kawamura, K., Severinghaus, J. P., Albert, M. R., Courville, Z. R., Fahnestock, M. A., Scambos, T., et al. (2013). Kinetic fractionation of gases by deep air convection in polar firn. *Atmospheric Chemistry and Physics*, *13*(21), 11141–11155. https://doi.org/10.5194/acp-13-11141-2013

Kipfer, R., Aeschbach-Hertig, W., Peeters, F., & Stute, M. (2002). Noble Gases in Lakes and Ground Waters. *Reviews in Mineralogy and Geochemistry*, *47*(1), 615–700. https://doi.org/10.2138/rmg.2002.47.14

Mayers, C.J., B.J. Andraski, C.A. Cooper, S.W. Wheatcraft, D.A. Stonestrom, and R.L. Michel (2005), Modeling tritium transport through a deep unsaturated zone in an arid environment, *Vadose Zone J.*, 4(4), 967-976, doi:10.2136/vzj2004.0179.

Mazor, E. (1972). Paleotemperatures and other hydrological parameters deduced from noble gases dissolved in groundwaters; Jordan Rift Valley, Israel. *Geochimica et Cosmochimica Acta*, *36*(12), 1321–1336. https://doi.org/10.1016/0016-7037(72)90065-8

Mourzenko, V.V., C. Varloteaux, S. Guillon, S., J.-F. Thovert, E. Pili, and P.M. Adler (2014), Barometric pumping of a fractured porous medium, *Geophys. Res. Lett*, 41(19), doi:10.1002/2014GL060865.

Phillips, F. M. (Fre. M. (1981). *Noble gases in ground water as paleoclimatic indicators*. The University of Arizona.

Reid, R. C., Prausnitz, J. M., & Sherwood, T. K. (1977). *The Properties Of Gases And Liquids* (3rd ed.). New York: McGraw-Hill.

Severinghaus, J. P., & Battle, M. O. (2006). Fractionation of gases in polar ice during bubble close-off: New constraints from firn air Ne, Kr and Xe observations. *Earth and Planetary Science Letters*, *244*(1–2), 474–500. https://doi.org/10.1016/j.epsl.2006.01.032

Severinghaus, J. P., Bender, M. L., Keeling, R. F., & Broecker, W. S. (1996). Fractionation of soil gases by diffusion of water vapor, gravitational settling, and thermal diffusion. *Geochimica et Cosmochimica Acta*, *60*(6), 1005–1018. https://doi.org/10.1016/0016-7037(96)00011-7

Severinghaus, J. P., Sowers, T., Brook, E. J., Alley, R. B., & Bender, M. L. (1998). Timing of abrupt climate change at the end of the Younger Dryas 8 interval from thermally fractionated gases in polar ice. *Nature*, *391*(6663), 141–146. https://doi.org/10.1038/34346

Severinghaus, J. P., Grachev, A., & Battle, M. (2001). Thermal fractionation of air in polar firn by seasonal temperature gradients. *Geochemistry, Geophysics, Geosystems*, *2*(7), n/a-n/a. https://doi.org/10.1029/2000GC000146

Stanley, R. H. R., & Jenkins, W. (2013). Noble Gases in Seawater as Tracers for Physical and Biogeochemical Ocean Processes. In *The Noble Gases as Geochemical Tracers* (pp. 55–79). https://doi.org/10.1007/978-3-642-28836-4_4

Stonestrom, D. A., Abraham, J. D., Andraski, B. J., Baker, R. J., Mayers, C. J., Michel, R. L., et al. (2004). Monitoring radionuclide contamination in the unsaturated zone: Lessons learned at the Amargosa Desert Research Site, Nye County, Nevada. In *Workshop on long-term performance monitoring of metals and radionuclides in the subsurface, Reston, VA* (pp. 21–22). Reston, VA.

Stute, M., & Schlosser, P. (1993). Climate Change in Continental Isotopic Records. In *Climate Change in Continental Isotopic Records* (Vol. 78, p. 374). https://doi.org/10.1029/GM078

Stute, M., Forster, M., Frischkorn, H., Serejo, A., Clark, J. F., Schlosser, P., et al. (1995). Cooling of Tropical Brazil (5C) During the Last Glacial Maximum. *Science*, *269*(5222), 379–383. https://doi.org/10.1126/science.269.5222.379

Tempest, K. E., & Emerson, S. (2013). Kinetic isotopic fractionation of argon and neon during air-water gas transfer. *Marine Chemistry*, *153*, 39–47. https://doi.org/10.1016/j.marchem.2013.04.002

Tomonaga, Y., Blättler, R., Brennwald, M. S., & Kipfer, R. (2012). Interpreting noble-gas concentrations as proxies for salinity and temperature in the world’s largest soda lake (Lake Van, Turkey). *Journal of Asian Earth Sciences*, *59*, 99–107. https://doi.org/10.1016/j.jseaes.2012.05.011

Tyroller, L., Brennwald, M. S., Mächler, L., Livingstone, D. M., & Kipfer, R. (2014). Fractionation of Ne and Ar isotopes by molecular diffusion in water. *Geochimica et Cosmochimica Acta*, *136*(0), 60–66. https://doi.org/http://dx.doi.org/10.1016/j.gca.2014.03.040

Walvoord, M. A., Stonestrom, D. A., Andraski, B. J., & Striegl, R. G. (2004). Constraining the inferred paleohydrologic evolution of a deep unsaturated zone in the Amargosa Desert. *Vadose Zone Journal*, *3*(2), 502–512. https://doi.org/10.2136/vzj2004.0502

Walvoord, M. A., Striegl, R. G., Prudic, D. E., & Stonestrom, D. A. (2005). CO2 dynamics in the Amargosa Desert: Fluxes and isotopic speciation in a deep unsaturated zone. *Water*

Resources Research, *41*(2), 1–15. https://doi.org/10.1029/2004WR003599

Weeks, E. P., Earp, D. E., & Thompson, G. M. (1982). Use of atmospheric fluorocarbons F-11 and F-12 to determine the diffusion parameters of the unsaturated zone in the Southern High Plains of Texas. *Water Resources Research*, *18*(5), 1365–1378. https://doi.org/10.1029/WR018i005p01365

Weisbrod, N., M. I. Dragila, U. Nachshon, and M. Pillersdorf (2009), Falling through the cracks: The role of fractures in Earth-atmosphere gas exchange, *Geophys. Res. Lett.*, *36*(2), doi:10.1029/2008GL036096.

Chapter 3

Precise Determination of Ar, Kr and Xe Isotopic Fractionation Due to Diffusion and Dissolution in Fresh Water

Abstract

Dissolved noble gases are ideal conservative tracers of physical processes in the Earth system due to their chemical and biological inertness. Although bulk concentrations of dissolved Ar, Kr, and Xe are commonly measured to constrain physical models of atmosphere, ocean, and terrestrial hydrosphere processes, stable isotope ratios of these gases (e.g. ^{136}Xe/^{129}Xe) are seldom used because of low signal-to-noise ratios. Here we present the first results from a new method of dissolved gas sampling, extraction and analysis that permits measurement of stable Ar, Kr, and Xe isotope ratios at or below ~5 per meg amu^{-1} precision (1σ), two orders-of-magnitude below conventional Kr and Xe isotopic measurements. This gain in precision was achieved by quantitative extraction and subsequent purification of dissolved noble gases from 2-L water samples via helium sparging and viscous dual-inlet isotope ratio mass spectrometry. We have determined the solubility fractionation factors ($\boldsymbol{\alpha}_{sol}$) for stable Ar, Kr, and Xe isotope ratios between ~2 and 20 ºC via laboratory equilibration experiments. We have also conducted temperature-controlled air-water gas exchange experiments to estimate the kinetic fractionation factors ($\boldsymbol{\alpha}_{kin}$) of these isotope ratios. We find that both $\boldsymbol{\alpha}_{sol}$ and $\boldsymbol{\alpha}_{kin}$, normalized by isotopic mass

difference (Δm), decrease in magnitude with atomic number but are proportional to Δm for isotope ratios of the same element. With the new ability for high precision isotopic measurements, we suggest that dissolved Kr and Xe isotope ratios in groundwater represent a promising, novel geochemical tool with important applications for groundwater modeling, water resource management, and paleoclimate.

3.1. Introduction

Because of their chemical and biological inertness, dissolved noble gases are widely used as quantitative geochemical tracers of physical processes in seawater and groundwater (Aeschbach-Hertig & Solomon, 2013; Stanley & Jenkins, 2013). Bulk dissolved noble gas concentrations – rather than isotope ratios – are frequently studied to constrain physical processes in the atmosphere, ocean, and terrestrial hydrosphere. Exceptions include dissolved helium isotope ratios, which exhibit large variations in nature (e.g. Jenkins et al., 1972; Torgersen and Clarke, 1985), and radiogenic and fissiogenic noble gas isotope ratios in extremely old (>1 Ma) groundwater (e.g. Lippmann et al., 2003). Common applications of dissolved noble gas measurements include quantifying groundwater recharge temperatures (e.g. Aeschbach-Hertig et al., 2000; Mazor, 1972; Stute et al., 1995) and abiotic properties of air-sea gas exchange (Hamme & Severinghaus, 2007; Loose et al., 2016; Stanley & Jenkins, 2013). Among recent studies that have measured dissolved Ar, Kr, and Xe isotope ratios in seawater or groundwater, typical analytical 1-σ precision is on the order of 1‰ (Stanley et al., 2009; Wen et al., 2016), with the exception of one single higher-precision study of seawater Ar isotope ratios (Nicholson et al., 2010).

Here we present results from a new sampling, extraction and analysis system for high-precision measurement of dissolved stable Ar, Kr, and Xe isotope ratios. Quantitative extraction of dissolved gases from large water samples collected in air-tight 2-L flasks was achieved by sparging with ultra-high purity helium. Dissolved gases were subsequently purified and measured via viscous dual-inlet multicollector isotope ratio mass spectrometry. The observed order-0.01‰ precision of individual isotope ratio measurements across replicate samples analyzed via this method represents a two orders-of-magnitude improvement over existing analytical techniques. Using this 2-L water sample method, we have carried out air-water gas-exchange experiments to determine the kinetic fractionation factors of Ar, Kr, and Xe isotopes in fresh water. A separate set of experiments to determine solubility fractionation factors was also conducted, by measuring noble gas isotope ratios in both the dissolved and gas phases of an equilibrated closed system, using fresh water ranging from ~2 to 20 °C.

To our knowledge, these are the first solubility fractionation factor measurements of Kr and Xe isotope ratios in water. We discuss the sensitivity of observed solubility and kinetic fractionation factors to temperature and isotopic mass differences. We also compare our results to previous estimates of $^{40}/_{36}$Ar solubility and kinetic fractionation factors (Tempest & Emerson, 2013; Tyroller et al., 2014) and a recent study which found no fractionation (at order-1‰ precision) of Kr or Xe isotope ratios due to diffusion through water (Tyroller et al., 2018). Finally, we discuss the implications of our new findings for the potential of Kr and Xe isotope ratios in groundwater as quantitative indicators of past water-table depth.

3.2. Methods

3.2.1. Dissolved gas sampling, extraction, purification, and analysis

In this study, 2-L water samples were collected in evacuated glass flasks by a method similar to that of Hamme and Emerson (2004). Custom glass flasks were used, fitted with two 9-mm Louwers-Hapert valves, each with two inner Viton o-rings separated by a ~0.04 cm^3 space for sealing redundancy. To collect a sample, the neck of an evacuated flask was first inserted into ~25 cm of PVC tubing (~1.25 cm inner diameter), forming an elongated neck. Next, ambient air inside the elongated neck was flushed out by inserting a thin nylon tube (0.25 cm inner diameter) carrying N_2 from a compressed gas cylinder. With N_2 flowing, a second thin nylon tube (0.25-0.5 cm inner diameter) was inserted carrying the water sample from either the laboratory equilibration bath or a groundwater well. With the elongated tube filled completely with water, the N_2 tube was removed and the flask valve was opened only enough to expose the inner o-ring to the water. This allowed any air in the cavity between the two o-rings to be flushed out. Care was taken to dislodge any bubbles. Once the elongated neck was free of bubbles, sample collection was begun by opening the valve to allow water to enter the flask. The valve position was adjusted throughout sampling to ensure that a roughly 20 cm column of water sat in the elongated neck between the valve and ambient air. Once ~95% full, the valve was closed leaving a small headspace to allow for any possible thermal expansion of the water during storage. The cavity between the two o-rings, and the space between the outer o-ring and a cap on the end of the neck, were flushed with N_2 to minimize any possible permeation of atmospheric noble gases into the sample headspace during storage.

Dissolved gases were quantitatively extracted using a helium carrier-gas sparging system (Figure 3.1). For each sample, water was first introduced to the evacuated system and poured into the extraction vessel. Any residual gas in the flask was then cryogenically transferred to a stainless-steel diptube immersed in liquid helium (~4 K) for 15 minutes, and then the sample flask (now evacuated) was closed to the system. Ultra-high purity tank helium was then introduced to the system, bringing the total pressure to ~1 atm before beginning a 90-minute sparging. During the sparging period, a Metal Bellows MB-41 pump recirculated helium at ~1 L_{STP} min^{-1}, inducing bubbling through a fritted disc (with ~10^{-4} m diameter pores) at the base of the extraction vessel and thereby stripping gases from solution. These liberated gases were then carried through two glass traps at -80 ^{0}C to remove water vapor before being trapped in the 4K diptube. The gaseous helium, which cannot be trapped in the diptube due to its low boiling point, continually circulated through the system during the 90-minute extraction. To avoid adsorption saturation of the available surface area in the diptube, the tube was progressively lowered from ~15 cm above the liquid helium dewar to complete immersion over the sparging period.

At the end of the sparging period, residual helium was pumped to waste before closing the diptube and removing it from the liquid helium dewar. Trapped gases were warmed to room temperature and then exposed to SAES Zr/Al getter sheets and Ti sponge at ~900 ^{0}C for 125 minutes. To absorb any released H_2, the getter oven temperature was subsequently lowered to ~300 ^{0}C for five minutes and then remaining noble gases were cryogenically trapped into a second diptube at 4K. After allowing at least three hours of homogenization at room temperature, the gettered gas sample pressure was measured in a calibrated volume attached to the inlet of a MAT 253 dual-inlet mass spectrometer in the Scripps Institution of Oceanography (SIO) Noble Gas Isotope Laboratory. The temperature of the volume was recorded to enable a subsequent manometric determination of dissolved Ar concentration. For each sample, Ar isotopes were analyzed first, followed by Xe isotopes and then Kr isotopes. During isotopic analyses of each separate gas, isotopes were measured by simultaneous collection, and Kr/Ar and Xe/Ar ratios via sequential, non-simultaneous peak jumping.

The measurements presented in this study were made as part of two wider analytical campaigns, which included measurements outside the scope of this study. The replacement of the ion source filament in mid-June 2018 separated campaign A (March-June 2018) from campaign B (June-October 2018). Because the replacement campaign-B filament had lower sensitivity than the original campaign-A filament, the ion beam intensities, integration times, and number of integration cycles were adjusted to achieve comparable precision. A summary of analytical parameters for each measurement campaign is presented in the supplemental materials (Supplemental Table 3.S1). Each sample analyzed in both measurement campaigns was measured against the same working standard (ST-AEW1).

3.2.2. Measurements, corrections, and reproducibility

For each dissolved gas sample, eight independent isotope ratios were measured in addition to Xe/Ar ratios, Kr/Ar ratios, and Ar concentrations (via manometry). Xe and Kr concentrations were subsequently determined by multiplying measured Xe/Ar and Kr/Ar ratios by Ar concentrations. All gas and isotope ratios are reported in units of ‰ with respect to the well-mixed atmosphere:

$$\delta^{h}/_{l} \equiv \left(\frac{(\mathrm{h/l})_{meas}}{(\mathrm{h/l})_{atm}} - 1\right) 10^{3} \tag{3.1}$$

where *h* and *l* refer to heavy and light gases or isotopes, respectively. Atmospheric air, routinely collected from the end of the research pier at SIO, was analyzed relative to working standard ST-AEW1 throughout the measurement campaigns. For Kr and Xe isotope measurements, aliquots of ST-AEW1 were mixed with pure Ar to match the Kr/Ar and Xe/Ar ratios of atmospheric air. This served two important purposes: first, it minimized chemical slope corrections (Severinghaus et al.,

2003) in these measurements; second, it ensured that the run pressures in both the sample and standard bellows of the mass spectrometer were equal (whereas the pressures would differ by a factor of three for Xe isotope measurements of pure air vs ST-AEW1).

We report the precision of measured isotope ratios as pooled standard deviations of replicate samples, σ_{pld}, from the mean of replicates from the same source. That is, for *n* total replicate samples collected from *k* distinct water sources (e.g. equilibration experiments, groundwater wells):

$$\sigma_{\text{pld}} \equiv \sqrt{\frac{\sum_{i,j=1}^{n,k}(\delta_i - \overline{\delta_j})^2}{n-k}} \tag{3.2}$$

σ_{pld} values for individual measured isotope ratios during each campaign are presented in Table 3.1 and Figure 3.2.

To minimize redundancy in the presentation of measured Xe and Kr isotope ratios, we make use of the nearly linear mass proportionality of Kr and Xe isotopic fractionation, following Orsi (2013), to define the following mass difference-normalized, error-weighted mean variables (in units of per meg amu^{-1}):

$$\delta^{*}\text{Kr} \equiv \left(\frac{\frac{\delta^{86}/_{82}Kr}{\sigma^2{}_{86/82}} + \frac{\delta^{86}/_{83}Kr}{\sigma^2{}_{86/83}} + \frac{\delta^{86}/_{84}Kr}{\sigma^2{}_{86/84}}}{\frac{4}{\sigma^2{}_{86/82}} + \frac{3}{\sigma^2{}_{86/83}} + \frac{2}{\sigma^2{}_{86/84}}} \right) 10^3 \tag{3.3}$$

$$\delta^{*}\text{Xe} \equiv \left(\frac{\frac{\delta^{136}/_{129}Xe}{\sigma^2{}_{136/129}} + \frac{\delta^{134}/_{129}Xe}{\sigma^2{}_{134/129}} + \frac{\delta^{132}/_{129}Xe}{\sigma^2{}_{132/129}}}{\frac{7}{\sigma^2{}_{136/129}} + \frac{5}{\sigma^2{}_{134/129}} + \frac{3}{\sigma^2{}_{132/129}}} \right) 10^3 \tag{3.4}$$

The observed linear mass proportionality in our solubility and kinetic fractionation factors of Kr and Xe isotopes in water (Figure 3.7, Section 3.4.1) further justifies the use of δ*Kr and

δ^*Xe. The precision (σ_{pld}) of δ^*Kr and δ^*Xe was 2.9 and 3.2 per meg amu^{-1}, respectively, during campaign A and 5.3 and 5.2 per meg amu^{-1}, respectively, during campaign B.

Ar concentrations were determined manometrically, correcting for the contribution of Ne in air-equilibrated water (<0.1 % of total gas pressure) and non-ideality of Ar gas using the first Virial coefficient. Measured Ar concentrations were then corrected for incompleteness of extractions. Mean Ar extraction efficiency was determined to be 99.7 ± 0.1% based on four repeat experiments in which ^{40}Ar ion beam intensities were compared between dissolved gas samples and residual gases, which were subsequently extracted and processed identically.

Three separate small corrections, on the order of σ_{pld}, were made to measured isotope ratios for 1) the so-called "chemical slope" (the influence of Ar concentration differences between the sample and reference aliquots on Xe and Kr isotope ratios (Severinghaus et al., 2003)), 2) the sensitivity of measured Ar, Kr, and Xe isotope ratios to total pressure imbalances between sample and reference gas (Severinghaus et al., 2003), and 3) trace amounts of "apparent fractionation" by the dissolved gas extraction and/or purification methods, as follows.

To empirically estimate the apparent fractionation of individual Ar, Kr, and Xe isotope ratios due to extraction and/or purification, we carried out seven repeat experiments (hereafter "standard aliquot tests"). During each standard aliquot test, an aliquot of gas from working standard can ST-AEW2 was introduced to the extraction vessel, which was prepared with two liters of >99.9% degassed water (except for helium). The extraction and purification method were then carried out in an identical manner to an actual water sample. For each standard aliquot test, measured isotope ratios (versus ST-AEW2) were normalized to the mean of 18 measurements of ST-AEW2 vs ST-AEW1 carried out over the course of campaign A. In other words, an observed deviation of 0 ‰ from the known ST-AEW2 value would imply that there was no fractionation of the standard gas aliquot due to the extraction and purification methods.

For each measured isotope ratio, corrections were made to dissolved gas samples equal to the magnitudes of mean apparent fractionation across all standard aliquot tests (black squares in Figure 3.2), which in all cases were below campaign B σ_{pld} values. Although these corrections are sufficiently small to ensure confidence in the data presented in this study, their non-zero values suggest scope for future improvement of the method. We speculate that they may reflect two processes: slight kinetic fractionation associated with the order 0.1% incompleteness of extractions, and isobaric interference by substances resistant to Zr/Al and Ti gettering.

3.2.3. Solubility fractionation experiments

To determine the solubility fractionation factors ($\boldsymbol{\alpha}_{sol}$) of Ar, Kr, and Xe isotopes in fresh water at temperatures between ~2 and 20 °C, we conducted both closed-system (CS) and open-air (OA) equilibration experiments. These experiments are described in detail in Sections 3.2.3.1 and 3.2.3.2. Solubility fractionation factors, $\boldsymbol{\alpha}_{sol}$, are defined for an isotope ratio R as:

$$\alpha_{sol} \equiv \frac{R_{diss}}{R_{gas}} \tag{3.5}$$

where R_{gas} and R_{diss} refer respectively to isotope ratio R in the gas and dissolved phases at equilibrium. Throughout the text, we often refer to ε values where $\varepsilon \equiv \boldsymbol{\alpha} - 1$ (in units of ‰, per meg, or per meg amu^{-1}, if normalized by isotopic mass difference).

In individual OA experiments, 2-L water samples were collected from an isothermal bath of de-ionized (DI) water after 4-14 days of gas-exchange with laboratory air. In each sample, Ar, Kr, and Xe isotope ratios were analyzed and compared against atmospheric air. In CS experiments, an initially degassed reservoir of DI water was equilibrated with a pure noble gas headspace in a closed system surrounded by an isothermal water bath. At the end of each experiment, isotope ratios of a specific gas (Ar, Kr, or Xe) were analyzed both in the water and headspace.

The CS experiments – in which pressure, temperature, and humidity were constant throughout the equilibrating headspace – revealed that the OA experiments exhibited reproducible temperature-dependent biases, which were most significant for Ar isotopes at cold temperatures. We suggest that these biases were due to thermal diffusion (Grew & Ibbs, 1953) and water-vapor flux fractionation (Severinghaus et al., 1996) caused by gradients in temperature and absolute humidity between well-mixed atmospheric air in the laboratory and a thin stagnant air layer (hereafter SAL) above the water bath. A physical model for observed OA-CS differences is presented and discussed in Supplemental Section 3.S1. Due to the discovery of the SAL fractionation in the OA experiments, our determinations of ε_{sol} (Section 3.3.1) are based solely on the CS experiments.

3.2.3.1. Description of CS equilibration experiments

CS experiments were carried out by bringing ~200-300 cm^3 of initially degassed water to solubility equilibrium with a ~1.8 L headspace, filled with pure Ar, Kr and Xe at ~1 atm total pressure inside a closed ~2-L chamber at constant temperature (Supplemental Figure 3.S1). Each equilibration was carried out for at least 36 hours, during which the water reservoir was continuously stirred by a magnetic stirrer at 500 revolutions per minute. Upon completion of the experiment, a 2 cm^3 sample of headspace gas and a ~10 cm^3 sample of water were collected simultaneously. The headspace samples were collected in an aliquot chamber connected to the headspace throughout the duration of each experiment. Water samples were collected in a ~40 cm^3 glass volume evacuated immediately prior to sample collection. Dissolved gases were extracted from water samples under vacuum, using a magnetic stirrer to accelerate degassing, and collected in a stainless-steel dip tube immersed in liquid helium downstream of a -80 °C water trap. Extracted gas and headspace gas samples were gettered using SAES Zr/Al sheets for 90 minutes (for Ar isotope samples) and 60 minutes (for Kr and Xe isotope samples) at 900 °C. Purified headspace and dissolved gas samples were then measured on a MAT 253 mass spectrometer against a common reference gas (ST-AEW1). The measured δ values of the headspace and dissolved gas samples, δ_{hs} and δ_{diss}, respectively, were used to calculate $\boldsymbol{\alpha}_{sol}$:

$$\alpha_{sol} = \frac{\frac{\delta_{diss}}{1000}+1}{\frac{\delta_{hs}}{1000}+1} \tag{3.6}$$

where δ_{hs} and δ_{diss} are reported with respect to the same reference gas.

In total, 18 individual CS experiments were carried out: seven Ar isotope experiments, six Kr isotope experiments, and five Xe isotope experiments. In each Kr and Xe experiment, Kr/Ar and Xe/Ar ratios in the headspace were both ~10^{-3}, roughly ten and one hundred times larger than their respective atmospheric ratios. Isotopes of different gases could not be measured in the same experiments because pure Ar gas was added, in different proportions, to the dissolved gas samples for each Kr and Xe isotope experiment. The purpose of adding Ar was to ensure that Kr/Ar or Xe/Ar ratios were the same between headspace and dissolved gas samples. Ensuring constant Kr/Ar or Xe/Ar between headspace and dissolved samples fulfilled two important needs: 1) given the large solubility differences between Kr, Xe, and Ar, it allowed for the total gas pressure (mostly Ar) to be sufficiently high to ensure viscous flow during analysis, and 2) it circumvented the need for any chemical slope corrections (described in Section 3.2.2 for 2-L water samples). Because the equilibration temperature for each experiment was known, exact Ar concentrations could be added to dissolved gas samples based on the known solubility ratios of Kr, Xe and Ar in fresh water (Clever, 1979; Hamme & Emerson, 2004b).

Throughout each experiment, an Arduino microprocessor logged water temperatures at the top and bottom of the equilibration bath, as well as air temperature, humidity, and pressure just above the surface of the bath at ~2.5-minute intervals. Observations and a simple model both indicated that isotopic equilibration was achieved after 36 hours and that a 30-minute extraction time allowed for quantitative extraction of all dissolved gases (Supplemental Figures 4 and 5). For Ar isotopes, which have the largest-magnitude kinetic and solubility fractionation factors of the isotope ratios considered in this study (Sections 3.3.1 and 3.3.2), individual experiment anomalies of ε_{sol} from a linear trendline of ε_{sol} vs temperature revealed no dependence on equilibration time (between 1.5 and 2.5 days) or extraction time (between 30 and 55 minutes). In a simple two-box diffusive gas exchange model, we simulated the equilibration of 300 cm^3 of degassed water with a 1.8-L pure Ar headspace at 1 atm initial pressure and 2 °C. Numerical integration of this model at 0.5-min resolution suggested that $^{40}Ar/^{36}Ar$ would achieve solubility equilibrium (to within 1 per meg) within 1.3 days (Supplemental Figure 3.S4). This calculation used a conservatively low gas transfer velocity of 0.2 m day^{-1} (over three times smaller than gas transfer velocities observed in the experiments described in Section 3.3.2) and assumed both the CS solubility fractionation factors and kinetic fractionation factors found in this study (Figure 3.4). Because actual gas transfer velocities were likely much higher in CS experiments, we are confident that 36 hours is sufficient to achieve isotopic solubility equilibrium.

3.2.3.2. Description of OA equilibration experiments

Each OA experiment involved gas-exchange between a ~15-L bath of DI water and atmospheric air in the SIO Noble Gas Isotope Laboratory. The water bath was maintained at constant temperature by a recirculating chiller and mixed continuously by an overhead stirrer (Supplemental Figure 3.S2). Because exchange of laboratory air with outside atmosphere air is rapid, with an overturning timescale of ~10 minutes, we assume noble gas concentrations and isotopic ratios in the laboratory are atmospheric and constant over time. Individual OA equilibration experiments were carried out for 4-14 days, after which 2-L samples were collected using the sampling method described in Section 3.2.1. Each 2-L OA sample was analyzed for Ar, Kr, and Xe isotope ratios in addition to bulk Ar, Kr and Xe concentrations. In the absence of any fractionation between atmospheric air in the laboratory and the SAL above the equilibration bath, measured isotope ratios from OA samples, divided by their ratios measured in atmospheric air, would be equal to α_{sol}. In total, 17 OA samples from 12 total experiments were analyzed (two outlier samples collected from a single equilibration experiment at 2 °C were rejected).

We originally neglected to consider the possibility of fractionation between atmospheric air in the lab and the SAL above the water bath, which equilibrates with dissolved gases in solution. However, as described in Supplemental Section 3.S1, we observed small reproducible, temperature-dependent offsets between OA and CS-derived estimates of ε_{sol} (Supplemental Figures S6 and S7). In light of these offsets, our ultimate determination of solubility fractionation factors is restricted to the results of the CS experiments. However, we used the differences between OA and CS experiments to estimate a temperature-dependent fractionation factor between the SAL and atmospheric air, α_{SAL}, and its uncertainty, which we explicitly account for in the model-based interpretation of the kinetic fractionation experiments.

3.2.4. Kinetic fractionation experiments

To determine kinetic isotopic fractionation factors (α_{kin}), we designed and carried out three nearly identical gas-exchange experiments using the same temperature-controlled water bath used for OA equilibration experiments. The fractionation factor α_{kin} for diffusive gas exchange is defined by the ratio of heavy and light isotope piston velocities, k_h and k_l, respectively:

$$\alpha_{kin} \equiv \frac{k_h}{k_l} \tag{3.7}$$

Each experiment was conducted by first bringing the water bath used in the OA equilibration experiments to steady state at ~13 °C, then rapidly cooling the well-mixed bath over ~3 hours by ~10 °C, and finally collecting two replicate 2-L water samples over a period of ~10 minutes. These rapid cooling experiments (RCEs) induced rapid dissolution of atmospheric gases due to the increasing solubilities of Ar, Kr, and Xe in the cooling reservoir. By measuring bulk gas concentrations ([Ar], [Kr], and [Xe]) and isotope ratios in each sample and logging the water temperature and air pressure throughout each experiment, we were able to constrain a simple one-box diffusive model of gas exchange to numerically solve for α_{kin}. For each RCE, there were two stages of least-squares optimization required to arrive at a value and uncertainty range for α_{kin} for each separate isotope ratio.

In the first stage, we used the MATLAB nonlinear solver *fminsearch* to seek initial piston velocities, $k_{g,0}$, for Ar, Kr, and Xe that minimized squared deviations between replicate-mean measured gas concentrations, and concentrations modeled by numerically integrating equation 3.8 at 0.5 min resolution:

$$\frac{dC_g(t)}{dt} = \frac{1}{L}\, k_{g,0}\,(1 + \mu T(t))\left(C_{g,eq}(T(t), P(t)) - C_g(t)\right) \tag{3.8}$$

In equation 3.8 at time t (min), C_g is the dissolved concentration of gas g (mol cm^{-3}), L is the depth of the water reservoir (cm), μ is the fractional change in piston velocity for a change in temperature (^{o}C^{-1}) from a linear fit to the data of Jähne et al. (1987), T is the reservoir temperature at time t (^{o}C), and $C_{g,eq}$ is the solubility concentration (mol cm^{-3}) of gas g at temperature T and pressure P (Torr). For each integration of equation 3.8, the histories of T and P throughout each experiment were prescribed from RCE observations. We carried out 1000 monte carlo simulations per experiment for each of the three gases (Ar, Kr, and Xe), adding Gaussian perturbations to the measured concentrations with standard deviations equal to the pooled measurement standard deviations and to the temperature history based on the absolute temperature uncertainty associated with the sensors.

In the second stage, having already solved for a distribution of $k_{g,0}$ values for Ar, Kr, and Xe in the first stage, we again used *fminsearch* for each individual monte carlo simulation, isotope ratio, and experiment to seek a value of α_{kin} that minimized squared deviations between measured replicate-mean δ values and modeled experiment-end δ values (equations 3.9-3.11).

$$\frac{dC_h(t)}{dt} = \frac{1}{L}\alpha_{kin}\, k_{g,0}\, (1 + \mu T(t)) f_h\big(\alpha_{sol}\alpha_{SAL} C_{g,eq}(T(t), P(t)) - C_g(t)\big) \quad (3.9)$$

$$\frac{dC_l(t)}{dt} = \frac{1}{L}\, k_{g,0}\, (1 + \mu T(t))\, f_l\big(C_{g,eq}(T(t), P(t)) - C_g(t)\big) \quad (3.10)$$

$$\delta = \left(\frac{\frac{C_h}{C_l}}{\frac{f_h}{f_l}} - 1\right) 10^3 \quad (3.11)$$

In equations 3.9 and 3.10 at time *t*, C_h and C_l are the dissolved concentrations of the heavy and light isotope, respectively, and f_h and f_l are the mole fractions of the heavy and light isotope, respectively, in atmospheric air. We account for the observed fractionation of noble gas isotope ratios in the stagnant air layer by including the empirically estimated fractionation factor (α_{SAL}), which represents heavy-to-light temperature-dependent isotopic fractionation between atmospheric air and the stagnant air layer **(**Supplemental Figures 3.S6 and 3.S7**)** in equation 3.9. As in the first stage, we conducted 1000 monte carlo simulations in which Gaussian perturbations were added to the measured isotope ratios, solubility fractionation factor (α_{sol}), and SAL fractionation factor (α_{SAL}) determined from differences in linear fits of CS and OA data to experiment temperatures. By comparing modeled δ values at the end of the simulated experiment to measured δ values, we generated probability distributions of α_{kin} each isotope ratio in each experiment.

The equilibrium solubility concentrations, $C_{g,eq}$, and isotopic solubility ratios, α_{sol}, were prescribed from best fit curves based on the OA equilibration experiments described in section 3.2.3.2. By using the OA-experiment derived solubility curves, we eliminate any potential bias that could be introduced by using prior solubility curves in the literature that might not have accounted for the slight fractionation of the stagnant air layer. We note that our fitted OA-equilibration Ar, Kr, and Xe solubility curves agree well (within ~1% at all temperatures) with previously published Ar, Kr, and Xe solubility curves (Supplemental Figure 3.S11, Clever, 1979; Hamme and Emerson, 2004b).

3.3. Results

3.3.1. Solubility fractionation factors

We present the mass-normalized ε_{sol} values for Ar, Kr, and Xe isotope ratios between ~2 and 20 °C from the 18 CS-equilibration experiments carried out in this study (Figure 3.3). Table 3.1 provides the observed ε_{sol} values of individual isotope ratios (at 15°C) and their temperature dependences. Normalized by isotopic mass difference, argon isotopes exhibit the strongest solubility fractionation, followed by krypton and then xenon isotopes, at all temperatures. Interestingly, only the temperature sensitivity of Ar isotopic solubility fractionation is statistically significant from zero. The regression coefficient of ε_{sol} versus temperature for $^{40}Ar/^{36}Ar$ is -1.8 per meg amu^{-1} °C^{-1} ($R^2 = 0.92$, $p<<0.05$), whereas for Kr isotopes and Xe isotopes the coefficients are orders of magnitude smaller: -0.16 per meg amu^{-1} °C^{-1} ($R^2 = 0.07$, $p = 0.61$) and 0.05 per meg amu^{-1} °C^{-1} ($R^2 = 0.10$, $p = 0.60$), respectively. We estimate the 1-σ precision of individual CS experiments as the standard deviation of individual experiment ε_{sol} values from the linear temperature trendlines, which indicate Ar, Kr, and Xe isotopic precisions of 3.0 per amu^{-1}, 4.1 per meg amu^{-1}, and 1.3 per meg amu^{-1}, respectively.

The observed positive sign of ε_{sol} for all isotope ratios measured in this study is typical for monatomic and diatomic gas heavy-to-light isotope ratios (Benson & Krause, 1980, 1984; Klots & Benson, 1963; Knox et al., 1992; Muccitelli & Wen, 1978; Tempest & Emerson, 2013). Supplemental Figure 3.S12 also shows observed temperature-dependent ε_{sol} values for $\delta^{38}/_{36}$Ar (from this study) alongside experimental values from the literature for noble gas, O_2, and N_2 stable isotope ratios. At 20 °C, we find that ε_{sol} for $\delta^{40}/_{36}$Ar is 1.036 ± 0.012‰, agreeing reasonably well with Tempest and Emerson (2013) who found 1.07 ± 0.02‰ at the same temperature. Our results are also broadly consistent with a lower resolution compilation of 70 surface freshwater $\delta^{40}/_{36}$Ar isotope measurements, which found a mean value of 1.3 ± 0.2‰ (Beyerle et al., 2000). We know of no prior studies in which Kr or Xe isotopic solubility fractionation has been measured.

3.3.2. Kinetic fractionation factors

In all three rapid cooling experiments, each replicate-mean measured heavy-to-light isotope ratio decreased over time from its initial OA experiment steady-state value at ~13 °C, consistent with the canonical viewpoint that heavy isotopes diffuse more slowly than light isotopes. Bulk Ar, Kr, and Xe concentrations all increased as expected, indicating rapid gas uptake induced by cooling. The isotopic kinetic fractionation factors (ε_{kin} values) determined in these RCEs are shown in Figure 3.4 and Table 3.1. Weighted-mean α_{kin} values, calculated for each isotope ratio based on probability distributions resulting from 1000 monte carlo simulations for each RCE, were below unity in all cases. That is, for each measured isotope ratio in each experiment, we observed the lighter isotope to have a faster piston velocity than then heavier isotope.

To provide a visual illustration of the two data-model optimization stages required for the determination of α_{kin}, we show specific results from a single experiment (RCE1) in Figures 5 and 6. Figure 3.5 shows 1000 modeled simulations of Ar, Kr, and Xe concentrations over ~180 minutes, a period in which 12.9 ^{o}C water, brought to steady state in an OA experiment, was rapidly cooled by ~10 ^{o}C. As the water cooled, atmospheric Ar, Kr, and Xe were taken up resulting in measured ~5%, 6%, and 7% respective increases in concentration (relative to air-equilibrated 12.9 ^{o}C fresh water). The median initial piston velocities resulting from the 1000 monte carlo simulations were ~0.73, ~0.66, and ~0.66 m day^{-1} for Ar, Kr, and Xe, respectively. α_{kin} values for each isotope ratio were then simulated by prescribing these distributions of initial piston velocities to numerically integrate equations 3.9 and 3.10. Modeled Ar isotope histories, measured Ar isotopic fractionation, and probability distributions of resulting kinetic fractionation factors are shown (Figure 3.6). Experiment-specific results for each RCE are included in the Supplemental materials (Supplemental Figures 3.S8-3.S10).

We note that because the total gas added in these RCEs to the pre-existing Ar, Kr, and Xe in solution was only ~5-10%, and calculated ε_{kin} values were on the order of 1‰, the total observed fractionation (order 0.01-0.1‰) provided a relatively low signal-to-noise ratio. For this reason, the probability distributions for ε_{kin} values (Figures 3.4 and 3.6) span a range of order 0.1‰, considerably higher than σ_{pld} for any individual isotope ratio measured in this study. The values and uncertainty ranges for ε_{kin} found in this study are still useful for environmental tracer applications in groundwater and seawater (section 3.4.2) but could be resolved at even higher precision by conducting diffusion experiments with pure Ar, Kr, and Xe gas.

3.4. Discussion

3.4.1. Solubility and kinetic fractionation factors: comparison with past estimates, mass proportionality

The freshwater solubility fractionation factors presented in this study for Kr and Xe stable isotope ratios and $\delta^{38}/_{36}$Ar are, to our knowledge, the first ever published. However, prior experiments have measured the solubility fractionation factor for $\delta^{40}/_{36}$Ar at 20 °C (Tempest & Emerson, 2013) and the kinetic fractionation factors for $\delta^{40}/_{36}$Ar (Tempest & Emerson, 2013; Tyroller et al., 2014) and stable Kr and Xe isotopes (Tyroller et al., 2018). Our finding of -3.69 ± 0.25‰ for the kinetic fractionation factor (ε_{kin}) of $^{40}/_{36}$Ar agrees reasonably well with Tempest and Emerson (2013), who found values of -3.7‰ and -4.1‰ in two closed-system gas exchange experiments (Figure 3.4).

An unpublished freshwater ε_{sol} finding at 2 °C of 1.21‰ for $^{40}/_{36}$Ar was referenced in Nicholson et al. (2010), who used this value to interpret deep-ocean $\delta^{40}/_{36}$Ar solubility anomalies as constraints on ventilation of the deep ocean. The value obtained in our study at ~2 °C (1.163 ± 0.009‰) is slightly lower. Because Nicholson et al. (2010) observed deep-ocean $\delta^{40}/_{36}$Ar solubility anomalies on the order of 0.1‰, this difference may affect physical interpretation of these disequilibria. We suggest that future measurements of deep-ocean $\delta^{40}/_{36}$Ar and careful measurements of the solubility fractionation factor in seawater would be helpful in quantifying deep-ocean $\delta^{40}/_{36}$Ar disequilibrium. Additionally, we believe that our finding of Kr and Xe ε_{sol} values that are small and (within error) insensitive to temperature (Figure 3.3) has potential relevance to seawater applications. We suggest that Kr and Xe isotope ratios in the deep ocean may provide further constraints on kinetic fractionation during deep-water formation, since they should be rather insensitive to disequilibrium cooling and bubble injection.

We also compare our ε_{kin} estimates to prior studies which measured the diffusivity ratios of Ar, Kr, and Xe isotopes in water (Tyroller et al., 2014, 2018) by assuming that diffusivity ratios raised to the 2/3 power (B. Jähne et al., 1984; Ledwell, 1984) are equal to piston-velocity ratios for diffusive gas exchange across smooth interfaces. Tyroller et al. (2014) found an isotopic diffusivity ratio in water of 1.055 ± 0.004 for $^{36}/_{40}$Ar, equivalent to an ε_{kin} value of ~-35 ± 3‰ for $^{40}/_{36}$Ar (for exchange across a smooth interface). This value is clearly inconsistent both with our result and the independent finding of Tempest and Emerson (2013). Tyroller et al. (2018) conclude that Kr and Xe isotope kinetic fractionation in water is negligible, finding diffusivity ratios of unity within their measurement precision. However, the stated measurement precision of Tyroller et al. (2018) is equivalent to ~±1‰, which is the order of the Kr and Xe ε_{kin} values found in this study. We suggest that kinetic fractionation of Kr and Xe isotopes in water, though small, is in fact not negligible at our level of precision. In fact, mass-proportional differences among different isotope ratios of Kr and Xe are even discernable (Figure 3.7). We further suggest that higher-precision ε_{kin} estimates could be achieved by merging our dual-inlet mass spectrometry technique with a Barrer diffusion-cell experiment method (e.g. Tyroller et al., 2018, 2014).

Measured kinetic and solubility ε values (at 15 °C) are shown versus isotopic mass differences (Figure 3.7). We find that the magnitude of both solubility and kinetic fractionation, for Kr and Xe isotopes, increases linearly with isotopic mass difference. Extended regression lines of the presented data pass through the origin within measurement precision. The apparent linear mass dependences of Kr and Xe isotope fractionation due to dissolution and diffusive gas exchange justify the use of δ*Kr (Equation 3.3) and δ*Xe (Equation 3.4) for dissolved gas measurements. The observed Ar isotopic solubility and kinetic fractionation factors also increase in magnitude with isotopic mass difference, but the relationship does not appear to be exactly linear (e.g. the ratio of $^{40}/_{36}$Ar and $^{38}/_{36}$Ar ε_{sol} values is slightly below 2, the ratio of their isotopic mass differences; Table 3.1, Supplemental Figure 3.S12). Overall, our observations are consistent with the conclusions of other recent noble gas isotope studies in water (Bourg & Sposito, 2008; Tempest & Emerson, 2013; Tyroller et al., 2014, 2018), which all found that the kinetic-theory expectation of a uniform square-root relationship between mass and diffusivity ratios fails to account for both observed and modeled kinetic fractionation of noble gas isotopes in water.

3.4.2. Implications for heavy noble gas isotope ratios as geochemical tracers

The newly determined solubility and kinetic isotopic fractionation measurements presented in this study have implications for potential applications of dissolved Ar, Kr, and Xe isotopes as tracers of physical processes in the atmosphere, ocean, and terrestrial hydrosphere. Here we briefly consider one such application: δ^*Kr and δ^*Xe in groundwater as quantitative indicators of past water-table depth. Prior work has indicated that Kr and Xe isotopes in the unsaturated zone are fractionated from their ratios in the well-mixed troposphere by gravitational settling (Seltzer et al., 2017). The dissolution of unsaturated zone gases into groundwater at the water table should preserve this gravitational fractionation signal in the dissolved isotope ratios of Kr and Xe. Because gravitational fractionation is a nearly linear function of depth, quantitative reconstruction of past water-table depth may be possible by measuring dissolved δ^*Kr and δ^*Xe in ancient groundwater samples that have not experienced gas exchange since the time of recharge.

The finding of Kr and Xe isotopic fractionation factors near unity (ε_{sol} and ε_{kin} close to zero) implies that groundwater δ^*Kr and δ^*Xe should be extremely insensitive to the injection and fractionation of excess air, which is a confounding issue in noble-gas paleotemperature studies (e.g. Stute et al., 1995). To demonstrate the importance of this insensitivity, we assume that the isotopic composition of groundwater, $\delta_{diss,gw}$, reflects the gravitationally-fractionated isotopic composition of unsaturated zone air above the water table, $\delta_{UZ,WT}$, plus solubility fractionation and fractionation due to excess air:

$$\delta_{diss,gw} = \delta_{UZ,WT}(d) + \varepsilon_{sol}(T) + \varepsilon_{EA}(T, A, F) \tag{3.12}$$

In Equation 3.12, ε_{EA} is the isotopic fractionation due to excess air at a given recharge temperature *T*, amount of initially entrapped air *A*, and modification *F* of that entrapped air due to partial dissolution or re-equilibration. Excess air can be added to groundwater and fractionated via either the closed-system equilibration (CE, Aeschbach-Hertig et al., 1999) or partial re-equilibration (PR, Stute et al., 1995) models. Reconstructing the isotopic composition of unsaturated-zone air $\delta_{UZ,WT}$, at water-table depth *d*, requires knowledge of both ε_{sol} and ε_{EA} (Equation 3.12). By measuring bulk noble gas concentrations in a given groundwater sample to determine *T*, *A*, and *F*, the ε_{sol} values determined in this study can be substituted directly into Equation 3.12.

However, to quantify ε_{EA}, an excess-air model (typically either the CE or PR model) and the values of ε_{sol} and/or ε_{kin} presented in this study must be used. In Figure 3.8, we show that ε_{EA} is small in magnitude and largely insensitive to the choice of excess-air model, owing to the small values of ε_{sol} and ε_{kin} determined in this study. The range of *A* (the volumetric ratio of initially entrapped air to water) considered in Figure 3.8 covers the range of realistic values in groundwater. For reference, assuming complete dissolution of entrapped air (i.e. the unfractionated-air [UA] model), $A = 0$ corresponds to 0% neon supersaturation, ΔNe, while $A = 0.05$ corresponds to ΔNe = ~450%. As shown in Figure 3.8, differences between ε_{EA} calculated via the PR and CE models for typical values of fractionation and re-equilibration parameters, *F* and *R*, are typically ~5 per meg amu^{-1}, equivalent to ~1 m of gravitational settling fractionation. Similar results (~5-10 per meg amu^{-1} CE vs. PR differences) were found for Kr isotopic fractionation due to excess air

(Supplemental Figure 3.S13). We therefore suggest that dissolved δ*Kr and δ*Xe in groundwater represent promising new tracers of past water-table depth, based on our finding that ε_{EA} is small and rather insensitive to the choice of excess-air model.

3.5. Conclusions

In this study, we present results from a new method for high-precision measurement of Ar, Kr, and Xe stable isotope ratios in water. By conducting closed-system experiments at temperatures from ~2-20 °C, we have determined freshwater Ar, Kr, and Xe isotopic solubility fractionation factors and their temperature dependences. We also carried out three separate air-water gas exchange experiments in which gas disequilibrium was induced by rapid cooling of water for the purpose of modeling kinetic fractionation due to diffusion in water. The solubility and kinetic fractionation factors we found exhibit mass proportionality for different isotope ratios of a given element and decrease in isotopic mass-difference-normalized magnitude with increasing atomic number. The discovery of solubility and kinetic fractionation factors near unity for stable Kr and Xe isotopes gives promise to the potential for δ*Kr and δ*Xe in groundwater as a novel tool for the reconstruction of past water-table depths.

3.S1. Discussion of temperature-dependent OA vs CS experiment differences

The ε_{sol} results from the set of OA and CS experiments carried out in this study systematically diverged as a function of temperature. Specifically, OA ε_{sol} measurements were higher than CS ε_{sol} measurements (i.e. higher heavy-to-light isotope ratios in OA vs CS experiments), and this difference (Δε) decreased roughly linearly with temperature for Ar, Kr, and Xe isotope ratios (Figures 3.S6 and 3.S7). Ar isotope ratios exhibited the largest OA-CS Δε, followed by Kr and Xe isotope ratios, respectively. At 20 ºC, Δε was roughly zero for Ar, Kr and Xe isotope ratios.

We suggest that the observed gas-and-temperature-dependent pattern of OA-CS Δε is consistent with gas-phase diffusive fractionation in the OA experiments due to gradients in temperature and humidity between well-mixed atmospheric air in the laboratory and a stagnant air layer (SAL) above the OA water bath. The CS experiments, in which no temperature and humidity gradients can exist within the closed equilibration vessel, are not affected by this proposed fractionation. Therefore, differences between the two experiments should allow us to quantify and model the effects of SAL-atmospheric air fractionation.

We argue that two diffusive fractionation processes constructively interfere to produce positive OA-CS Δε at low temperatures: thermal diffusion and water-vapor flux fractionation. In the presence of a constant temperature difference in a column of stagnant air, heavy gases preferentially diffusive towards the colder region and light gases diffuse towards the warmer region (Grew & Ibbs, 1953). This effect, called thermal diffusion fractionation, is described by an isotope-ratio specific thermal diffusion sensitivity, **Ω**, and a temperature contrast, ΔT:

$$\varepsilon_{\text{therm}} = \Omega \Delta T \quad (3.S1)$$

where $\varepsilon_{\text{therm}}$ represents the heavy-to-light isotopic enrichment (in ‰, per meg, or per meg amu^{-1}) in the cold region at diffusive steady-state. **Ω** has been empirically determined as a function of temperature for Ar, Kr, and Xe isotope ratios (Grachev & Severinghaus, 2003; Kawamura et al., 2013). We suggest that the constant temperature contrast between the SAL, which has a temperature close to that of the water bath (<23 °C in all experiments), and the room air (~23 ± 1 °C) led to heavy-isotope enrichment in the SAL due to thermal diffusion in all OA experiments.

Water vapor flux fractionation refers to steady-state kinetic fractionation due to diffusion of water vapor into or out of a gas reservoir and was first observed and quantified in sand dune O_2 and N_2 isotopic measurements (Severinghaus et al., 1996). In the case of the OA experiments at cold temperatures (below ~12 °C), the mole fraction of water vapor, χ_{H2O}, in the cold SAL (relative humidity ~100%) is less than χ_{H2O} in the warm laboratory air (relative humidity ~50%). For example, for an OA experiment at 2 °C, χ_{H2O} would be ~0.007 in the SAL but ~0.014 in the laboratory air (assuming 50% relative humidity and 23 °C). At steady state, this χ_{H2O} difference drives diffusion of water vapor from the lab air into the SAL (where it condenses). Because the total pressure in the SAL and laboratory air must be equal, the mole fraction of noble gases must be larger in the SAL than in the laboratory air due to the steady-state diffusion of water vapor into the SAL, which advectively (without fractionating) sweeps noble gases from the lab air into the SAL. At steady state, then, noble gases must diffuse back from the SAL to the lab against the diffusive flux of water vapor in the opposite direction. For a given isotope ratio, there is steady-state enrichment of heavy-to-light isotopes in the SAL relative to lab air, because the binary diffusivity of the light isotope against water vapor, $D_{l\text{-}H2O}$, is greater than that of the heavy isotope, $D_{h\text{-}H2O}$. This effect is quantified by the following approximation (good to ~1 per meg):

$$\varepsilon_{\mathrm{H2O}} \approx \left[\left(\frac{1-\chi_{\mathrm{H2O,SAL}}}{1-\chi_{\mathrm{H2O,lab}}}\right)^{\frac{D_{\mathrm{l-H2O}}}{D_{\mathrm{h-H2O}}}-1} - 1\right] \tag{3.S2}$$

where $\varepsilon_{\mathrm{H2O}}$ refers to the heavy-to-light enrichment of an isotope ratio in the SAL relative to atmospheric air in the well mixed lab (Severinghaus et al., 1996). Binary diffusivity ratios are calculated using the method of Fuller et al. (1966) presented in Reid et al. (1977).

While these two effects, thermal diffusion and water-vapor flux fractionation, should both lead to heavy isotope enrichment at cold temperatures, they destructively interfere at temperatures between ~12 and 23 ºC. In this temperature range, the mole fractionation of water vapor in the SAL exceeds that of the lab air, causing $\varepsilon_{\mathrm{H2O}}$ to reverse in sign (i.e. light isotope enrichment in the SAL). However, because the SAL is still colder than lab air between 12 and 23 ºC, thermal fractionation still operates in the same sense (heavy isotope enrichment). The two effects should cancel completely at ~20 ºC.

Indeed, our observations are consistent with OA-CS Δε = 0 at ~20 ºC (Figure 3.S6) for ^{40}Ar/^{36}Ar ratios. The full effect of these two diffusive fractionation processes (i.e. the sum of equations 3.S1 and 3.S2) suggests Δε for ^{40}Ar/^{36}Ar of ~1‰ at ~2 ºC, roughly three times larger than observed. However, a simple model for Δε in which both effects are weakened by advective exchange between the SAL and lab air fits our observations for Ar, Kr, and Xe isotope ratios. Specifically, we propose the following physical model:

$$\Delta\varepsilon_{\mathrm{model}} \approx \beta\, [\varepsilon_{\mathrm{H2O}}(\mathrm{T}) + \varepsilon_{\mathrm{therm}}(\mathrm{T})] \tag{3.S3}$$

where β represents the fraction of gas exchange between the lab air and SAL that is diffusive. β is related to the Péclet number (Pe, the ratio of advective to diffusive transport) in that β = 1/(Pe +1). Advective gas exchange is unfractionating, so each effect – thermal diffusion fractionation and water-vapor flux fractionation – should scale linearly with β. In Figures 3.S6 and 3.S7, we compare observed and modeled OA-CS Δε for Ar, Kr and Xe isotope ratios.

In addition to the general good agreement between equation 3.S3 and observations, two lines of evidence support our hypothesis that thermal diffusion and water-vapor flux fractionation between the SAL and lab air, weakened by advective transport, explain the observed OA-CS experiment differences. First, the disappearance of OA-CS differences at 20 ºC is a strong prediction based on the destructive interference of ε_{H2O} and ε_{therm} that is supported by our observations. Second, the pattern of OA-CS $\Delta\varepsilon$ observations, largest for Ar isotopes and weakest for Xe isotopes, is consistent with physical predictions from this model.

However, because we cannot be entirely certain in our physical explanation, we use empirically derived linear temperature fits to OS-CS experiment differences to determine α_{SAL} (the temperature-dependent lab air-SAL fractionation factor for each isotope ratio) and its uncertainty. We apply α_{SAL} to the model-based interpretation of kinetic fractionation experiments, accounting for uncertainty in the empirical estimates by carrying out monte carlo simulations. The good agreement between our ^{40}Ar/^{36}Ar kinetic fractionation factor estimates derived from equations 3.9 through 3.11 (dependent on α_{SAL}) with the experiments of Tempest and Emerson (2013) is evidence that the OA-CS experiment differences properly quantify fractionation between the SAL and lab air.

Acknowledgements

We are grateful to Ross Beaudette, Bill Paplawsky, and Adam Cox for assistance and advice on designing the laboratory infrastructure that enabled this research. We also thank Michael Bender, Roberta Hamme, Ray Weiss, Martin Stute, Justin Kulongoski, Steve Emerson, Kevin Tempest, and Sarah Shackleton for helpful discussions, suggestions, and equipment loans that contributed to the early development of this work. This study was supported by NSF award #1702704 as well as an NSF Graduate Research Fellowship. All data and relevant model code are accessible in the Supplementary materials.

This chapter, in full, is a reproduction of material as it appears in Seltzer, A., Ng, J. and J. Severinghaus. Precise Determination of Ar, Kr, and Xe isotopic fractionation due to diffusion and

dissolution in fresh water, *Earth and Planetary Science Letters*, 2019. The dissertation author was the primary investigator and author of this work.

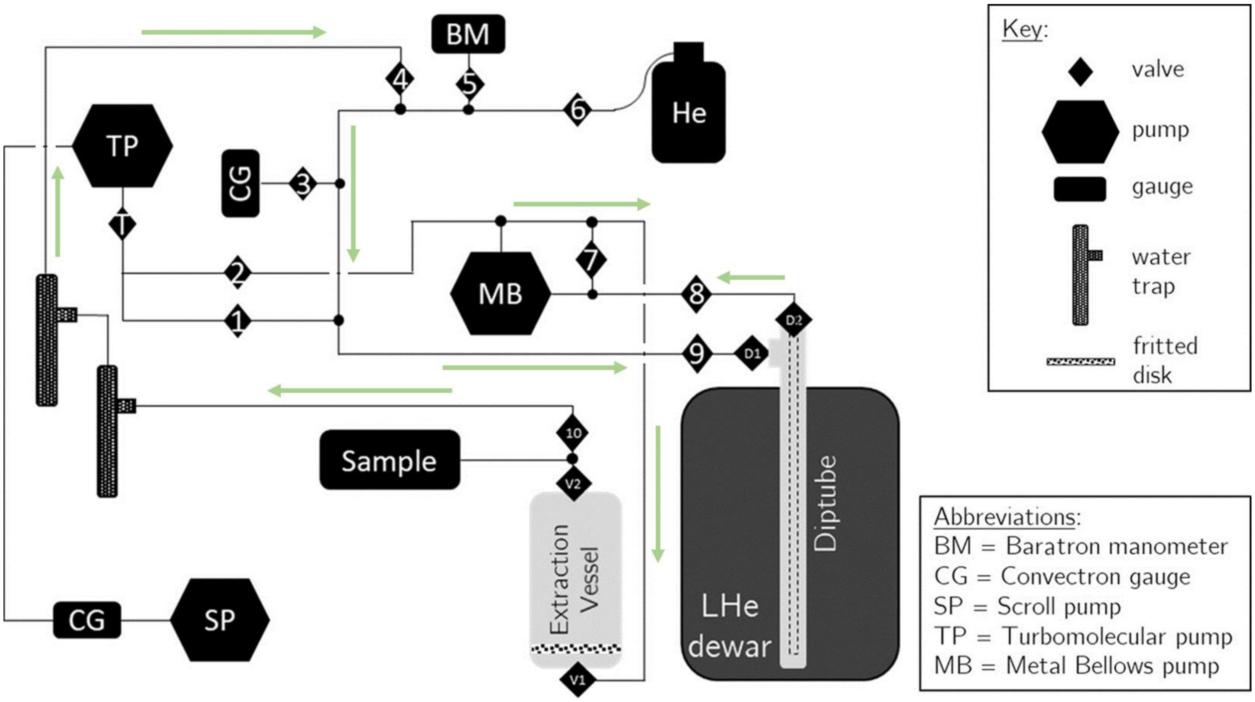

Figure 3.1: Dissolved gas extraction system. Arrows indicate flow direction of liberated dissolved gases and helium carrier gas.

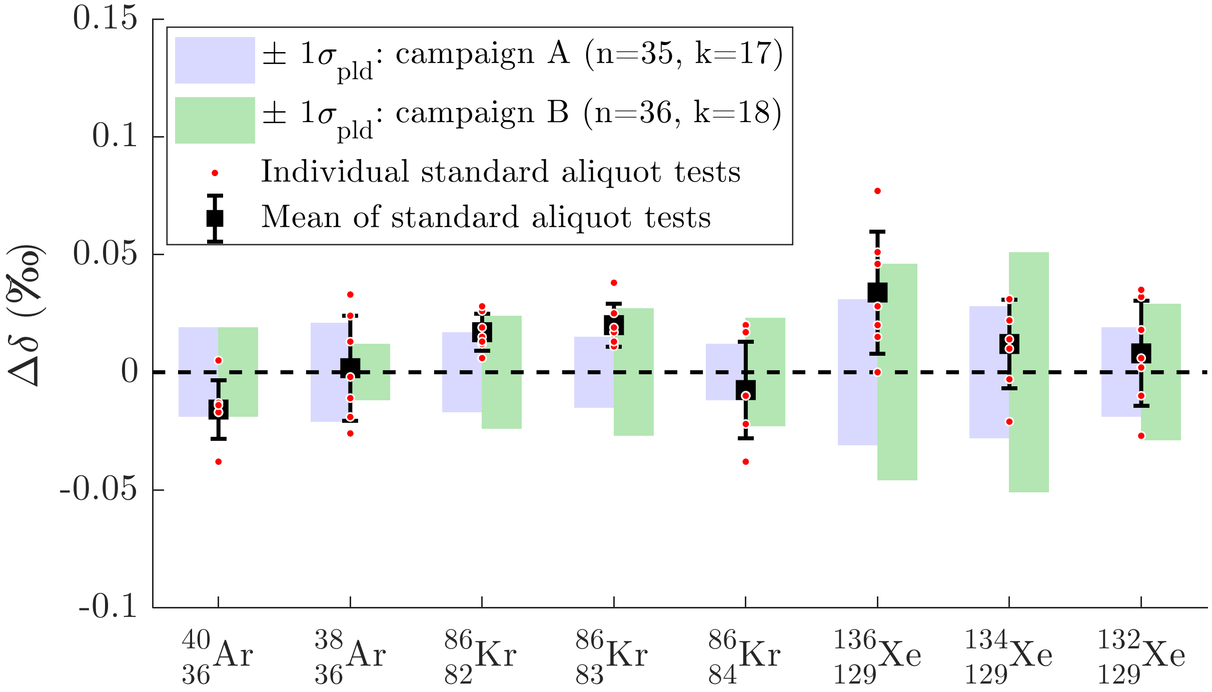

Figure 3.2: Reproducibility of isotope ratio measurements, expressed as pooled standard deviations, and results of repeat standard aliquot tests. Standard aliquot test values are reported as isotope ratio departures, Δδ, from the known composition of the reference gas used in the tests (ST-AEW2).

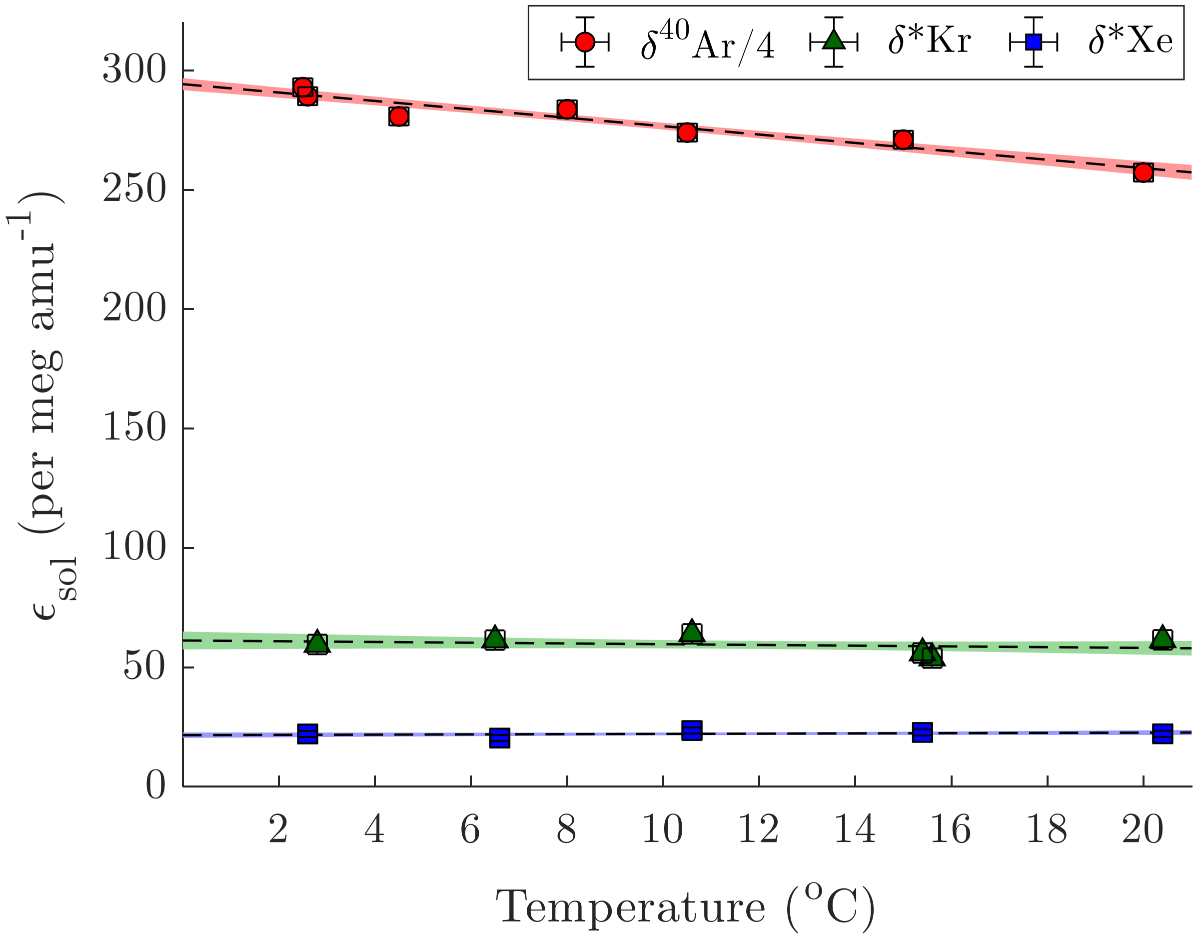

Figure 3.3: Mass-normalized freshwater solubility ε_{sol} values between ~2 and 20 ºC determined in closed-system (CS) equilibration experiments. Markers represent values for individual experiments, each constrained by a pair of measurements (one dissolved gas and one headspace gas measurement) at solubility equilibrium. Vertical error bars indicate individual measurement precision (±1σ), shaded error regions around dashed trendlines indicate ±1-σ range of linear fits, and horizontal error bars indicate ± 0.2 ºC absolute error of equilibration temperatures.

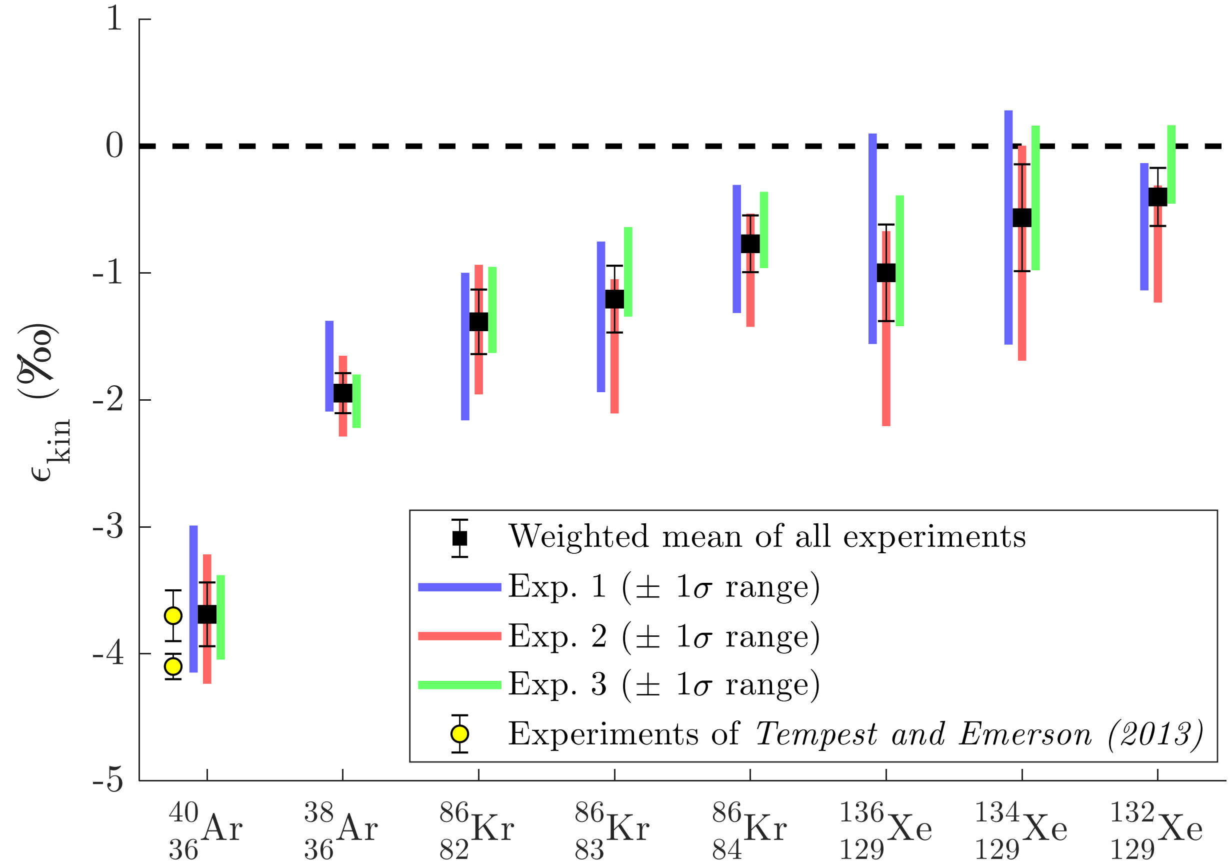

Figure 3.4: Weighted-mean $\varepsilon_{\mathrm{kin}}$ values for each isotope ratio measured across three rapid cooling experiments. Colored bars represent ±1-σ confidence ranges from three individual experiments (from least-squares fits of 1000 monte carlo simulations to observations for each experiment and isotope ratio). Yellow circles indicate results of two ^{40}Ar/^{36}Ar kinetic fractionation experiments presented in *Tempest and Emerson (2013)* using an independent experimental method.

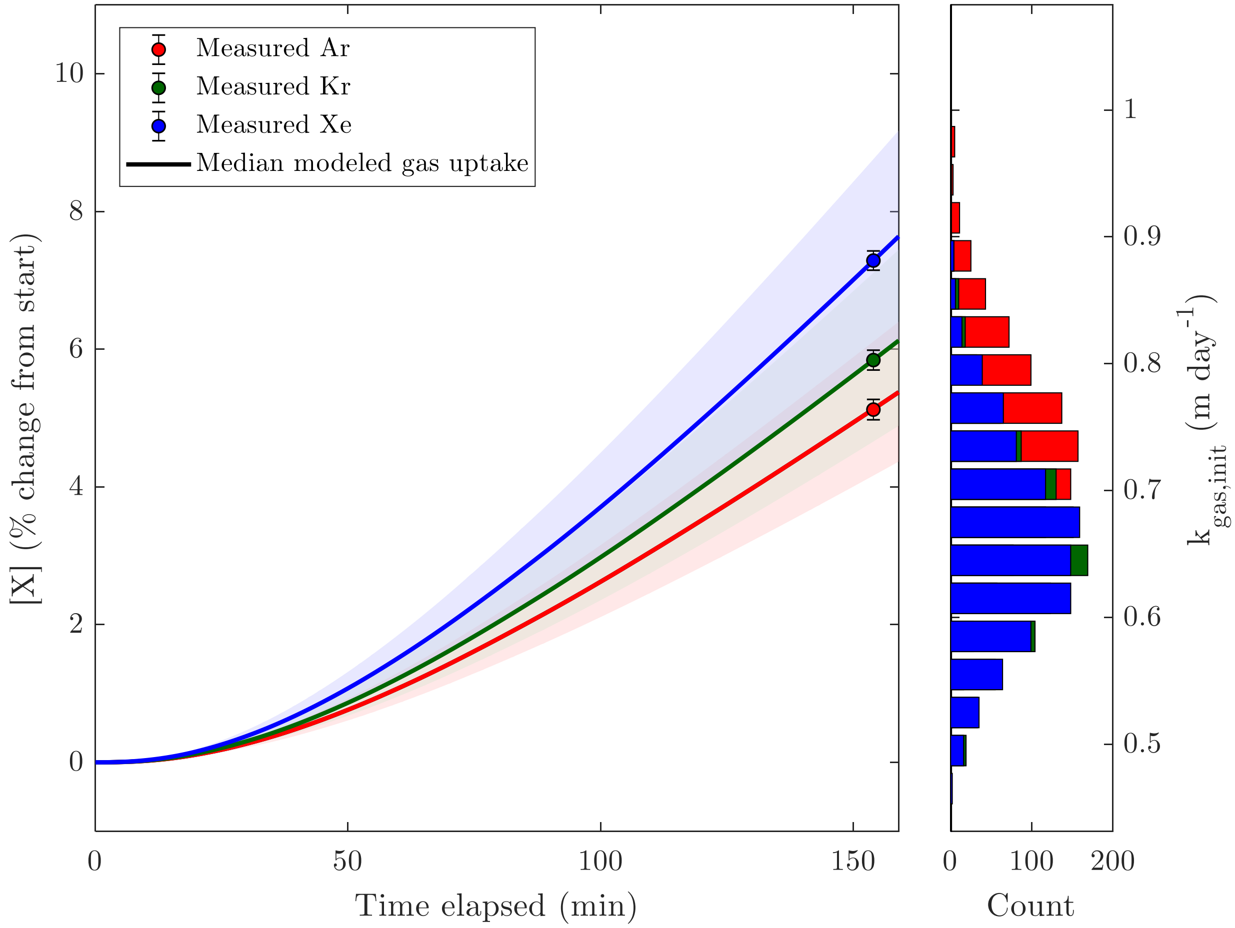

Figure 3.5: Modeled evolutions of Ar, Kr, and Xe gas concentrations ([X]) during RCE1, in which a water-bath brought to steady state in an OA experiment at 12.9 ºC over four days was cooled by ~10 ºC over ~3 hours. In the left panel, markers indicate replicate-mean measured [Ar], [Kr], and [Xe] (filled circles) and solid lines indicate median modeled gas uptake by fitted gas exchange model (shaded regions indicate 95% confidence intervals of 1000 monte carlo simulations per gas). In the right panel, histograms of modeled Ar, Kr, and Xe piston velocities (at start of experiment) are shown from 1000 monte carlo gas-exchange model-data fits (described in Section 3.2.4). Measured and modeled concentrations are presented as percent departures from initial steady-state OA experiment conditions for 12.9 ºC water.

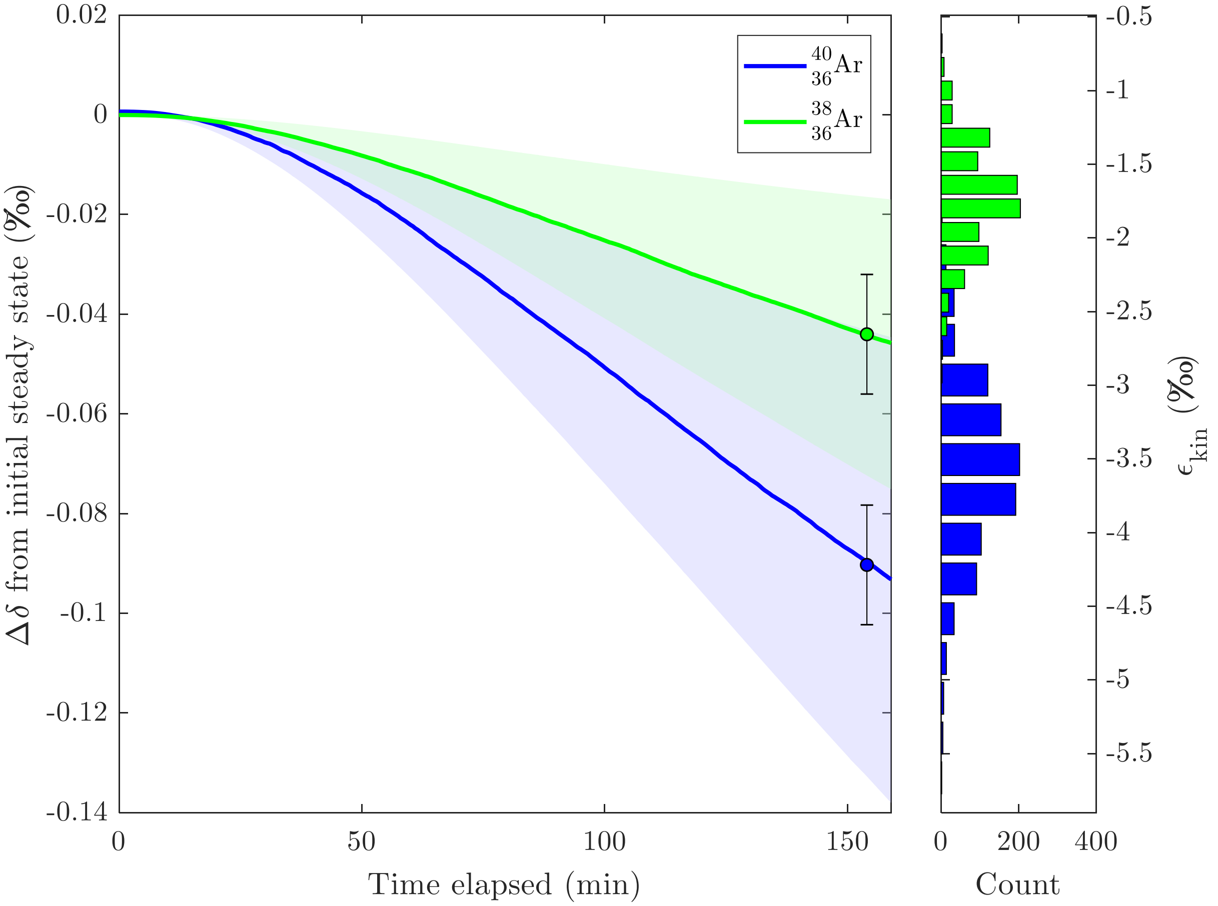

Figure 3.6: Modeled $\delta^{40}/_{36}$Ar and $\delta^{38}/_{36}$Ar departures over the course of RCE1 from values in steady-state OA experiments at 12.9 °C (Supplemental Figure 3.S6). Shaded regions indicate 95% confidence intervals of 1000 monte carlo simulations (per isotope ratio) and filled circles show replicate-mean replicate values with ±1-σ uncertainty. Distributions of ε_{kin} values shown in right panel reflect least-squares minimization of measured data to 1000 monte carlo simulations.

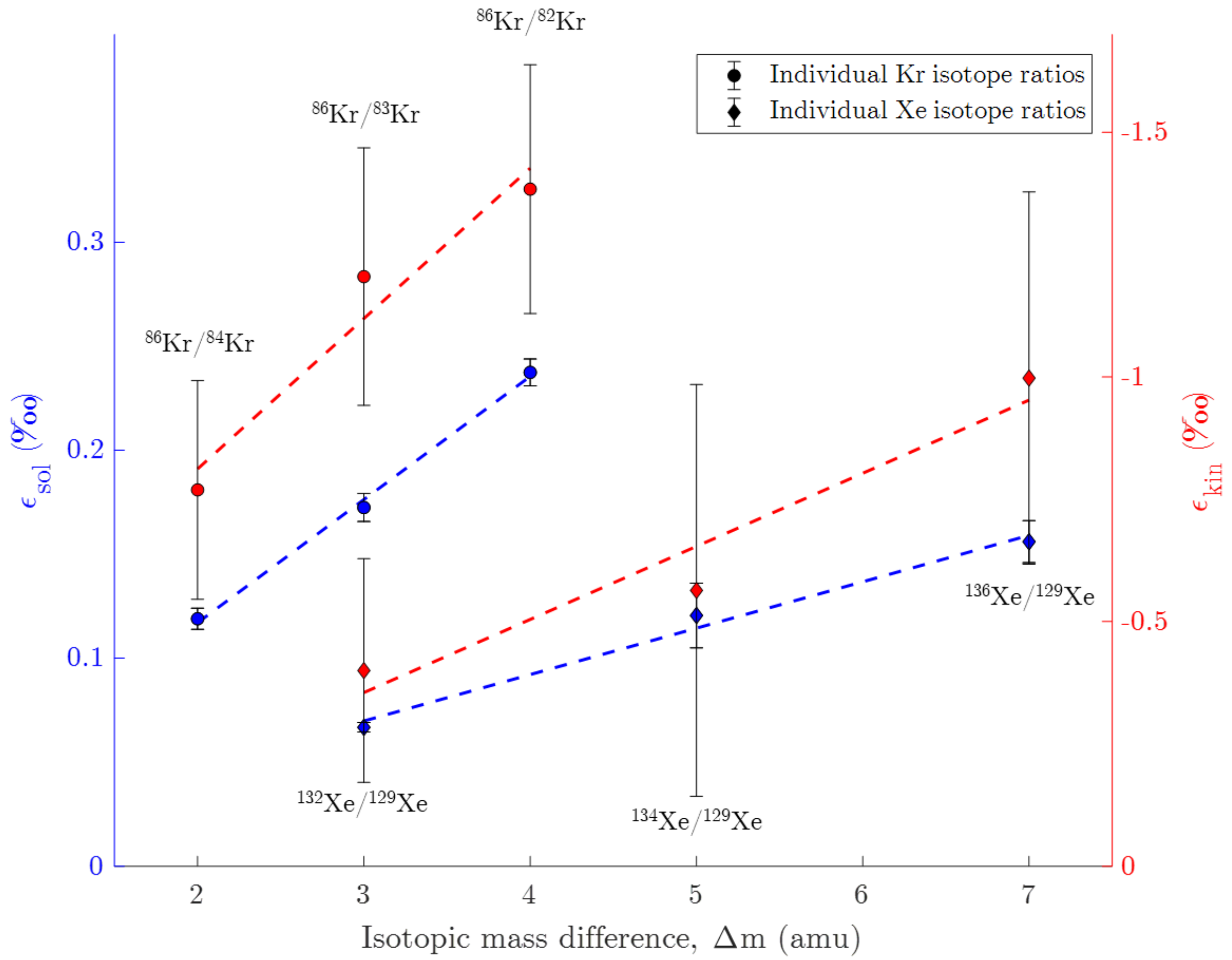

Figure 3.7: Individual isotope ratio ε_{sol} and ε_{kin} values versus isotopic mass difference Δm for stable isotope ratios of Kr and Xe. The ε_{sol} vs. Δm linear regression coefficients and intercepts, respectively, are 0.059‰ amu^{-1} and -0.001‰ for Kr isotope ratios and 0.022‰ amu^{-1} and 0.003‰ for Xe isotope ratios. The ε_{kin} vs. Δm linear regression coefficients and intercepts, respectively, are -0.307‰ amu^{-1} and -0.197‰ for Kr isotope ratios and -0.150‰ amu^{-1} and 0.094‰ for Xe isotope ratios. The intercepts for all four regression lines pass through the origin within ±1-σ uncertainty.

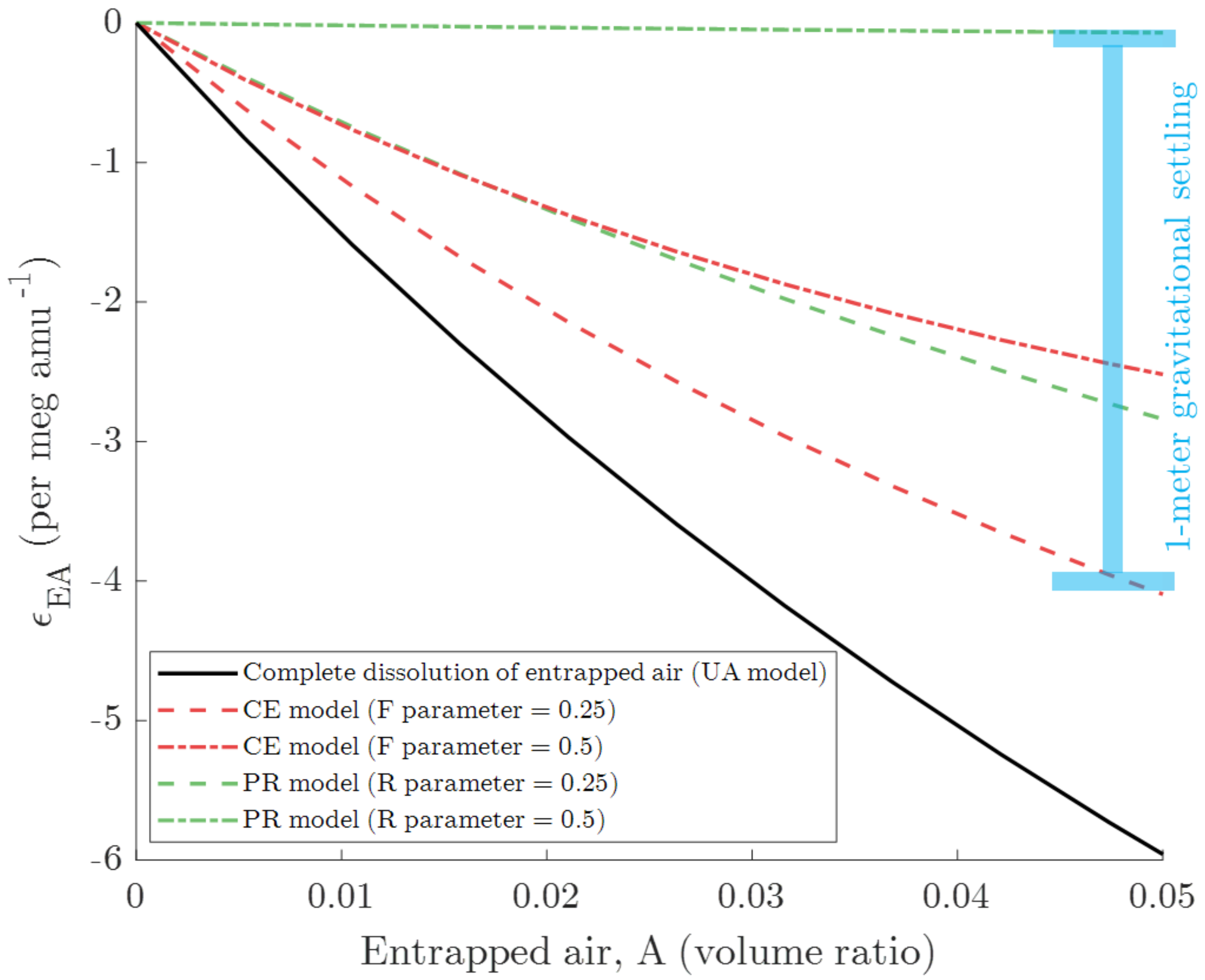

Figure 3.8: Sensitivity of ε_{EA} to entrapped air amount for Xe isotopes in groundwater (i.e. δ*Xe). Two common excess-air models (CE and PR models) and their shared limiting case of complete dissolution of entrapped air (i.e. the unfractionated excess air [UA] model: F=0, R=0) are considered. The F parameter in the CE model refers to the partiality of dissolution (the ratio of initial to final entrapped air to water volumetric ratios). The R parameter in the PR model refers to the degree of diffusive re-equilibration of supersaturated dissolved gases with the overlying unsaturated zone (such that higher R values indicate more complete re-equilibration). For comparison (blue scale), note that the fractionation due to 1 m of gravitational settling is ~4 per meg amu^{-1}.

Table 3.1: Ar, Kr, and Xe isotopic solubility (at 15 ºC) and kinetic fractionations (ε values) and measurement precision of campaigns A and B. ε and σ values have units of ‰, $d\varepsilon_{sol}/dT$ has units of ‰ $^{o}C^{-1}$, and Δm has units of amu.

	$\delta^{40}/_{36}Ar$	$\delta^{38}/_{36}Ar$	$\delta^{86}/_{82}Kr$	$\delta^{86}/_{83}Kr$	$\delta^{86}/_{84}Kr$	$\delta^{136}/_{129}Xe$	$\delta^{134}/_{129}Xe$	$\delta^{132}/_{129}Xe$
Δm	4	2	4	3	2	7	5	3
$\sigma_{pld,A}$	0.019	0.021	0.017	0.015	0.012	0.031	0.028	0.019
$\sigma_{pld,B}$	0.019	0.012	0.024	0.027	0.023	0.046	0.051	0.029
ε_{sol}	1.072	0.563	0.237	0.172	0.119	0.156	0.121	0.067
$d\varepsilon_{sol}/dT$	-0.007	-0.004	-0.001	0.000	-0.001	0.000	0.002	0.000
ε_{kin}	-3.689	-1.946	-1.384	-1.205	-0.769	-0.998	-0.564	-0.400

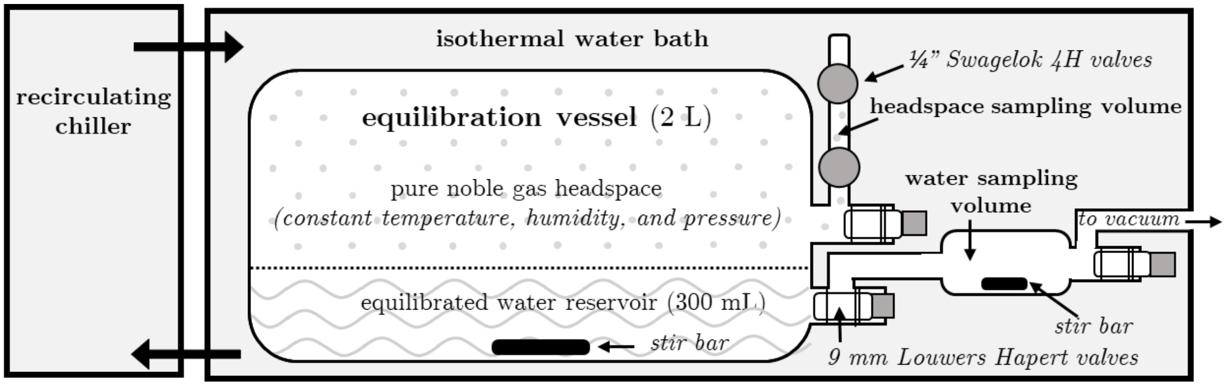

Figure 3.S1: Diagram of closed-system (CS) equilibration system. A small reservoir of initially degassed water (200-300 mL) reaches solubility equilibrium with a pure noble gas headspace (at ~1 atm total pressure) in a closed, ~2-L flask before headspace and water samples are collected. Headspace samples are collected by closing off the inner 4H valve and disconnecting the headspace sampling volume. Water samples are collected by allowing ~10 mL of water to enter initially evacuated water sampling volume, which is closed off to the vacuum line during sample collection.

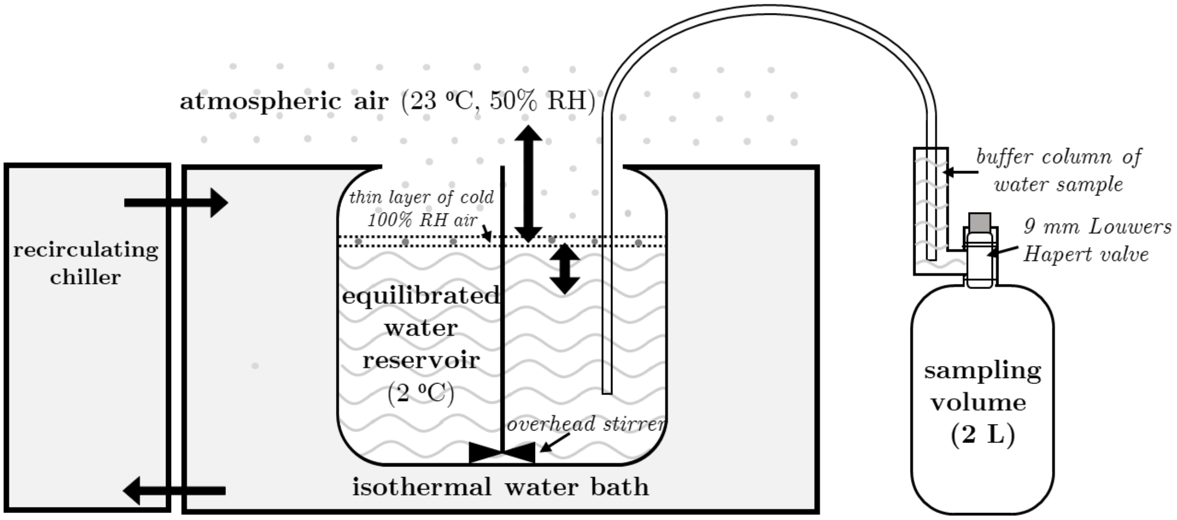

Figure 3.S2: Diagram of open-air (OA) equilibration system, in which a 2-L sample is collected from a ~20-L temperature-controlled water bath after four or more days. In this diagram, 2 ºC water is brought to dissolved isotopic steady state (over several days) with a thin layer of 2 ºC, water vapor-saturated air (referred to in the text as the stagnant air layer, SAL) presumed to be fractionated from well-mixed atmospheric air the laboratory (~50% relative humidity and 23 ºC) due to thermal diffusion and steady-state diffusion of water vapor from the room into the SAL.

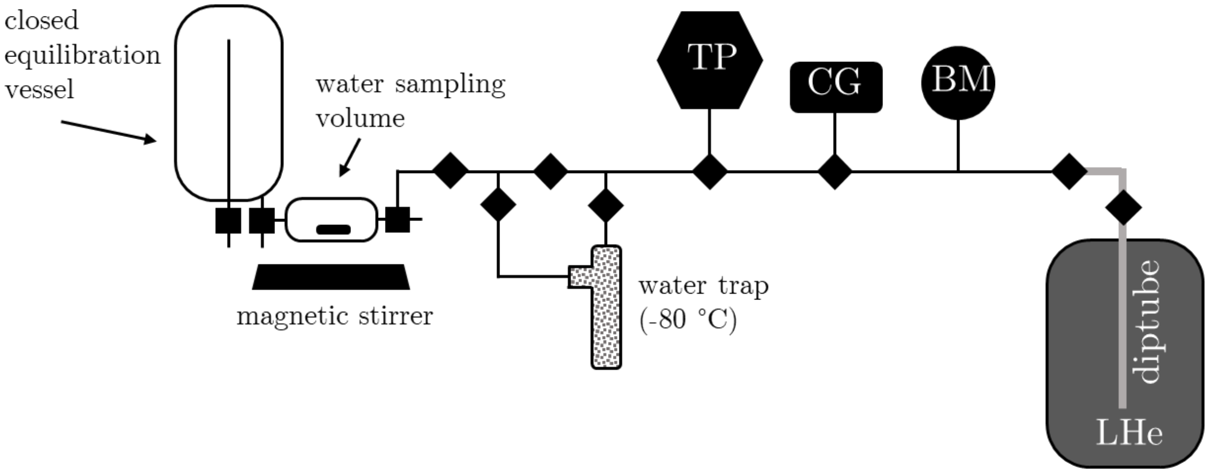

Figure 3.S3: Schematic of closed-system (CS) dissolved gas extraction method, in which gases are extracted under vacuum and cryogenically trapped in a diptube immersed in liquid helium. TP, CG, and BM refer to turbomolecular pump, Convectron gauge, and Baratron gauge, respectively.

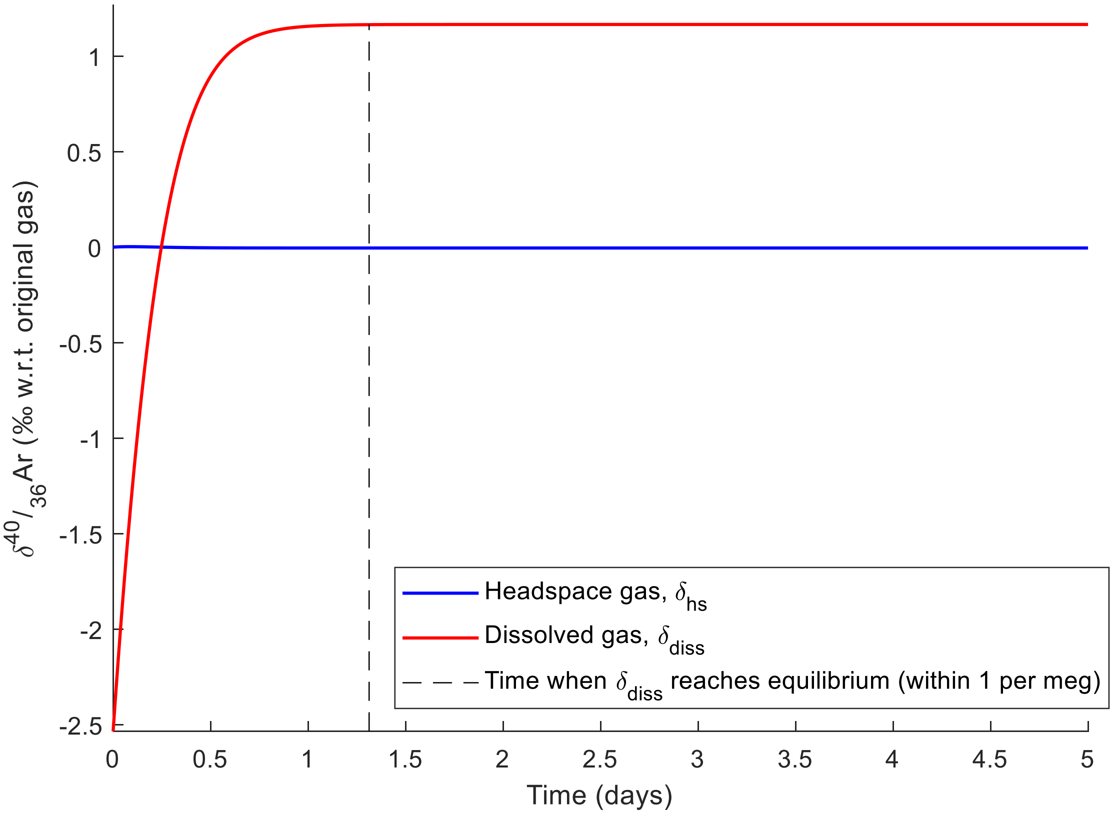

Figure 3.S4: Two-box (headspace and water) gas exchange model for CS experiments (here shown for ^{40}Ar/^{36}Ar) demonstrating that isotopic solubility equilibrium is reached in under 1.5 days. In this extreme case, a conservative 0.2 m day^{-1} piston velocity is assigned with a fractionation factor equal to that observed in the RCEs (α_{kin} = 0.9963). We assume a 2.5-cm thick column of water and initialize the model with completely degassed water in an isothermal, 2 ºC closed system.

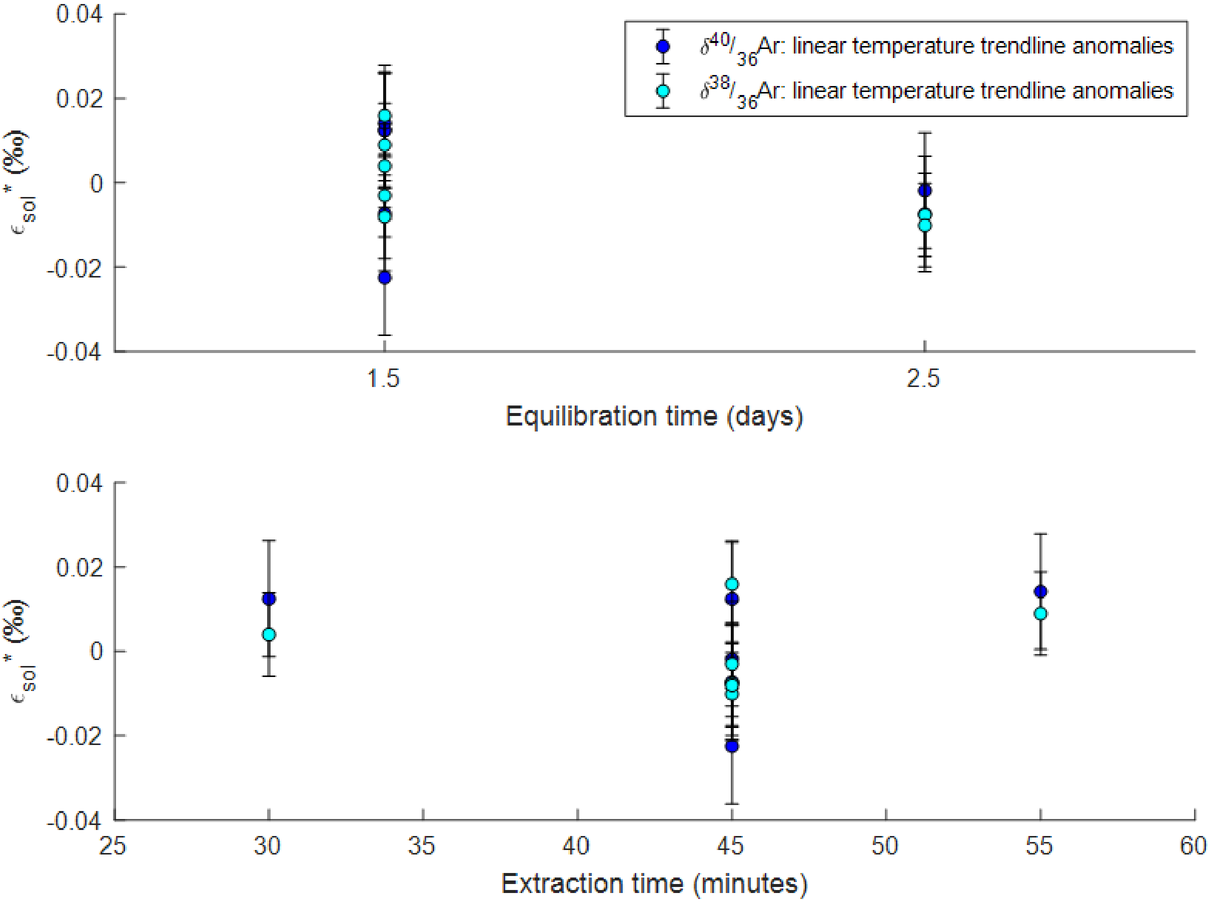

Figure 3.S5: Insensitivity of CS method to extraction and equilibration times for Ar isotope ratios demonstrated by absence of trend in linear regression anomalies of ε_{sol} versus temperature across seven experiments (i.e. $\varepsilon^*_{sol} = \varepsilon_{sol,\ measured} - \varepsilon_{sol,\ linear\ fit}$).

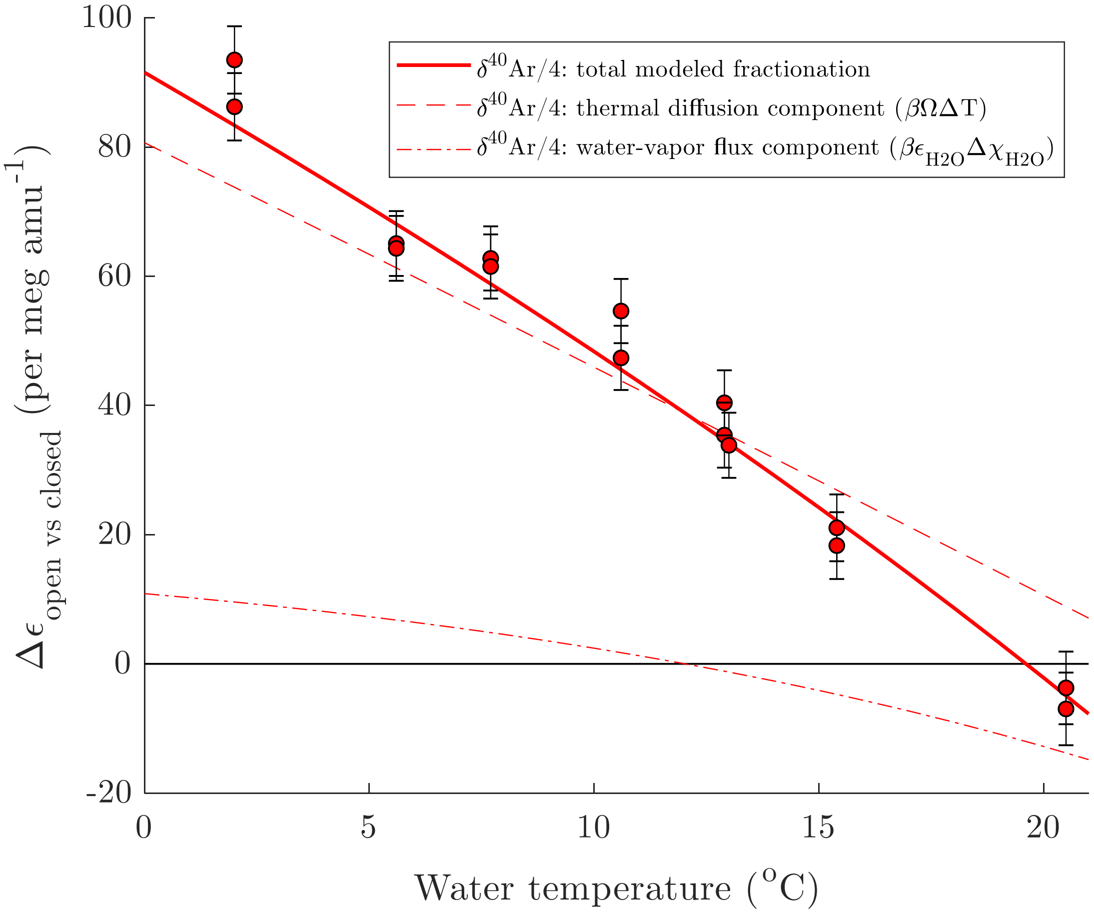

Figure 3.S6: Observed differences of OA experiments from linear fit to CS experimental values for ^{40}Ar/^{36}Ar as a function of temperature. The solid red line shows a physical model described in Supplemental Section 3.S1 comprised of thermal diffusion fractionation (dashed line) and water vapor flux fractionation (dot-dashed line).

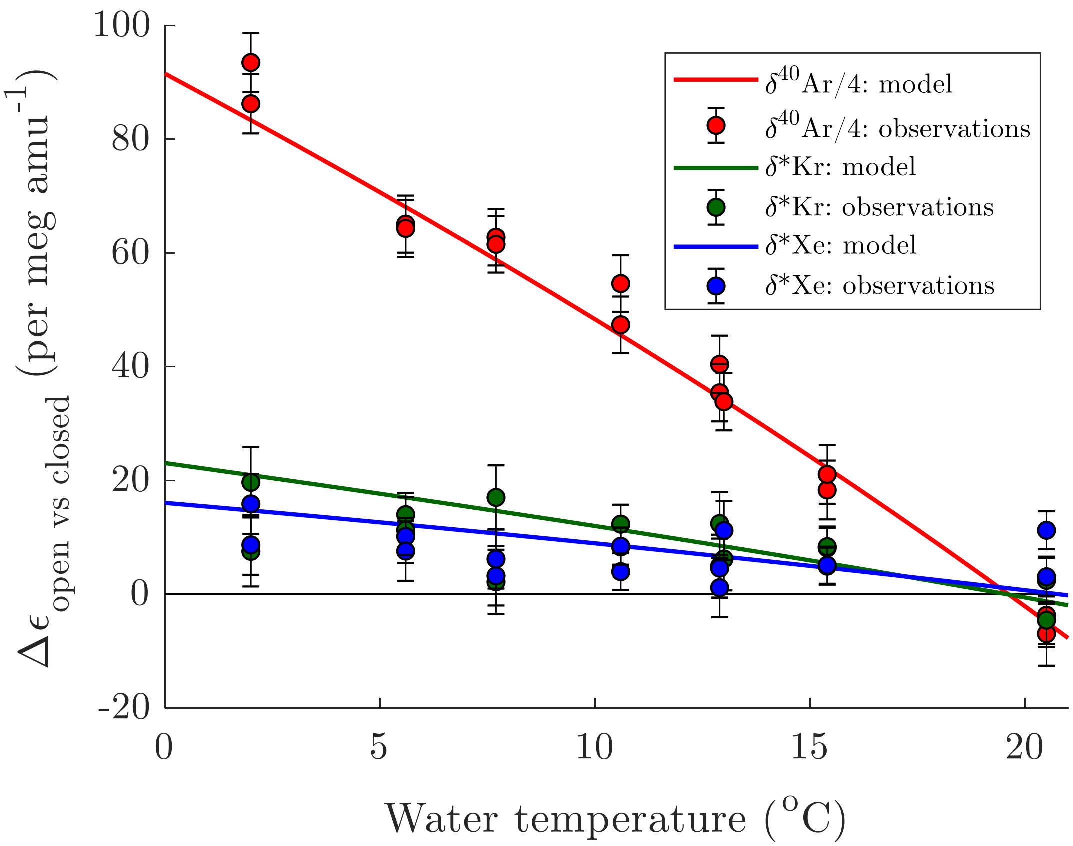

Figure 3.S7: Observed differences of OA experiments from linear fit to CS experimental values for Ar, Kr, and Xe isotope ratios as a function of temperature. Solid lines indicate physical model (described in Supplemental Section 3.S1) for isotope ratios of each gas. Note that linear fits to these data (not these modeled curves) are used to empirically estimate $\boldsymbol{\alpha}_{\text{SAL}}$ and its uncertainty for use in the RCE experiments to determine kinetic fractionation factors.

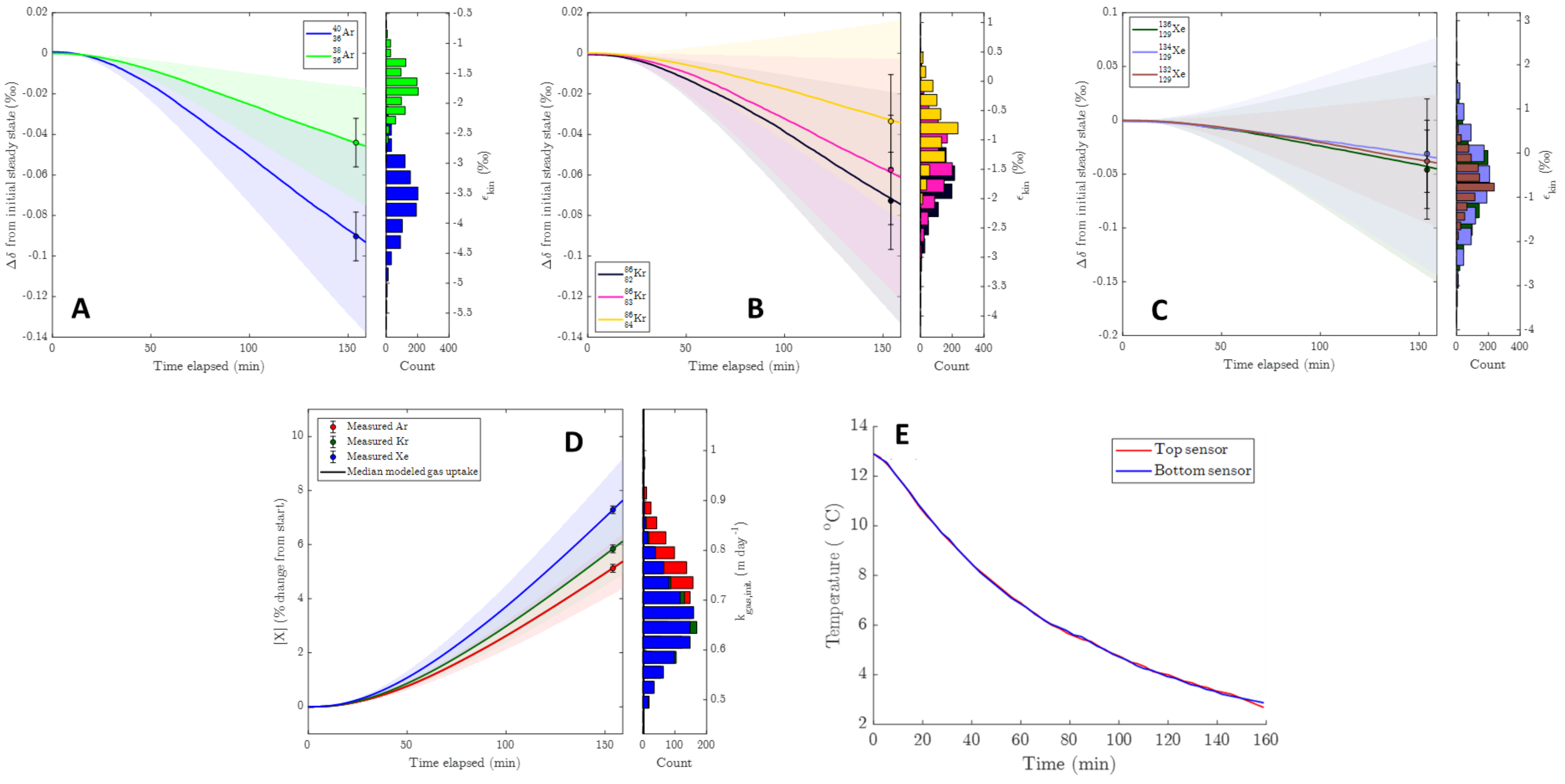

Figure 3.S8: Results from RCE1 for Ar isotopes (A), Kr isotopes (B), Xe isotopes (C), and bulk gases (D). Temperature log is shown in panel E.

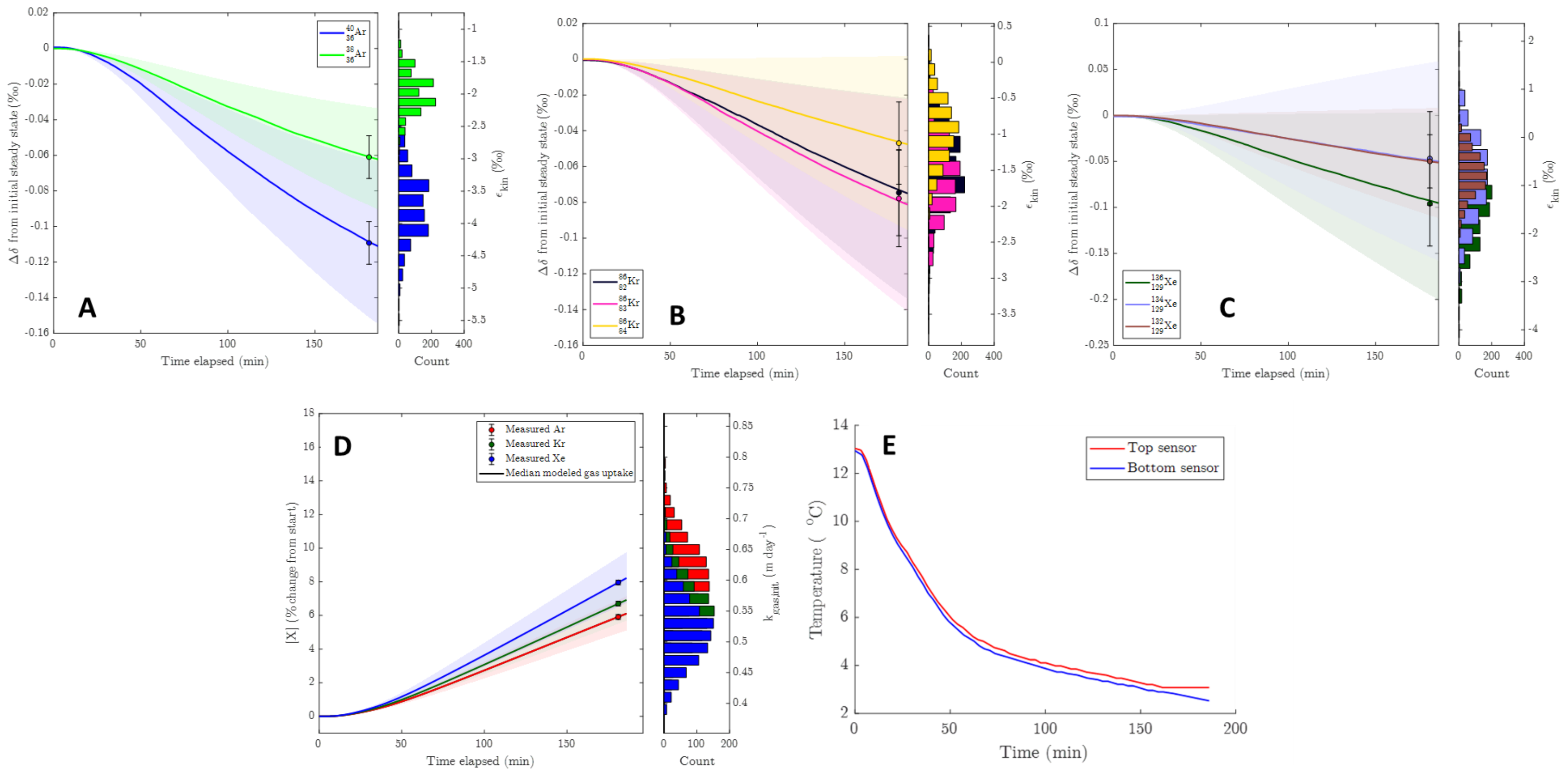

Figure 3.S9: Results from RCE2 for Ar isotopes (A), Kr isotopes (B), Xe isotopes (C), and bulk gases (D). Temperature log is shown in panel E.

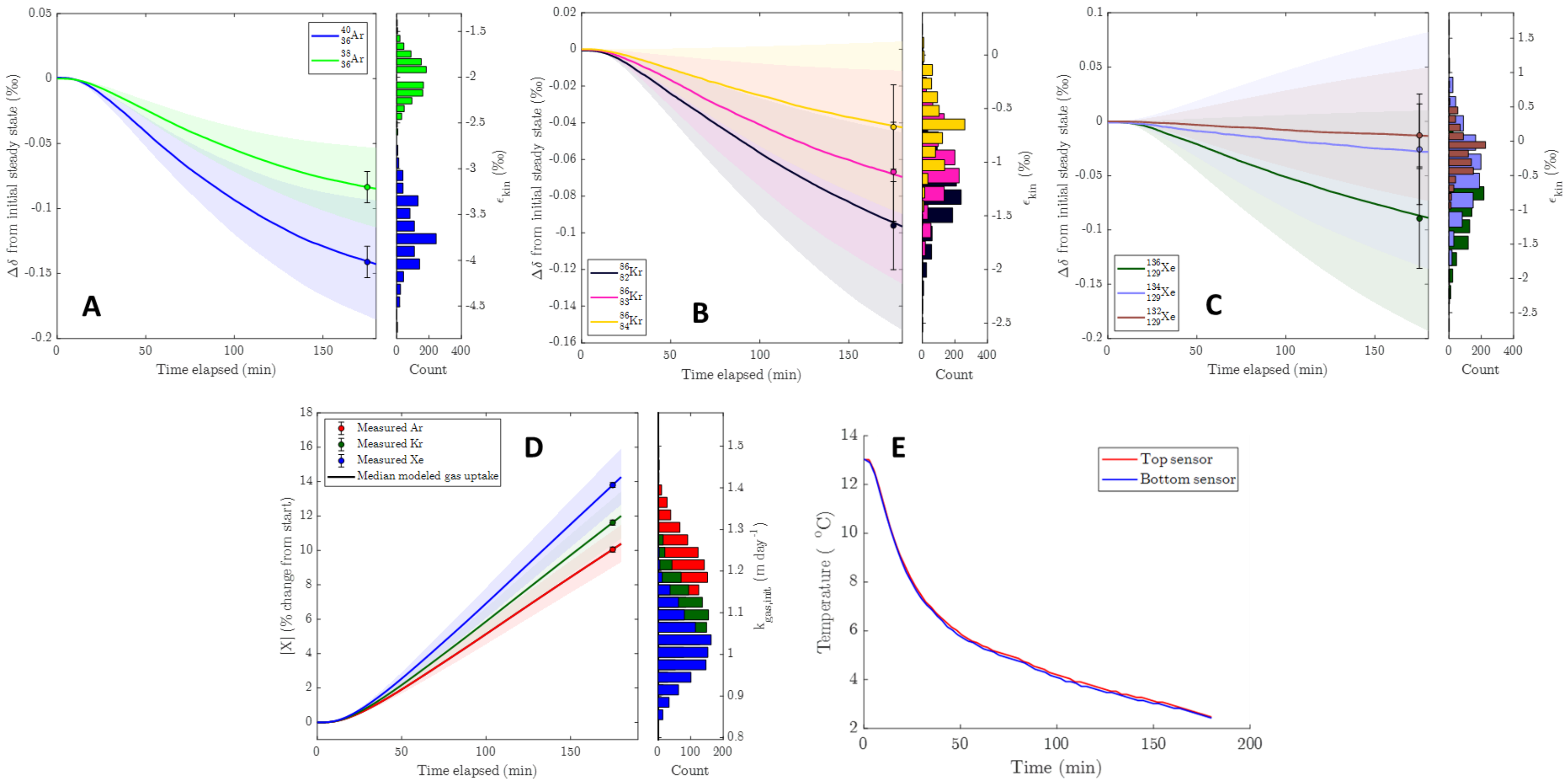

Figure 3.S10: Results from RCE3 for Ar isotopes (A), Kr isotopes (B), Xe isotopes (C), and bulk gases (D). Temperature log is shown in panel E.

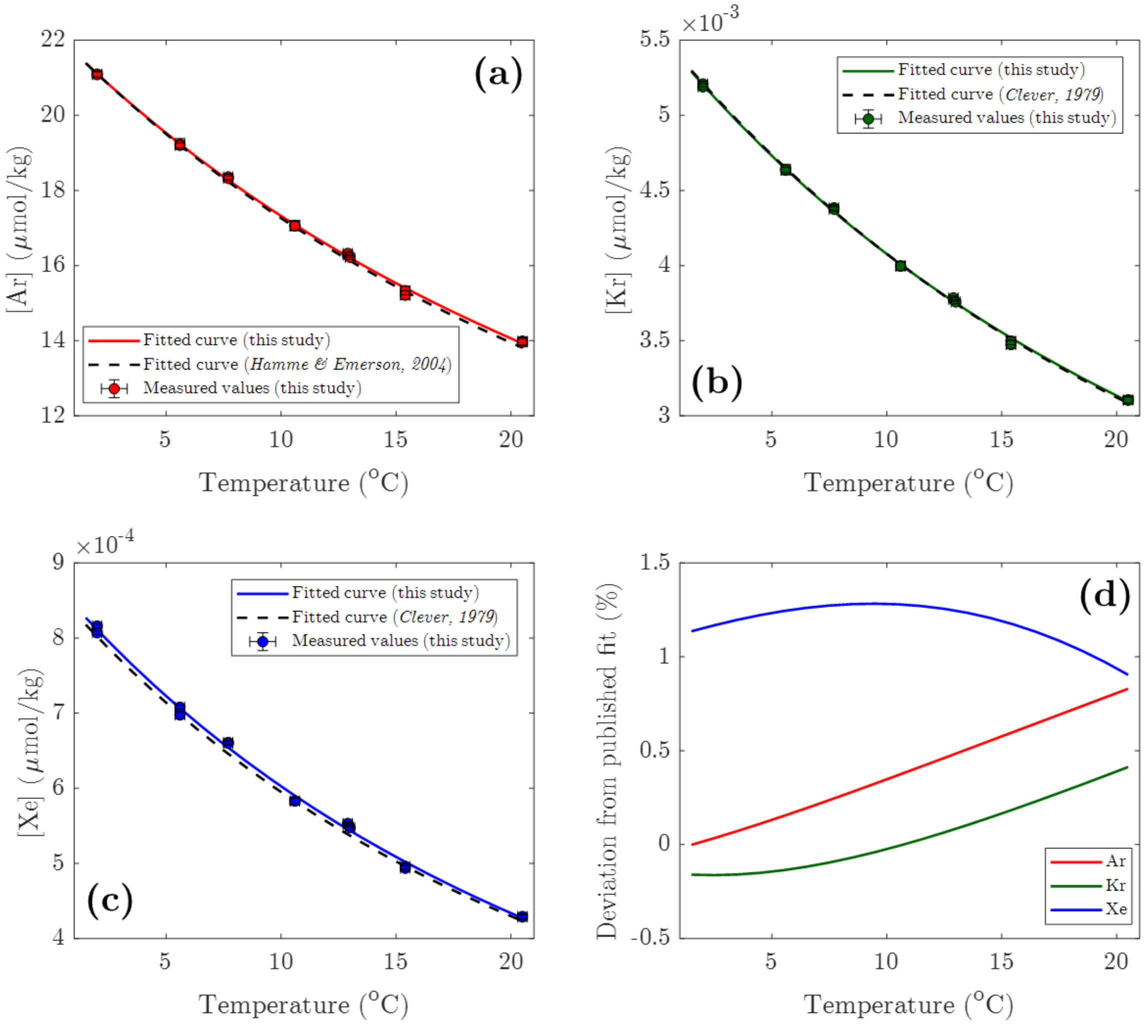

Figure 3.S11: OA experiment Ar concentrations (a), Kr concentrations (b), Xe concentrations (c), and offsets from literature values (d, Clever, 1979; Hamme and Emerson, 2004).

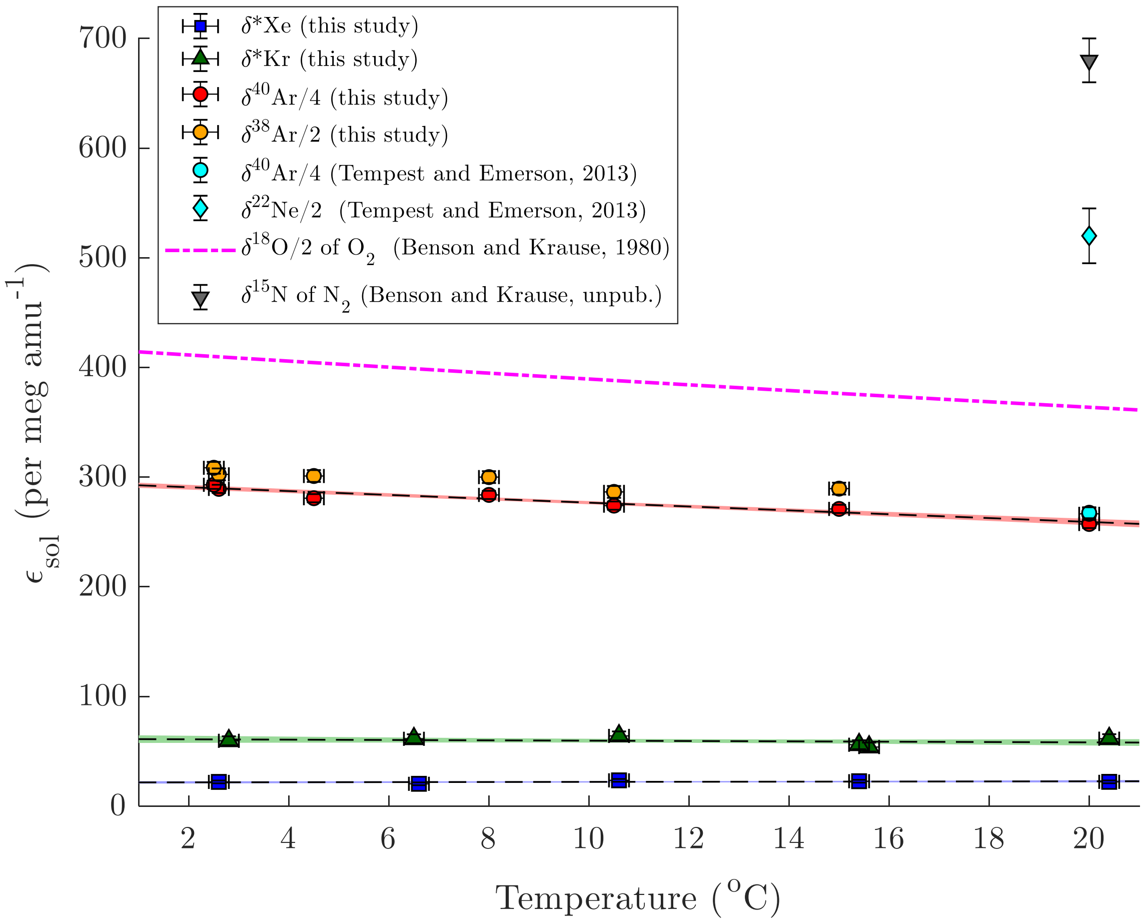

Figure 3.S12: Comparison of isotopic solubility εsol values determined in this study to those in the literature for isotope ratios of monatomic and diatomic gases. Note that He and H2 εsol values are omitted here because of their order-of-magnitude higher values (Benson and Krause, 1980; Muccitelli and Wen, 1978). The unpublished N2 εsol value shown here was first presented in Table 1 of Knox et al. (1992).

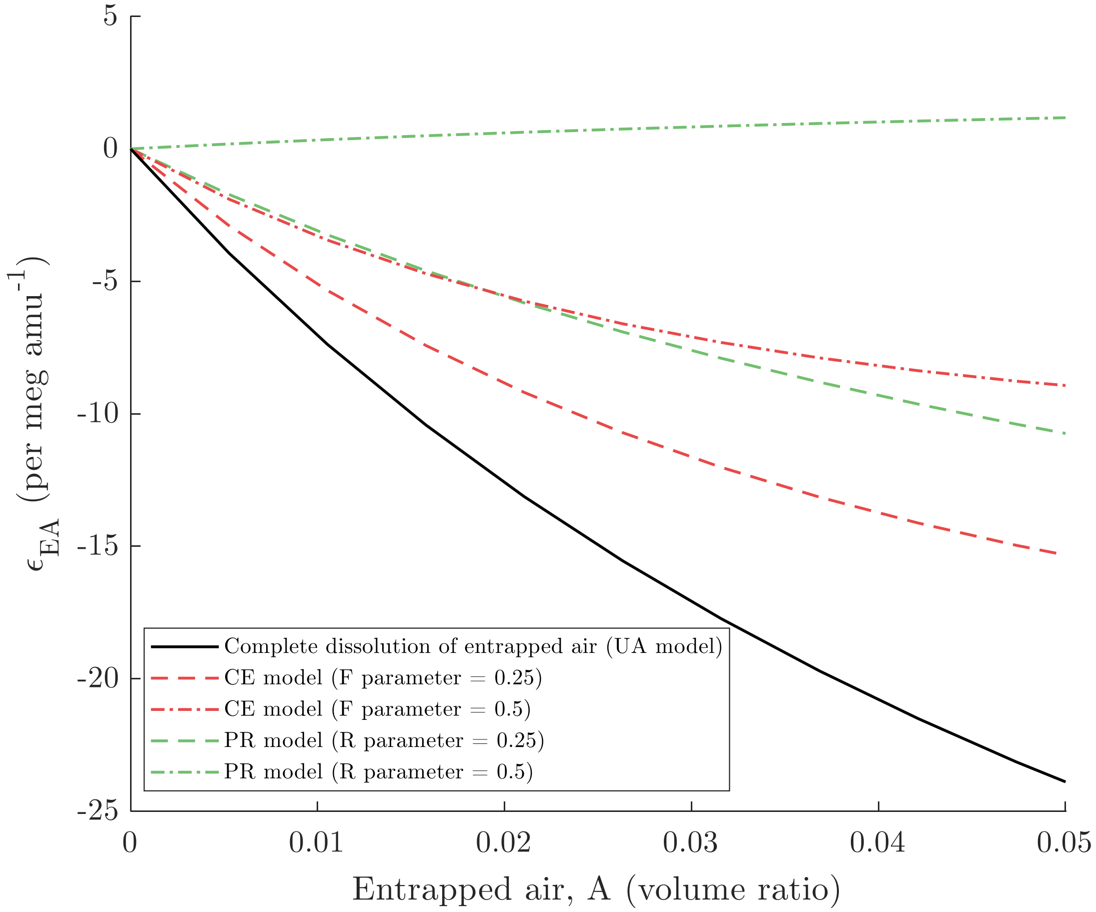

Figure 3.S13: Sensitivity of ε_{EA} to entrapped air amount for Kr isotopes in groundwater (i.e. δ^*Kr). Two common excess-air models (CE and PR models) and their shared limiting case of complete dissolution of entrapped air (i.e. the unfractionated excess air [UA] model: F=0, R=0) are considered. The F parameter in the CE model refers to the partiality of dissolution (the ratio of initial to final entrapped air to water volumetric ratios). The R parameter in the PR model refers to the degree of diffusive re-equilibration of supersaturated dissolved gases with the overlying unsaturated zone (such that higher R values indicate more complete re-equilibration).

Table 3.S1: Analytical parameters of isotopic analyses on MAT 253 mass spectrometer for measurement campaigns A and B

	Ar isotope analyses			***Kr isotope analyses***			***Xe isotope analyses***		
	# int. cycles	**voltage**	**resistance**	**# int. cycles**	**voltage**	**resistance**	**# int. cycles**	**voltage**	**resistance**
Campaign A	32	9 V (40Ar)	3E8 Ω	75	1.2 V (82Kr)	1E12 Ω	100	0.9 V (132Xe)	1E12 Ω
Campaign B	32	9 V (40Ar)	3E8 Ω	100	0.8 V (82Kr)	1E12 Ω	150	0.65 V (132Xe)	1E12 Ω

References

Aeschbach-Hertig, W., & Solomon, D. K. (2013). The Noble Gases as Geochemical Tracers. In P. Burnard (Ed.), *The Noble Gases as Geochemical Tracers* (pp. 81–122). Verlag: Springer. https://doi.org/10.1007/978-3-642-28836-4

Aeschbach-Hertig, W., Peeters, F., Beyerle, U., & Kipfer, R. (1999). Interpretation of dissolved atmospheric noble gases in natural waters. *Water Resources Research*, *35*(9), 2779–2792. https://doi.org/10.1029/1999WR900130

Aeschbach-Hertig, W., Peeters, F., Beyerle, U., & Kipfer, R. (2000). Palaeotemperature reconstruction from noble gases in ground water taking into account equilibration with entrapped air. *Nature*, *405*(6790), 1040–4. https://doi.org/10.1038/35016542

Benson, B. B., & Krause, D. (1980). Isotopic fractionation of helium during solution: A probe for the liquid state. *Journal of Solution Chemistry*, *9*(12), 895–909. https://doi.org/10.1007/BF00646402

Benson, B. B., & Krause, D. (1984). *The concentration and isotopic fractionation of oxygen dissolved in freshwater and seawater in equilibrium with the atmosphere' Determination of the Henry coeficient*. *Limnol. Oceanogr* (Vol. 29). Retrieved from https://aslopubs.onlinelibrary.wiley.com/doi/pdf/10.4319/lo.1984.29.3.0620

Beyerle, U., Aeschbach-Hertig, W., Imboden, D. M., Baur, H., Graf, T., & Kipfer, R. (2000). A mass, spectrometric system for the analysis of noble gases and tritium from water samples. *Environmental Science and Technology*, *34*(10), 2042–2050. https://doi.org/10.1021/es990840h

Bourg, I. C., & Sposito, G. (2008). Isotopic fractionation of noble gases by diffusion in liquid water: Molecular dynamics simulations and hydrologic applications. *Geochimica et Cosmochimica Acta*, *72*(9), 2237–2247. https://doi.org/10.1016/j.gca.2008.02.012

Clever, H. L. (Ed). (1979). *Krypton, Xenon, and Radon-Gas Solubilities* (1st ed.). Tarrytown, N.Y.: Pergamon.

Fuller, E. N., Schettler, P. D., & Giddings, J. C. (1966). A new method for prediction of binary gas-phase diffusion coefficients. *Industrial and Engineering Chemistry*, *16*(10), 551. https://doi.org/10.1016/0042-207X(66)90400-3

Grachev, A. M., & Severinghaus, J. P. (2003). Determining the thermal diffusion factor for 40Ar/36Ar in air to aid paleoreconstruction of abrupt climate change. *Journal of Physical Chemistry A*, *107*(23), 4636–4642. https://doi.org/10.1021/jp027817u

Grew, K. E., & Ibbs, T. L. (1953). Thermal diffusion in gases. *Quarterly Journal of the Royal Meteorological Society*, *79*(341), 458–458. https://doi.org/10.1002/qj.49707934127

Hamme, R. C., & Emerson, S. R. (2004a). Measurement of dissolved neon by isotope dilution using a quadrupole mass spectrometer. *Marine Chemistry*, *91*(1–4), 53–64. https://doi.org/10.1016/J.MARCHEM.2004.05.001

Hamme, R. C., & Emerson, S. R. (2004b). The solubility of neon, nitrogen and argon in distilled water and seawater. *Deep-Sea Research Part I: Oceanographic Research Papers*, *51*(11), 1517–1528. https://doi.org/10.1016/j.dsr.2004.06.009

Hamme, R. C., & Severinghaus, J. P. (2007). Trace gas disequilibria during deep-water formation. *Deep-Sea Research Part I: Oceanographic Research Papers*, *54*(6), 939–950. https://doi.org/10.1016/j.dsr.2007.03.008

Jähne, B., Huber, W., Dutzi, A., Wais, T., & Ilmberger, J. (1984). Wind/Wave-Tunnel Experiment on the Schmidt Number — and Wave Field Dependence of Air/Water Gas Exchange. In *Gas Transfer at Water Surfaces* (pp. 303–309). Dordrecht: Springer Netherlands. https://doi.org/10.1007/978-94-017-1660-4_28

Jähne, B., Heinz, G., & Dietrich, W. (1987). Measurement of the diffusion coefficients of sparingly soluble gases in water. *Journal of Geophysical Research*, *92*(C10), 10767. https://doi.org/10.1029/JC092iC10p10767

Jenkins, W. J., Beg, M. A., Clarke, W. B., Wangersky, P. J., & Craig, H. (1972). Excess3He in the Atlantic Ocean. *Earth and Planetary Science Letters*, *16*(1), 122–126. https://doi.org/10.1016/0012-821X(72)90245-2

Kawamura, K., Severinghaus, J. P., Albert, M. R., Courville, Z. R., Fahnestock, M. A., Scambos, T., et al. (2013). Kinetic fractionation of gases by deep air convection in polar firn. *Atmospheric Chemistry and Physics*, *13*(21), 11141–11155. https://doi.org/10.5194/acp-13-11141-2013

Klots, C. E., & Benson, B. B. (1963). Isotope Effect in the Solution of Oxygen and Nitrogen in Distilled Water. *The Journal of Chemical Physics*, *38*(4), 890–892. https://doi.org/10.1063/1.1733778

Knox, M., Quay, P. D., & Wilbur, D. (1992). Kinetic isotopic fractionation during air-water gas transfer of O_2, N_2, CH_4, and H_2. *Journal of Geophysical Research*, *97*(C12), 20335. https://doi.org/10.1029/92JC00949

Ledwell, J. J. (1984). The Variation of the Gas Transfer Coefficient with Molecular Diffusity. In *Gas Transfer at Water Surfaces* (pp. 293–302). Dordrecht: Springer Netherlands. https://doi.org/10.1007/978-94-017-1660-4_27

Lippmann, J., Stute, M., Torgersen, T., Moser, D. P., Hall, J. A., Lin, L., et al. (2003). Dating ultra-deep mine waters with noble gases and 36Cl, Witwatersrand Basin, South Africa. *Geochimica et Cosmochimica Acta*, *67*(23), 4597–4619. https://doi.org/10.1016/S0016-7037(03)00414-9

Loose, B., Jenkins, W. J., Moriarty, R., Brown, P., Jullion, L., Naveira Garabato, A. C., et al. (2016). Estimating the recharge properties of the deep ocean using noble gases and helium isotopes. *Journal of Geophysical Research: Oceans*, *121*(8), 5959–5979. https://doi.org/10.1002/2016JC011809

Mazor, E. (1972). Paleotemperatures and other hydrological parameters deduced from noble gases dissolved in groundwaters; Jordan Rift Valley, Israel. *Geochimica et Cosmochimica Acta*, *36*(12), 1321–1336. https://doi.org/10.1016/0016-7037(72)90065-8

Muccitelli, J., & Wen, W.-Y. (1978). Solubilities of hydrogen and deuterium gases in water and their isotope fractionation factor. *Journal of Solution Chemistry*, *7*(4), 257–267. https://doi.org/10.1007/BF00644273

Nicholson, D., Emerson, S., Caillon, N., Jouzel, J., & Hamme, R. C. (2010). Constraining ventilation during deepwater formation using deep ocean measurements of the dissolved gas ratios 40 Ar/ 36 Ar, N 2 /Ar, and Kr/Ar. *Journal of Geophysical Research*, *115*(C11), C11015. https://doi.org/10.1029/2010jc006152

Orsi, A. (2013). Temperature reconstruction at the West Antarctic Ice Sheet Divide, for the last millennium, from the combination of borehole temperature and inert gas isotope. Retrieved from https://escholarship.org/uc/item/02g3c5fq

Reid, R. C., Prausnitz, J. M., & Sherwood, T. K. (1977). *The properties of gases and liquids, Third Edition,McGraw-Hill*. *McGraw-Hill (1977)*. https://doi.org/10.1002/aic.690240634

Seltzer, A. M., Severinghaus, J. P., Andraski, B. J., & Stonestrom, D. A. (2017). Steady state fractionation of heavy noble gas isotopes in a deep unsaturated zone. *Water Resources Research*, *53*(4), 2716–2732. https://doi.org/10.1002/2016WR019655

Severinghaus, J. P., Bender, M. L., Keeling, R. F., & Broecker, W. S. (1996). Fractionation of soil gases by diffusion of water vapor, gravitational settling, and thermal diffusion. *Geochimica et Cosmochimica Acta*, *60*(6), 1005–1018. https://doi.org/10.1016/0016-7037(96)00011-7

Severinghaus, J. P., Grachev, A., Luz, B., & Caillon, N. (2003). A method for precise measurement of argon 40/36 and krypton/argon ratios in trapped air in polar ice with applications to past firn thickness and abrupt climate change in Greenland and at Siple Dome, Antarctica. *Geochimica et Cosmochimica Acta*, *67*(3), 325–343. https://doi.org/10.1016/S0016-7037(02)00965-1

Stanley, R. H., Baschek, B., Lott III, D. E., Jenkins, W. J., Baschek, B., Lott III, D. E., & Jenkins, W. J. (2009). A new automated method for measuring noble gases and their isotopic ratios in water samples. *Geochem. Geophys. Geosyst*, *10*, 5008. https://doi.org/10.1029/2009GC002429

Stanley, R. H. R., & Jenkins, W. (2013). Noble Gases in Seawater as Tracers for Physical and Biogeochemical Ocean Processes. In *The Noble Gases as Geochemical Tracers* (pp. 55–79). https://doi.org/10.1007/978-3-642-28836-4_4

Stute, M., Forster, M., Frischkorn, H., Serejo, A., Clark, J. F., Schlosser, P., et al. (1995). Cooling of Tropical Brazil (5C) During the Last Glacial Maximum. *Science*, *269*(5222), 379–383. https://doi.org/10.1126/science.269.5222.379

Tempest, K. E., & Emerson, S. (2013). Kinetic isotopic fractionation of argon and neon during air-water gas transfer. *Marine Chemistry*, *153*, 39–47. https://doi.org/10.1016/j.marchem.2013.04.002

Torgersen, T., & Clarke, W. B. (1985). Helium accumulation in groundwater, I: An evaluation of sources and the continental flux of crustal 4He in the Great Artesian Basin, Australia. *Geochimica et Cosmochimica Acta*, *49*(5), 1211–1218. https://doi.org/10.1016/0016-7037(85)90011-0

Tyroller, L., Brennwald, M. S., Mächler, L., Livingstone, D. M., & Kipfer, R. (2014). Fractionation of Ne and Ar isotopes by molecular diffusion in water. *Geochimica et Cosmochimica Acta*, *136*(0), 60–66. https://doi.org/http://dx.doi.org/10.1016/j.gca.2014.03.040

Tyroller, L., Brennwald, M. S., Busemann, H., Maden, C., Baur, H., & Kipfer, R. (2018). Negligible fractionation of Kr and Xe isotopes by molecular diffusion in water. *Earth and Planetary Science Letters*, *492*, 73–78. https://doi.org/10.1016/J.EPSL.2018.03.047

Wen, T., Castro, M. C., Nicot, J.-P., Hall, C. M., Larson, T., Mickler, P., & Darvari, R. (2016). Methane Sources and Migration Mechanisms in Shallow Groundwaters in Parker and Hood Counties, Texas—A Heavy Noble Gas Analysis. *Environmental Science & Technology*, *50*(21), 12012–12021. https://doi.org/10.1021/acs.est.6b01494

Chapter 4

Dissolved Kr and Xe Isotopes in Groundwater Preserve Gravitational Signals of Past Water-Table Depth

Abstract

Future changes in rainfall are potentially destabilizing to societies, thus estimations of past hydrologic conditions are essential for understanding trends and improving models that predict these changes. Here we demonstrate that past water-table depth, a proxy for hydroclimate, can be quantitatively reconstructed from dissolved Kr and Xe isotopes in groundwater. By making the first-ever high precision ($\leq$0.005 ‰ amu^{-1}) measurements of these dissolved isotope ratios, we find that depth-proportional signals of gravitational settling in soil air at the time of recharge are recorded in groundwater. Analyses of groundwater samples from California enable successful reconstruction of known modern groundwater levels and reveal a distinct 17.9 ± 1.6 m decline in water-table depth in a southern California aquifer system during the last glacial termination. This finding indicates a substantial hydroclimatic shift from the wetter glacial period to a more arid Holocene that is accompanied by 6.5 ± 0.6 ºC of surface warming. Water-table depth reconstruction improves upon and complements the existing paleo-temperature application of noble gases and may identify regions more prone to future drought or extreme wet conditions.

4.1. Main text

Noble gases dissolved in groundwater have a wide range of physical applications for climatology and hydrogeology, owing to their chemical and biological inertness. For example, past mean-annual surface temperatures derived from noble gases in paleo-groundwater comprise some of the most reliable terrestrial temperature reconstructions of the last glacial period (Aeschbach-Hertig et al., 2000; Stute et al., 1995). Physical models of groundwater recharge, transport, contamination, and age also are frequently constrained by noble gas measurements (Barry et al., 2018; Manning & Solomon, 2003; Schlosser et al., 1988). Although dissolved noble gas concentrations and helium isotopes are routinely measured, groundwater Kr and Xe stable isotope studies are rare because fractionation signals are generally smaller than typical order 1-10 ‰ amu^{-1} analytical uncertainties.

Here we apply a newly developed technique (Seltzer et al., 2019) to make the first-ever measurements of stable Kr and Xe isotope ratios in groundwater at high precision (≤5 per meg amu-1; where 1 per meg = 0.001‰ = 0.0001%). Measurement of Kr and Xe isotope ratios, along with Ar isotopes and Ar, Kr, and Xe concentrations, in 58 groundwater samples from 36 wells allowed us to test a simple fractionation model constrained by recent experimental determinations of noble gas isotopic solubility and diffusivity ratios (Seltzer et al., 2019). Our findings suggest that Kr and Xe isotope ratios in groundwater record the depth to water at the time of recharge. We present an inverse model to reconstruct past water-table depth (WTD) based on noble gas measurements, demonstrate its accuracy in reproducing observed water levels in modern groundwater, and apply it to a suite of paleo-groundwater samples from San Diego, California, which reveal a ~20-m decline in WTD during the last deglaciation indicative of a hydroclimatic shift from the wetter glacial period to more arid Holocene.

A theoretical model for gas-phase isotopic fractionation in porous media, validated by soil air observations, suggests that dissolved Kr and Xe stable isotope ratios in unsaturated-zone (UZ) air are primarily fractionated from the well-mixed atmosphere by gravitational settling (Seltzer et al., 2017; Severinghaus et al., 1996). Gravitational settling is a well understood process by which molecular diffusion in stagnant air in hydrostatic balance leads to a nearly linear increase in heavy-to-light gas ratios with depth (Schwander, 1989). Past measurements of inert gases in polar firn (Craig et al., 1988; Sowers et al., 1992) and UZ air (Seltzer et al., 2017; Severinghaus et al., 1996) have been found to be in close agreement with the theoretical gravitational settling slope (e.g. ~4.0 per meg amu^{-1} m^{-1} at ~20 ºC).

Thermal diffusion (Grew & Ibbs, 1953) and steady-state UZ-to-atmosphere water-vapor fluxes (Severinghaus et al., 1996) both weakly oppose the influence of gravitational settling on UZ air isotopic composition (Figure 4.1). In the presence of a temperature gradient, thermal diffusion acts to concentrate heavy gases towards the cooler end of a column of gas. Thermal diffusion decreases heavy-to-light isotope ratios in deep UZ air, which is warmed by geothermal heat from below, relative to the atmosphere. Isotope ratios of the lighter noble gases (He, Ne, and Ar) are more strongly affected by thermal diffusion than Kr and Xe isotope ratios, per mass unit difference (Kawamura et al., 2013; Severinghaus et al., 2003). At steady-state, the flux of water vapor from the moist UZ to drier overlying surface air leads to a kinetic isotopic fractionation that also affects the lighter noble gases more than Kr and Xe (Seltzer et al., 2017; Severinghaus et al., 1996). This fractionation is induced by vertical partial pressure gradients of dry air constituents between the atmosphere and UZ, which drive steady-state molecular diffusion of atmospheric noble gases into the UZ against an upwards flux of water vapor (Severinghaus et al., 1996).

Air at the bottom of the UZ dissolves into groundwater at the water table, thereby transferring the signal of UZ air fractionation to dissolved isotope ratios in groundwater, as depicted in an idealized model of an unconfined aquifer system (Figure 4.1). Small isotopic solubility differences, constrained by recent determinations (Seltzer et al., 2019), lead to slight further enrichment of heavy-to-light isotope ratios. Over time, as the uppermost groundwater is gradually displaced downward by subsequent recharge, it is sequestered from UZ air and retains its isotopic composition.

In this conceptual model, a dissolved isotope ratio (δ_{diss}) is fractionated from initial atmospheric composition (δ_{atm}, where $\delta_{atm} = 0$ by definition) by steady-state diffusive processes in UZ air (ε_{UZ}), isotopic solubility fractionation (ε_{sol}), and the injection of excess UZ air by dissolution of entrapped bubbles (εEA):

$$\delta = \varepsilon_{UZ} + \varepsilon_{sol} + \varepsilon_{EA} \tag{4.1}$$

Solubility fractionation arises from the slightly different solubilities of heavy and light Kr and Xe isotopes in water (Seltzer et al., 2019). The isotopic influence of excess air opposes that of solubility fractionation by an amount that depends on the quantity of initially entrapped air and the completeness of its dissolution under the assumption of a closed water-bubble system at solubility equilibrium (Aeschbach-Hertig et al., 2000). A recent study of solubility and kinetic fractionation of Kr and Xe isotopes in fresh water demonstrated that ε_{EA} is negligible (order 1 per meg amu^{-1}) and ε_{sol} is largely insensitive to temperature (Seltzer et al., 2019). In principle, therefore, differences between dissolved Kr and Xe isotope ratios in groundwater and atmospheric air should primarily arise from only two processes: gravitational settling, which is the primary control on ε_{UZ}, and solubility fractionation (Figure 4.1).

To test this expectation, we compare the mass difference-normalized, error-weighted means of Kr and Xe heavy-to-light isotope ratios (δ*Kr and δ*Xe, respectively) in 58 groundwater samples collected from three regions in California: Fresno, the Mojave Desert, and San Diego (Figure 4.2). Because gravitational settling depends only on isotopic mass difference, it leads to an identical increase in these mass difference-normalized isotope ratios with depth (i.e. δ*Kr and δ*Xe will covary with a slope of 1 if fractionated only by gravitational settling).

Indeed, we find that δ*Kr and δ*Xe in all samples are greater than or equal to εsol, and a linear regression through all measurements has a slope of 1.16 ± 0.02 ($R^2 = 0.98$). The 40 Fresno and San Diego samples fall along a linear trendline with a slope of 1.03 ± 0.04 that originates at the solubility equilibrium value. As described above, other non-gravitational isotopic fractionation processes in UZ air and groundwater generally exhibit different δ*Kr vs. δ*Xe slopes from gravitational settling and are both opposite in sign and smaller in magnitude. For context, gravitational settling fractionation in UZ air above water tables at least two meters below the surface exceeds the expected individual magnitudes of Kr and Xe isotopic fractionation associated with (a) thermal diffusion driven by a 2 ºC water-table-to-surface temperature difference; (b) a steady-state water-vapor flux from the moist UZ into 20 ºC, 65% relative humidity surface air; and (c) complete dissolution of entrapped air bubbles yielding excess air equivalent to 50% Ne supersaturation (ΔNe; Figure 4.2).

Mojave Desert groundwater samples exhibit slight departures from the expected concordant Kr and Xe relationship that are most apparent in samples collected from regions of deep present-day water table depths (>50 m). We suspect that an additional physical process systematically affects these deep samples. Two candidate mechanisms are disequilibrium kinetic fractionation (Kawamura et al., 2013) driven by barometric pumping or oxygen consumption

(Freundt et al., 2013; Hall et al., 2012) without equimolar replacement by CO_2 in deep UZ air (Supplementary Section 4.5). In Figure 4.2, we demonstrate that a simple model for the latter process, in which the combined mole fractions of O_2 and CO_2 are 5% lower in the deep UZ than overlying atmospheric air may explain the discordant Mojave Desert data. The 5% hypothesized depletion falls within the observed range of O_2 consumption in past UZ air studies (Freundt et al., 2013; Hall et al., 2012).

The close agreement of groundwater δ*Kr and δ*Xe with the expected gravitational slope is encouraging for quantitative reconstruction of past WTD based on isotopic measurements. To explore this possible application, we developed an inverse model that estimates past WTD, recharge temperature, and excess air parameters (Aeschbach-Hertig et al., 2000) constrained by measured noble gas isotope ratios and elemental concentrations. With knowledge of both recharge temperature and WTD, it is now possible to quantify and remove the contributions of UZ fractionation and geothermal heat to reconstructions of past surface temperature, thereby resolving two longstanding concerns about noble gas paleo-thermometry (Stute & Schlosser, 1993). Our inverse model approach merges existing models for equilibrium dissolution and excess air (Aeschbach-Hertig et al., 2000) and UZ air fractionation (Seltzer et al., 2017) in an iterative loop that converges on best estimates of WTD and temperature (Supplementary Figure 4.S2). Analytical measurement uncertainties are propagated to estimate probability distributions of WTD and temperature via Monte Carlo simulations.

We first tested this inverse model with five samples collected from two Fresno wells of relatively young recharge age, ~650 and ~35 years, which were constrained by multiple independent dating tools. Using measured Ar, Kr, and Xe isotope ratios and elemental concentrations, we reconstructed WTDs for comparison with nearby historical water-level observations. The younger samples, which have a mean recharge year of 1983 CE (± 5 years), agree closely with the mean of nearby water-level observations in the early 1980s (Figure 4.3). The older samples fall within the range of decadal variability prior to 1950, before major development of the Fresno region, and likely reflect mean mid-to-late Holocene region WTD, resulting from the temporal smoothing of isotopic composition by dispersive mixing (Supplementary Section 4.3).

To investigate the potential for WTD reconstruction as a novel tool for paleoclimate, we collected and analyzed samples from 23 San Diego monitoring wells, 18 of which contain groundwater from a confined regional aquifer system with ^{14}C-dated recharge ages between 5 ka and 40 ka (Supplementary Section 4.4). Our Kr and Xe isotope-based reconstructions reveal considerably shallower WTDs throughout the latter portion of last glacial period (LLGP; defined here as 15-40 ka) before dropping an average of 17.9 ± 1.6 meters during the last glacial-interglacial transition (Figure 4.4). Our finding of a shallower mean WTD during the LLGP is consistent with previous paleoclimate proxy reconstructions and model simulations (Bromwich et al., 2004; COHMAP members, 1988; Kulongoski et al., 2009; Lora et al., 2016; Oster et al., 2015), which have suggested that glacial-period wintertime storm tracks were displaced southward due to interaction of the mean atmospheric circulation over western North America with the Laurentide Ice Sheet (LIS), delivering enhanced rainfall to the southwestern United States. A decline in WTD during the last glacial termination is indicative of shift towards drier conditions, possibly linked to a northward migration of the wintertime storm tracks in response to the receding LIS. Although smoothing of abrupt climate signals in groundwater by dispersive mixing (Stute & Schlosser, 1993) precludes placing tight constraints on the timing of the deglacial WTD shift, the apparent timing of roughly 15 ka is temporally consistent with the rapid lowering of the LIS (Peltier et al., 2015). Simulation of mean WTD over an assumed recharge area by a high-resolution groundwater model (Fan et al., 2013) indicates a present-day regional-mean WTD of 47 m, which is substantially below the 21 m LLGP-mean WTD.

For the first time, we are able to reconstruct surface temperature by accounting for both geothermal heat and UZ air fractionation in the San Diego regional aquifer samples. We find that the mean temperature during the LLGP was 13.7 ± 0.3 ºC before warming to 20.2 ± 0.5 ºC in the Holocene, which closely matches modern regional surface temperatures (Supplementary Figure 4.S8). Two San Diego multiple-depth well sites exhibit high apparent LLGP recharge temperatures, which may have a geothermal origin or may indicate adsorption (Supplementary Figure 4.S9) and thus are excluded from our surface temperature analysis. We demonstrate that any effect on Kr and Xe isotopes in these two samples, and therefore on WTD estimation, is negligible (Supplementary Section 4.4, Figure 4.S10).

Two wells with outlier reconstructed WTDs have apparent 14C-based recharge ages of approximately 24 ka and 12 ka, which may be temporally consistent with other studies that have proposed evidence for a local "glacial megadrought" and wet Younger Dryas stadial, respectively. Measurements of various physical, geochemical, and biological proxies from Lake Elsinore, roughly 100 km north of our San Diego study area, independently suggest extreme aridity persisting from around 27.5 to 25.5 ka (Feakins et al., 2019; Heusser et al., 2015; Kirby et al., 2018), which is within the dating uncertainty of the approximately 24 ka groundwater sample. A record of groundwater-discharge deposits from southeastern Arizona suggests the persistence of a shallow, near-surface regional water table from around 50 ka to 15 ka, after which the water-table lowered, except for a brief rebound to wet conditions during the Younger Dryas stadial around 12.5 ka (Pigati et al., 2009). Although reconstructed WTDs from these San Diego wells in principle support the notions of regional dry and wet periods around 24 ka and 12 ka, respectively, we cannot be certain that these reconstructed WTDs represent climatic signals rather than anomalous hydrogeological conditions. Similarly, the preservation of climatic signals from these several thousand year periods would require minimal dispersive mixing along the flow path, which we cannot conclude based on our limited knowledge of the groundwater flow system.

Based on the observed concordance with gravitational settling fractionation, we suggest that Kr and Xe isotopic measurements in groundwater represent a promising new tool for hydrogeology and paleoclimatology. By analyzing dissolved Kr and Xe isotope ratios at high precision for the first time, we have (a) confirmed the dominant role of UZ gravitational settling in setting dissolved Kr and Xe isotope ratios in groundwater, (b) found close agreement between observed and reconstructed WTDs in Fresno samples of recent recharge, and (c) quantified a pronounced decrease in San Diego regional WTD during the last deglaciation. While future experiments may shed light on small departures from gravitational expectation as seen in the Mojave Desert samples, our findings offer strong support for the notion that heavy noble gas isotopes in groundwater are quantitative recorders of WTD at the time of recharge. Knowledge of past WTD not only provides an important correction to groundwater noble gas paleo-temperature reconstruction, but also adds complementary hydroclimate information. Future applications to constrain regional-scale groundwater flow models may enable quantitative reconstruction of past precipitation-minus-evaporation rates and improve our understanding of groundwater hydrogeology in aquifer systems presently supporting large populations.

4.S1. Field and Laboratory Methods

In this study, a total of 58 groundwater samples from 36 wells were collected in evacuated two-liter flasks and analyzed in the Scripps Institution of Oceanography (SIO) Noble Gas Isotope Laboratory. The borosilicate glass flasks used in this study were made to include two necks leading to 9-mm diameter Louwers-Hapert valves with double o-ring inner and outer seals. Sampling flasks were prepared, stored, and filled following procedures described in Seltzer et al. (2019), which are based on seawater dissolved gas sampling techniques (Hamme & Emerson, 2004). Before and after sample collection, the necks and cavities between the inner two o-rings were flushed with nitrogen gas before the cavities were sealed and necks closed off with rubber caps. All samples were collected within five days of evacuation and analyzed within two weeks of collection. A comparison of replicate sample differences in $\delta^{40}/_{36}$Ar across one year of distilled water, groundwater, and seawater sample analyses, including those in this study, revealed no sensitivity to storage time either before or after sampling, confirming that any fractionation due to permeation of noble gases across the double o-ring seals and through the N_2 filled necks and cavities was below analytical detection (Seltzer et al., 2019).

In the field, three well casing volumes were purged from each well prior to sampling. Flasks were first prepared for sampling by attaching 1.25-cm inner-diameter Tygon tubing to the outer neck of the flask and flushing the tubing up to the inner o-ring seal with N_2 gas flowing through 0.3-cm Nylon tubing inserted into the Tygon tubing. With the N_2 gas flowing, 0.6-cm outer diameter Nylon tubing was connected to the groundwater pump and inserted into the Tygon tubing up to the inner o-ring seal. The 0.3-cm diameter tubing was then removed and the Tygon tubing was flushed with the groundwater, with care taken to dislodge any bubbles. At this point, sampling began by cracking open the Louwers-Hapert valve to allow groundwater to enter the evacuating flask while maintaining a buffer volume of groundwater in the neck and Tygon tubing to prevent any incorporation of atmospheric air. Once the flask was ~95% full, the Louwers-Hapert valve was closed and the cavity between the o-rings as well as the neck volume were filled again with N_2 gas and capped.

At SIO, samples were weighed both before and after sampling for the purpose of determining bulk dissolved gas concentrations via manometry. Dissolved gases were quantitatively extracted from each sample by sparging with gaseous helium and cryogenically trapping liberated gases in a diptube immersed in a 4-K liquid helium dewar(Seltzer et al., 2019). After a sample was initially connected via 0.5” ultra-torr fittings to the extraction line, the space between the o-ring seal and vacuum line connection was evacuated to <0.1 mTorr and leak checked. Next, the sample was poured into a 6-L extraction vessel, which was initially under vacuum, and all remaining gases in the two-liter flask were cryogenically trapped over a 15-minute period. At this point, the now-evacuated two-liter flask was closed off to the extraction line and 1 atm of ultra-high-purity helium gas was added to the entire line, connected to a flow-through diptube (in liquid helium) and recirculating Metal Bellows MB-41 pump. Over a 90-minute extraction period, the helium gas was recirculated at a 1 L min^{-1} flow rate and the diptube was progressively lowered into the dewar to prevent saturation of available surface area for gas trapping. After this period, helium gas was pumped away and the diptube was closed off and removed from the liquid helium dewar. Repeated testing of this extraction technique demonstrated that 99.7 ± 0.1% of dissolved gases were extracted (Seltzer et al., 2019). For each sample, extracted gases were gettered both by SAES Zr/Al sheets and Ti sponge for 130 minutes at 900 ºC to remove all reactive gases. The remaining (noble) gases were then cryogenically transferred into another diptube immersed in liquid helium.

After allowing at least three hours at room temperature for homogenization, the gases in the diptube were expanded into a calibrated volume attached to the inlet of a MAT 253 isotope-ratio mass spectrometer and total pressure was measured using a 100-Torr Baratron capacitance manometer. With knowledge of the sample weight, total (noble) gas pressure, volume, and measurement temperature, dissolved Ar concentrations were calculated by making a slight correction for the presence of Ne (~0.1% of total noble gas pressure) and gas non-ideality using the first Virial coefficient. The sample was then introduced to the bellows of the mass spectrometer and given 10 minutes for homogenization before analysis. Over a ~9-hour analysis period, isotope ratios of Ar, Kr, and then Xe were measured in sequence with multi-collector Faraday cups, followed by elemental ratios (Kr/Ar and Xe/Ar) via peak jumping. Dissolved isotope and elemental ratios were measured dynamically against a working standard gas (Severinghaus et al., 2003). Atmospheric air samples were collected and analyzed against this same working standard to normalize all measured isotope and elemental ratios to the well mixed atmosphere.

In this study, we report all measured isotope ratios as delta values with respect to atmospheric air, such that:

$$\delta = \frac{\left(\frac{h}{l}\right)_{smp}}{\left(\frac{h}{l}\right)_{atm}} - 1 \tag{4.S1}$$

where δ is given in ‰ or per meg and *h* and *l* are heavy and light isotopes in a sample ("smp") or atmospheric air ("atm"). Throughout the study, samples were analyzed in two measurement campaigns, separated by the replacement of the ion source filament in June 2018. For each campaign ("A" and "B"), we estimate ratio-specific measurement precision from the pooled standard deviations of replicate samples for each of eight total isotope ratios measured in each sample. Table S1 lists the heavy and light isotopes measured for each of these ratios as well as the campaign A and B pooled standard deviations (σ_{pld}), the standard error of atmospheric air measurements against the working standard gas (SE_{atm}), the standard error of standard aliquot tests (SE_{ext}), which were carried out to correct for any fractionation induced by extraction and/or purification as described in detail in Seltzer et al. (2019), and the absolute error associated with chemical slope corrections (SE_{CS}), which we assume is equal to 10% of the average correction magnitude. The chemical slope correction is a routine correction (Petrenko et al., 2006), which we make to Kr and Xe isotope ratios due to sample and standard differences in Ar/Kr and Ar/Xe ratios and was determined empirically through tests carried out nine times between August 2017 and September 2018, in which pure Ar was added to aliquots of standard gas in different proportions to test for apparent isotopic sensitivity to Ar/Kr and Ar/Xe ratios.

Formally, the standard error of a given delta value measured in *N* replicate samples is given by the quadrature sum of measurement precision (divided by $\sqrt{N}$) and standard errors of atmospheric air measurements and corrections for extraction/purification and chemical slope:

$$SE_{tot} = \sqrt{\frac{\sigma_{pld}^2}{N} + SE_{atm}^2 + SE_{ext}^2 + SE_{CS}^2} \qquad (4.S2)$$

Bulk Kr and Xe concentrations were determined by first normalizing measured δKr/Ar and δXe/Ar ratios to atmospheric ratios (COESA, 1976) to determine absolute Xe/Ar and Kr/Ar in samples and then multiplying Xe/Ar and Kr/Ar by the measured dissolved Ar concentration. Kr/Ar and Xe/Ar were assumed equal to the measured ratios of ^{84}Kr/^{40}Ar and ^{132}Xe/^{40}Ar, respectively. In campaigns A and B, dissolved Ar, Kr, and Xe concentration pooled standard deviations were ±~0.7% and ~0.4%, respectively.

We make use of the linear mass dependence of soil air fractionation processes (Seltzer et al., 2017) and solubility fractionation (Seltzer et al., 2019) for Kr and Xe isotopes to define the mass difference-normalized, error-weighted mean parameters δ*Kr and δ*Xe in units of per meg amu^{-1}:

$$\delta^{*}\mathrm{Kr} = \frac{\frac{\delta^{86}_{82}Kr}{4}\left(\frac{4}{SE_{tot,\frac{86}{82}}}\right)^{2} + \frac{\delta^{86}_{83}Kr}{3}\left(\frac{3}{SE_{tot,\frac{86}{83}}}\right)^{2} + \frac{\delta^{86}_{84}Kr}{2}\left(\frac{2}{SE_{tot,\frac{86}{84}}}\right)^{2}}{\left(\frac{4}{SE_{tot,\frac{86}{82}}}\right)^{2} + \left(\frac{3}{SE_{tot,\frac{86}{83}}}\right)^{2} + \left(\frac{2}{SE_{tot,\frac{86}{84}}}\right)^{2}} \qquad (4.S4)$$

and

$$\delta^{*}\mathrm{Xe} = \frac{\frac{\delta^{132}_{129}Xe}{3}\left(\frac{3}{SE_{tot,\frac{132}{129}}}\right)^{2} + \frac{\delta^{134}_{129}Xe}{5}\left(\frac{5}{SE_{tot,\frac{134}{129}}}\right)^{2} + \frac{\delta^{136}_{129}Xe}{7}\left(\frac{7}{SE_{tot,\frac{136}{129}}}\right)^{2}}{\left(\frac{3}{SE_{tot,\frac{132}{129}}}\right)^{2} + \left(\frac{5}{SE_{tot,\frac{134}{129}}}\right)^{2} + \left(\frac{7}{SE_{tot,\frac{136}{129}}}\right)^{2}} \qquad (4.S5)$$

For a single replicate sample, the campaign A and B total uncertainties (for $N=1$, $SE_{tot} = \sigma_{\mathrm{tot}}$) were 3.6 and 5.2 per meg amu^{-1} for δ*Xe and 3.5 and 5.0 per meg amu^{-1} for δ*Kr, respectively.

The assumption of linear mass dependence can be tested by comparing measured ratios to isotopic mass difference (Figure 4.S1), for processes such as soil air fractionation (gravitational settling, thermal diffusion, and water-vapor flux fractionation) and solubility fractionation. In Figure 4.S1, we plot fractionation (ε) vs isotopic mass difference (Δm) for the steady-state soil air fractionation model (shown for δ*Xe in Figure 4.1) for individual Kr and Xe isotope ratios. Modeled UZ air values (at 50 m) are shown in Figure 4.S1. The model assumes soil air fractionation occurs due to gravitational settling, thermal diffusion (due to a 30 ºC km^{-1} geothermal gradient) and water-vapor flux fractionation driven by mean annual surface air relative humidity and temperature of 70% and 20 ºC, respectively. The full equations governing these three fractionation processes are presented in Supplementary Section 4.2 (Inverse Model Overview). In Figure 4.S1, each marker indicates the fractionation of an individual isotope ratio with mass difference Δm (e.g. 7 amu for $\delta^{136}/_{129}$Xe). We suggest that this linearity justifies the use of simple δ*Xe and δ*Kr notation for presentation purposes. For the full inverse model (described in

Supplementary Section 4.2), however, each isotope ratio is treated independently, and no assumption of linear mass dependence is needed.

4.S2. Inverse Model Overview

In this study, two separate inverse models were coupled in an iterative loop and constrained by measurements made in each sample. One model solves for mean annual surface temperature (MAST) and is constrained by noble gas concentrations and the other solves for water-table depth (WTD) and is constrained by noble gas isotope ratios.

The first inverse model estimates dissolution parameters (recharge temperature and excess air) from dissolved concentrations, employing an adapted version of the widely used Closed-system Equilibration (CE) model (Aeschbach-Hertig et al., 2000, 2008). This model is identical to the CE model except that instead of assuming that unsaturated zone (UZ) air at the water table is unfractionated from atmospheric noble gas composition, it assumes Ar/air, Kr/air, and Xe/air ratios are fractionated by gravitational settling, thermal diffusion, and water-vapor flux fractionation. The magnitude of total UZ air fractionation for a given elemental or isotopic ratio is $\varepsilon_{UZ.}$ This model requires knowledge of surface pressure, which we prescribe based on elevation. It yields estimates of recharge temperature (T, ^{o}C), initially entrapped air volumetric ratio (A, volume air/volume water), and dissolution amount (F, final air volume / initial air volume).

The second inverse model concerns UZ fractionation (ε_{UZ}), yielding estimates of the two free parameters governing ε_{UZ}: WTD (which sets the gravitational settling signal) and surface water-vapor mole fraction (X_{H2O}, which sets the water-vapor flux fractionation). This model requires the known geothermal gradient to determine thermal diffusion and water-vapor flux fractionations between unfractionated surface air and UZ air above the water table.

Formally, the first model solves for a dissolved concentration of a gas X (Ar, Kr, or Xe), *[X]*, in terms of T, A, F following the formulation of Aeschbach-Hertig et al. (2008):

$$[X] = [X]_{eq}(T, P, \varepsilon_{UZ}) * \left[1 + \frac{(1-F)A*H(T)}{1+FA*H(T)}\right] \tag{4.S6}$$

where the subscript "eq" indicates solubility equilibrium and H is the Henry coefficient ($H \equiv [X]_{air}/[X]_{eq}$). Here, solubility equilibrium refers to specifically to an equilibrium between groundwater dissolved gases and overlying UZ air (importantly not atmospheric air) at the water table. The solubility concentrations (and henry coefficients) are prescribed using the recently redetermined noble gas solubility functions of Jenkins et al. (2019). With knowledge of T, A, and F, ε_{sol} and ε_{EA} can be determined from the known isotopic solubility functions (Seltzer et al., 2019) and extension of the CE model to isotope ratios, respectively. We note that Seltzer et al. (2019) used newly measured Kr and Xe isotopic solubility and diffusivity fractionation factors to demonstrate that ε_{EA} is insensitive to the choice of excess air model at the single per meg amu^{-1} level. Extension S6 to determine ε_{EA} for the CE model results in:

$$\varepsilon_{EA} = \frac{(1+AH_g)(1+AF_{CE}H_g\alpha_{sol})}{(1+AH_g\alpha_{sol})(1+AF_{CE}H_g)} - 1 \tag{4.S7}$$

where H_g is the henry coefficient for either bulk Xe or Kr and $\alpha_{sol} = 10^{-6}\varepsilon_{sol} + 1$ (if ε_{sol} is given in per meg). Note that multiplying equation 4.S7 (or any subsequent equation concerning ε values) by 10^6 will give units of per meg.

The second model computes ε_{UZ} for individual isotopic or elemental ratios as a function of WTD, X_{H2O}, and geothermal gradient (Γ). It assumes that steady-state fractionation (in per meg) of UZ air above the water table is due to gravitational settling, thermal diffusion, and water-vapor flux fractionation, such that:

$$\varepsilon_{UZ} = \varepsilon_{grav} + \varepsilon_{H2O} + \varepsilon_{therm} \tag{4.S8}$$

Gravitational settling fractionation (Schwander, 1989), ε_{grav}, is parameterized by:

$$\varepsilon_{grav} = e^{(WTD*\Delta m*g)/(RT)} - 1 \qquad (4.S9)$$

where R is the ideal gas constant (m^3 Pa K^{-1} mol^{-1}), T is UZ air temperature (K), g is gravitational acceleration (m s^{-2}), and WTD and Δm are given in m and in g mol^{-1}, respectively. The parameterization for steady-state water-vapor flux fractionation (Severinghaus et al., 1996), ε_{H2O}, is given by:

$$\varepsilon_{H2O} \approx \left(\frac{1\text{-}e_{sat}/P_{tot}}{1\text{-}\chi_{H2O}}\right)^{\frac{D_{h\text{-}H2O}}{D_{l\text{-}H2O}}-1} - 1 \qquad (4.S10)$$

where X_{H2O} is the mole fraction of water vapor in mean surface air, e_{sat} is saturation vapor pressure in UZ air above the water table, P_{tot} is total UZ air pressure above the water table, and $\frac{D_{h\text{-}H2O}}{D_{l\text{-}H2O}}$ is the binary diffusivity ratio of heavy and light gases or isotopes against water vapor (Fuller et al., 1966). Thermal diffusion fractionation is given by:

$$\varepsilon_{therm} = -\Omega*\Gamma*WTD \qquad (4.S11)$$

where Γ is the geothermal gradient (in °C m^{-1}) and Ω is thermal diffusion sensitivity for a given gas or isotope ratio (Grachev & Severinghaus, 2003; Kawamura et al., 2013).

As illustrated in Figure 4.S2, the two inverse models are coupled in an iterative algorithm to estimate WTD and T from measurements of Kr and Xe isotope ratios and bulk noble gas concentrations from a single sample, with geothermal gradient and elevation prescribed. MAST can then be determined by subtracting $\Gamma \cdot WTD$ from T, thus removing the contribution of geothermal heat from the estimated recharge temperature (at WTD). The algorithm begins by first assuming no fractionation of elemental noble gas ratios in UZ air (i.e. $\varepsilon_{UZ} = 0$) and inverts the CE model via non-linear least squares (Levenberg-Marquardt algorithm) to find initial estimates of T, A, and F constrained by noble gas concentration measurements. Then, ε_{EA} for each Kr and Xe isotope ratio is computed via equation 4.S7 and ε_{UZ} for each isotope ratio is estimated by subtracting ($\varepsilon_{EA} + \varepsilon_{sol}$) from δ. These six Kr and Xe isotope ratio estimates of ε_{UZ} are used to invert the UZ air fractionation model (i.e. equation 4.S8), again via non-linear least squares, to estimate WTD and X_{H2O}. Note that because Kr and Xe isotopes are very weakly sensitive to water-vapor flux fractionation, estimates of X_{H2O} are poorly constrained and the least-squares solver is bounded to a surface-air relative humidity range between 25 and 100%. Next, using these parameters, ε_{UZ} is calculated for Ar/air, Kr/air, and Xe/air and the CE model is again inverted, this time assuming a fractionated UZ air composition above the water table to get a new set of T, A, and F estimates. These new estimates feed back into the UZ air model, and this back-and-forth process is repeated until WTD and T values converge within 50 cm and 0.2 ºC, respectively.

Ultimately, for each groundwater sample this algorithm is carried out in 1000 separate Monte Carlo simulations, in which normally distributed random numbers with standard deviations equal to SE_{tot} are added to each measured isotope ratio and gas concentration. The results are thus 1000-element distributions of estimated WTD and T_{surf}, which provide uncertainties on these parameters. For tritiated (young) water samples, where ^{40}K-derived radiogenic ^{40}Ar can be neglected, Ar isotope ratios were also used to constrain the inverse model.

The performance of the coupled-inverse model approach is investigated by looking at measurement-model residuals ($\delta_{res} = \delta_{measurement} - \delta_{model}$) for each individual sample analyzed in this study. In Figure 4.S3, Kr and Xe isotope residuals (δ^*Kr_{res} and δ^*Xe_{res}) are shown as a function of reconstructed WTD as well as study area. Across all Fresno and San Diego samples, there is no apparent trend of isotopic residuals with reconstructed WTD, and mean δ^*Kr_{res} and δ^*Xe_{res} are +4 and -2 per meg amu^{-1}, respectively, each equivalent to one meter or less of gravitational settling fractionation. These small residuals add confidence to reconstructed WTDs in Fresno and San Diego samples at the several-meter scale. However, the fact that they are anti-correlated (positive

Kr residuals and negative Xe residuals, on average) may indicate that a minor process is not captured by the model, perhaps causing WTD biases at or below the 1-meter scale. Mojave Desert samples exhibit large, anti-correlated δ^*Kr_{res} and δ^*Xe_{res}, which appear to increase with reconstructed WTD up to maximum absolute values of 50 per meg amu^{-1}, equivalent to WTD biases of over 10 m for 90-125 m reconstructed WTDs. For these samples, δ^*Kr_{res} values are positive and δ^*Xe_{res} values are negative, likely indicating the failure of the model to capture a systematic process, perhaps the same process we suspect may play a minor role (at the single per meg amu^{-1} level) in the Fresno and San Diego samples. We therefore do not attempt to interpret reconstructed WTD in the Mojave Desert samples. In Supplementary Text Section 4.5, we propose and formally consider several physical processes that may explain the large isotopic residuals in the Mojave Desert samples.

4.S3. Fresno Groundwater Study: Detailed Description

Five two-liter groundwater samples were collected from two wells located ~50 m apart at a site southeast of the city of Fresno, California. Two samples were collected from monitoring well 180-MW, which has a perforation interval from 65-68 meters below the land surface (mbls). Three samples were collected from the deeper supply well 180-1, which has a wider perforation interval from 125 to 186 mbls. The groundwater supplied to both wells comes from a regional unconfined aquifer system, which consists of fluvial deposits and generally flows from east to west (Saraceno et al., 2018).

Although the city of Fresno was densely populated throughout the 20th century, the area directly surrounding these wells was historically agricultural until becoming more densely settled over the past ~30 years (Saraceno et al., 2018). To estimate the local WTD at the time of recharge near these wells, we analyzed historical water-level records maintained by the California Department of Water resources (available online from https://data.cnra.ca.gov/dataset/periodic-groundwater-level-measurements) and considered all historical measurements from wells with a 10-km radius of the 180-1/180-MW sampling site. As shown in Figure 4.S4, the historical records appear to cluster into two distinct groups: one exhibiting substantial mid-20th century drawdown and another which appears to follow decadal-scale (natural) variability until the late 20th century. These groups exhibit a strong spatial dependence: all wells showing severe drawdown in the 1950s (specifically, with mean 1960s water levels below 15 m) lie within the densely populated Fresno city center to the northwest of the sampling site. We therefore separate these two groups along spatial criteria, such that all wells northwest of the 180-1/180-MW site belong to the first group (substantial mid-20th century groundwater abstraction), and all other wells (within the 10-km radius) belong to the second. These well groups are identified by the colors red and blue, respectively, in Figure 4.S4. Because the 180-1/180-MW site and its surrounding area was sparsely populated until the early 1990s, the most appropriate local WTD history is represented by the second group of wells, consisting of historical records from 76 individual wells.

Groundwater samples from 180-MW were dated using three independent tracers: ^{85}Kr, ^{3}H/^{3}He, and SF_6. In each case, piston flow age distributions were determined by carrying out 100 Monte Carlo simulations, as shown in Figure 4.S5, perturbing measurements and atmospheric histories with normally-distributed random numbers with standard deviations equal to analytical uncertainties. For ^{85}Kr, dissolved activity was measured at Argonne National Lab, and the European baseline atmospheric history (Bollhöfer et al., 2019) was used, interpolated to 0.1-year resolution and assigned a 5% 1σ uncertainty. For SF_6, dissolved measurements were made by gas chromatography at USGS Reston Groundwater Dating Lab. Historical atmospheric SF_6

measurements were taken from the National Oceanic and Atmospheric Administration's Niwot Ridge, Colorado, USA site (data available online from https://www.esrl.noaa.gov/gmd/dv/site/NWR.html) and UZ air SF_6 concentration at the time of recharge was determined based on the known SF_6 solubility (Bullister et al., 2002), accounting for recharge temperature and excess air (via the CE model) based on bulk Ne, Ar, Kr, and Xe measurements made by the United States Geological Survey (USGS). USGS $^{3}He/^{4}He$ measurements and Lawrence Livermore National Lab ^{3}H measurements were used to determine $^{3}H/^{3}He$ piston flow ages assuming that the $^{3}He/^{4}He$ ratio in well 180-1 (which is ^{3}H dead) represents the background terrigenous helium isotope ratio. Piston flow age distributions form each age tracer yielded median recharge dates in the 1980s (Figure 4.S5): 1980.0 from ^{85}Kr, 1981.2 from SF_6, and 1987.6 from $^{3}H/^{3}He$. These piston flow ages imply an effective vertical velocity of ~1 m yr^{-1}, as the perforation interval of well 180-MW is ~40 m below the water table. Thus, the impact of dispersive mixing during sampling through the 3-m screened interval is unlikely to substantially bias recharge ages (Solomon et al., 1998). The close agreement of SF_6 and ^{85}Kr age distributions, which both appear older than the $^{3}H/^{3}He$ date, is in principle consistent with the well-known young bias of $^{3}H/^{3}He$ dating due to diffusive loss of radiogenic ^{3}He (Schlosser et al., 1989). However, because the apparent vertical velocity is rather high, we conservatively determine the most probable recharge date to be the mean of the median ages from each tracer's distribution, 1983, and assign an uncertainty of ± 5 years. Because the WTD fluctuations exhibit decadal-scale variability (Figure 4.3), the agreement of these three age tracers gives high confidence in comparing noble gas isotope-derived WTDs to early-to-mid 1980s historical water levels in the region.

Groundwater age in the deeper well (180-1), which has a large screen allowing for mixing of water of varying recharge age, was estimated based on SF_6, ^{85}Kr, $^{3}H/^{3}He$, ^{14}C, and ^{39}Ar. No ^{3}H or ^{85}Kr was detected (within error) and SF_6 concentrations were consistent with pre-1960s recharge, while ^{39}Ar and ^{14}C yielded piston flow ages of ~650 and ~6000 years respectively. Because ^{39}Ar has a ~20 times shorter half-life than ^{14}C, this is consistent with the groundwater from well 180-1 representing a mixture of water ranging in age from the mid Holocene to the last century. A more complete discussion of groundwater mixing and multi-tracer age estimation in these wells is the subject of another, ongoing study. Here we simply note that multiple age tracers confirm that 180-MW groundwater reflects 1980s recharge and that 180-1 groundwater reflects a mixture of mid-to-late Holocene recharge.

4.S4. San Diego Groundwater Study: Detailed Description

Thirty-five two-liter groundwater samples were collected from a coastal aquifer system in San Diego, California. These samples were collected and analyzed from 23 monitoring wells pertaining to six separate multiple-depth, monitoring-well sites, which span a latitudinal range of ~13 km and longitudinal range of ~5 km (Figs. 4.4, 4.S6). Each monitoring well has a narrow perforated interval (generally 6 m), which limits dispersive mixing during sampling. The six sites are marked by the black polygons in Figure 4.S6. The coastal aquifer system is composed of a shallow, locally recharged, unconfined aquifer overlying a confined, regional aquifer composed of poorly consolidated marine sediment (Anders et al., 2014). The regional aquifer is of primary interest to this study because the large spatial and temporal scales of UZ-groundwater exchange prior to confinement and intra-aquifer dispersive mixing integrate contemporaneous geochemical signals over a wide region. Indeed, the close agreement of the WTD reconstructions (Figure 4.4) from regional-aquifer groundwater of similar recharge age (e.g. the clustering of 11 noble gas-derived WTD reconstructions near 20 meters from last glacial period samples across many well sites, Figure 4.4) is consistent with the notion that deep, confined groundwater reflects integrated signals over a wide spatial range.

Recharge to the confined regional aquifer occurs to the east of the well sites, presumably beginning at the foothills of the Laguna and Cuyamaca mountains, where the dominant surficial geology transitions from lower-permeability metavolcanic and igneous rocks to higher-permeability sediment. These concomitant changes in topography and geology are shown in Figure 4.S6 along with a box designating a probable regional recharge area, bounded by well site locations to the north, south, and west and the geologic and topographic transitions to the east. The transitions to both low-lying topography and sediment occur ~10-15 km east of the well sites. Anders et al. (2014) hypothesized that regional recharge may originate further east at higher elevations, based on observations of lower δ^{18}O of deep, low-^{14}C samples. However, the mean δ^{18}O of the deep samples is ~1‰ lower than shallow, local Holocene recharge, which is consistent in magnitude with a glacial-interglacial climate signal, rather than an elevational signal. Indeed, a groundwater study in the western Mojave Desert also found glacial δ^{18}O values ~1‰ below Holocene δ^{18}O (Kulongoski et al., 2009), consistent with other reconstructions of glacial-interglacial changes in precipitation δ^{18}O over southwestern United States (Jasechko et al., 2015). We, therefore, suggest that recharge to the San Diego regional aquifer occurs primarily through the high permeability sediment at low elevation to the west of the onset of steep topography.

Because fine-grained sediment, which separates the shallow unconfined aquifer from the regional confined aquifer, does not occur uniformly throughout the study area, we assume that groundwater from non-artesian wells that is both younger than 5 ka (based on ^{14}C) and shallower than 150 m is part of the unconfined aquifer. Four sampled wells fit these local-recharge criteria. As evidence supporting this designation, the noble-gas reconstructed WTDs across the four samples identified as local recharge range widely (from 6 to 49 m) in a manner correlated with present-day local WTDs. We estimate representative modern local WTDs at a given well location by subtracting the groundwater elevation measured at the time of well installation from the mean surface elevation within a 1-km radius of the well. In Figure S7, replicate-mean noble gas-derived WTDs are compared to estimated mean present-day local WTD within 1-km of the well location. The large variability of these reconstructed WTDs from contemporaneous mid-Holocene groundwater contrasts with the close agreement of WTDs from contemporaneous regional groundwater.

For a representative comparison of regional mean WTD in the present day to reconstructed past WTDs from noble gas measurements, we analyzed output from a measurement-constrained groundwater model (Fan et al., 2013) at high resolution (~1 km x 1 km grid cells). We included all grid cells within the assumed recharge area (box in Figs. 4.4 and 4.S6) except for those cells containing surface water. Unsurprisingly, single grid cells are highly dependent on local topography, such that WTD is deeper in higher elevation grid cells. Thus, there is great variability in modeled WTD over the box due to hilly topography. The mean WTD across surface-water-free grid cells (N=242) is 46.8 ± 24.7 m (1σ). Although this mean depth is distinctly lower than the ~20-m mean reconstructed WTD over the last glacial period, consistent with wetter glacial-period conditions, we caution against interpretation of the ~8 m apparent difference between the model-mean value and reconstructed Holocene-mean WTD as a meaningful result of climate change or human activities.

All San Diego groundwater samples were dated with ^{14}C of dissolved inorganic carbon (DIC), correcting for the contribution of dissolved ^{14}C-free carbonate to total DIC using a two end-member mixing model (Pearson & Hanshaw, 1970). In this model, a dilution factor (q) is calculated from measured δ^{13}C ($\delta^{13}C_{meas}$), initial δ^{13}C ($\delta^{13}C_0$) and carbonate rock δ^{13}C ($\delta^{13}C_{rock}$), the latter two of which are assumed to be -25‰ and 0‰ (vs PDB).

$$q = \frac{\delta^{13}\mathrm{C_{meas}} - \delta^{13}\mathrm{C_{rock}}}{\delta^{13}\mathrm{C_0} - \delta^{13}\mathrm{C_{rock}}} \tag{4.S12}$$

Radiocarbon ages (t_{14C}, in years) can then be calculated from measured ^{14}C activity (a_{14C}) by:

$$t_{14C} = -8267 \ln\left(\frac{a_{14C}}{q}\right) \tag{4.S13}$$

and converted to calibrated age using the IntCal13 calibration curve (Reimer et al., 2013). To account for uncertainty in the mixing model assumption, we carry out 100 Monte Carlo simulations for each sample, adding normally distributed random perturbations to measured a_{14C} and $\delta^{13}C_{meas}$ of 0.1% modern carbon and 2‰, respectively. The median calibrated age from these simulations is taken as the most probable estimate of mean recharge age. However, we caution against strict interpretation of groundwater recharge age, as groundwater is best understood conceptually as a mixture of individual parcels each with different transit times since entering the saturated zone (Bethke & Johnson, 2008). We therefore adopt ±2 ka minimum error bars on each ^{14}C age, even though the Monte Carlo age distribution is in some cases narrower. Several samples in this study also were dated with ^{81}Kr, which in all cases agreed with ^{14}C-derived ages but was of limited use given the ±~15 ka uncertainties associated with ±2-4% ^{81}Kr analytical uncertainty. One approximately ^{14}C-dead sample from a 607-m deep well was found to have 41 ± 2% modern ^{81}Kr activity, consistent with an effective recharge age between ~280 and 310 ka. Interestingly, the Kr and Xe isotopes in this sample were in solubility equilibrium with atmospheric air (i.e. overlapping the square in Figure 4.2), implying a WTD of zero. We hypothesize that this deep, ancient groundwater may have been directly recharged from a lake or river, without passing through an unsaturated zone, perhaps during the marine isotope stage (MIS) 8, a glacial period. Many relatively flat, inter-montane valleys are present throughout the eastern part of the study area, although they are currently dry.

As described in the Materials and Methods (Section 4.2), we also reconstructed mean surface temperatures from bulk noble gas concentrations, in addition to WTDs. In Figure 4.S8, reconstructed mean annual surface temperature is shown for all samples from the shallow and regional aquifers, except for (a) the ~300-ka old, zero-WTD sample and (b) a shallow sample with a reconstructed WTD of ~7-m, both of which are too shallow for the noble gas paleothermometry requirement of no seasonal temperature cycle at the WTD (Martin Stute & Schlosser, 1993), and (c) glacial-period samples from the SDHF and SDBP well sites. The mean Holocene reconstructed surface temperature, 20.2 ± 0.5 ºC (± 1 SE), is in close agreement with mean 1979–2018 ERA5 and NCEP reanalysis surface (0-7 cm) soil temperatures in the assumed recharge region, which are 19.7 ºC and 19.8 ºC, respectively. The average surface temperature during the late last glacial period (LLGP), 13.7 ± 0.3 ºC (± 1 SE), indicates 6.0-6.5 ºC of warming from the LLGP to Holocene. A warm (~20 ºC) reconstructed temperature at 13.6 ka and two cooler temperatures (16-17 ºC) found at 12.6 and 11.9 ka may represent recharge from the Bolling-Allerod interstadial and Younger Dryas stadial, respectively, but dating uncertainties make this speculative.

The LLGP-aged samples from well sites SDBP and SDHF (diamond and left-facing triangle markers in Figs. 4.4, 4.S6, 4.S8-9), which are located close to one another, are anomalous in their Kr and Xe concentrations. As shown in Figure 4.S9, the mean Ar concentrations in SDBP and SDHF LLGP samples are similar to LLGP samples from other sites (with one exception), while Kr concentrations are generally lower, and Xe concentrations are substantially lower (~12%

on average). Surface temperature reconstructions based on these values appear extremely warm (~25 ºC) and are clearly inconsistent with the 13-14 ºC LLGP temperatures consistently observed at other sites as well as our climatological understanding of the LLGP. We note that the single SDHF sample (replicated twice) with low [Ar] is the same ~24 ka sample with a deep (~45 m) WTD, which may be linked to the reported glacial "megadrought" in southern California around this time (Feakins et al., 2019; Heusser et al., 2015; Kirby et al., 2018). Thus, the low [Ar] may indicate low excess air in this sample, since excess air has been suggested to correlate inversely with WTD (Heaton & Vogel, 1981; Ingram et al., 2007). This sample also appears lower than other LLGP SDHF and SDBP samples in [Kr], although by a lesser relative amount than for [Ar], but is virtually indistinguishable from other SDBP and SDHF samples in terms of [Xe]. Because the impact of excess air is largest for less soluble gases, this pattern (largest differences for [Ar], smallest for [Xe]) supports the notion that this sample has relatively low excess air compared to other LLGP samples and is consistent with its deep reconstructed WTD.

We offer two hypotheses for the low Kr and Xe concentrations in these samples. First, because these sites are located close together and along an east-west line parallel to groundwater flow, it is possible that a source of geothermal heat along their shared flow path was present during the LLGP. In this case, these noble gas concentrations would reflect the true recharge temperatures, affected by an anomalous local geothermal feature. A second hypothesis is that a strongly adsorbing mineral along their shared flow path removed Kr and Xe. Xe and, to a lesser extent, Kr, are known to be susceptible to adsorption (Podosek et al., 1981; Yang et al., 2003), which has been demonstrated to be independent of any isotopic fractionation (Bernatowicz & Podosek, 1986; Marrocchi & Marty, 2013). This adsorption would cause a warm bias in reconstructed temperature. Although we must reject the noble gas temperatures derived from the LLGP SDBP and SDHF samples as being representative of regional conditions, we note that any influence of either a geothermal heat source or adsorption on isotopic composition is small relative to the contribution of gravitational settling. For example, the sensitivity of Kr and Xe isotopic solubility fractionation to temperature is extremely small (<0.25 per meg amu^{-1} ^{o}C^{-1}), such that even a 10 ^{o}C change in recharge temperature is equivalent to less than one meter of gravitational settling fractionation (4.0 per meg amu^{-1}). Similarly, excess air fractionation and thermal diffusion fractionation are equivalent in magnitude to only single meters of gravitational settling fractionation (Fig 2). As further evidence that isotopic ratios are not affected by the process responsible for the low Kr and Xe in LLGP SDBP and SDHF samples, δ*Kr and δ*Xe residuals from these samples are indistinguishable from other LLGP samples (Figure 4.S10). Similarly, WTDs reconstructed from these samples closely match those from other LLGP sites. Thus, while we have insufficient evidence to determine which, if either, of these two proposed hypotheses is correct, it is highly probable that the Kr and Xe isotopic composition of these samples, relative to gravitational settling fractionation at the meter scale, is insensitive to whichever process is responsible for the low Kr and Xe concentrations.

4.S5. Mojave Desert Groundwater Study: Detailed Description

A total of 18 groundwater samples were collected over a large spatial extent (from 34.4 to 35.0 ^{o}N and from 117.4 to 118.1 ^{o}W) of the western Mojave Desert. These samples were collected from 11 total supply wells, unlike the narrow-screened monitoring wells from which the San Diego samples were collected. These supply wells were each screened over large depth intervals, potentially allowing for mixing of waters of different recharge age. We do not attempt to interpret these samples in a paleoclimatic context.

As described in the main text and shown in Figs. 4.2 and 4.S3, the Mojave groundwater samples exhibit a discordant δ*Kr vs δ*Xe relationship from the San Diego and Fresno samples, which fall close to the predicted line for isotopic fractionation due only to gravitational settling and solubility fractionation. This Mojave-specific feature manifests itself as positive $\delta^*\mathrm{Kr}_{\mathrm{res}}$ and negative $\delta^*\mathrm{Xe}_{\mathrm{res}}$ when fitting measurements to the WTD/temperature model. In other words, individual samples plot above the expected fractionation line for gravitational settling and solubility fractionation on a plot of δ*Kr vs δ*Xe (Figure 4.S11). This isotopic feature is most pronounced for samples with higher δ*Kr and δ*Xe, which yield deeper apparent WTDs. We can think of two candidate mechanisms that are not accounted for in our UZ air fractionation model but which have been observed before in porous media and found to fractionate noble gases in manner consistent with our Kr and Xe isotopic observations.

The first candidate process is steady-state kinetic fractionation of noble gases driven by a diffusive atmosphere-to-UZ flux of O_2 in response to O_2 consumption in the deep UZ. The so-called "O_2 depletion" (OD) model was previously introduced to account for anomalously low reconstructed noble gas temperatures caused by enrichment of noble gas partial pressures above the water table (Hall et al., 2005). In this model, steady-state consumption of O_2 in the deep UZ, leads to non-equimolar replacement in UZ air by CO_2 (because CO_2 is highly soluble), such that the sum of partial pressures of O_2 and CO_2 decreases. Because total UZ air pressure remains constant, the deficit of (O_2 + CO_2) from deep UZ air leads to advective replacement by other dry air constituents, such that the partial pressure of noble gases in UZ air increases directly with (O_2 + CO_2) deficit. Decreases in the (O_2 + CO_2) mole fraction in UZ air of several percent (note: dry air has an O_2 + CO_2 mole fraction of ~21%) and associated increases in noble gas partial pressures have been observed in several studies (Freundt et al., 2013; Hall et al., 2012). If a decrease in (O_2

+ CO_2) partial pressure and corresponding increase in noble gas partial pressures in deep UZ air is maintained at steady state, the partial pressure gradient between noble gases in deep UZ air and surface air will drive an upwards diffusive flux against downward diffusion of O_2, causing kinetic isotopic fractionation of noble gases. This kinetic fractionation can be thought of as an inverse analog to water-vapor flux fractionation (Severinghaus et al., 1996), such that steady-state diffusion of noble gases out of the UZ leads to enrichment of heavy-to-light isotope ratios in UZ air relative to the atmosphere due to the higher diffusivity of the lighter isotope.

We can model this isotopic fractionation (ε_{O2}) using an equation analogous to equation 4.S10, making use of the approximation given in Severinghaus et al. (1996):

$$\varepsilon_{O2} \approx \left(\frac{D_{h\text{-}O2}}{D_{l\text{-}O2}} - 1\right)\Delta X_{O2} \tag{4.S14}$$

where ΔX_{O2} is the mole fraction difference in (O_2 + CO_2) between UZ air and atmospheric air (negative if the UZ air mole fraction is lower), and $\frac{D_{h\text{-}O2}}{D_{l\text{-}O2}}$ is the ratio of binary diffusivities against O_2 for a heavy and light isotope of a noble gas (Fuller et al., 1966). Normalized by isotopic mass difference $\frac{D_{h\text{-}O2}}{D_{l\text{-}O2}} - 1$ is greater for Kr isotope ratios (-1.6‰ amu^{-1}) than for Xe isotope ratios (-0.7‰ amu^{-1}). Thus, for negative ΔX_{O2}, isotopic fractionation is positive (enrichment of heavy isotopes) and affects Kr isotopes more strongly than Xe isotopes. In Figure 4.S11, expected δ*Kr and δ*Xe fractionation is shown for ΔX_{O2} = -0.5%. One can see that O_2 depletion fractionation acting in addition to gravitational settling and solubility fractionation would cause dissolved Kr and Xe isotope to plot above the gravity/solubility line in Figure 4.S11, consistent with the Mojave observations. In this case, WTDs would be overestimated by our model because oxygen depletion, like gravitational settling, leads to enrichment of δ*Kr and δ*Xe. Because this enrichment, unlike gravitational settling, is not 1:1 for δ*Kr and δ*Xe, it could explain the positive $\delta^*\mathrm{Kr}_{\mathrm{res}}$ and negative $\delta^*\mathrm{Xe}_{\mathrm{res}}$ we observe in the Mojave Desert samples (Figure 4.S3).

The second candidate process, which we call "kinetic disequilibrium" fractionation, is caused by storm-driven barometric pumping of the UZ. Kinetic disequilibrium acts against gravitational settling by lowering both δ*Kr and δ*Xe in different proportions, such that δ*Xe is decreased more than δ*Kr. In the envisioned scenario, barometric pumping of the UZ initially disrupts gravitational settling by effectively mixing gravitationally enriched air with unfractionated atmospheric air (δ=0). Then, once pumping has ceased, UZ air composition is driven back towards gravitational equilibrium by molecular diffusion. Because Xe is slower diffusing than Kr, and because light isotopes are faster diffusing than heavy isotopes, there is kinetic fractionation that affects the isotope ratios of Kr and Xe differently. If the characteristic timescale between barometric pumping events is shorter than the timescale for molecular diffusion to return the Kr and Xe isotopic composition of deep UZ air back to the expected steady-state composition (driven only by gravitational settling, thermal diffusion, and water-vapor flux fractionation) then the isotopic signal of kinetic disequilibrium will persist and be transmitted to groundwater via dissolution at the water table.

Barometric pumping fractionation has been observed in polar firn air (Kawamura et al., 2013), and a 2-D firn air model (Birner et al., 2018) has simulated the combined effects of layering and barometric pumping to determine the isotopic mass-difference normalized sensitivities of Kr and Xe to kinetic disequilibrium. This simulation would suggest that δ*Kr and δ*Xe would both decrease due to barometric pumping, with δ*Xe affected 39% more than δ*Kr, as shown in Figure 4.S11. If this process is responsible for the deviation of Mojave Desert samples from the gravity/solubility expectation line, then our inverse model would underestimate true WTD and yield negative δ^*Xe_{res} and positive δ^*Kr_{res}, again consistent with our observations (Figure 4.S3).

Although we cannot conclusively differentiate between these two possible explanations for the Mojave Desert Kr and Xe isotope observations, the apparent sensitivity of Mojave δ^*Xe_{res} and δ^*Kr_{res} to WTD is consistent with fractionation due to molecular diffusion in UZ air. The timescale for diffusive re-equilibration increases quadratically with depth (i.e. the e-folding timescale for 1-D diffusive re-equilibration, τ, is equal to z^2/D, where z is UZ depth and D is molecular diffusivity). In shallow UZ air, repeated barometric pumping or O_2 consumption may cause short-lived fractionation of UZ air that quickly returns to the expected ε_{UZ} predicted by our (mostly gravitational) steady-state UZ air model. In other words, the timescale of diffusive re-equilibration may be shorter than the timescales of O_2 consumption and barometric pumping for shallower UZ air. However, in deep UZ air, the timescale of O_2 consumption or barometric pumping events maybe shorter than the diffusive-equilibration timescale, leaving behind a signal of kinetic fractionation in the steady-state UZ air composition above the WTD, which ultimately dissolves into groundwater. In extreme cases, such as these Mojave Desert samples, this can lead to over or under estimation of ~100-m deep WTDs by 10-20 m based on Kr and Xe isotopic composition. In principle, Ar isotopes and noble gas temperatures could help identify which mechanism is at play and, ideally, provide a correction for more robust WTD determination. However, $^{40}/_{36}Ar$ is affected by β decay of ^{40}K and $^{38}/_{36}Ar$ is measured at ~10 per meg amu^{-1} precision ($\pm 1\sigma$) and is significantly more sensitive to solubility fractionation, excess air, thermal diffusion, and water-vapor flux fractionation, rendering it difficult to conclusively identify an anomalous fractionation signal associated with O_2 depletion or kinetic disequilibrium. We suggest that Ne isotope measurements at high precision in future studies may provide a useful clue, as $\delta^{22}/_{20}Ne$ is negligibly affected by kinetic disequilibrium (because Ne is fast diffusing relative to Kr and Xe) but strongly affected by O_2 depletion ($\frac{D_{h\text{-}O2}}{D_{l\text{-}O2}} - 1$ is -14‰ amu^{-1} for $\delta^{22}/_{20}$Ne, 20 times larger than for δ*Xe). The noble gas-derived mean annual surface temperature in one deep-WTD Mojave sample of LLGP age did appear extremely low (~10 ºC), lower than the expected LLGP mean surface temperature (~4-5 ºC below present day ~17 ºC MAST) and is therefore in principle consistent with the O_2 depletion hypothesis. However, this temperature estimate is too underconstrained to meaningfully draw any conclusions about which isotopic fractionation mechanism may be at play. We suggest that future dissolved isotopic analyses, including Ne isotopes, may provide evidence in support of either of these candidate mechanisms.

Acknowledgments

We thank Ross Beaudette, Sarah Shackleton, Bill Paplawski, Ray Weiss, and Adam Cox for analytical advice, support, and equipment loans, and Greg Mendez, Ernesto Araiza, Kate Durkin, Matt Pendergraft, Robert Kent, and Ray Cordero for assistance in sampling. This work as supported by NSF awards EAR-1702704 (to JS), EAR-1702571 (to MS), an NSF Graduate Research Fellowship (to AS). This chapter, in full, has been submitted for publication in *Nature Communications*: Seltzer, A., Ng, J., Danskin, W., Kulongoski, J., Gannon, R., Stute, M., and J. Severinghaus, Dissolved Kr and Xe Isotope Ratios in Groundwater Preserve Gravitational Signals of Past Water-Table Depth. The dissertation author was the primary investigator and author of this work.

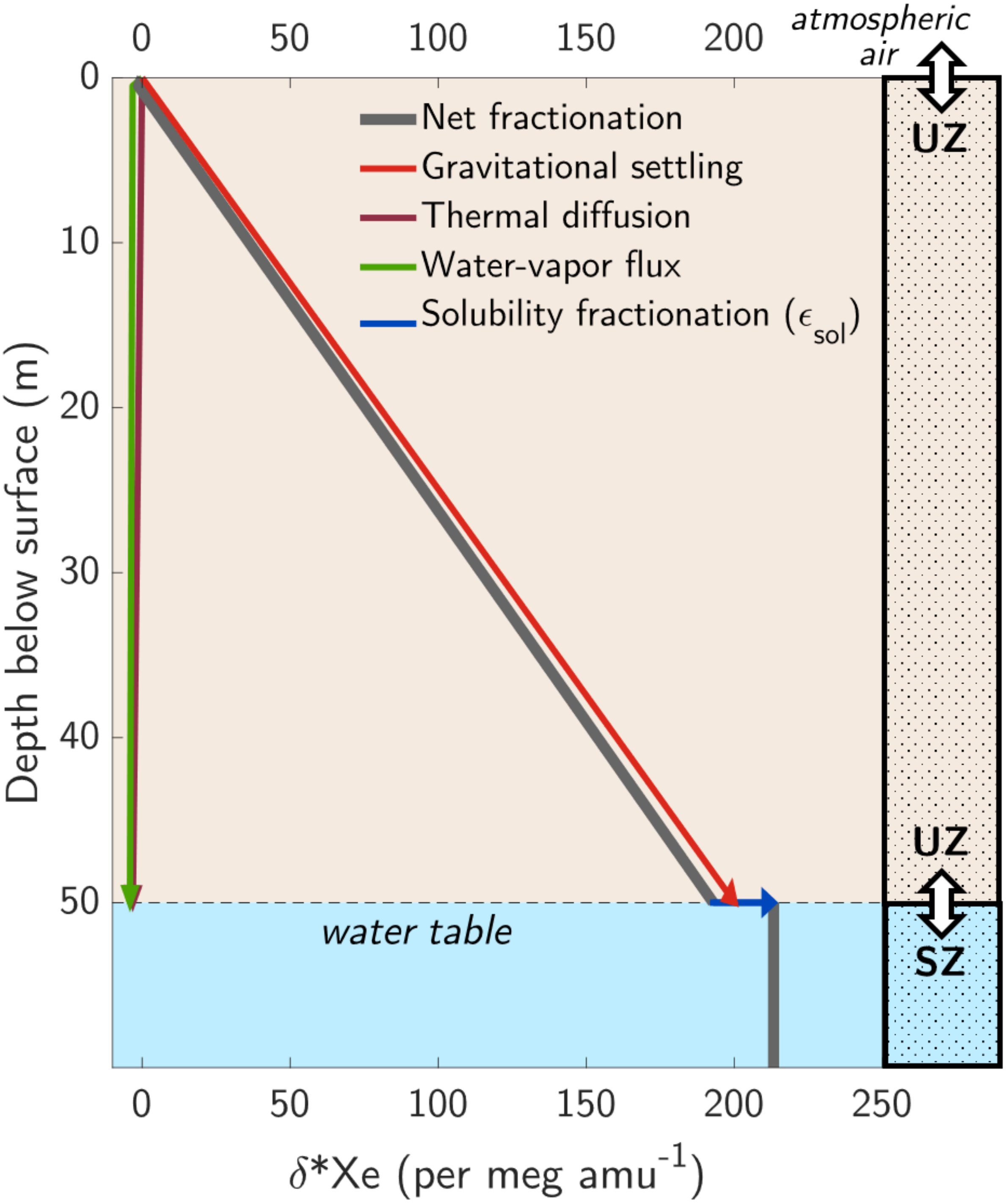

Figure 4.1. A steady-state model of xenon isotopic fractionation in an idealized unconfined aquifer. Gravitational settling causes mass difference-normalized, heavy-to-light xenon isotope ratios (δ*Xe) in UZ air to increase with depth below the land surface, relative to atmospheric air. At the water table, dissolved gases in the saturated zone (SZ) equilibrate with deep UZ air. Solubility fractionation causes δ*Xe to further increase in the dissolved phase relative to the gas phase

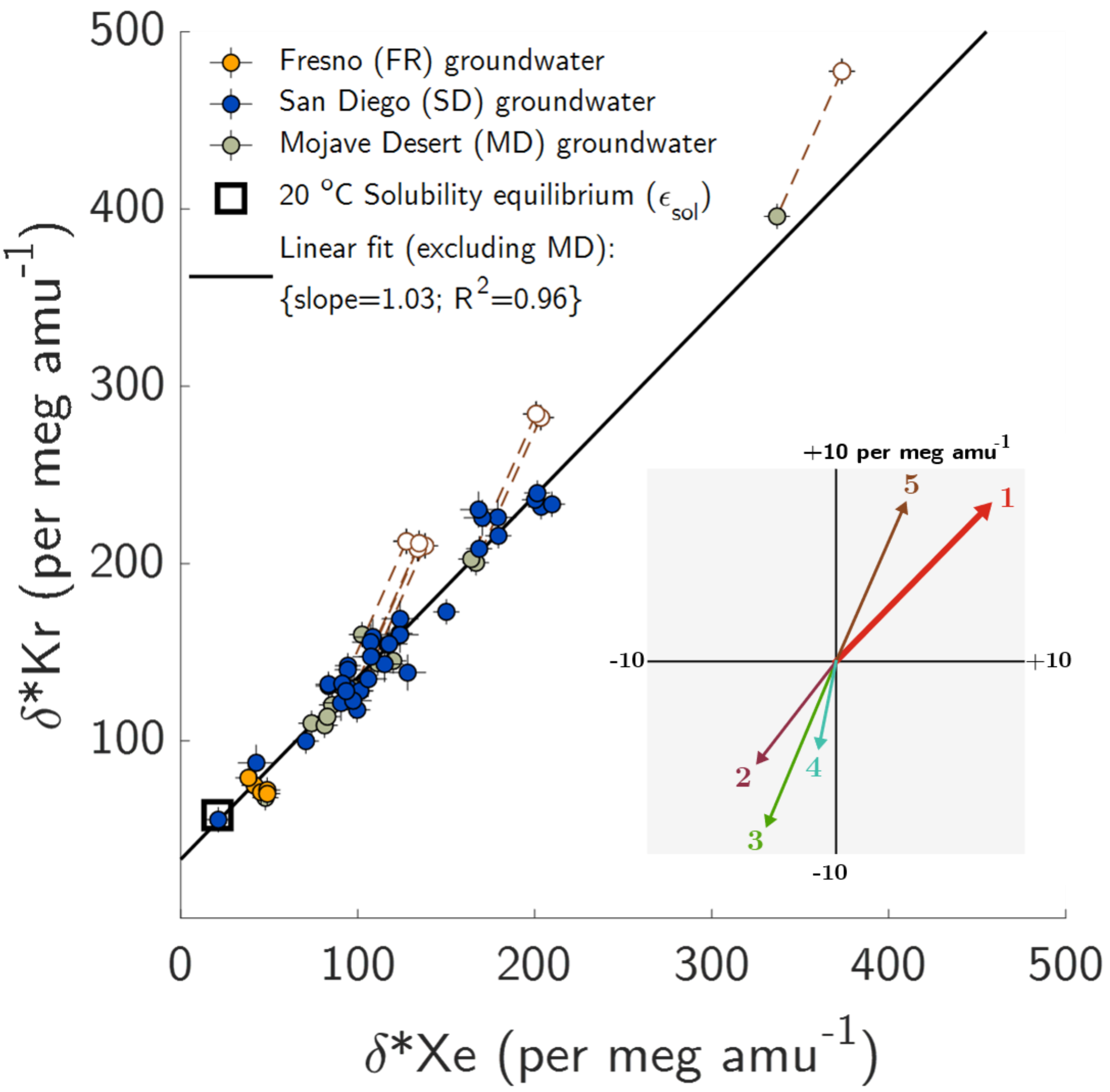

Figure 4.2. Dissolved Kr and Xe isotope ratios in 58 groundwater samples collected from 36 wells illustrate the dominance of gravitational settling in driving isotopic departures from solubility equilibrium. MD samples for which δ*Kr exceeds 200 per meg amu^{-1} are shown both as original values (open circles) and corrected for fractionation due to oxygen consumption (Supplemental Section 4.5). Error bars indicate ± 2-σ error. Inset: predicted fractionation associated with (1) two meters of gravitational settling; (2) thermal diffusion caused by a 2 ºC difference between the surface and water table; (3) a steady-state WT-to-atmosphere water-vapor flux driven by a 0.81% WT-atmosphere absolute humidity difference (equivalent to 20 ºC, 65% relative humidity surface air); (4) complete dissolution of unfractionated excess air (equivalent to 50% ΔNe); and (5) steady-state oxygen depletion leading to a 0.5% atmosphere-to-deep-UZ difference in the sum of O_2 and CO_2.

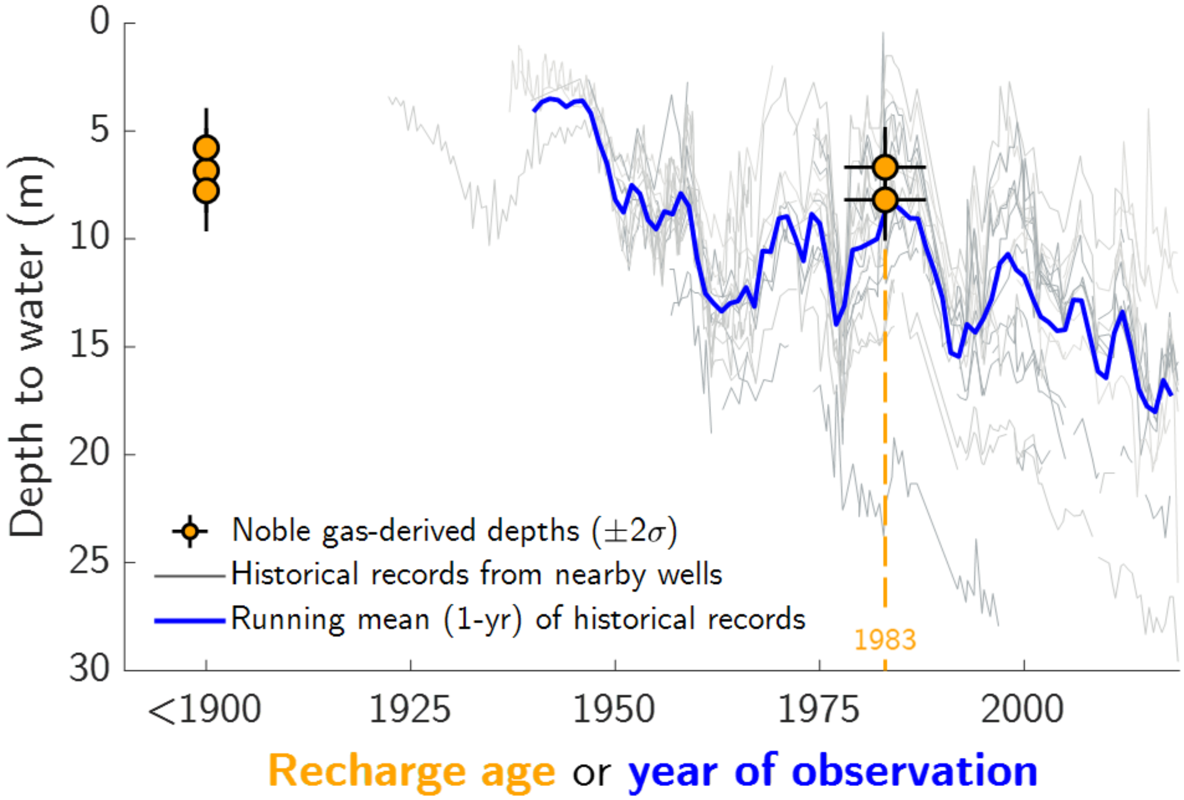

Figure 4.3. Comparison of noble gas isotope-derived WTDs to historical water-level observations near two adjacent wells sampled in March 2018 near Fresno, California. Depths are relative to the land surface. Historical records from within a 10-km radius of the sample site were included, except for those from the highly populated city center, which dropped substantially in the mid-20th century (Supplementary Figure 4.S4). Multiple age tracers were used to determine probable recharge ages (Supplementary Figure 4.S5).

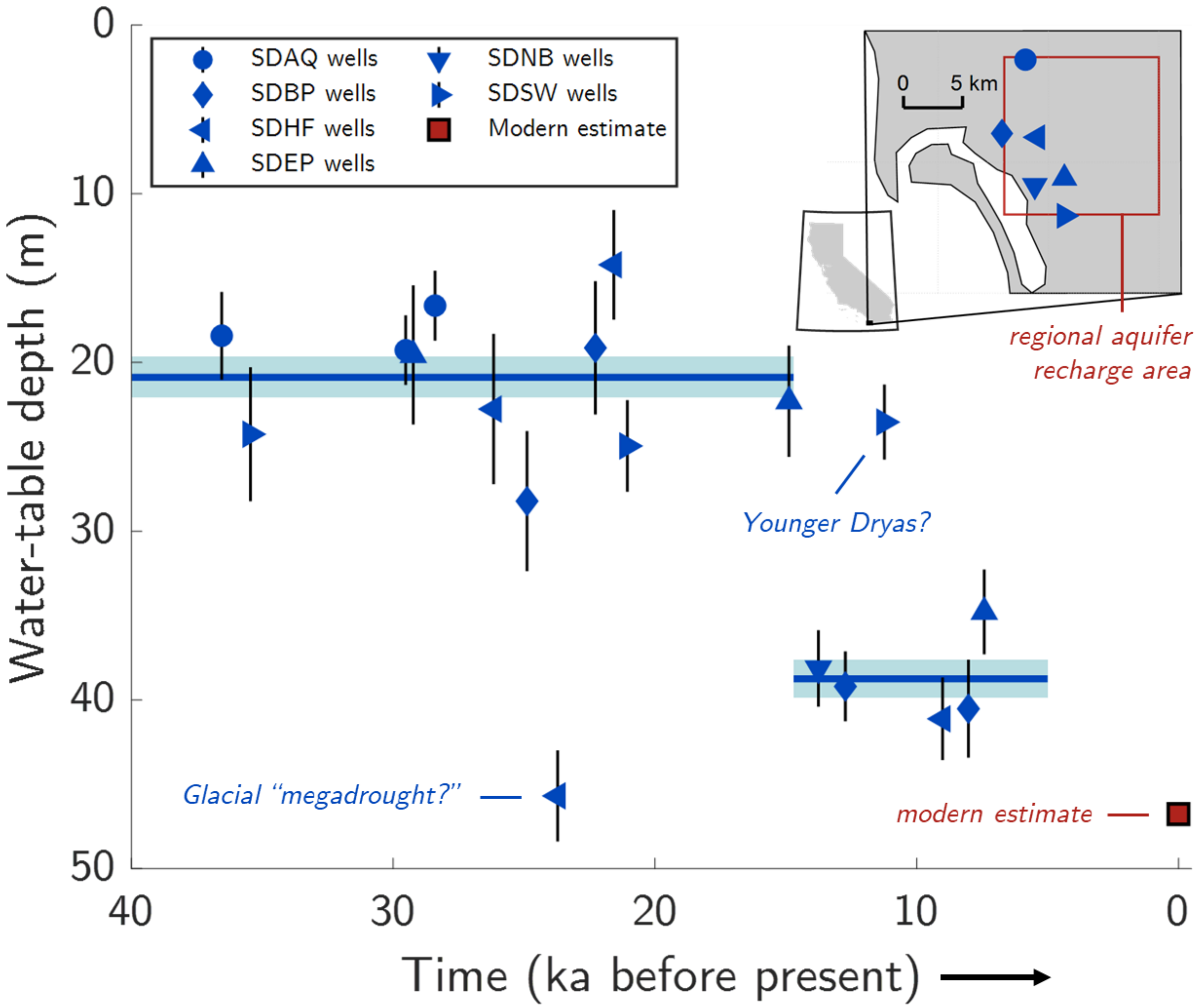

Figure 4.4. Time series of reconstructed WTD in the San Diego regional aquifer system, in meters below the land surface. Blue markers and error bars (±2σ) indicate replicate-mean WTD derived from samples collected from wells at multiple depths at six sites (indicated by marker shapes). Pre and post 15-ka mean WTDs (lines with ±2-SE shaded regions) exclude two extreme WTD observations that could be reflect a previously documented glacial dry period and wet Younger Dryas stadial. The present-day mean WTD over the assumed recharge area (inset) was estimated by a high-resolution, observation-constrained groundwater model (red square marker). Groundwater age uncertainties are roughly ±2 ka (Supplementary Section 4).

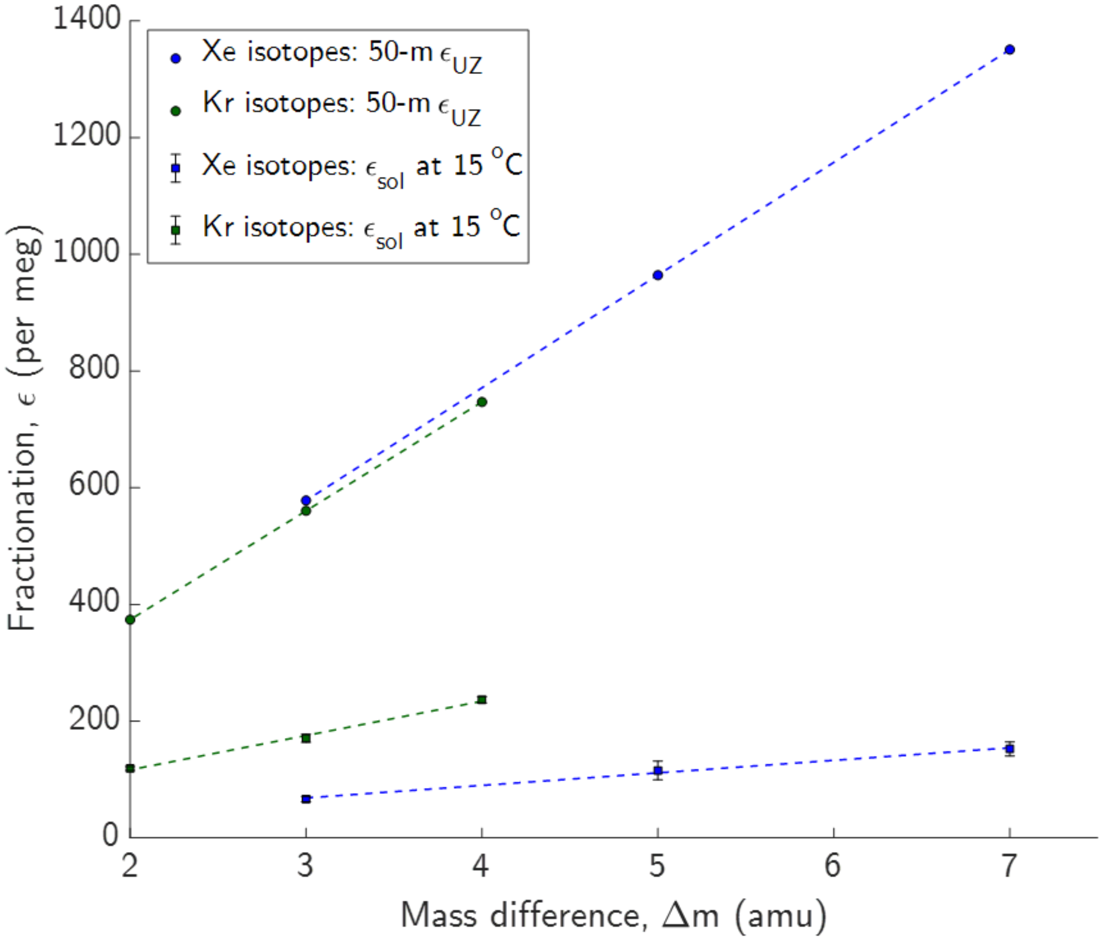

Figure 4.S1: Linear mass dependence of Xe and Kr isotope fractionation in steady-state soil air model (shown in Figure 4.1 for δ*Xe) and solubility fractionation at 15 ºC, for reference.

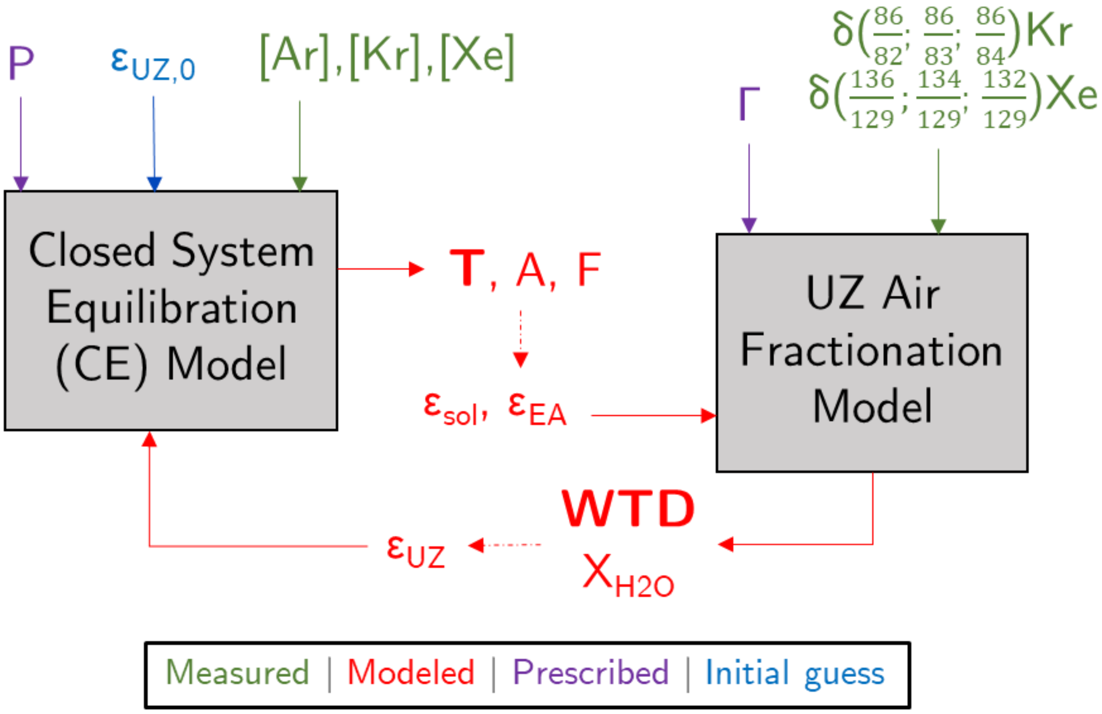

Figure 4.S2. Process diagram for iterative, coupled inverse modeling of surface temperature and WTD. The CE model is initially solved for T, A, and F based on the assumption of unfractionated WTD UZ air, constrained by measured concentrations and prescribed surface pressure. Using T, A, and F, ε_{sol} and ε_{EA} are determined for individual Kr and Xe isotope ratios. Then, measured Kr and Xe isotope ratios, prescribed Γ, and estimates of ε_{sol} and ε_{EA} are used to constrain the UZ air fractionation model to estimate WTD and X_{H2O}. In turn, ε_{UZ} for elemental ratios is determined (from WTD, Γ, and X_{H2O}), and the CE model is re-evaluated to produce updated estimates of T, A, and F. The soil air fractionation model is re-evaluated using updated ε_{sol} and ε_{EA} values. The iterative coupling of the two models proceeds until estimates of WTD and T converge to within 50 cm and 0.2 ^{o}C, respectively, for successive iterations. The entire process is repeated in 1000 Monte Carlo simulations, with random Gaussian error prescribed to each measured parameter in each simulation, to yield distributions of WTD and T from each groundwater sample. Finally, T is converted to MAST by subtracting Γ·WTD.

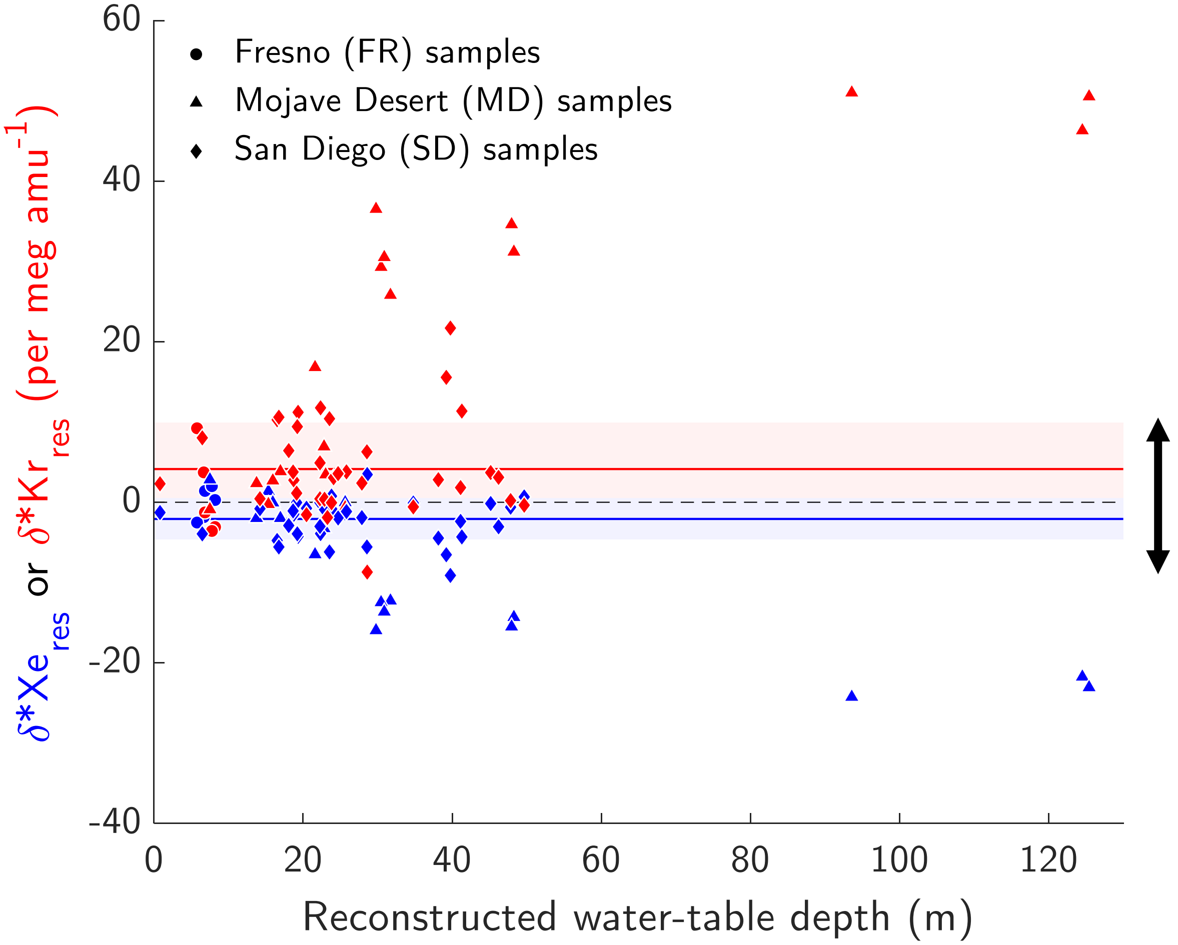

Figure 4.S3. Model-measurement Kr (red) and Xe (blue) isotopic residuals for each of the 58 samples analyzed in this study. Marker shapes indicate study area and solid lines indicate Fresno-and-San-Diego-only mean residuals. Shaded error regions indicate ±1-σ range of Fresno-and-San-Diego-only residuals. Arrows indicate ±2.5 meters of gravitational settling fractionation, for context.

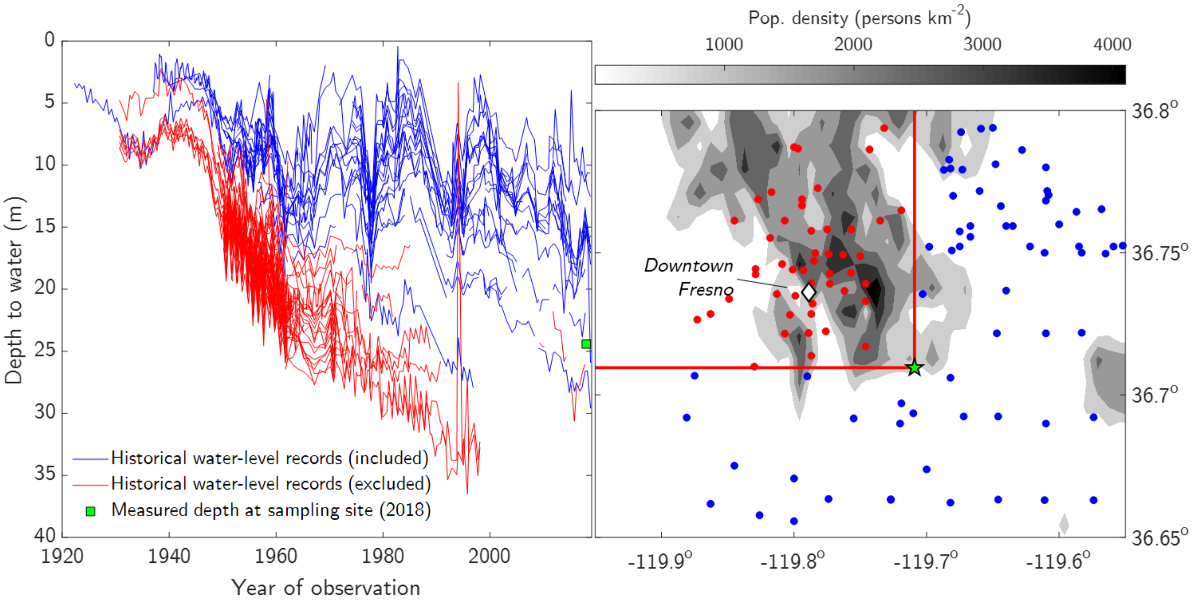

Figure 4.S4. Historical water-level records near Fresno, California, from the California Department of Water Resources Water Data Library. In the left panel, time series of observed water levels are shown for all sites within a 10 km radius of sampling location. Historical water-level observations to the northwest of sampling location are shown in red and excluded from the noble gas-based water table depth comparisons (Figure 3). As shown in the right panel, these excluded observations are primarily from the population-dense Fresno city center, which presumably experienced more substantial mid-20th century groundwater abstraction than did the less populated portions of Fresno county. Locations of historical observations are superimposed on a map of year-2000 population density (CIESIN, 2018), and the sampling location is marked by a green star in the center of the map.

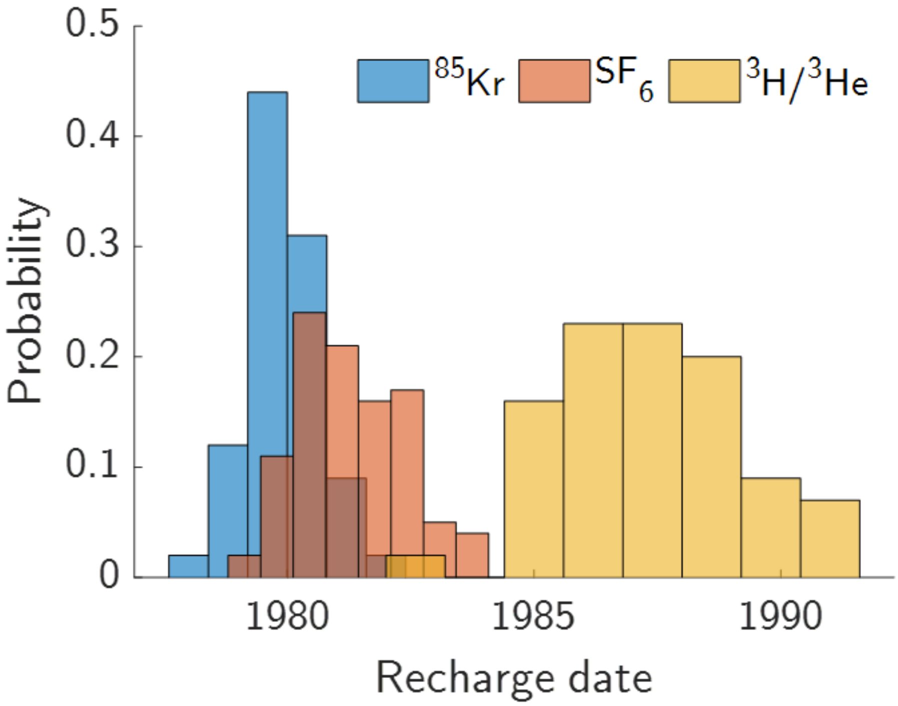

Figure 4.S5. Recharge date probability distributions for groundwater sampled from well 180-MW based on measured ^{85}Kr, SF$_6$, and ^{3}H/^{3}He ratios. In Figure 3, we assume a recharge date given by averaging the medians of each probability distribution. We assume this average recharge date, 1983, is accurate to within ± 5 years.

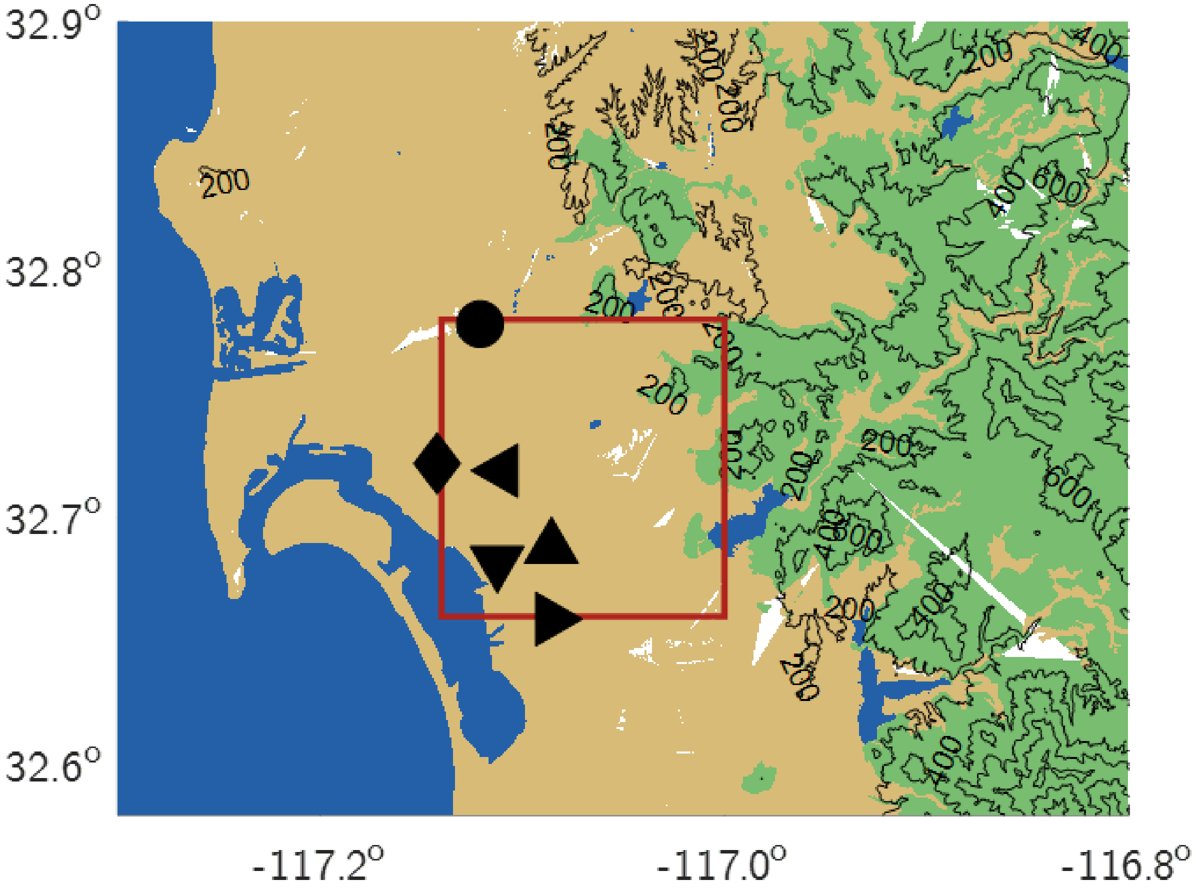

Figure 4.S6. San Diego study area. Six multiple-depth, monitoring-well sites are marked by black polygons. The assumed recharge area for deep, regional groundwater flow to these sites is indicated by the red box. Beige coloring indicates unconsolidated sediment, green indicates igneous or metamorphic rock, and blue indicates water. Elevation contours, spaced by 200 meters from sea level to 600 meters, are labeled in meters. These surficial geology and digital elevation models are available from the USGS (San Diego Hydrogeology project; https://ca.water.usgs.gov/projects/sandiego/).

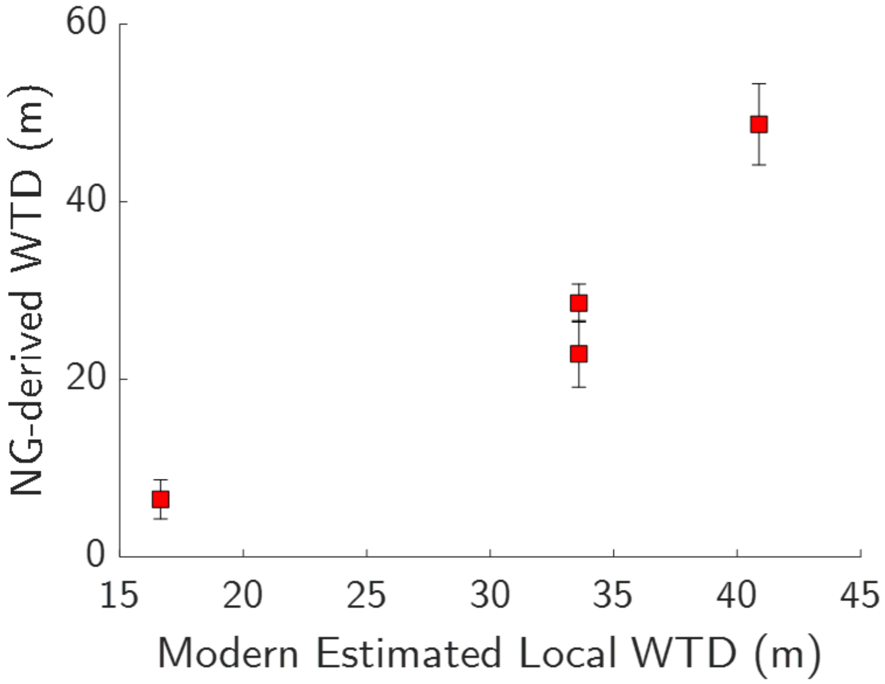

Figure 4.S7: Comparison of noble gas-derived WTDs to present-day estimated WTDs at the locally recharged groundwater sites. WTDs are estimated for a 1-km radius around each well by subtracting the measured water-table elevation at the time of recharge from the average surface elevation within a 1-km radius of the well. The large range of noble gas-derived WTDs among the contemporaneous mid-Holocene samples and the correlation with present-day local WTD is consistent with the assumption that this groundwater reflects a locally heterogeneous signal, not a regionally homogenous one.

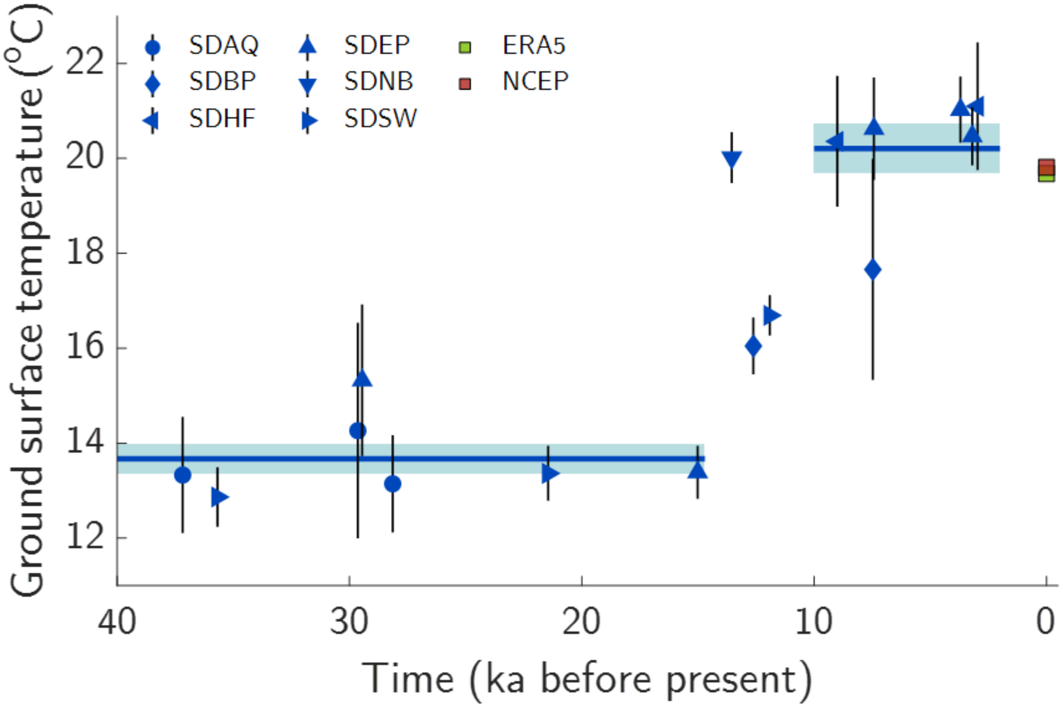

Figure 4.S8. Reconstructed San Diego surface temperatures since the last glacial period. Samples from well sites are identified by symbol (consistent with Figures 4.4 and 4.S6) and site name. ERA5 and NCEP reanalysis 1979-2018 mean surface soil temperatures are shown for comparison (square markers). Surface temperatures are found by subtracting the measured geothermal gradient at a well site multiplied by the reconstructed WTD.

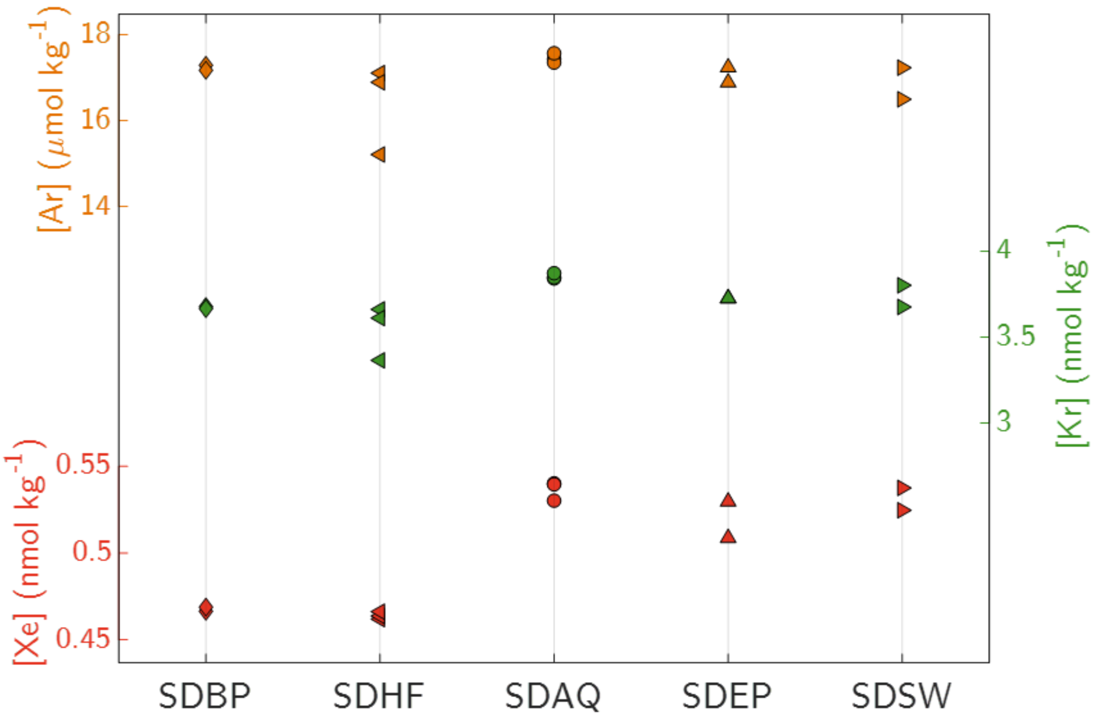

Figure 4.S9. Comparison of LLGP (15-40 ka recharge age) sample-mean Ar, Kr, and Xe concentrations across well sites. SDBP and SDHF samples have distinctly lower Xe concentrations and slightly lower Kr concentrations than other LLGP samples. We hypothesize that either a geothermal heat source or highly adsorbing mineral along the shared flow path may explain these low concentrations, but both theoretical considerations and isotopic observations suggest that there is no associated isotopic fractionation of these samples.

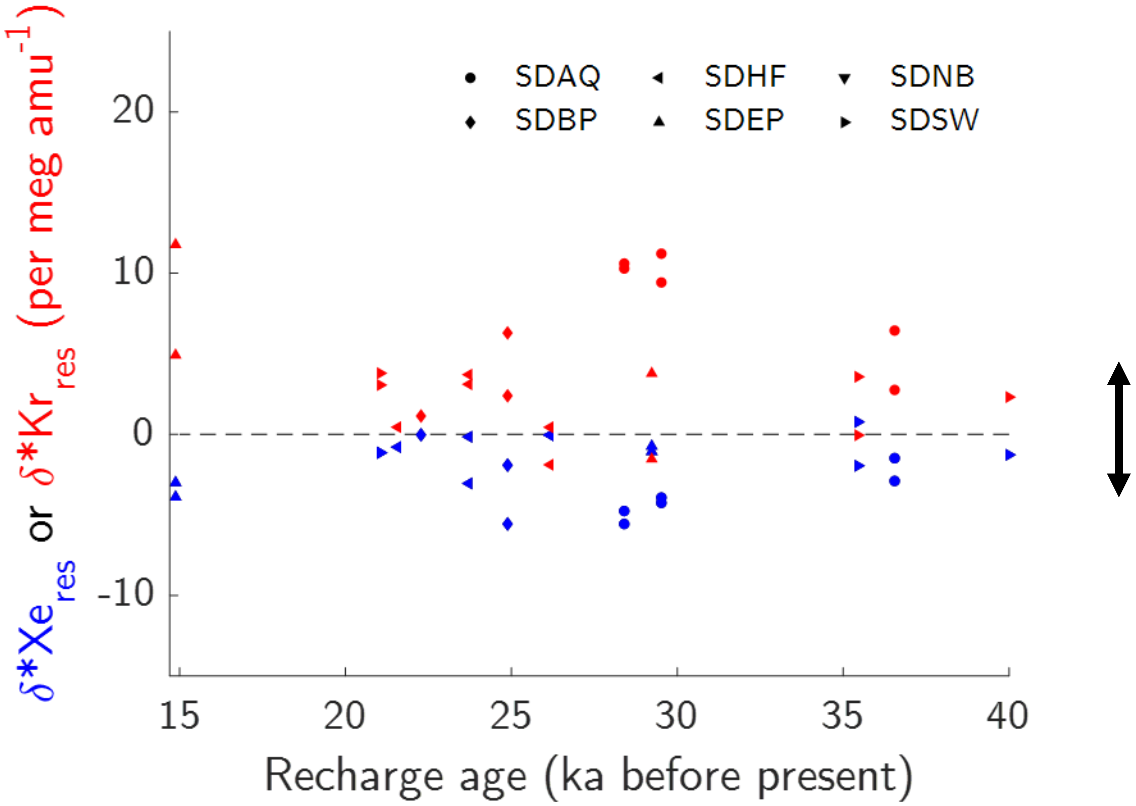

Figure 4.S10. Isotopic measurement-model residuals from inverse model fitting of LLGP groundwater samples. The Xe and Kr isotope residuals from SDBP and SDHF samples that display low Kr and Xe concentrations are not distinct from other LLGP samples, implying that the process responsible for the low Kr and Xe did not cause isotopic fractionation. Arrows indicate equivalent range to ±1-m of gravitational settling fractionation.

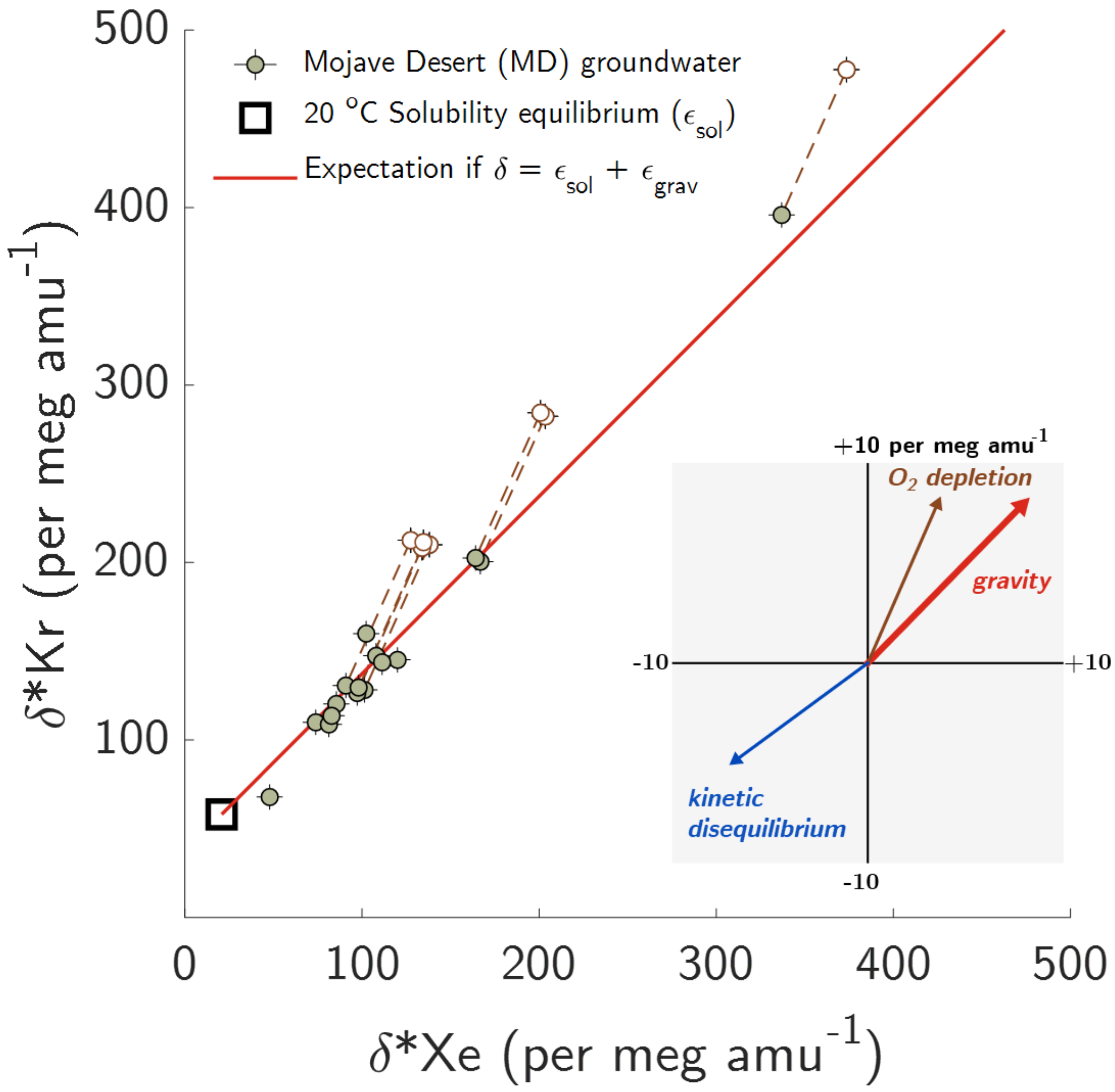

Figure 4.S11. Mojave Desert δ*Kr and δ*Xe (reproduced from Fig. 2) compared to the expectation that isotopic fractionation is governed solely by solubility fractionation and gravitational settling in UZ air prior to dissolution. A possible correction is shown for 5% oxygen depletion ($\Delta X_{O2} = -0.05$), brining several uncorrected values (open circles) in closer agreement with the expected trendline. Shown in the inset are Kr and Xe isotopic fractionation associated with (a) 2 m of gravitational settling, (b) 0.5% O_2 depletion ($\Delta X_{O2} = -0.005$), and (c) kinetic disequilibrium due to barometric pumping (-5 per meg amu^{-1} for δ*Kr).

Table 4.S1. Isotope ratios measured in this study and associated uncertainty metrics. Heavy and light isotope masses (mh and ml) are given in amu; uncertainty metrics are given in per meg.

Ratio	m_h	m_l	$\sigma_{pld,A}$	$\sigma_{pld,B}$	SE_{atm}	SE_{ext}	SE_{CS}
$\delta^{40}/_{36}$Ar	40	36	19	19	3	5	n/a
$\delta^{38}/_{36}$Ar	38	36	21	12	5	8	n/a
$\delta^{86}/_{82}$Kr	86	82	17	24	10	4	1
$\delta^{86}/_{83}$Kr	86	83	15	27	7	5	1
$\delta^{86}/_{84}$Kr	86	84	12	23	4	11	5
$\delta^{136}/_{129}$Xe	136	129	31	46	17	9	2
$\delta^{134}/_{129}$Xe	134	129	28	52	18	9	3
$\delta^{132}/_{129}$Xe	132	129	19	28	10	6	1

References

Aeschbach-Hertig, W., Peeters, F., Beyerle, U., & Kipfer, R. (2000). Palaeotemperature reconstruction from noble gases in ground water taking into account equilibration with entrapped air. Nature, 405(6790), 1040–4. https://doi.org/10.1038/35016542

Aeschbach-Hertig, W., El-Gamal, H., Wieser, M., & Palcsu, L. (2008). Modeling excess air and degassing in groundwater by equilibrium partitioning with a gas phase. Water Resources Research, 44(8). https://doi.org/10.1029/2007WR006454

Anders, R., Mendez, G. O., Futa, K., & Danskin, W. R. (2014). A Geochemical Approach to Determine Sources and Movement of Saline Groundwater in a Coastal Aquifer. Groundwater, 52(5), 756–768. https://doi.org/10.1111/gwat.12108

Barry, P. H., Kulongoski, J. T., Landon, M. K., Tyne, R. L., Gillespie, J. M., Stephens, M. J., et al. (2018). Tracing enhanced oil recovery signatures in casing gases from the Lost Hills oil field using noble gases. Earth and Planetary Science Letters, 496, 57–67. https://doi.org/10.1016/j.epsl.2018.05.028

Bernatowicz, T. J., & Podosek, F. A. (1986). Adsorption and isotopic fractionation of Xe. Geochimica et Cosmochimica Acta, 50(7), 1503–1507. https://doi.org/10.1016/0016-7037(86)90324-8

Bethke, C. M., & Johnson, T. M. (2008). Groundwater Age and Groundwater Age Dating. Annual Review of Earth and Planetary Sciences, 36(1), 121–152. https://doi.org/10.1146/annurev.earth.36.031207.124210

Birner, B., Buizert, C., Wagner, T. J. W., & Severinghaus, J. P. (2018). The influence of layering and barometric pumping on firn air transport in a 2-D model. The Cryosphere, 12. https://doi.org/10.5194/tc-12-2021-2018

Bollhöfer, A., Schlosser, C., Schmid, S., Konrad, M., Purtschert, R., & Krais, R. (2019). Half a century of Krypton-85 activity concentration measured in air over Central Europe: Trends and relevance for dating young groundwater. Journal of Environmental Radioactivity, 205–206, 7–16. https://doi.org/10.1016/J.JENVRAD.2019.04.014

Bromwich, D. H., Toracinta, E. R., Wei, H., Oglesby, R. J., Fastook, J. L., Hughes, T. J., et al. (2004). Polar MM5 Simulations of the Winter Climate of the Laurentide Ice Sheet at the LGM*. Journal of Climate, 17(17), 3415–3433. https://doi.org/10.1175/1520

Bullister, J. L., Wisegarver, D. P., & Menzia, F. A. (2002). The solubility of sulfur hexafluoride in water and seawater. Deep Sea Research Part I: Oceanographic Research Papers, 49(1), 175–187. https://doi.org/10.1016/S0967-0637(01)00051-6

COESA. (1976). U.S. Standard Atmosphere. Washington, D.C.

COHMAP members. (1988). Climatic changes of the last 18,000 years: observations and model simulations. Science, 241(4869), 1043–1052. https://doi.org/10.1126/science.241.4869.1043

Craig, H., Horibe, Y., & Sowers, T. (1988). Gravitational separation of gases and isotopes in polar ice caps. Science, 242(4886), 1675–8. https://doi.org/10.1126/science.242.4886.1675

Fan, Y., Li, H., & Miguez-Macho, G. (2013). Global Patterns of Groundwater Table Depth. Science, 339(6122), 940–943. https://doi.org/10.1126/science.1229881

Feakins, S. J., Wu, M. S., Ponton, C., & Tierney, J. E. (2019). Biomarkers reveal abrupt switches in hydroclimate during the last glacial in southern California. Earth and Planetary Science Letters, 515, 164–172. https://doi.org/10.1016/J.EPSL.2019.03.024

Freundt, F., Schneider, T., & Aeschbach-Hertig, W. (2013). Response of noble gas partial pressures in soil air to oxygen depletion. Chemical Geology, 339, 283–290. https://doi.org/10.1016/j.chemgeo.2012.07.026

Fuller, E. N., Schettler, P. D., & Giddings, J. C. (1966). A new method for prediction of binary gas-phase diffusion coefficients. Industrial and Engineering Chemistry, 16(10), 551. https://doi.org/10.1016/0042-207X(66)90400-3

Grachev, A. M., & Severinghaus, J. P. (2003). Determining the thermal diffusion factor for 40Ar/36Ar in air to aid paleoreconstruction of abrupt climate change. Journal of Physical Chemistry A, 107(23), 4636–4642. https://doi.org/10.1021/jp027817u

Grew, K. E., & Ibbs, T. L. (1953). Thermal diffusion in gases. Quarterly Journal of the Royal Meteorological Society, 79(341), 458–458. https://doi.org/10.1002/qj.49707934127

Hall, C. M., Castro, M. C., Lohmann, K. C., & Ma, L. (2005). Noble gases and stable isotopes in a shallow aquifer in southern Michigan: Implications for noble gas paleotemperature reconstructions for cool climates. Geophysical Research Letters, 32(18), n/a-n/a. https://doi.org/10.1029/2005GL023582

Hall, C. M., Castro, M. C., Lohmann, K. C., & Sun, T. (2012). Testing the noble gas paleothermometer with a yearlong study of groundwater noble gases in an instrumented monitoring well. Water Resources Research, 48(4). https://doi.org/10.1029/2011WR010951

Hamme, R. C., & Emerson, S. R. (2004). Measurement of dissolved neon by isotope dilution using a quadrupole mass spectrometer. Marine Chemistry, 91(1–4), 53–64. https://doi.org/10.1016/j.marchem.2004.05.001

Heaton, T. H. E., & Vogel, J. C. (1981). “Excess air” in groundwater. Journal of Hydrology. https://doi.org/10.1016/0022-1694(81)90070-6

Heusser, L. E., Kirby, M. E., & Nichols, J. E. (2015). Pollen-based evidence of extreme drought during the last Glacial (32.6-9.0 ka) in coastal southern California. Quaternary Science Reviews, 126, 242–253. https://doi.org/10.1016/j.quascirev.2015.08.029

Ingram, R. G. S., Hiscock, K. M., & Dennis, P. F. (2007). Noble gas excess air applied to distinguish groundwater recharge conditions. Environmental Science & Technology, 41(6), 1949–55. Retrieved from http://www.ncbi.nlm.nih.gov/pubmed/17410789

Jasechko, S., Lechler, A., Pausata, F. S. R., Fawcett, P. J., Gleeson, T., Cendón, D. I., et al. (2015). Late-glacial to late-Holocene shifts in global precipitation d18O. Climate of the Past, 11(10), 1375–1393. https://doi.org/10.5194/cp-11-1375-2015

Jenkins, W. J., Lott, D. E., & Cahill, K. L. (2019). A determination of atmospheric helium, neon, argon, krypton, and xenon solubility concentrations in water and seawater. Marine Chemistry, 211, 94–107. https://doi.org/10.1016/J.MARCHEM.2019.03.007

Kawamura, K., Severinghaus, J. P., Albert, M. R., Courville, Z. R., Fahnestock, M. A., Scambos, T., et al. (2013). Kinetic fractionation of gases by deep air convection in polar firn. Atmospheric Chemistry and Physics, 13(21), 11141–11155. https://doi.org/10.5194/acp-13-11141-2013

Solomon, D., Cook, P. G., & Sanford, W. E. (1998). Dissolved Gases in Subsurface Hydrology. Isotope Tracers in Catchment Hydrology, 291–318. https://doi.org/10.1016/B978-0-444-81546-0.50016-1

Kirby, M. E., Heusser, L., Scholz, C., Ramezan, R., Anderson, M. A., Markle, B., et al. (2018). A late Wisconsin (32–10k cal a BP) history of pluvials, droughts and vegetation in the Pacific south-west United States (Lake Elsinore, CA). Journal of Quaternary Science, 33(2), 238–254. https://doi.org/10.1002/jqs.3018

Kulongoski, J. T., Hilton, D. R., Izbicki, J. A., & Belitz, K. (2009). Evidence for prolonged El Nino-like conditions in the Pacific during the Late Pleistocene: a 43ka noble gas record from California groundwaters. Quaternary Science Reviews, 28(23–24), 2465–2473. https://doi.org/10.1016/j.quascirev.2009.05.008

Lora, J. M., Mitchell, J. L., & Tripati, A. E. (2016). Abrupt reorganization of North Pacific and western North American climate during the last deglaciation. Geophysical Research Letters, 43(22), 11,796-11,804. https://doi.org/10.1002/2016GL071244

Manning, A. H., & Solomon, D. K. (2003). Using noble gases to investigate mountain-front recharge. Journal of Hydrology, 275(3–4), 194–207. https://doi.org/10.1016/S0022-1694(03)00043-X

Marrocchi, Y., & Marty, B. (2013). Experimental determination of the xenon isotopic fractionation during adsorption. Geophysical Research Letters, 40(16), 4165–4170. https://doi.org/10.1002/grl.50845

Oster, J. L., Ibarra, D. E., Winnick, M. J., & Maher, K. (2015). Steering of westerly storms over western North America at the Last Glacial Maximum. Nature Geoscience, 8(3), 201–205. https://doi.org/10.1038/ngeo2365

Pearson, F. J. J., & Hanshaw, B. B. (1970). Sources of Dissolved Carbonate Species in Groundwater and their Effects on Carbon-14 Dating. In Isotopes in Hydrology 1970 (pp. 271–285). Vienna: International Atomic Energy Agency. Retrieved from http://www.iaea.org/inis/collection/NCLCollectionStore/_Public/45/025/45025950.pdf

Peltier, W. R., Argus, D. F., & Drummond, R. (2015). Space geodesy constrains ice age terminal deglaciation: The global ICE-6G_C (VM5a) model. Journal of Geophysical Research: Solid Earth, 120(1), 450–487. https://doi.org/10.1002/2014JB011176

Petrenko, V. V., Severinghaus, J. P., Brook, E. J., Reeh, N., & Schaefer, H. (2006). Gas records from the West Greenland ice margin covering the Last Glacial Termination: a horizontal ice core. Quaternary Science Reviews, 25(9–10), 865–875. https://doi.org/10.1016/j.quascirev.2005.09.005

Pigati, J. S., Bright, J. E., Shanahan, T. M., & Mahan, S. A. (2009). Late Pleistocene paleohydrology near the boundary of the Sonoran and Chihuahuan Deserts, southeastern

Arizona, USA. Quaternary Science Reviews, 28(3–4), 286–300. https://doi.org/10.1016/J.QUASCIREV.2008.09.022

Podosek, F. A., Bernatowicz, T. J., & Kramer, F. E. (1981). Adsorption of xenon and krypton on shales. Geochimica et Cosmochimica Acta, 45(12), 2401–2415. https://doi.org/10.1016/0016-7037(81)90094-6

Reimer, P. J., Bard, E., Bayliss, A., Beck, J. W., Blackwell, P. G., Ramsey, C. B., et al. (2013). IntCal13 and Marine13 Radiocarbon Age Calibration Curves 0–50,000 Years cal BP. Radiocarbon, 55(4), 1869–1887. https://doi.org/10.2458/azu_js_rc.55.16947

Saraceno, J., Kulongoski, J. T., & Mathany, T. M. (2018). A novel high-frequency groundwater quality monitoring system. https://doi.org/10.1007/s10661-018-6853-6

Schlosser, P., Stute, M., Dörr, H., Sonntag, C., & Münnich, K. O. (1988). Tritium/3He dating of shallow groundwater. Earth and Planetary Science Letters, 89(3–4), 353–362. https://doi.org/10.1016/0012-821X(88)90122-7

Schlosser, P., Stute, M., Sonntag, C., & Otto Münnich, K. (1989). Tritiogenic 3He in shallow groundwater. Earth and Planetary Science Letters, 94(3–4), 245–256. https://doi.org/10.1016/0012-821X(89)90144-1

Schwander, J. (1989). The transformation of snow to ice and the occlusion of gases. In H. Oeschger & C. C. Langway (Eds.), The Environmental Record in Glaciers and Ice Sheets (pp. 53–67). New York: Wiley.

Seltzer, A. M., Severinghaus, J. P., Andraski, B. J., & Stonestrom, D. A. (2017). Steady state fractionation of heavy noble gas isotopes in a deep unsaturated zone. Water Resources Research, 53(4), 2716–2732. https://doi.org/10.1002/2016WR019655

Seltzer, A. M., Ng, J., & Severinghaus, J. P. (2019). Precise determination of Ar, Kr and Xe isotopic fractionation due to diffusion and dissolution in fresh water. Earth and Planetary Science Letters, 514, 156–165. https://doi.org/10.1016/J.EPSL.2019.03.008

Severinghaus, J. P., Bender, M. L., Keeling, R. F., & Broecker, W. S. (1996). Fractionation of soil gases by diffusion of water vapor, gravitational settling, and thermal diffusion. Geochimica et Cosmochimica Acta, 60(6), 1005–1018. https://doi.org/10.1016/0016-7037(96)00011-7

Severinghaus, J. P., Grachev, A., Luz, B., & Caillon, N. (2003). A method for precise measurement of argon 40/36 and krypton/argon ratios in trapped air in polar ice with applications to past firn thickness and abrupt climate change in Greenland and at Siple Dome, Antarctica. Geochimica et Cosmochimica Acta, 67(3), 325–343. https://doi.org/10.1016/S0016-7037(02)00965-1

Sowers, T., Bender, M., Raynaud, D., & Korotkevich, Y. S. (1992). δ 15 N of N 2 in air trapped in polar ice: A tracer of gas transport in the firn and a possible constraint on ice age-gas age differences. Journal of Geophysical Research, 97(D14), 15683. https://doi.org/10.1029/92JD01297

Stute, M., & Schlosser, P. (1993). Principles and Applications of the Noble Gas Paleothermometer. In P. K. Savin, S. K. C., L. J., & M. S. (Eds.), Climate Change in Continental Isotopic Records, Volume 78 (pp. 89–100). American Geophysical Union (AGU). https://doi.org/10.1029/gm078p0089

Stute, M., Forster, M., Frischkorn, H., Serejo, A., Clark, J. F., Schlosser, P., et al. (1995). Cooling of Tropical Brazil (5C) During the Last Glacial Maximum. Science, 269(5222), 379–383. https://doi.org/10.1126/science.269.5222.379

University, C. for I. E. S. I. N.-C.-C. (2018). Gridded Population of the World, Version 4 (GPWv4): Population Density, Revision 11. Palisades, NY: NASA Socioeconomic Data and Applications Center (SEDAC). Retrieved from https://doi.org/10.7927/H49C6VHW

Yang, J., Lewis, R. S., & Anders, E. (2003). Sorption of noble gases by solids, with reference to meteorites. I. Magnetite and carbon. Geochimica et Cosmochimica Acta, 46(6), 841–860. https://doi.org/10.1016/0016-7037(82)90042-4

Chapter 5

Heavy noble gas isotopes as new constraints on the ventilation of the deep ocean

Abstract

Past studies of noble gas concentrations in the deep ocean have revealed widespread, several percent undersaturation of Ar, Kr, and Xe. However, the physical explanation for these disequilibria remains unclear. To gain insight into undersaturation set by deep-water formation, we measured heavy noble gas isotope and elemental ratios from the deep North Pacific using a new analytical technique. To our knowledge, these are the first high-precision seawater profiles of ^{38}Ar/^{36}Ar and Kr and Xe isotope ratios. To interpret isotopic disequilibria, we carried out a suite of laboratory experiments to measure solubility fractionation factors in seawater. In the deep North Pacific, we find undersaturation of heavy-to-light Ar and Kr isotope ratios, suggesting an important role for rapid cooling-driven, diffusive air-to-sea gas transport in setting the deep-ocean undersaturation of heavy noble gases. These isotope ratios represent promising new constraints for quantifying physical air-sea gas exchange processes, complementing noble gas concentration measurements.

5.1. Introduction

Due to their chemical and biological inertness, dissolved noble gases in seawater are useful tools for disentangling physical from biogeochemical processes (Hamme et al., 2017; Stanley & Jenkins, 2013). Among other applications, noble gases have been used to constrain bubble injection (e.g. Emerson & Bushinsky, 2016; Stanley et al., 2009), diapycnal mixing rates (e.g. Ito et al., 2007), oxygen production (e.g. Spitzer & Jenkins, 1989), nutrient fluxes (e.g. Stanley et al., 2015), and the strength of the carbon solubility pump (Hamme et al., 2019; Nicholson et al., 2010). In the deep ocean, solubility disequilibria of noble gas concentrations display a globally consistent pattern (Hamme & Severinghaus, 2007; Jenkins et al., 2016; Loose et al., 2016): supersaturation of light, less soluble noble gases (He and Ne) and undersaturation of heavy, more soluble noble gases (Ar, Kr, and Xe). Deep-ocean Ne supersaturation is well understood to result from bubble injection during surface air-sea gas exchange or subsurface melting of glacial ice (Hamme & Emerson, 2002; Loose & Jenkins, 2014). However, the cause of heavy noble gas undersaturation in the deep ocean remains less clear.

Two distinct physical explanations have been proposed, each of which concerns the strong temperature dependences of heavy noble gas solubilities. The first theory suggests that disequilibrium arises from incomplete air-to-sea transport of heavy noble gases during deep-water formation (Hamme et al., 2017; Hamme & Severinghaus, 2007; Nicholson et al., 2010). In this hypothesis, rapid wintertime cooling of the mixed layer increases gas solubilities, driving diffusive uptake by surface waters until they subduct, at which point gas exchange ceases and the signal of undersaturation is transported to the deep ocean. The second theory suggests that disequilibrium is caused by subsurface melting of glacial ice (Loose et al., 2016; Loose & Jenkins, 2014). In this hypothesis, the latent heat required for ice shelf melting is supplied by seawater, which cools and inherits gas from air bubbles liberated from melted ice, which completely dissolve under hydrostatic pressure. Undersaturation of Ar, Kr, and Xe therefore emerges because increases in solubility due to latent cooling are not fully compensated by the addition of gas from ice bubbles.

Here we explore the potential for isotope ratios of Ar, Kr, and Xe to provide constraints on mechanisms of deep-ocean heavy noble gas disequilibrium. While $^{40}Ar/^{36}Ar$ ratios in seawater have been measured once before at <1‰ precision (Nicholson et al., 2010), recent analytical developments have enabled high-precision measurement of dissolved $^{38}Ar/^{36}Ar$ and stable Kr and Xe isotope ratios in water (Seltzer et al., 2019). Ar, Kr, and Xe isotope ratios exhibit a range of sensitivities to bubble injection, cooling, and diffusive gas uptake as a result of their different solubility and kinetic fractionation factors (Seltzer et al., 2019). In this study, we analyzed Ar, Kr, and Xe isotope ratios at high precision in a small set of seawater samples collected from the deep North Pacific. We interpret our observations using a framework for isotopic fractionation that extends existing idealized models of bulk gas disequilibrium. This framework is informed by recent determinations of isotopic fractionation factors in freshwater (Seltzer et al., 2019) as well as new measurements of seawater isotopic solubility fractionation presented in this study.

5.2. Methods

5.2.1 Laboratory determination of isotopic solubility fractionation in seawater

Solubility fractionation factors (α_{sol}) of Ar, Kr, and Xe isotope ratios in seawater were measured via closed-system laboratory equilibration experiments at Scripps Institution of Oceanography (SIO) in early 2019. α_{sol} is defined at a given temperature and salinity as:

$$\alpha_{sol} = \frac{(H/L)_{diss}}{(H/L)_{gas}} \tag{5.1}$$

for a heavy isotope (H) and light isotope (L) at solubility equilibrium between the dissolved phase and gas phase at 100% relative humidity. In each experiment, 200-400 mL of seawater from the SIO pier (sterilized by ultra-violet light and a series of 100 and 25 μm filter bags) was equilibrated with a ~2-L pure noble gas headspace at ~1 atm for 36 hours at a constant temperature between ~2 and 25 ºC following the closed system equilibration method of Seltzer et al. (2019). At the end of each experiment, a 2 mL headspace gas sample and 10-30 mL equilibrated seawater sample were collected. Dissolved gases from the seawater sample were quantitatively extracted by magnetic stirring under vacuum, and dissolved gas and headspace samples were each gettered using SAES Zr-Al sheets and Ti sponge at 900 ºC for 1 hr. Isotope ratios in purified dissolved gas and headspace samples were analyzed on a Thermo-Finnigan MAT 253 mass spectrometer against a common reference gas. In total, 12 experiments were carried out: five each for Kr and Ar isotopes (at 34.6 ± 0.1 psu and 35.4 ± 0.1 psu, respectively), and two for Xe isotopes (at 36.8 ± 0.1 psu).

Figure 5.1 shows the results of these seawater solubility fractionation experiments as ε values (where $\varepsilon_{sol} \equiv \alpha_{sol} - 1$, in per mil) alongside freshwater data (Seltzer et al., 2019). For Ar, Kr, and Xe at a given temperature, we find greater relative enrichment of heavy-to-light isotopes dissolved in seawater than in freshwater. This finding is consistent with ^{4}He/^{3}He solubility fractionation, which is also greater in seawater than in freshwater (Benson & Krause, 1980). In our experiments, the salinity effect on solubility fractionation is most pronounced for Ar isotopes and is insignificant for Kr and Xe isotopes. Surprisingly, the isotopic salinity effect does not appear to be strictly mass dependent, as the seawater-freshwater ε_{sol} difference for ^{38}Ar/^{36}Ar (two mass-unit difference) is similar in magnitude to that of ^{40}Ar/^{36}Ar (four mass-unit difference). The standard errors of seawater ε_{sol} values for the isotope ratios considered in this study range from ±4 per meg for ^{40}Ar/^{36}Ar to ±7 per meg for ^{86}Kr/^{82}Kr (1 per meg = 0.001 ‰).

5.2.2. Seawater sample collection and analysis

Seawater samples were collected from 10-L Niskin bottles on Hawaii Ocean Time-series (HOT) cruise 303 in June 2018. In total, 13 samples were collected at Station ALOHA (22.75 °N 158 °W) ranging from 250 m to 4.7 km depth. A mixed layer sample was collected from Station Kahe (21.34 °N 158.27 °W) at 6 m depth. Seawater was collected in pre-evacuated 2-L glass flasks following procedures described by Seltzer et al. (2019), based on a method for smaller dissolved gas samples (Hamme & Emerson, 2004a).

At SIO, dissolved gases were quantitatively extracted by sparging with ultra-high purity helium gas in a recirculating loop, trapping all non-helium gases in a stainless-steel diptube immersed in liquid helium (Seltzer et al., 2019). Extracted gases were then purified by gettering with SAES Zr-Al sheets at 900 °C for 130 minutes. For all samples collected below 500 m, stable isotope and elemental ratios of Ar, Kr, and Xe were analyzed on a Thermo-Finnigan MAT 253. Due to insufficient gas content, only Ar isotopes and elemental ratios were measured in the shallowest two samples at 6 m and 250 m, which were 26.8 and 14.5 °C, respectively. Prior to mass spectrometry, dissolved Ar concentrations were measured by manometry.

To interpret HOT 303 measurements, we report dissolved gas ratios and concentrations relative to solubility equilibrium at 1 atm and 100% relative humidity using the newly determined noble gas solubility functions from Jenkins et al. (2019) and the isotopic solubility fractionation factors in seawater determined in this study. These solubility anomalies are defined for gas concentrations, ΔC, and ratios, $\Delta\delta$, as follows:

$$\Delta C \equiv \frac{C}{C_{eq}(S,\theta)} - 1 \tag{5.2}$$

$$\Delta\delta \equiv \frac{R/R_{atm}}{\alpha_{sol}(S,T)} - 1 \tag{5.3}$$

where C is a measured dissolved gas concentration (μmol kg^{-1}), C_{eq} is a concentration at solubility equilibrium at potential temperature θ (°C) and salinity S (psu) assuming equilibration with unfractionated atmospheric air at 1 atm pressure and 100% relative humidity. In Equation 3, R is a gas or isotope ratio and R_{atm} is that ratio in the well-mixed atmosphere.

In this study, measured gas ratios are reported either as (a) δ values referenced to atmospheric air, or (b) solubility anomalies, Δδ. For each of these variables, we account for uncertainties based on measurement reproducibility, error in systematic mass spectrometry and extraction system corrections, error in atmospheric reference gas analysis, and uncertainty in α_{sol} (which only affects Δδ). Details are provided in Supplementary Section 5.S1.

5.3. Observations from the deep North Pacific (HOT 303, June 2018)

Figure 5.2 shows measured depth profiles of HOT-303 Ar, Kr, and Xe isotope ratios beside solubility equilibrium values. Across eight samples collected from the deep ocean (defined hereafter as below 2000 m), we observe mean $\delta^{40}/_{36}$Ar, $\delta^{38}/_{36}$Ar, $\delta^{86}/_{82}$Kr, and $\delta^{136}/_{129}$Xe of 1.065 ± 0.013‰, 0.582 ± 0.013‰, 0.220 ± 0.009‰, and 0.177 ± 0.003‰ (±1σ). Replicate 2-L samples were collected at ~1000, 2800, 4000, and 4700 m, and single samples were collected at all other depths. Both $\delta^{40}/_{36}$Ar and $\delta^{38}/_{36}$Ar increase from the surface to deep ocean, and Kr and Xe isotope ratios are relatively constant with depth from ~600 to 4700 m.

Solubility anomalies of measured isotope and gas ratios, Δδ and ΔKr/Ar, are shown in Figure 5.3 as a function of depth. In the deep ocean, we find that Ar and Kr isotope ratios fall significantly below solubility equilibrium (at the 95% confidence level). Mean $\Delta\delta^{40}/_{36}$Ar, $\Delta\delta^{38}/_{36}$Ar, $\Delta\delta^{86}/_{82}$Kr below 2000 m are -125 ± 10 per meg, -64 ± 13 per meg, -37 ± 15 per meg (± 1 SE), respectively. Deep-ocean mean $\Delta\delta^{136}/_{129}$Xe is -2 ± 25 per meg. While uncertainties prevent meaningful interpretation of this small value, we suggest that future gains in analytical precision and large-volume sampling campaigns could resolve Xe isotopic disequilibria at the single per meg level.

ΔKr/Ar determined in this study closely matches ΔKr/Ar measured from an August 2004 HOT cruise (HOT-162, Hamme & Severinghaus, 2007). In the deep ocean, mean HOT 303 and HOT-162 ΔKr/Ar are -6.6‰ and -6.2‰, respectively, relative to recently redetermined Kr and Ar solubilities in seawater (Jenkins et al., 2019). To our knowledge these are the first $\delta^{38}/_{36}$Ar, Kr, and Xe isotope ratios in seawater at <1‰ precision and the second $\delta^{40}/_{36}$Ar measurements. Nicholson et al. (2010) measured $\delta^{40}/_{36}$Ar in the Northwest Pacific and Eastern Tropical Atlantic and presented $\delta^{40}/_{36}$Ar data from HOT cruises in 2001, 2002, and 2003, finding mean values at ~4000 m of 1.206‰, 1.121‰, and 1.131‰, respectively. The deep-ocean mean $\delta^{40}/_{36}$Ar found in this study is ~55-65 per meg below the 2002 and 2003 HOT data. Nicholson et al. (2010) interpret isotopic disequilibria by comparing their measurements to a freshwater solubility fractionation experiment from 2002. Their freshwater solubility fractionation values are similarly higher than the freshwater $\delta^{40}/_{36}$Ar solubility function found in Seltzer et al. (2019) at 1 °C and 25 °C by ~40-50 per meg. Given these disagreements, we do not attempt to directly compare the implied $\Delta\delta^{40}/_{36}$Ar of Nicholson et al. (2010) with our finding. Instead, we simply note that their 2002 and 2003 HOT analyses yield the same sign and order of magnitude of $\Delta\delta^{40}/_{36}$Ar as our measurements.

In the surface ocean, we observe ΔKr/Ar near zero (~0.3‰) and negative $\Delta\delta^{40}/_{36}$Ar and $\Delta\delta^{38}/_{36}$Ar (-107 ± 20 per meg and -51 ± 20 per meg, respectively). The surface and intermediate ocean data will be discussed in a separate study. However, here we note that although $\Delta\delta^{40}/_{36}$Ar appears similar in the warm surface ocean and cold deep ocean, the physical mechanisms driving isotopic disequilibrium in the warm surface ocean are distinct from the deep ocean (Supplementary Section 5.S2).

5.4. Interpreting solubility disequilibria: a unified framework for dissolved gas concentrations (ΔC) and ratios (Δδ)

To gain insight into processes setting the observed isotopic disequilibria in the deep North Pacific, we have extended existing idealized equations for bulk gas disequilibria, ΔC, to gas ratios. Prior studies have proposed linear combinations of ΔC for individual disequilibrium mechanisms, each acting on initially air-saturated seawater at 100% relative humidity and 1 atm pressure. These processes include warming or cooling (Hamme et al., 2017; Hamme & Emerson, 2002; Hamme & Severinghaus, 2007), bubble injection (Emerson & Bushinsky, 2016; Liang et al., 2013; Nicholson et al., 2011; Stanley et al., 2009), submarine melting of glacial ice (Loose & Jenkins, 2014), diapycnal mixing (Ito et al., 2007; Ito & Deutsch, 2006; Spitzer & Jenkins, 1989), and other processes both for cases of no gas exchange (e.g. in the ocean interior or under sea ice) or diffusive air-sea gas exchange such that a quasi-steady state is reached at which ΔC is temporally constant. To extend equations for ΔC to Δδ, we make use of an alternate definition for Δδ for a ratio of gases or isotopes i and j:

$$\Delta\delta = \frac{C_i/C_{i,eq}}{C_j/C_{j,eq}} - 1 = \frac{\Delta C_i + 1}{\Delta C_j + 1} - 1 \qquad (5.4)$$

One key benefit of considering disequilibrium of ratios rather than concentrations is that ratios are unaffected by barometric pressure, which can be several percent below 1 atm in high-latitude regions of deep-water formation (Loose et al., 2016).

Figure 5.4 shows the influence of seven distinct processes on $\Delta\delta^{86}/_{82}$Kr, $\Delta\delta^{40}/_{36}$Ar, and on ΔKr/Ar, and ΔNe/Ar. (Note: in Supplementary Section 5.S3, we define ΔC for each process formally.) The disequilibria modeled in Figure 5.4 result from the following processes acting on an initially air-saturated 2-°C, 35-psu, 100-m mixed layer:

- cooling and warming of 2 °C without air-sea gas exchange
- constant cooling of 1.2 °C month^{-1} inducing a quasi-steady state diffusive air-to-gas flux to maintain constant ΔC under 10 m s^{-1} winds (with gas exchange parameterized by the Wanninkhof, 2014)
- the addition of 0.5% glacial meltwater by subsurface ice-shelf melting using parameters given in Loose et al. (2016) and assuming a 100-m firn thickness
- small bubble dissolution (0.025 mol$_{air}$ m^{-3}) without air-sea diffusive gas exchange
- steady-state small bubble dissolution (0.125 mol$_{air}$ m^{-2} day^{-1}) balanced by diffusive re-exchange with the atmosphere
- kinetic fractionation of atmospheric air ratios in the molecular boundary layer above the air-sea interface due to steady-state diffusion against the upward flux of water vapor.

The last process above, hereafter "water vapor flux fractionation," is a ternary fractionation that arises from differences in binary diffusivities of two gases or isotopes against water vapor (Severinghaus et al., 1996). Because a steady-state gradient exists between the mole fractions of water vapor at the air-sea interface (100% relative humidity) and in the turbulently mixed air above (~80% relative humidity), an inverse mole fraction gradient exists for all other dry air constituents, driving steady-state diffusion and inducing kinetic fractionation (Supplementary Figure 5.S2). Because this effect scales with saturation vapor pressure, it can be significant above warm water. For example, at 26.5 °C and 80% relative humidity it causes steady-state fractionation of -115 per meg and -60 per meg for $\delta^{40}/_{36}$Ar and $\delta^{38}/_{36}$Ar, respectively, close to our observations of -107 ± 20 per meg and -51 ± 20 per meg in the mixed layer at Station Kahe. In contrast, above cold water, water vapor flux fractionation is greatly reduced and therefore is only a minor contributor to isotopic fractionation in the cold, high-latitude-sourced deep ocean.

Four of the processes shown in Figure 5.4 yield negative ΔKr/Ar and positive ΔNe/Ar, consistent with global deep-ocean observations (Hamme et al., 2017; Hamme & Severinghaus, 2007; Jenkins et al., 2016; Loose et al., 2016). Of these processes, only one causes substantially negative Δδ for Ar and Kr isotope ratios: rapid cooling-induced diffusive gas uptake. Cooling of the mixed layer drives air-to-sea diffusion, inducing kinetic fractionation of isotope ratios (negative Δδ) due to the faster diffusivities of light isotopes. Critically important is the difference between cooling-driven gas uptake and glacial meltwater input, the two leading hypotheses for the undersaturation of heavy noble gases in the deep ocean. Whereas both processes yield ~-1% ΔKr/Ar, consistent with observations, cooling-driven diffusive gas uptake and glacial meltwater input fractionate isotope ratios in diverging directions (e.g. -90 per meg vs +38 per meg for $\delta^{40}/_{36}$Ar). Glacial meltwater input causes positive Δδ because gravitational enrichment of firn air prior to occlusion in bubbles fractionates $\delta^{40}/_{36}$Ar and $\delta^{86}/_{82}$Kr (~2‰ over a 100-m firn column) more strongly than does solubility fractionation (ε_{sol} ~ 1.2‰ and 0.25‰, respectively). The deep HOT data therefore suggest an important role for rapid cooling-driven diffusive gas uptake in setting the undersaturation of heavy noble gases in the deep ocean.

In Figure 5.5, we present a possible combination of processes that may simultaneously explain these isotopic observations as well as previous Kr/Ar and Ne/Ar measurements in the deep ocean at Station ALOHA (Hamme & Severinghaus, 2007). In this deep-water formation scenario, which most resembles North Atlantic-like deep convection, mixed layer deepening during late fall first entrains radiatively warmed water at the base of the shallower summer mixed layer, leading to supersaturation. Superimposed on this supersaturation is a small, steady-state water vapor flux fractionation in the cold air-side molecular sublayer. Then, as the surface ocean rapidly cools, noble gases are taken up both by bubble-mediated and diffusive exchange before the surface layer sinks and loses contact with the atmosphere, locking in signals of kinetic isotopic fractionation and bulk undersaturation. We assume here all that all bubbles completely dissolve, however we note that partial dissolution of bubbles (e.g. Keeling, 1993) may be another source of kinetic fractionation.

We suggest that future observations of deep-ocean noble gas isotopic disequilibria over a wide spatial range may reveal differences in the relative importance of the North Atlantic and Southern Oceans in ventilating the deep ocean (Gebbie et al., 2010; Johnson, 2008; Khatiwala et al., 2012; Rae & Broecker, 2018) due to their considerably different formation and gas exchange processes, which likely lead to different fingerprints of noble gas elemental and isotopic fractionation.

5.5 Conclusions

In this study, we introduced a framework for investigating the influence of physical gas-exchange mechanisms during deep-water formation on the isotopic composition of heavy noble gases. We carried out experiments to determine isotopic solubility fractionation factors in seawater and discovered slightly greater isotopic discrimination in seawater than in freshwater. To explore mechanisms of inert gas disequilibrium caused by deep-water formation, we collected and analyzed a small set of samples from the deep North Pacific and found undersaturation of heavy-to-light Ar and Kr isotope ratios, which point to the importance of rapid cooling-driven diffusive gas uptake. We suggest that future measurements of Ar, Kr, and Xe isotope ratios, with moderate gains in analytical precision and paired with measurements of He, Ne, Ar, Kr, and Xe, will provide additional sensitive constraints for quantifying physical drivers of deep-ocean ventilation and may potentially inform biogeochemical isotopic tracers such as oxygen and carbon isotopes.

5.S1: Analytical precision and error analysis

For isotopic δ values measured in 2-L seawater samples in this study, we account for (a) random measurement error represented by the pooled standard deviation, σ_{pld}, of replicate samples analyzed using the same method between June and October 2018, (b) systematic errors associated with small corrections made for pressure imbalance between sample and standard bellows on the MAT 253 and variable Kr/Ar and Xe/Ar ratios across samples (the "chemical slope", Petrenko et al., 2006) as well as apparent fractionation during extraction based on standard aliquot tests (Seltzer et al., 2019), and (c) the standard error of atmospheric air measurements, which we analyzed regularly against a common reference gas. For Δδ values, error in seawater α_{sol} is also taken into account. Formally, we define the standard error (SE) of the mean of N Δδ values as:

$$\mathrm{SE} \equiv \sqrt{\frac{\sigma_{pld}^2}{N} + \mathrm{SE}_{atm}^2 + \mathrm{SE}_{ms}^2 + \mathrm{SE}_{ext}^2 + \mathrm{SE}_{sol}^2} \qquad (5.S1)$$

where σ is the standard deviation of N Δδ values and SE_{atm}, SE_{ms}, SE_{ext}, and SE_{sol} refer to standard errors associated with replicate atmospheric air measurements, mass spectrometer corrections, extraction system corrections, and error in the isotopic solubility curves in seawater. Additional uncertainty in elemental ratios is accounted for based on the difference between solubility curves [e.g. ~2‰ for Kr/Ar determined using (a) Weiss & Kyser (1978) and Hamme & Emerson (2004b) versus (b) Jenkins et al. (2019)].

5.S2: Overview of water vapor flux fractionation hypothesis

Gas exchange between turbulently well-mixed near-surface air and seawater is limited by molecular diffusive sublayers on both sides of the air-sea interface (e.g. Hasse & Liss, 1980; Liss & Slater, 1974; Wanninkhof et al., 2009). For sparingly soluble gases (like noble gases), the rate of gas transport across the air-sea interface is controlled by water-side resistance and, as a result, much focus has been dedicated to modeling the water-side diffusive sublayer and parameterizing the dependence of apparent gas transfer velocity k on molecular diffusivity in water D (e.g. Danckwerts, 1951; Ledwell, 1984; Liss & Slater, 1974; Soloviev et al., 1994). Differences in k between noble gas isotopes arise, therefore, arise from isotopic diffusivity differences in water and induce kinetic fractionation during air-to-sea gas transport, which we suggest is a leading role for the isotopic disequilibrium we have observed in the deep ocean.

However, while the air-side diffusive sublayer is unimportant for the rate of air-sea gas exchange, kinetic fractionation across this layer changes the isotopic composition of air in immediate contact with the sea surface from well-mixed atmospheric air above. In other words, due to fractionation in the air-side sublayer, a gas or isotope ratio R_{SS} immediately above the sea surface differs from R_{atm}, that ratio in the well-mixed atmosphere. The definition of $\Delta\delta$ (that is, R_{diss}/R_{eq} -1), assumes that $R_{eq} = \alpha_{sol}R_{atm}$, where R_{eq} is the dissolved gas or isotope ratio at solubility equilibrium, R_{atm} is the ratio in well-mixed atmospheric air, and R_{diss} is a measured dissolved ratio. However, dissolved gases in the surface ocean equilibrate with the steady-state composition of air immediately above the sea surface, which has gas or isotope ratio R_{SS}. Any fractionation across the air-side sublayer that causes R_{SS} to deviate from R_{atm} will therefore affect $\Delta\delta$.

It is well known that isotopic diffusivity differences lead to kinetic fractionation of water vapor isotopes (e.g. δD, $\delta^{18}O$) due to diffusive transport through the air-side boundary layer driven by evaporation from the sea surface (e.g. Merlivat & Coantic, 1975; Merlivat & Jouzel, 1979). We suggest that slight fractionation of noble gases and their isotopes similarly occurs across the air-side molecular sublayer at steady state due to the gradient in water vapor mole fraction. We describe this fractionation with the following example, illustrated in Figure 5.S1. In the vapor-saturated air immediately above 25 °C seawater (assuming no air-sea temperature difference) the mole fraction of water vapor is ~3.1%. In the turbulently well-mixed air above the air-side molecular sublayer, relative humidity over seawater is generally close to 80% (indeed it was consistently ~80% during the HOT 303 cruise in 2018). Therefore, at steady-state, there exists a ~0.6% mole fraction gradient across the air-side molecular sublayer. Because total pressure is the same throughout the sublayer, the mole fractions of all other dry air constituents (including noble gases) must increase proportionally with height above the sea surface, as shown in Figure 5.S1. At steady state, there exists a partial pressure gradient in noble gases across the sublayer driving downward diffusive (kinetically fractionating) transport of noble gases against an upward diffusive flux of water vapor, which is balanced by advective (unfractionating) upward transport of dry air by water vapor. Because light isotopes are faster diffusing against water vapor than heavy isotopes, the air in immediate contact with the sea surface has a heavy-to-light isotope ratio below that of well-mixed atmospheric air.

This water vapor flux fractionation was first identified in sand dune air oxygen and nitrogen isotope ratios and was subsequently reproduced in laboratory experiments, and quantitatively modeled (Severinghaus et al., 1996). Recently, it has been observed and modeled for CO_2 isotopic fractionation in leaves (Farquhar & Cernusak, 2012), and noble gas isotopes in unsaturated zone air (Seltzer et al., 2017) and in laboratory air-water gas exchange experiments (Seltzer et al., 2019). To within ~1 per meg, the steady-state effect is given by

$$\Delta C_{vapor} \approx \left(\left(\frac{D_{i\text{-}H2O}}{D_{air\text{-}H2O}} - 1 \right) \cdot (1\text{-}RH) \cdot e_{sat} - 1 \right) \tag{5.S2}$$

where D is a binary diffusivity against water vapor ($cm^2\ s^{-1}$), RH is relative humidity of surface air (assumed 0.8), and e_{sat} is saturation vapor pressure (atm). For ^{40}Ar and ^{36}Ar, $\frac{D_{40\text{-}H2O}}{D_{36\text{-}H2O}}$ is ~0.983 (Fuller et al., 1966). Thus, for 80% relative humidity, 25 ºC air, water vapor flux fractionation alone leads to $\Delta\delta_{vapor} \approx -103$ per meg. Due to the strong temperature dependence of e_{sat}, the effect is ~five times smaller in 1 ºC, 80% relative humidity air. For ^{86}Kr and ^{82}Kr, $\frac{D_{86\text{-}H2O}}{D_{82\text{-}H2O}}$ is ~0.996, meaning that water vapor flux fractionation is ~five times smaller for ^{86}Kr/^{82}Kr than for ^{40}Ar/^{36}Ar.

The effect of water vapor flux fractionation on elemental ratios is small compared to processes like cooling and bubble injection. For example, at 80% relative humidity and 25 ºC, the contribution of water vapor flux fractionation to ΔKr/Ar is ~ -1.1 ‰, while 1 ºC of subsurface cooling (without gas exchange) leads ΔKr/Ar to decrease by ~7 ‰. For comparison, whereas the influence of water vapor flux fractionation in this example is ~7 times smaller than cooling for ΔKr/Ar, it is ~15 times larger than cooling for $\Delta\delta^{40}/_{36}$Ar (-103 vs -7 per meg). Future laboratory studies and surface ocean observations are needed to test the theory that water vapor flux fractionation is a leading factor in setting $\Delta\delta^{40}/_{36}$Ar in warm surface water.

5.S3: Formulation of separable inert gas disequilibrium processes (ΔC)

Subsurface warming/cooling without gas exchange (e.g. beneath mixed layer or under sea-ice):

$$\Delta C_{\mathrm{warm/cool,no\ gasex}}=\frac{C_i}{C_i^{eq}\cdot\frac{dC_i^{eq}}{dT}\Delta T}-1 \tag{5.S3}$$

where ΔT is a warming or cooling (without gas exchange) in ^{o}C and $\frac{dC_i^{eq}}{dT}$ is the temperature sensitivity of the solubility of gas *i* in mol m^{-3} ^{o}C^{-1}.

Injection and complete dissolution of atmospheric air bubbles:

$$\Delta C_{\mathrm{bubble,no\ gasex}}=\frac{V_{\mathrm{bubble}}\cdot\chi_i}{C_i^{eq}} \tag{5.S4}$$

where V_{bubble} is the injected (and completely dissolved) amount of atmospheric air (mol m^{-3}) and χ_i is the mole fraction of gas *i* in dry air.

Injection and complete dissolution balanced by diffusive exchange (quasi-steady-state):

$$\Delta C_{\mathrm{bubble,gasex}}=\frac{B_{\mathrm{inj}}\cdot\chi_i}{k_i\ C_i^{eq}} \tag{5.S5}$$

where B_{inj} is the rate of injection and complete dissolution of atmospheric air bubbles (mol m^{-2}), and k_i is the gas transfer velocity of gas or isotope *i* (m day^{-1}).

Melting of glacial ice (and corresponding cooling of water) and input of trapped bubbles:

$$\Delta C_{\mathrm{gmw}}=\frac{(1-f_{\mathrm{mw}})\cdot C_i^{eq}(\theta_0,S_0)+f_{\mathrm{mw}}\cdot\lambda\cdot(\frac{P}{RT})\cdot\chi_i\cdot e^{(m_i-m_{\mathrm{air}})\cdot g\cdot z_{\mathrm{firn}}/(RT)}}{C_i^{eq}\left((1-f_{\mathrm{mw}})\cdot\theta_0+f_{\mathrm{mw}}\cdot\theta_{\mathrm{gmw}},(1-f_{\mathrm{mw}})\cdot S_0+f_{\mathrm{mw}}\cdot S_{\mathrm{gmw}}\right)}-1 \tag{5.S6}$$

where f_{mw} is the fraction of meltwater, $C_i^{eq}(\theta_0,S_0)$ is the initial solubility equilibrium concentration of gas *i* dissolved in water with initial potential temperature θ_0 and salinity S_0, λ is the volumetric ratio of air bubbles in ice (assumed to be 0.11), P is the surface pressure above glacial ice (assumed to be 1 atm), R is the ideal gas constant, T is the firn temperature (assumed -25 ^{o}C), χ_i is the mole fraction of gas *i* in dry air, m is the molar weight of gas *i* or air in grams, g is the gravitational constant in m/s^2, and z_{firn} is the bubble close-off depth in firn (assumed to be 100 m). The final solubility equilibrium concentration is calculated for a mixture of f_{mw} between initial potential temperature and salinity, θ_0 and S_0, and glacial-meltwater potential temperature and salinity, θ_{gmw} and S_{gmw}, assumed to be -88 ºC and 0 psu, respectively.

<u>Cooling-induced diffusive gas uptake (quasi-steady-state):</u>

$$\Delta C_{\mathrm{cool,gasex}} = -\frac{dT}{dt} \cdot \frac{dC_i^{eq}}{dT} \cdot \frac{h}{k_i} \tag{5.S7}$$

where $\frac{dT}{dt}$ is a rate of temperature change in ºC day^{-1}, $\frac{dC_i^{eq}}{dT}$ is the temperature sensitivity of the solubility of gas *i* in mol m^{-3} ºC^{-1}, h is the mixed-layer depth, and k_i is a gas transfer velocity in m day^{-1}.

Acknowledgements

We thank Dan Sadler and the captains and crew of *R/V Ka'imikai-O-Kanaloa* for enabling our seawater collection, Roberta Hamme for sampling advice, Manuel Belmonte and May-Linn Paulsen for salinity measurements, and Bill Paplawski, Martin Tresguerres, Steve Emerson, Susan Becker, Adam Cox, and Ross Beaudette for technical support and equipment loans. This work was supported by two NSF Graduate Research Fellowships, the Shepard Foundation, Hawaiian Airlines, and NSF award EAR-1702704.

This chapter, in full, has been accepted for publication in *Geophysical Research Letters*: Seltzer, A., Pavia, F., Ng, J., and J. Severinghaus, Heavy Noble Gas Isotopes as New Constraints on the Ventilation of the Deep Ocean, *Geophysical Research Letters*, 2019. The dissertation author was the primary investigator and author of this work.

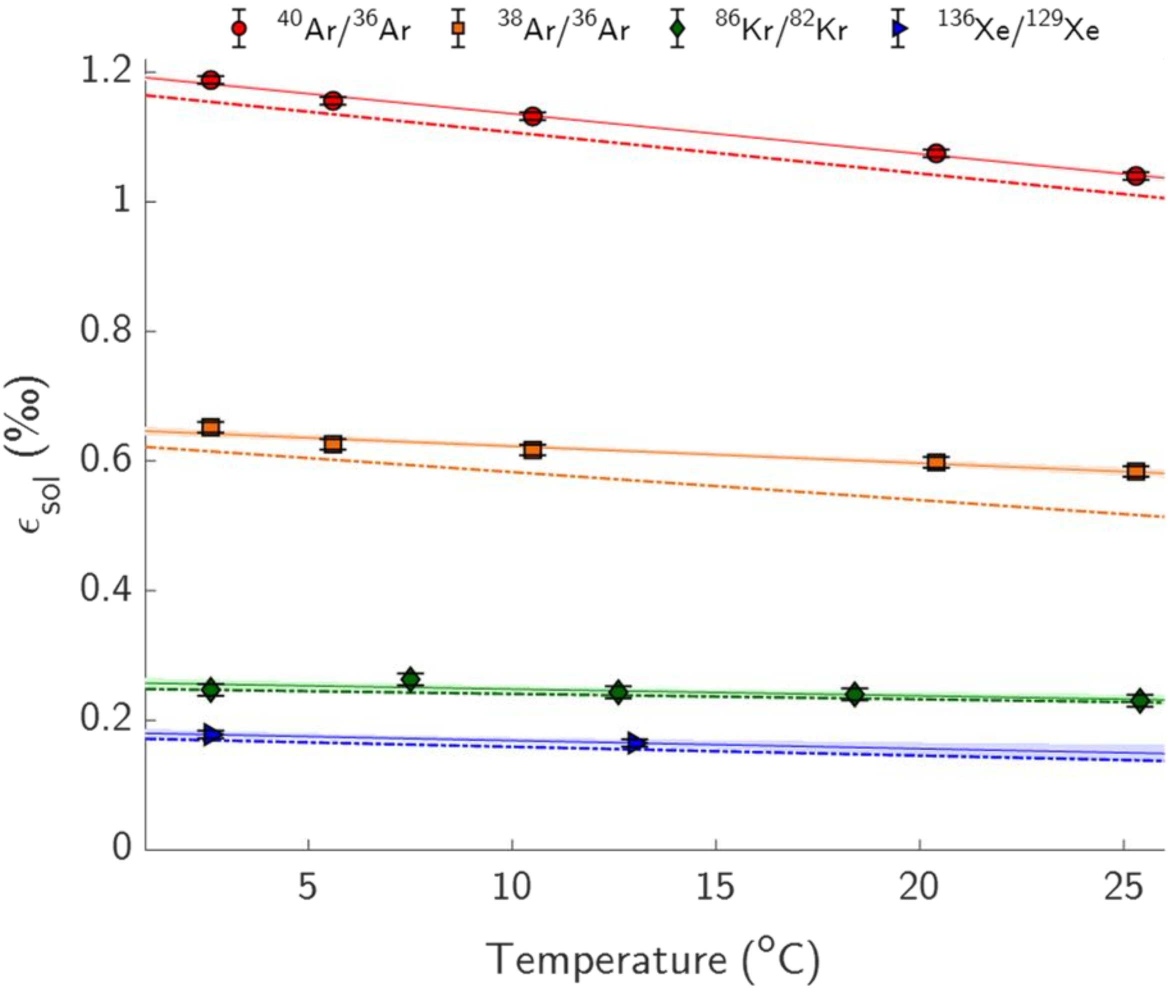

Figure 5.1: Ar, Kr, and Xe isotopic solubility fractionation in seawater (markers and solid lines: this study) and freshwater (dashed lines: Seltzer et al., 2019) versus temperature. Error bars indicate ±1-σ and ±1-SE ranges of individual experiments and temperature trendlines, respectively.

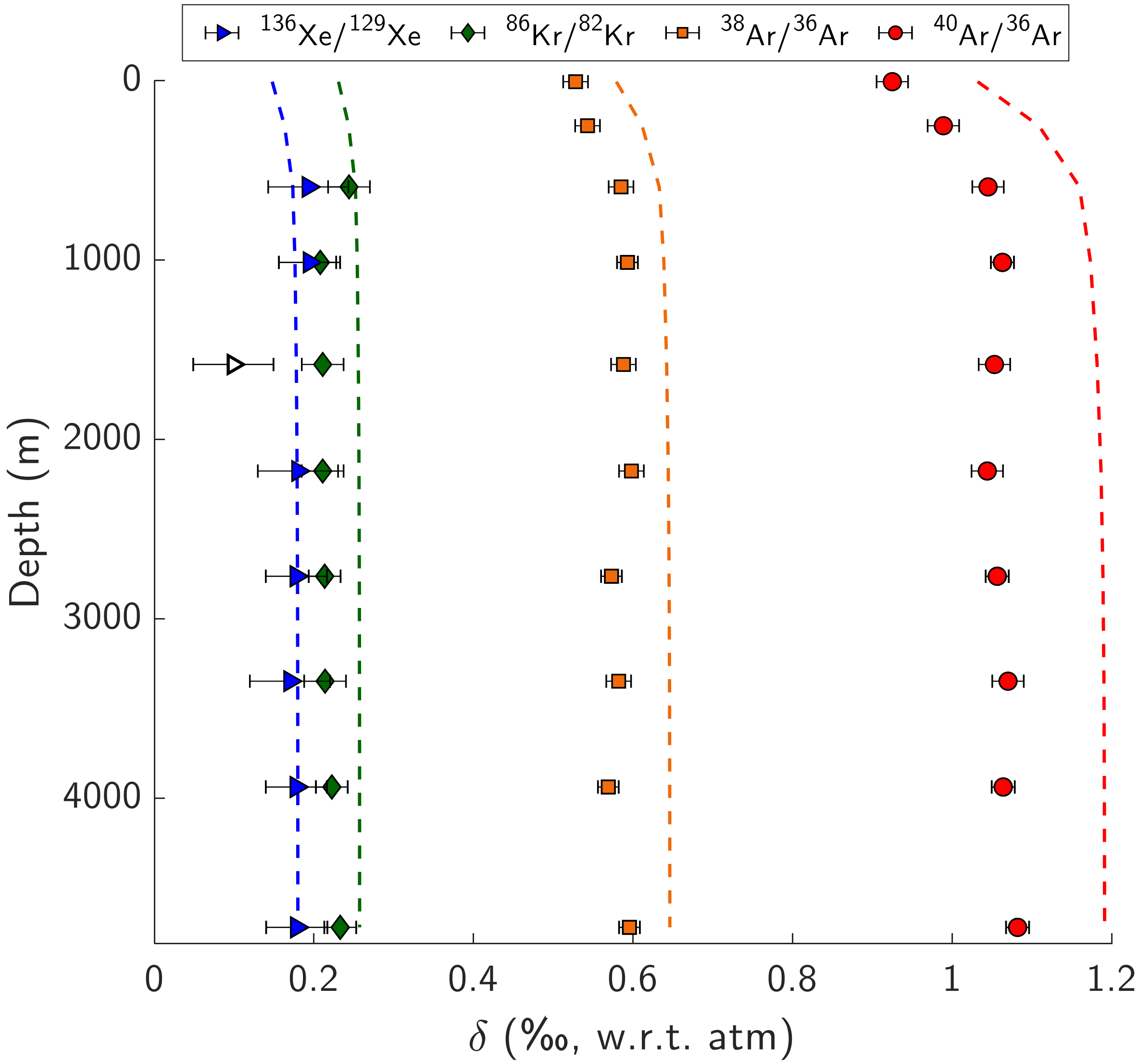

Figure 5.2: Measured HOT-303 profiles of dissolved Ar, Kr, and Xe isotope ratios, relative to atmospheric air (in ‰). Error bars indicate standard errors of depth-mean values. An outlier Xe isotope measurement at ~1.6 km is shaded white. Dashed lines indicate our measured seawater solubility equilibria (ε_{sol}).

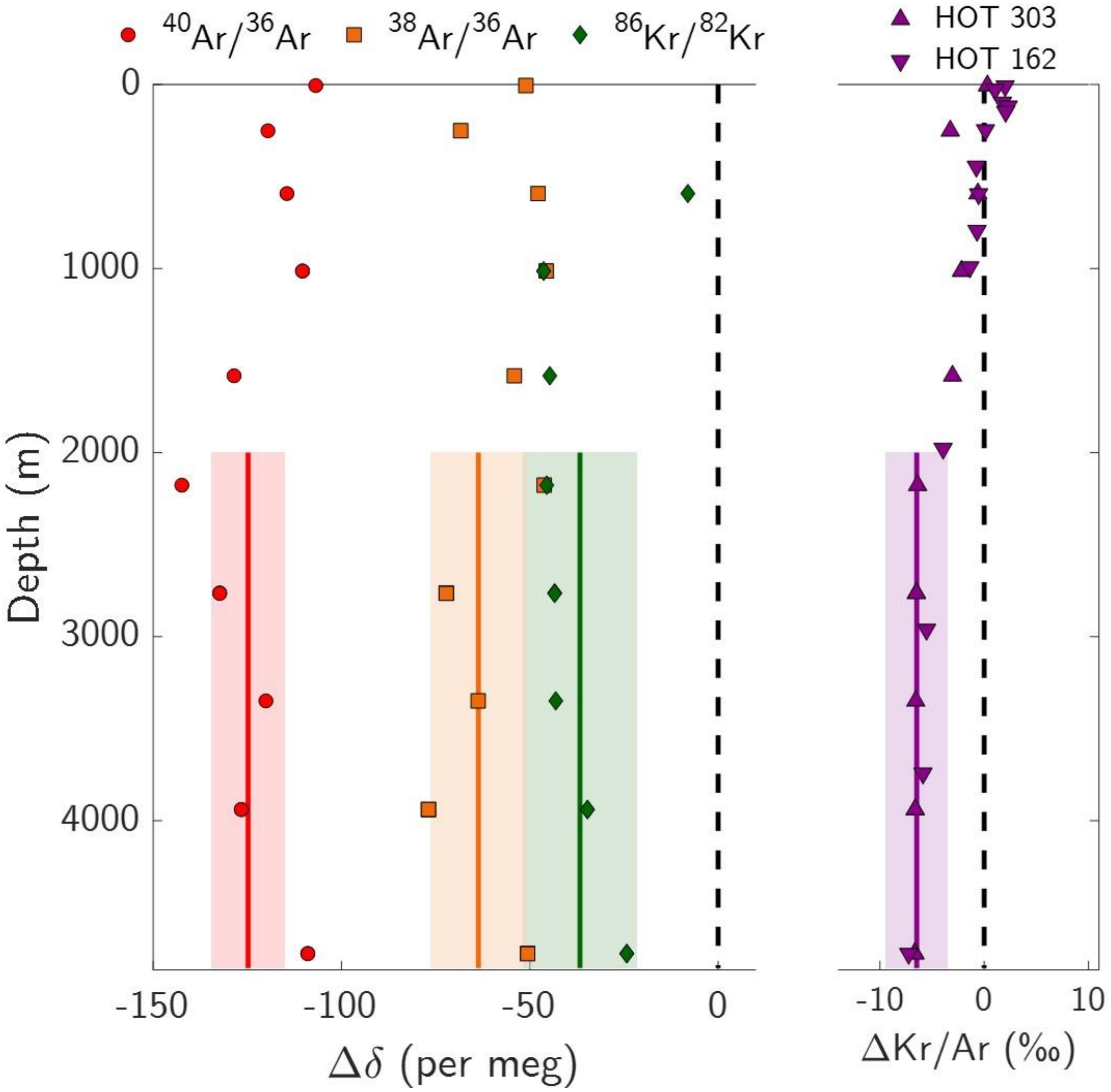

Figure 5.3: Solubility disequilibria for measured stable isotope ratios (left panel) and Kr/Ar ratios (right panel). Solid lines and shaded regions indicate mean and standard error of deep-ocean (>2000 m) disequilibria. All measurements are from HOT 303, except for the HOT 162 Kr/Ar data (Hamme and Severinghaus, 2007).

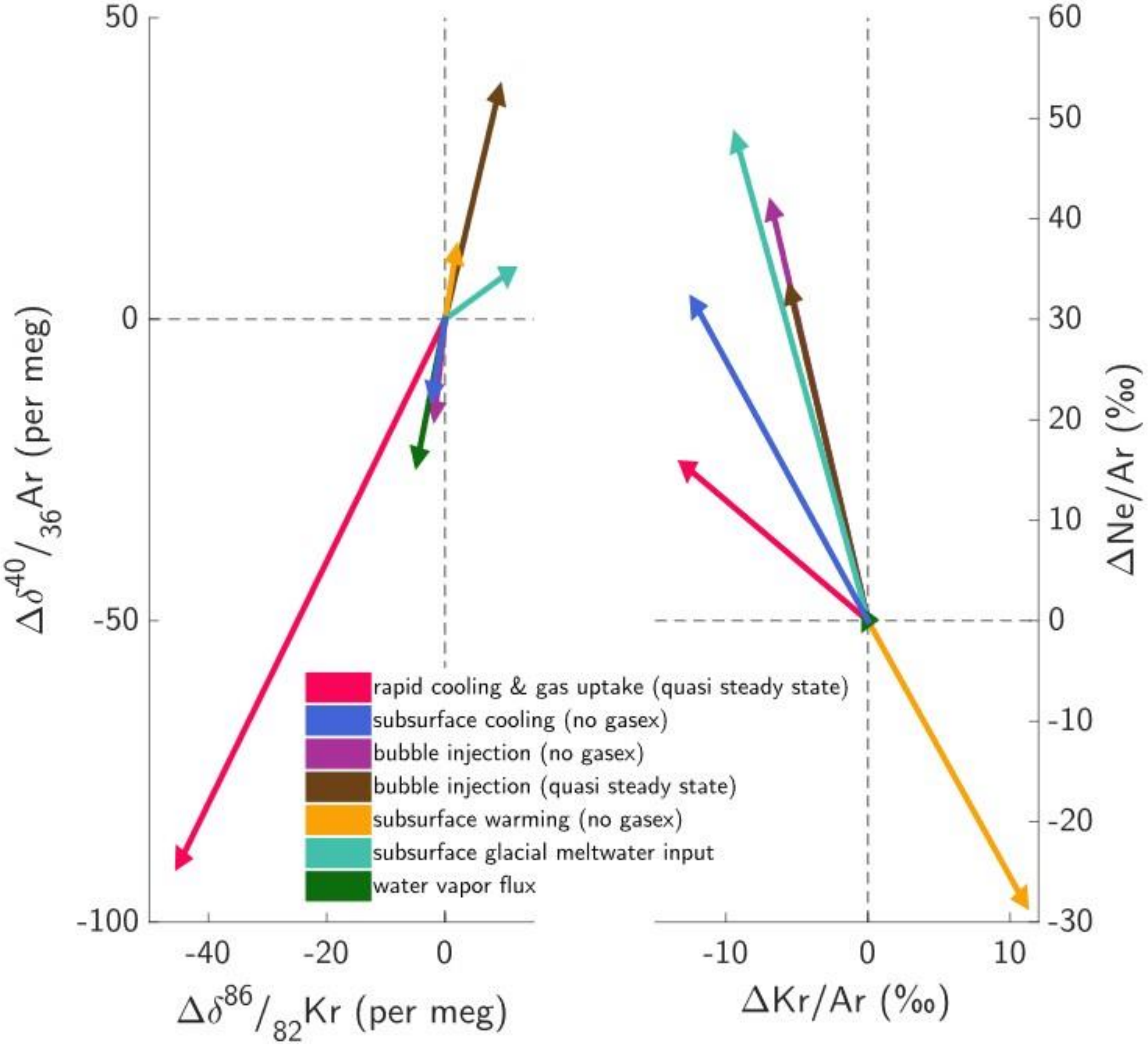

Figure 5.4: Idealized expectations for isotope and elemental ratio disequilibria resulting from seven processes detailed in Section 5.4. For each process, an initially air-saturated ($\Delta C=0$, $\Delta\delta = 0$) 100-m mixed layer at 2 ºC and 35 psu is assumed.

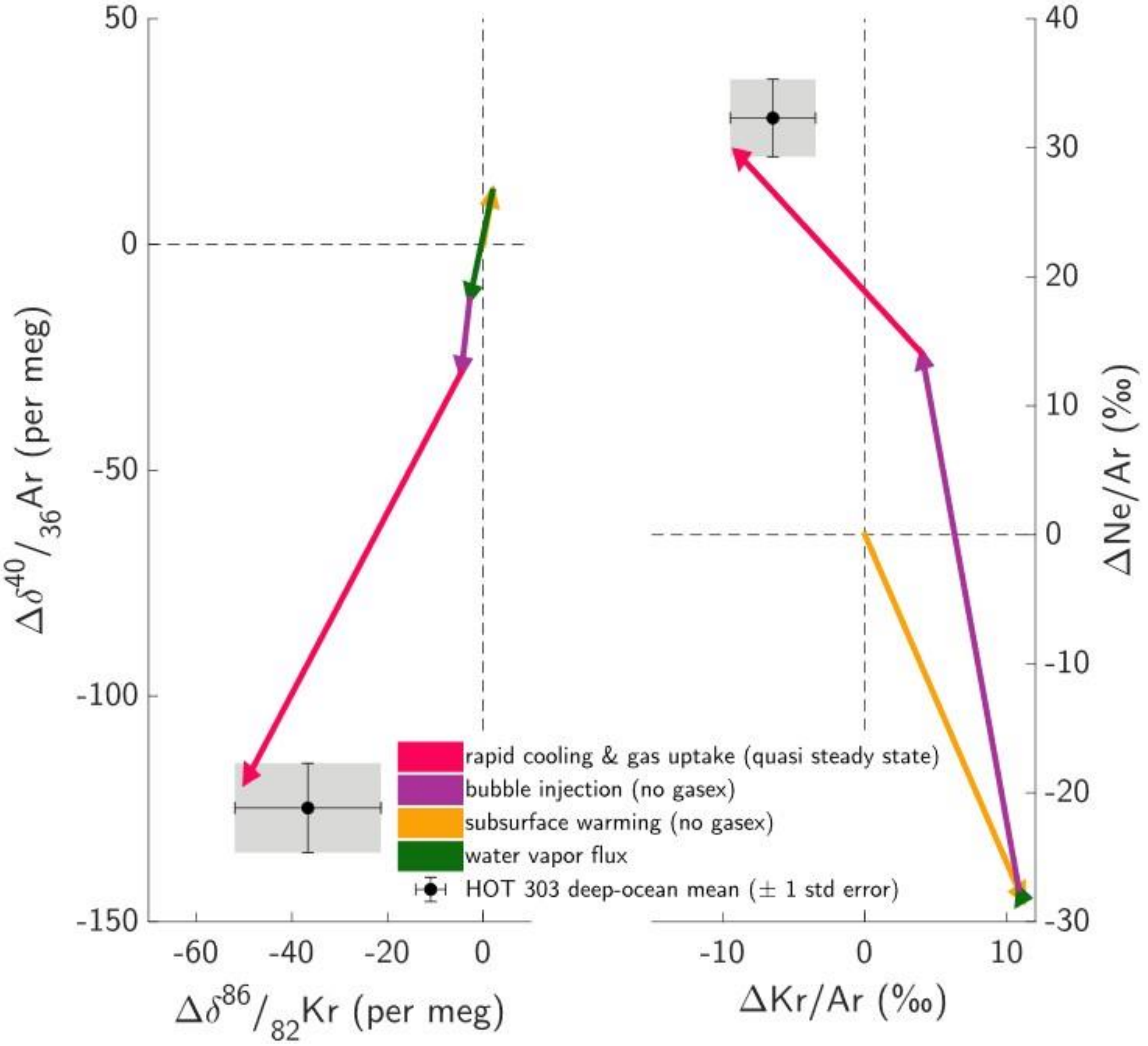

Figure 5.5: Possible combination of disequilibrium mechanisms that may explain HOT-303 deep ocean observations. In this scenario, rapid cooling (1.2 °C month^{-1}) of the surface ocean occurs after the deepening of a shallow summer mixed layer and entrainment of radiatively warmed (by 2 °C) water. Injection and complete dissolution of air bubbles (0.025 mol$_{air}$ m^{-3}) and diffusive gas uptake lead to fractionation of isotope and elemental ratios prior to subduction.

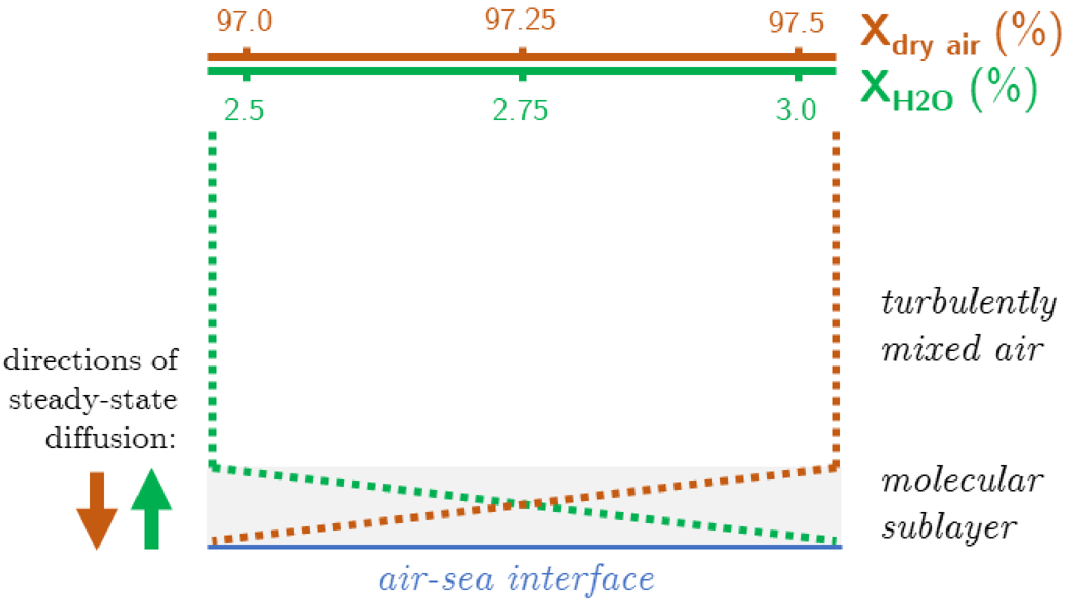

Figure 5.S1: Schematic of water-vapor flux fractionation above 25 ^oC seawater. Because relative humidity in the turbulently well-mixed air above the air-side molecular sublayer is 80%, there exists a steady-state gradient in water vapor mole fraction across the sublayer, decreasing with height above the air-sea interface. Because total pressure is constant with height, an inverse gradient exists for dry air constituents, including the noble gases. At steady-state, downward diffusion of dry air is balanced by upward advection due to water vapor. The former process induces kinetic fractionation, while the latter is unfractionating.

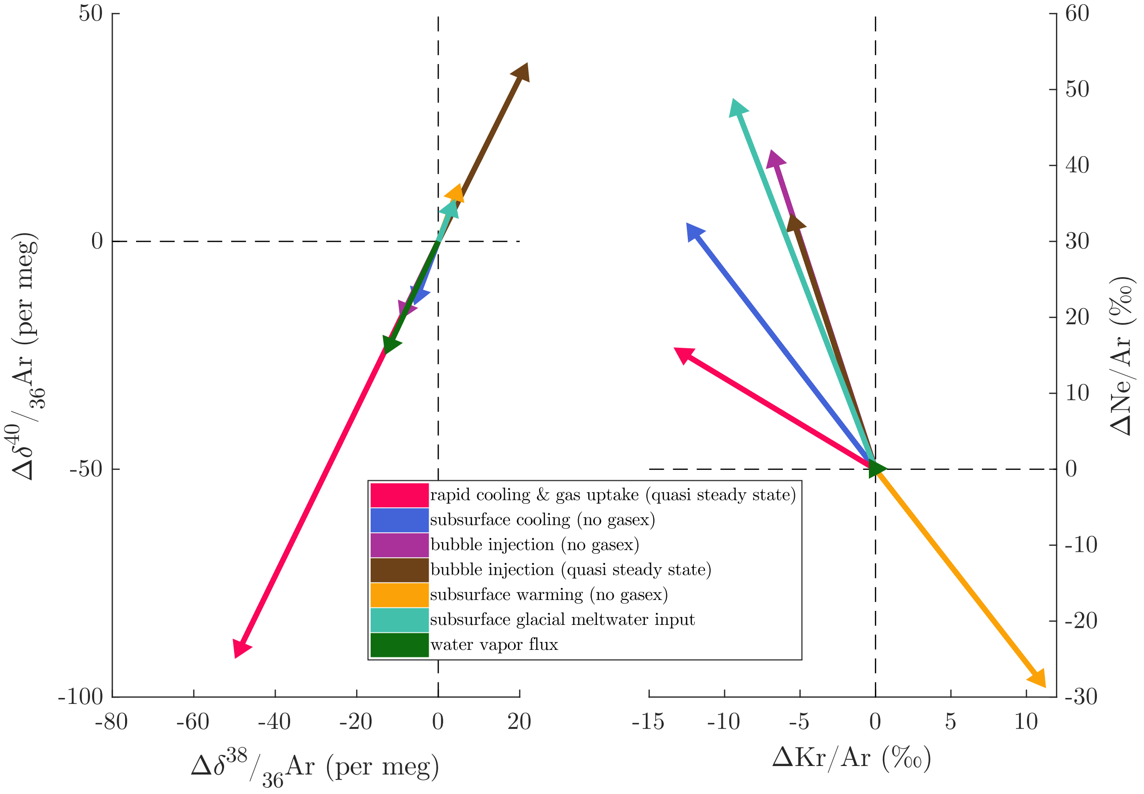

Figure 5.S2: Seven mechanisms of solubility disequilibrium (see Figure 5.4) shown here for $\Delta\delta^{40}/_{36}$Ar, $\Delta\delta^{38}/_{36}$Ar, ΔKr/Ar, and ΔNe/Ar.

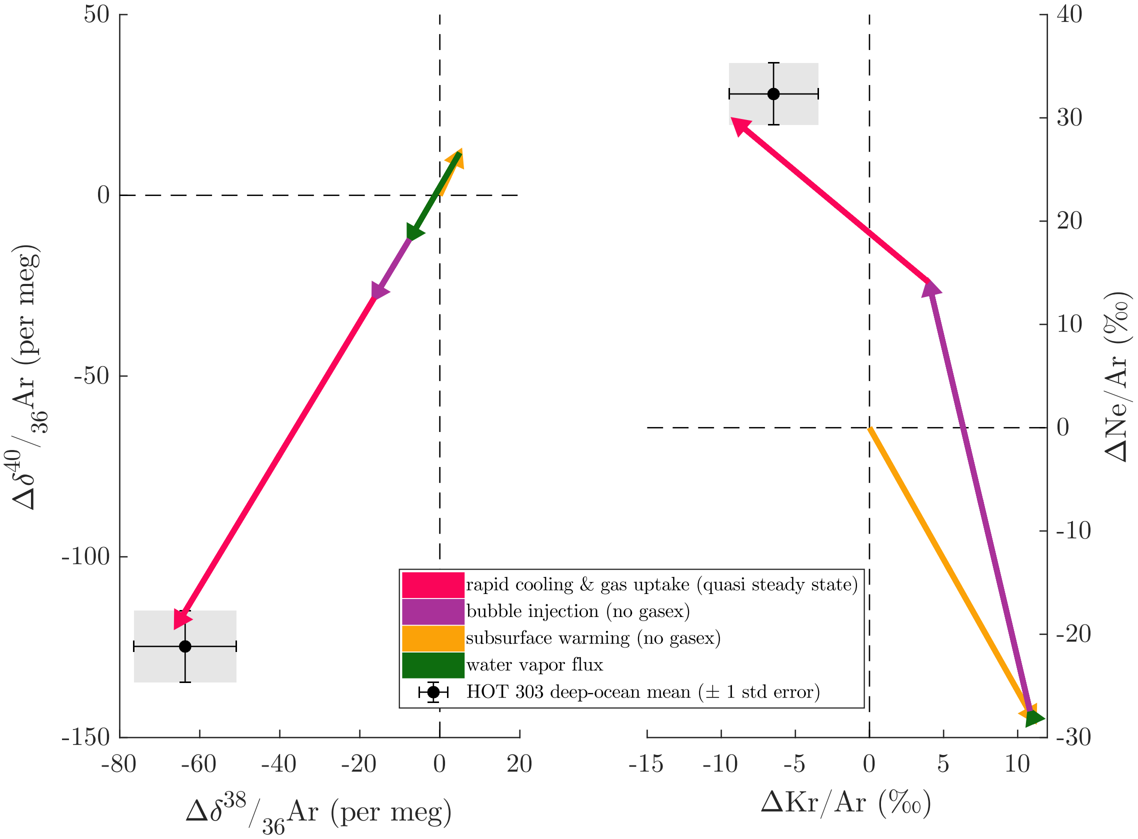

Figure 5.S3: Potential sequence of disequilibrium processes during deep-water formation (see Figure 5.5) shown here for $\Delta\delta^{40}/_{36}$Ar, $\Delta\delta^{38}/_{36}$Ar, ΔKr/Ar, and ΔNe/Ar.

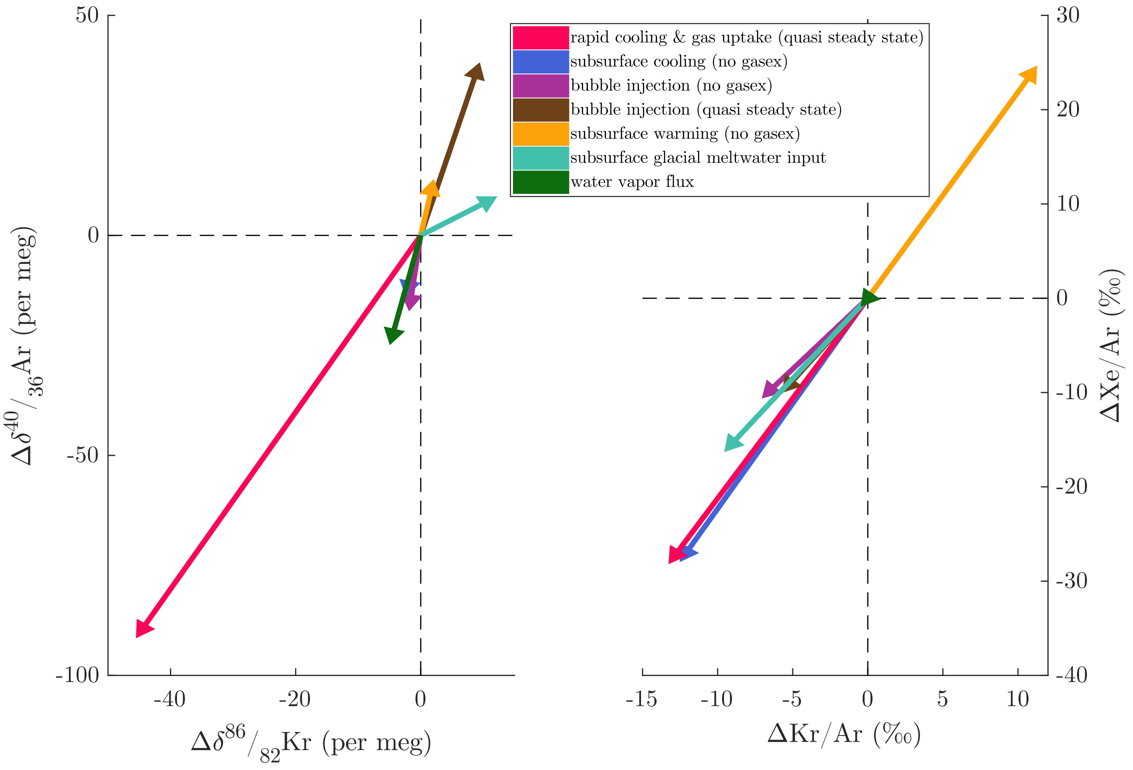

Figure 5.S4: Seven mechanisms of solubility disequilibrium (see Figure 5.4) shown here for $\Delta\delta^{40}/_{36}$Ar, $\Delta\delta^{86}/_{82}$Kr, ΔKr/Ar, and ΔXe/Ar.

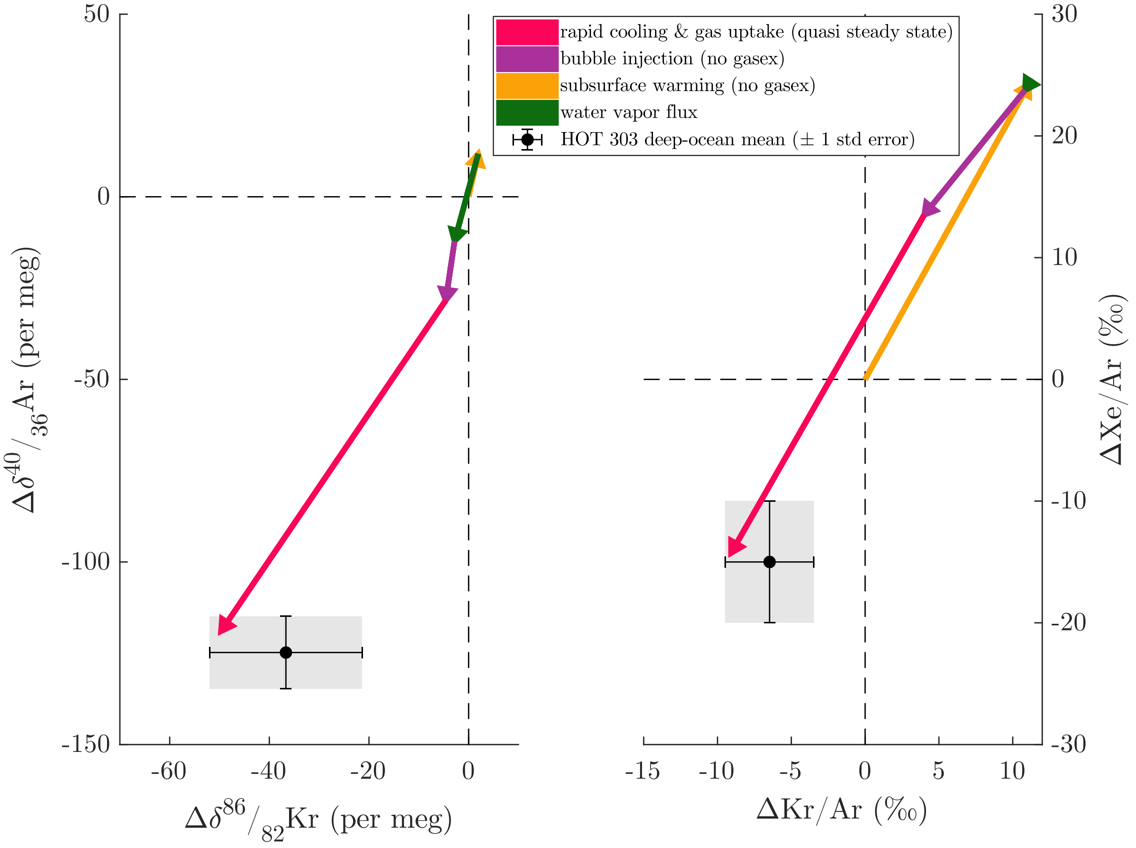

Figure 5.S5: Potential sequence of disequilibrium processes during deep-water formation (see Figure 5.5) shown here for $\Delta\delta^{40}/_{36}$Ar, $\Delta\delta^{86}/_{82}$Kr, ΔKr/Ar, and ΔXe/Ar.

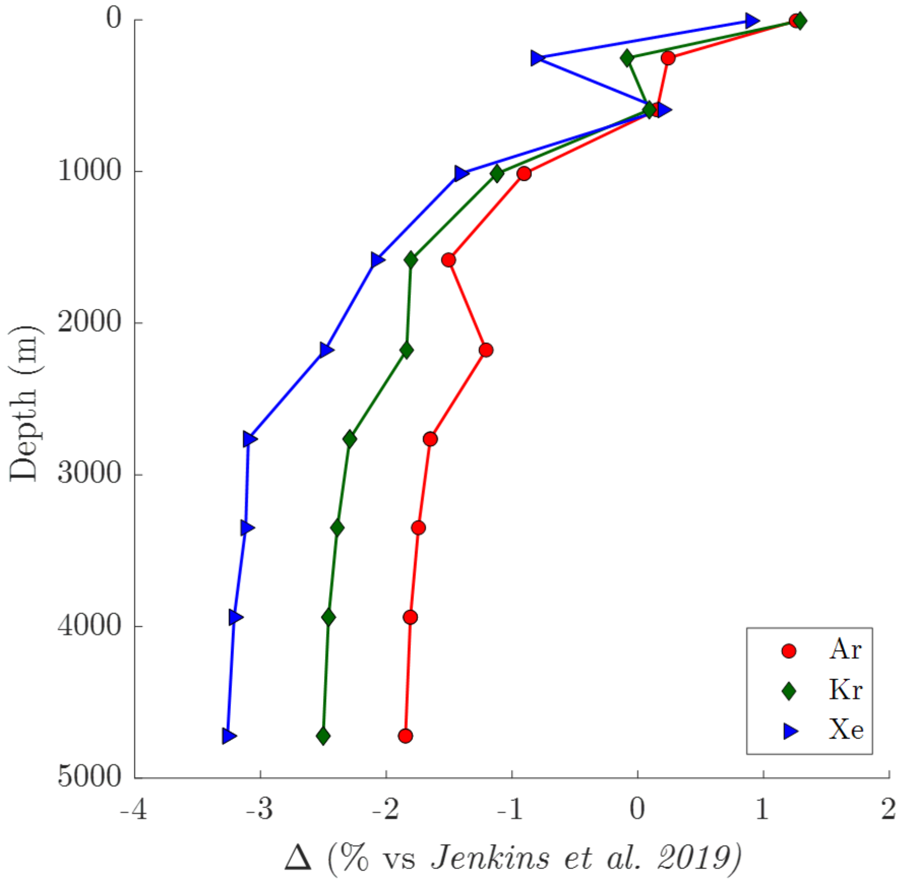

Figure 5.S6: Ar, Kr, and Xe solubility anomalies (relative to Jenkins et al., 2019 solubility curves) calculated based on manometric determination of Ar concentrations and conversion of δKr/Ar and δXe/Ar to Kr and Xe concentrations assuming dry-air Kr and Xe mole fractions used by Jenkins et al., 2019.

Table 5.S1: Isotope ratios measured in this study and associated uncertainty metrics. Heavy and light isotope masses (m_h and m_l) are given in amu; uncertainty metrics are given in per meg.

Ratio	m_h	m_l	σ_{pld}	SE_{atm}	SE_{ms}	SE_{ext}	SE_{sol}
$\delta^{40}/_{36}Ar$	40	36	19	3	1	5	4
$\delta^{38}/_{36}Ar$	38	36	12	5	1	8	6
$\delta^{86}/_{82}Kr$	86	82	24	10	2	4	7
$\delta^{86}/_{83}Kr$	86	83	27	7	3	5	7
$\delta^{86}/_{84}Kr$	86	84	23	4	1	11	8
$\delta^{136}/_{129}Xe$	136	129	46	17	6	9	7
$\delta^{134}/_{129}Xe$	134	129	52	18	19	9	6
$\delta^{132}/_{129}Xe$	132	129	28	10	12	6	6

References

Benson, B. B., & Krause, D. (1980). Isotopic fractionation of helium during solution: A probe for the liquid state. *Journal of Solution Chemistry*, *9*(12), 895–909. https://doi.org/10.1007/BF00646402

Danckwerts, P. V. (1951). Significance of Liquid-Film Coefficients in Gas Absorption. *Industrial & Engineering Chemistry*, *43*(6), 1460–1467. https://doi.org/10.1021/ie50498a055

Emerson, S., & Bushinsky, S. (2016). The role of bubbles during air-sea gas exchange. *Journal of Geophysical Research: Oceans*, *121*(6), 4360–4376. https://doi.org/10.1002/2016JC011744

Farquhar, G. D., & Cernusak, L. A. (2012). Ternary effects on the gas exchange of isotopologues of carbon dioxidep ce_2484 1221..1231. https://doi.org/10.1111/j.1365-3040.2012.02484.x

Fuller, E. N., Schettler, P. D., & Giddings, J. C. (1966). A new method for prediction of binary gas-phase diffusion coefficients. *Industrial and Engineering Chemistry*, *16*(10), 551. https://doi.org/10.1016/0042-207X(66)90400-3

Gebbie, G., Huybers, P., Gebbie, G., & Huybers, P. (2010). Total Matrix Intercomparison: A Method for Determining the Geometry of Water-Mass Pathways. *Journal of Physical Oceanography*, *40*(8), 1710–1728. https://doi.org/10.1175/2010JPO4272.1

Hamme, R. C., & Emerson, S. R. (2002). Mechanisms controlling the global oceanic distribution of the inert gases argon, nitrogen and neon. *Geophysical Research Letters*, *29*(23), 35-1-35–4. https://doi.org/10.1029/2002GL015273

Hamme, R. C., & Emerson, S. R. (2004a). Measurement of dissolved neon by isotope dilution using a quadrupole mass spectrometer. *Marine Chemistry*, *91*(1–4), 53–64. https://doi.org/10.1016/j.marchem.2004.05.001

Hamme, R. C., & Emerson, S. R. (2004b). The solubility of neon, nitrogen and argon in distilled water and seawater. *Deep-Sea Research Part I: Oceanographic Research Papers*, *51*(11), 1517–1528. https://doi.org/10.1016/j.dsr.2004.06.009

Hamme, R. C., & Severinghaus, J. P. (2007). Trace gas disequilibria during deep-water formation. *Deep-Sea Research Part I: Oceanographic Research Papers*, *54*(6), 939–950. https://doi.org/10.1016/j.dsr.2007.03.008

Hamme, R. C., Emerson, S. R., Severinghaus, J. P., Long, M. C., & Yashayaev, I. (2017). Using Noble Gas Measurements to Derive Air-Sea Process Information and Predict Physical Gas Saturations. *Geophysical Research Letters*, *44*(19), 9901–9909. https://doi.org/10.1002/2017GL075123

Hamme, R. C., Nicholson, D. P., Jenkins, W. J., & Emerson, S. R. (2019). Using Noble Gases to Assess the Ocean's Carbon Pumps. *Annual Review of Marine Science*, *11*(1), 75–103. https://doi.org/10.1146/annurev-marine-121916-063604

Hasse, L., & Liss, P. S. (1980). Gas exchange across the air-sea interface, *32*, 470–518. https://doi.org/10.3402/tellusa.v32i5.10602

Ito, T., & Deutsch, C. (2006). Understanding the saturation state of argon in the thermocline: The role of air-sea gas exchange and diapycnal mixing. https://doi.org/10.1029/2005GB002655

Ito, T., Deutsch, C., Emerson, S., & Hamme, R. C. (2007). Impact of diapycnal mixing on the saturation state of argon in the subtropical North Pacific. *Geophysical Research Letters*, *34*(9). https://doi.org/10.1029/2006GL029209

Jenkins, W. J., Lott, D. E., German, C. R., Cahill, K. L., Goudreau, J., & Longworth, B. (2016, April 2). The deep distributions of helium isotopes, radiocarbon, and noble gases along the U.S. GEOTRACES East Pacific Zonal Transect (GP16). *Marine Chemistry*. https://doi.org/10.1016/j.marchem.2017.03.009

Jenkins, W. J., Lott, D. E., & Cahill, K. L. (2019). A determination of atmospheric helium, neon, argon, krypton, and xenon solubility concentrations in water and seawater. *Marine Chemistry*, *211*, 94–107. https://doi.org/10.1016/J.MARCHEM.2019.03.007

Johnson, G. C. (2008). Quantifying Antarctic Bottom Water and North Atlantic Deep Water volumes. *Journal of Geophysical Research*, *113*(C5), C05027. https://doi.org/10.1029/2007JC004477

Keeling, R. F. (1993). On the role of large bubbles in air-sea gas exchange and supersaturation in the ocean. *Journal of Marine Research*, *51*(2), 237–271. https://doi.org/10.1357/0022240933223800

Khatiwala, S., Primeau, F., & Holzer, M. (2012). Ventilation of the deep ocean constrained with tracer observations and implications for radiocarbon estimates of ideal mean age. *Earth and Planetary Science Letters*, *325–326*, 116–125. https://doi.org/10.1016/J.EPSL.2012.01.038

Ledwell, J. J. (1984). The Variation of the Gas Transfer Coefficient with Molecular Diffusity. In *Gas Transfer at Water Surfaces* (pp. 293–302). Dordrecht: Springer Netherlands. https://doi.org/10.1007/978-94-017-1660-4_27

Liang, J.-H., Deutsch, C., McWilliams, J. C., Baschek, B., Sullivan, P. P., & Chiba, D. (2013). Parameterizing bubble-mediated air-sea gas exchange and its effect on ocean ventilation. *Global Biogeochemical Cycles*, *27*(3), 894–905. https://doi.org/10.1002/gbc.20080

Liss, P. S., & Slater, P. G. (1974). Flux of Gases across the Air-Sea Interface. *Nature*, *247*(5438), 181–184. https://doi.org/10.1038/247181a0

Loose, B., & Jenkins, W. J. (2014). The five stable noble gases are sensitive unambiguous tracers of glacial meltwater. *Geophysical Research Letters*, *41*(8), 2835–2841. https://doi.org/10.1002/2013GL058804

Loose, B., Jenkins, W. J., Moriarty, R., Brown, P., Jullion, L., Naveira Garabato, A. C., et al. (2016). Estimating the recharge properties of the deep ocean using noble gases and helium isotopes. *Journal of Geophysical Research: Oceans*, *121*(8), 5959–5979. https://doi.org/10.1002/2016JC011809

Merlivat, L., & Coantic, M. (1975). Study of mass transfer at the air-water interface by an isotopic method. *Journal of Geophysical Research*, *80*(24), 3455–3464. https://doi.org/10.1029/jc080i024p03455

Merlivat, L., & Jouzel, J. (1979). Global climatic interpretation of the deuterium-oxygen 16 relationship for precipitation. *Journal of Geophysical Research*, *84*(C8), 5029–5033. https://doi.org/10.1029/JC084iC08p05029

Nicholson, D., Emerson, S., Caillon, N., Jouzel, J., & Hamme, R. C. (2010). Constraining ventilation during deepwater formation using deep ocean measurements of the dissolved gas ratios 40 Ar/ 36 Ar, N 2 /Ar, and Kr/Ar. *Journal of Geophysical Research*, *115*(C11), C11015. https://doi.org/10.1029/2010jc006152

Nicholson, D. P., Emerson, S. R., & Khatiwala, S. (2011). An inverse approach to estimate bubble-mediated air-sea gas flux from inert gas measurements. *IOP Conf. Ser.: Earth Environ. Sci*, (1), 223–237.

Petrenko, V. V., Severinghaus, J. P., Brook, E. J., Reeh, N., & Schaefer, H. (2006). Gas records from the West Greenland ice margin covering the Last Glacial Termination: a horizontal ice core. *Quaternary Science Reviews*, *25*(9–10), 865–875. https://doi.org/10.1016/j.quascirev.2005.09.005

Rae, J. W. B., & Broecker, W. (2018). What fraction of the Pacific and Indian oceans' deep water is formed in the Southern Ocean? *Biogeosciences*, *15*, 3779–3794. https://doi.org/10.5194/bg-15-3779-2018

Seltzer, A. M., Severinghaus, J. P., Andraski, B. J., & Stonestrom, D. A. (2017). Steady state fractionation of heavy noble gas isotopes in a deep unsaturated zone. *Water Resources Research*, *53*(4), 2716–2732. https://doi.org/10.1002/2016WR019655

Seltzer, A. M., Ng, J., & Severinghaus, J. P. (2019). Precise determination of Ar, Kr and Xe isotopic fractionation due to diffusion and dissolution in fresh water. *Earth and Planetary Science Letters*, *514*, 156–165. https://doi.org/10.1016/J.EPSL.2019.03.008

Severinghaus, J. P., Bender, M. L., Keeling, R. F., & Broecker, W. S. (1996). Fractionation of soil gases by diffusion of water vapor, gravitational settling, and thermal diffusion. *Geochimica et Cosmochimica Acta*, *60*(6), 1005–1018. https://doi.org/10.1016/0016-

7037(96)00011-7

Soloviev, A. V., Schlüssel, P., Soloviev, A. V., & Schlüssel, P. (1994). Parameterization of the Cool Skin of the Ocean and of the Air-Ocean Gas Transfer on the Basis of Modeling Surface Renewal. *Journal of Physical Oceanography*, *24*(6), 1339–1346. https://doi.org/10.1175/1520-0485(1994)024<1339:POTCSO>2.0.CO;2

Spitzer, W. S., & Jenkins, W. J. (1989). Rates of vertical mixing, gas exchange and new production: Estimates from seasonal gas cycles in the upper ocean near Bermuda. *Journal of Marine Research*, *47*(1), 169–196. https://doi.org/10.1357/002224089785076370

Stanley, R. H. R., & Jenkins, W. (2013). Noble Gases in Seawater as Tracers for Physical and Biogeochemical Ocean Processes. In *The Noble Gases as Geochemical Tracers* (pp. 55–79). https://doi.org/10.1007/978-3-642-28836-4_4

Stanley, R. H. R., Jenkins, W. J., Lott, D. E., & Doney, S. C. (2009). Noble gas constraints on air-sea gas exchange and bubble fluxes. *Journal of Geophysical Research*, *114*(C11), C11020. https://doi.org/10.1029/2009JC005396

Stanley, R. H. R., Jenkins, W. J., Doney, S. C., & Lott, D. E. (2015). The 3 He flux gauge in the Sargasso Sea: A determination of physical nutrient fluxes to the euphotic zone at the Bermuda Atlantic Time-series Site. *Biogeosciences*, *12*(17), 5199–5210. https://doi.org/10.5194/bg-12-5199-2015

Wanninkhof, R. (2014). Relationship between wind speed and gas exchange over the ocean revisited. *Limnology and Oceanography: Methods*, *12*(6), 351–362. https://doi.org/10.4319/lom.2014.12.351

Wanninkhof, R., Asher, W. E., Ho, D. T., Sweeney, C., & McGillis, W. R. (2009). Advances in Quantifying Air-Sea Gas Exchange and Environmental Forcing. *Annual Review of Marine Science*, *1*(1), 213–244. https://doi.org/10.1146/annurev.marine.010908.163742

Weiss, R. F., & Kyser, T. K. (1978). Solubility of Krypton in Water and Seawater. *J. Chem. Eng. Data*, *23*(I), 69–72. https://doi.org/10.1021/je60076a014

Chapter 6

Does $\delta^{18}O$ of O_2 record meridional shifts in tropical rainfall?

Abstract

Marine sediments, speleothems, paleo lake elevations, and ice core methane and $\delta^{18}O$ of O_2 ($\delta^{18}O_{atm}$) records provide ample evidence for repeated abrupt meridional shifts in tropical rainfall belts throughout the last glacial cycle. To improve understanding of the impact of abrupt events on the global terrestrial biosphere, we present composite records of $\delta^{18}O_{atm}$ and inferred changes in fractionation by the global terrestrial biosphere ($\Delta\varepsilon_{LAND}$) from discrete gas measurements in the WAIS Divide (WD) and Siple Dome (SD) Antarctic ice cores. On the common WD timescale, it is evident that maxima in $\Delta\varepsilon_{LAND}$ are synchronous with or shortly follow small-amplitude WD CH_4 peaks that occur within Heinrich stadials 1,2, 4 and 5 – periods of low atmospheric CH_4 concentrations. These local CH_4 maxima have been suggested as markers of abrupt climate responses to Heinrich events. Based on our analysis of the modern seasonal cycle of gross primary productivity (GPP)-weighted $\delta^{18}O$ of terrestrial precipitation (the source water for atmospheric O_2 production), we propose a simple mechanism by which $\Delta\varepsilon_{LAND}$ tracks the centroid latitude of terrestrial oxygen production. As intense rainfall and oxygen production migrate northward, $\Delta\varepsilon_{LAND}$ should decrease due to the underlying meridional gradient in rainfall $\delta^{18}O$. A southward shift should increase $\Delta\varepsilon_{LAND}$. Monsoon intensity also influences $\delta^{18}O$ of precipitation, and although we cannot determine the relative contributions of the two mechanisms,

both act in the same direction. Therefore, we suggest that abrupt increases in $\Delta\varepsilon_{LAND}$ unambiguously imply a southward shift of tropical rainfall. The exact magnitude of this shift, however, remains under-constrained by $\Delta\varepsilon_{LAND}$.

6.1. Introduction

The last glacial cycle shows two modes of abrupt climate variability, both with a center of action in the North Atlantic. The first are Dansgaard-Oeschger (D-O) events, most clearly identified in Greenland ice core records (Andersen et al., 2004; Dansgaard et al., 1993). D-O events refer to abrupt Northern Hemisphere warming, on the timescale of decades, followed by more gradual cooling. In the Southern Hemisphere, D-O events exhibit the opposite response, cooling followed by warming, lagging the Northern Hemisphere by several centuries on average (Buizert et al., 2015). Most D-O events can be linked to abrupt variations in the strength and/or northward heat transport of the Atlantic Meridional Overturning Circulation (Lynch-Stieglitz, 2017). The second mode of abrupt climate change are Heinrich events (HE), periods of extreme cold in the North-Atlantic associated with extensive layers of ice rafted detritus in ocean. Heinrich events occur within longer Heinrich stadial (HS) periods (Hemming, 2004).

High-resolution records of marine sediments (Peterson et al., 2000), ice core methane (Rhodes et al., 2015), speleothem calcite δ^{18}O (Cheng et al., 2016; Kanner et al., 2012; Wang et al., 2017; Wang et al., 2001; Wang et al., 2008), and lake elevations (Goldsmith et al., 2017; Yu et al., 2013) all demonstrate that abrupt meridional shifts in tropical rainfall belts occurred repeatedly during the last glacial cycle in response to both D-O events and HEs. This response is also observed in climate models, which consistently simulate a shift of tropical rainfall towards the warmer hemisphere (Broccoli et al., 2006; Chiang & Bitz, 2005; Cvijanovic et al., 2013).

Understanding the impact of these events on global hydrology, monsoon systems, and terrestrial biosphere remains a key goal of paleoclimate research.

Measurements of long-lived atmospheric gases trapped in ice cores offer an opportunity to better constrain past global processes due to the short atmospheric mixing time and therefore globally integrated signal of these gases. Measurements of concentrations and isotopic ratios of atmospheric gases have provided important clues into the biogeochemical responses to substantial climate changes in the past. Motivated by the recent high-resolution West Antarctic Ice Sheet (WAIS) Divide (WD) ice core methane record (Rhodes et al., 2015), in this study we explore a new record of atmospheric oxygen isotopes from WD and revisit published measurements in the Siple Dome (SD) ice core. A composite WD-SD record of atmospheric oxygen isotopes allows us to investigate past changes in the isotopic fractionation of O_2 on a common timescale (C. Buizert et al., 2015) with other recent records.

Past changes in the Dole Effect – the amount by which $\delta^{18}O$ of atmospheric O_2 ($\delta^{18}O_{atm}$) exceeds that of seawater (Dole, 1935; Morita, 1935) – have been shown to be closely linked to terrestrial hydroclimate (Bender et al., 1994; Landais et al., 2010; Reutenauer et al., 2015; Severinghaus et al., 2009). We quantitatively explore a simple relationship between meridional shifts in terrestrial oxygen production and $\delta^{18}O$ of oxygen production-weighted terrestrial rainfall ($\delta^{18}O_{precip}$) over the modern seasonal cycle using spatially gridded monthly observations. We use these observations as a guide to consider instantaneous changes in O_2 fractionation during HEs and discuss the implications of these changes, and related changes in atmospheric CH_4, for the meridional distribution of tropical rainfall associated with these events.

6.1.1 The Siple Dome and WAIS Divide ice cores

The 1004-meter-long SD ice core (81.65° S 148.81° W) was drilled in the late 1990s at an elevation of 621 m above sea level. The site has modern-day mean-annual surface temperature and accumulation rates of -24.5°C and 13.5 cm ice equivalent per year, respectively (Taylor et al., 2004). The youngest 8.2 ka of the record were dated by visual and electrical counting of annual layers (Taylor et al., 2004), tuned to stratigraphic markers, while the older portion of the ice core was dated by synchronization of CH_4 and $\delta^{18}O_{atm}$ measurements to the GISP2, Greenland ice core (Brook et al., 2005). The 3,404-meter-long WD ice core (79.48° S, 112.11° W) was drilled at an elevation of 1766 m between 2007 and 2011. Present mean-annual air temperature and accumulation rate at the WD ice core site are -30°C and 22 cm ice equivalent per year (Banta et al., 2008; Morse et al., 2002).The youngest 31.2 ka (2850 m) was dated by annual-layer counting (Sigl et al., 2016) while the oldest portion of the core (up to ~68 ka) was dated by CH_4 synchronization to the Greenland NGRIP ice core, scaled linearly to match the timing of abrupt events recorded in U/Th dated speleothem records (Buizert et al., 2015).

6.1.2 $\delta^{18}O_{atm}$ and the Dole Effect: a brief overview

The enrichment of $\delta^{18}O_{atm}$ relative to $\delta^{18}O$ of mean seawater ($\delta^{18}O_{sw}$) is known as the Dole Effect (Dole, 1935; Morita, 1935) and has a modern-day value of ~23.88‰ (Barkan & Luz, 2005). Most of the Dole Effect is attributable to the isotopic discrimination of marine and terrestrial respiration, both of which preferentially utilize ^{16}O, thus enriching atmospheric O_2 in ^{18}O (Bender et al., 1994; Luz & Barkan, 2011). Photosynthesis does not fractionate the $^{18}O/^{16}O$ ratio of chloroplast water (e.g. Helman et al., 2005), and therefore the $\delta^{18}O$ of O_2 produced by photosynthesis is equal to the $\delta^{18}O$ of the plant source water (ultimately derived from precipitation) plus fractionation due to evapotranspiration. Past changes in the Dole Effect estimated from measurements of atmospheric oxygen isotopes in ice core bubbles and reconstructions of $\delta^{18}O_{sw}$ from marine sediment cores have been shown to be small over the past 130 ka, during which the standard deviation of the Dole Effect was only 0.24‰ (Bender et al., 1994).

Variability in the Dole Effect throughout the past glacial-interglacial cycle has been hypothesized to be related to terrestrial hydrology based on coherence with atmospheric CH_4 measured in ice core bubbles (Bender et al., 1994), comparison with Chinese cave records (Severinghaus et al., 2009) and climate modeling experiments (Reutenauer et al., 2015). To investigate instantaneous changes in the isotopic fractionation of atmospheric O_2, Severinghaus et al. (2009) used a one-box model deconvolution to account for the smoothing effect of the ~1000 year residence time of atmospheric O_2. The parameter $\Delta\varepsilon_{LAND}$, associated with this box model, approximately represents changes from the present in globally integrated (mostly) terrestrial O_2 isotopic fractionation:

$$\Delta\varepsilon_{LAND} \equiv \Delta\varepsilon_L - \Delta\varepsilon_{RL} - \Delta\varepsilon_{RO}\left(1 - \frac{1}{f_L}\right) \tag{6.1}$$

where $\Delta\varepsilon_L$ refers to the change from present in the fractionation of terrestrially produced oxygen relative to seawater, $\Delta\varepsilon_{RL}$ and $\Delta\varepsilon_{RO}$ respectively refer to changes from present in terrestrial and marine effective respiratory fractionation, and f_L is the fraction of oxygenesis occurring on land. Because the three terms in equation 6.1 are not independently discernible, Severinghaus et al. (2009) derive a formula for $\Delta\varepsilon_{LAND}$ in terms of knowable quantities: $\delta^{18}O_{sw}$, $\delta^{18}O_{atm}$ and time derivative of $\delta^{18}O_{atm}$ ($d\delta^{18}O_{atm}/dt$). The calculation of $\Delta\varepsilon_{LAND}$ in terms of these variables is described in section 6.2.1. $\Delta\varepsilon_{LAND}$, as estimated from SD $\delta^{18}O_{atm}$ measurements, is strongly correlated with Dongge cave $\delta^{18}O$ (Wang et al., 2005; Wang et al., 2001) over the past 12 ka (Severinghaus et al., 2009). Before this period, uncertainty in the original SD gas timescale prevented reliable high-precision comparison with other paleoclimate records. Improving the timescale for SD $\delta^{18}O_{atm}$ measurements is therefore a key goal of this work.

Modeling results from a recent freshwater hosing experiment suggest that changes in $\delta^{18}O_{atm}$ over a HS are dominated by changes in $\delta^{18}O_{precip}$ over the terrestrial biosphere (Reutenauer et al., 2015). In terms of equation 6.1, this finding suggests that $\Delta\varepsilon_{LAND}$ may be driven by $\Delta\varepsilon_{L}$. Below we build on the conclusion of this recent modeling study by exploring a composite WD-SD $\Delta\varepsilon_{LAND}$ record on an improved timescale and drawing insights from the modern seasonal cycles of terrestrial oxygenesis and $\delta^{18}O_{precip}$.

6.2. Methods

6.2.1. $\delta^{18}O_{atm}$ measurements, curve fitting and determination of $\Delta\varepsilon_{LAND}$

Ice samples from WAIS Divide were analyzed at Scripps Institution of Oceanography (SIO) between 2009 and 2016. A total of 1,037 ~15g ice samples were measured for $\delta^{15}N$ of N_2, $\delta^{18}O_{atm}$, $\delta O_2/N_2$ and $\delta Ar/N_2$, following the procedures of Petrenko et al. (2006) and Severinghaus et al. (2009). Measured values are reported relative to ratios measured in atmospheric air collected off Scripps Pier (La Jolla, CA). 560 unique depths were sampled, with 434 measured multiple times (2-4 replicate samples). To determine $\delta^{18}O_{atm}$, measured $\delta^{18}O$ of O_2 was corrected for gravitational settling by $\delta^{15}N$ and for gas loss by pair differences of $\delta O_2/N_2$ and $\delta Ar/N_2$, following Severinghaus et al. (2009). A brief overview of these corrections is given in Appendix 6.A. The pooled standard deviation of replicate gravity-and-gas-loss corrected $\delta^{18}O$ measurements at WD is 0.0085‰.

In order to evaluate a smooth derivative for the calculation of $\Delta\varepsilon_{LAND}$, discrete WD $\delta^{18}O_{atm}$ values were fit to a Fourier series ranging from 1/697 to 3.2 cycles ka^{-1} (spacing: 1/697 cycles ka^{-}

^{1}) by a Bayesian, weighted, linear least-squares technique, which *a priori* assumes a red spectrum and factors this assumption into the cost function (Severinghaus et al., 2009, Appendix 6.A). The time derivatives of SD (on its original timescale) and WD $\delta^{18}O_{atm}$ fitted curves were used to determine depth-gas age tie points between the two cores.

After synchronization of SD gas ages to the WD2014 timescale (Section 6.2.2), a composite fitted curve and time derivative of $\delta^{18}O_{atm}$ were calculated using all discrete SD and WD $\delta^{18}O_{atm}$ younger than 50.12 ka BP. $\Delta\varepsilon_{LAND}$ was calculated independently in three ways, from fitted $\delta^{18}O_{atm}$ curves and derivatives in 1) SD only, 2) WD only, and 3) the composite SD-WD record, each time using the same smoothed, interpolated $\delta^{18}O_{sw}$ record (Waelbroeck et al., 2002):

$$\Delta\varepsilon_{\mathrm{LAND}} = \frac{1}{f_L}\left(\delta^{18}\mathrm{O}_{\mathrm{atm}} - \delta^{18}\mathrm{O}_{\mathrm{sw}} + \tau\frac{d\delta^{18}\mathrm{O}_{\mathrm{atm}}}{dt}\right) \tag{6.2}$$

where f_L is the fraction of photosynthesis occurring on land (assumed to be 0.65) and τ is the residence time of atmospheric O_2 (1 ka).

6.2.2. Synchronization of Siple Dome gas ages to WAIS Divide

Siple Dome gas ages between 50 ka and 1950 CE were synchronized with the WAIS Divide WD2014 timescale (Buizert et al., 2015) using the smooth annual layer thickness (ALT) method of Fudge et al. (2014). The ALT method, as applied in this study, is a standard regularized linear least-squares method (Aster et al., 2013) that estimates an annual layer thickness history constrained by depth-gas age tie points and smoothness of the ALT time series. Integration of the resulting time series of annual layer thicknesses yields a gas age-depth chronology. Formally, the ALT method seeks an optimal annual layer thickness history, **m**, that minimizes the cost function C as defined:

$$C = \left\|\frac{\mathbf{Gm\text{-}d}}{\boldsymbol{\sigma}}\right\|_2^2 + \alpha\|\mathbf{Lm}\|_2^2 \tag{6.3}$$

where **G** is a matrix that maps annual layer thicknesses **m** to depths **d** corresponding to tie points of a given gas age. **L** is a second-derivative operator and α is a trade-off parameter between smoothness and tie-point agreement (the notation $\| \|_2^2$ indicates the squared L2 norm of the argument). Depth constraints are weighted based on individual estimates of tie point uncertainty, $\boldsymbol{\sigma}$, as discussed in detail in Appendix 6.B.

In total, 56 tie points were used to constrain the ALT inverse problem: 36 from SD and WD records of $d\delta^{18}O_{atm}/dt$, and 20 from SD and WD CH_4 records. Because $\delta^{18}O_{atm}$ is smoothly varying on millennial timescales due to the ~1 ka atmospheric residence time of O_2, WD and SD $d\delta^{18}O_{atm}/dt$ time series (calculated from fitted curves of $\delta^{18}O_{atm}$ at 10-year resolution, Appendix 6.A) were instead used for synchronization. Tie points based on $d\delta^{18}O_{atm}/dt$ were determined by calculating the midpoint times of abrupt transitions common to both records. CH_4-based tie points were determined by value-matching unambiguous abrupt transitions identified in the two records, within a prescribed error range of ±15 ppb. More complete explanations of the tie-point selection process, an estimate of its uncertainty, the application of the ALT method, and sensitivity tests are provided in Appendix 6.B. Figure 6.1 shows the fitted SD $\delta^{18}O_{atm}$ curve on its original (Brook et al., 2005) and WD2014-synchronized timescales alongside the WD $\delta^{18}O_{atm}$ discrete measurements and fitted curve. Figure 6.2 shows the synchronization results as a comparison between the original and new SD gas timescales, CH_4 and $d\delta^{18}O_{atm}/dt$ tie points, and the annual (gas) layer thickness profile of the new and original timescales.

6.2.3. Modern seasonal cycle analysis

To explore seasonal changes in the precipitation supplied to terrestrial oxygen production (Section 6.3.2), modern mean monthly gridded datasets of gross primary productivity (GPP; Jung et al., 2011) and $\delta^{18}O_{precip}$ (Terzer et al., 2013) were analyzed. The $\delta^{18}O_{precip}$ isoscape product used for our analysis (Section 6.3.2) was created from regionalized cluster-based water isotope prediction (RCWIP) constrained by 57,000 Global Network of Isotopes in Precipiation (GNIP) measurements from 1960 to 2009 (IAEA, 2017; IAEA/WMO, 2017; Terzer et al., 2013). The gridded monthly mean GPP product used in our study was determined from upscaled eddy covariance observations (FLUXNET) from 1982-2011 (Jung et al., 2011).

To estimate monthly terrestrial GPP-weighted $\delta^{18}O_{precip}$, monthly-mean isoscapes (originally 1/6° x 1/6°) were regridded using MATLAB's geoloc2grid function to 0.5° x 0.5° resolution to match the resolution of the GPP dataset. GPP data were converted from carbon (or, equivalently, oxygen after accounting for a photosynthetic quotient) fluxes to total emissions by multiplying by grid cell area. In equations 6.4 and 6.5 below, GPP refers to an emission, rather than a flux, and is therefore independent of latitude-varying grid cell area. Only land area between 60°S and 84°N was included due to data availability, with several gaps over low-GPP regions like the Sahara Desert and Greenland. Monthly global terrestrial GPP-weighted mean $\delta^{18}O_{precip}$ was calculated as follows:

$$\overline{\delta^{18}O_{precip}(t)} = \frac{\int_{-60}^{84}\int_{0}^{360} GPP(\varphi,\lambda,t)\delta^{18}O_{precip}(\varphi,\lambda,t)d\lambda d\varphi}{\int_{-60}^{84}\int_{0}^{360} GPP(\varphi,\lambda,t)d\lambda d\varphi} \tag{6.4}$$

where $\overline{\delta^{18}O_{precip}(t)}$ is terrestrial GPP-weighted mean $\delta^{18}O_{precip}$ during month t, and φ and λ refer to center latitudes and longitudes of terrestrial grid cells with spacing $d\lambda = d\varphi = 0.5°$.

The centroid latitude of terrestrial oxygenesis (φ_{TOE}) is defined as the latitude at which f_{GPP}, the meridionally cumulative fraction total monthly GPP, equals 0.5. Integrating northward from 60°S, we define φ_{TOE} such that:

$$f_{GPP}(\varphi_{TOE}) = \frac{\int_{-60}^{\varphi_{TOE}}\int_{0}^{360} GPP(\varphi,\lambda,t)d\lambda d\varphi}{\int_{-60}^{84}\int_{0}^{360} GPP(\varphi,\lambda,t)d\lambda d\varphi} = 0.5 \tag{6.5}$$

In practice, we estimate φ_{TOE} at finer resolution than the 0.5° spacing by first calculating zonal integrals around each band of grid cells and then linearly interpolating such that $d\varphi$ in equation 6.5 equals 0.006.

6.3. Results

6.3.1. $\Delta\varepsilon_{LAND}$ variations over past 50 ka

The WD-SD composite $\Delta\varepsilon_{LAND}$ record is shown in Figure 6.3 alongside a composite East Asian speleothem record of calcite $\delta^{18}O$ (Cheng et al., 2016) and discrete and continuous CH_4 records from WD (Rhodes et al., 2015; Sowers, 2012). The speleothem $\delta^{18}O$ record has been corrected for seawater $\delta^{18}O$ changes (Waelbroeck et al., 2002) and is shown both unsmoothed and smoothed (200-yr boxcar filter). There are several notable features of the composite $\Delta\varepsilon_{LAND}$ time series and its comparison to these other records.

First, $\Delta\varepsilon_{LAND}$ is positively and significantly correlated with the seawater-corrected East Asian speleothem $\delta^{18}O$ record ($r = 0.70$, $p < 0.0001$, both records interpolated linearly to 200-year resolution between 50 and 0 ka BP). The regression coefficient, β, over the entire 50-ka time window is 0.215 $‰_{atm}$ $‰_{pdb}^{-1}$. β varies between 0.387 $‰_{atm}$ $‰_{pdb}^{-1}$ during the Holocene (0-12 ka) to 0.168 $‰_{atm}$ $‰_{pdb}^{-1}$ during the last glacial period (12-50 ka). Although the reason for the glacial-interglacial change in β is unclear and a worthy topic of future study, the high correlation ($r = 0.62$, $p < 0.0001$) beyond the ~0-12 ka window originally considered by *Severinghaus et al.* (2009) confirms that the $\Delta\varepsilon_{LAND}$ and the Asian cave records share common variability throughout the last glacial period in addition to the Holocene. We note that the misalignment of $\Delta\varepsilon_{LAND}$ and Chinese cave $\delta^{18}O$ excursions during HS2 may indicate a dating error in the WAIS Divide timescale. The remainder of our analysis is focused on comparison with the WAIS Divide CH_4 record which shares a common timescale (WD2014) with the composite $\Delta\varepsilon_{LAND}$ record. Absolute dating errors in WD2014 therefore do not hamper comparison of these two records.

Second, over the portion of the last glacial period covered by this record (~50-12 ka BP), $\Delta\varepsilon_{LAND}$ only consistently exceeds 0‰ (for more than a century) during the Younger Dryas and HS 1, 2, 4 and 5. $\Delta\varepsilon_{LAND}$ exhibits pronounced abrupt increases (downward in Figure 6.3) during HEs. Following HE 1, 2, 4 and 5 – all of predominant Hudson strait origin (Hemming, 2004) – $\Delta\varepsilon_{LAND}$ abruptly increases by ~0.1-0.3‰ over 200 to 300 years and remains generally high for ~1-2 thousand years. The timings of $\Delta\varepsilon_{LAND}$ maxima during each of HS 1, 2, 4, and 5 all occur within the proposed time windows of abrupt, large-scale climate responses to each HE (Rhodes et al., 2015, Figure 6.4). Similarly, these proposed windows of HE climate correspond to periods of sustained above-average $\Delta\varepsilon_{LAND}$ values. Uncertainty in the measurement of $\delta^{18}O_{atm}$ and the computation of its time derivative preclude meaningful analysis of centennial-scale changes in $\Delta\varepsilon_{LAND}$ of below ~0.05‰.

Increases in $\Delta\varepsilon_{LAND}$ over HSs stand in contrast to repeated decreases during D-O warmings. Notably, atmospheric CH_4 increases during both D-O warmings and HE 1, 2, 4 and 5 (Northern Hemisphere cooling events). Thus, the relationship between $\Delta\varepsilon_{LAND}$ and atmospheric CH_4 reverses in sign between Northern Hemisphere warming and cooling. In Section 6.4 we discuss the implications of this reversal for inference of the position of the thermal equator and tropical rainfall belts.

3.2 Seasonal cycle of terrestrial photosynthetic source water $\delta^{18}O$

We analyzed monthly-mean datasets of $\delta^{18}O_{precip}$ and GPP on land (Section 6.2.3) to test the sensitivity of GPP-weighted mean $\delta^{18}O_{precip}$ to the median latitude of oxygenesis over the seasonal cycle, which serves as a rough analogue for past shifts in the thermal equator. Figure 6.5

shows December-January-February (DJF) and June-July-August (JJA) mean spatial distributions of $\delta^{18}O_{precip}$ and GPP. Throughout all seasons, $\delta^{18}O_{precip}$ generally trends isotopically lighter northward between the southern mid-latitudes and northern high-latitudes. The meridional trend in GPP, however, exhibits a strong seasonal dependence in its sign. As the northern terrestrial biosphere grows from boreal spring to summer, a northern maximum develops in the mid-to-high latitudes (Figure 6.6), shifting the centroid of terrestrial oxygen production northward. During boreal fall and winter, northern hemisphere productivity decreases, shifting terrestrial oxygenesis southward toward the relatively seasonally invariable southern tropical maximum near 5°S.

For the purpose of quantifying meridional shifts in terrestrial GPP, we define the terrestrial oxygenesis equator (TOE) as the latitude of the terrestrial GPP centroid (Figure 6.S1, Section 6.2.3). In simpler terms, half of all terrestrial oxygen production occurs to the north and half to the south of the seasonally varying TOE. The TOE shifts from ~5°S in boreal winter to ~35°N in boreal summer (Figure 6.7).

To determine the direct influence of $\delta^{18}O_{precip}$ on the $\delta^{18}O$ of O_2 produced by the terrestrial biosphere, we calculated monthly GPP-weighted mean $\delta^{18}O_{precip}$. Throughout the entire seasonal cycle, GPP-weighted mean $\delta^{18}O_{precip}$ varies by ~2.6‰, with the isotopically lightest and heaviest GPP-weighted precipitation occurring during boreal summer and winter, respectively. GPP-weighted mean $\delta^{18}O_{precip}$ was found to be strongly and significantly correlated with TOE latitude over the seasonal cycle ($r = 0.95$, $p < 0.0001$), with a mean sensitivity of -0.066‰ per degree TOE latitude. Applying a last glacial ice mask (Argus et al., 2014) such that GPP was set to zero of glaciated land areas at 26 ka, we find the mean sensitivity of GPP-weighted mean $\delta^{18}O_{precip}$ remains similar (-0.072‰/°latitude).

6.4. Discussion

Considering the observed seasonal-cycle relationship between the TOE and global terrestrial GPP-weighted mean $\delta^{18}O_{precip}$, here we propose a mechanism by which meridional shifts in the TOE are unambiguously recorded in the sign of $\Delta\varepsilon_{LAND}$ changes. Although the seasonal cycle is an imperfect analog for abrupt climate change during the last glacial period, the analysis presented in Section 6.3.2 highlights the importance of the meridional distribution of oxygen production for the GPP-weighted mean $\delta^{18}O$ of photosynthetic source water. Specifically, a northward shift of the TOE (e.g. during a D-O warming) lowers global GPP-weighted mean $\delta^{18}O_{precip}$ while a southward shift (e.g., during a HS) does the opposite. We suggest that the sign of this relationship is robust over long timescales although the magnitude likely varies. A simple experiment in which the modern terrestrial GPP climatology (with a 26-ka ice mask) is perturbed by reducing Northern Hemisphere GPP and increasing Southern Hemisphere GPP each uniformly by 25% suggests that several-degree-latitude shifts in the TOE may produce changes in terrestrial GPP-weighted mean $\delta^{18}O_{precip}$ that are comparable in magnitude (order 0.1‰) to $\Delta\varepsilon_{LAND}$ changes over HSs (Figure 6.S4). To further explore this notion, we consider our original definition of $\Delta\varepsilon_{LAND}$ (equation 6.1). In this definition, $\Delta\varepsilon_L$ encompasses all changes in global leaf water isotopic composition, which may be divided into separate source water and evapotranspiration components:

$$\Delta\varepsilon_L = \Delta\delta^{18}O_S + \Delta\varepsilon_{ET} \tag{6.6}$$

$\delta^{18}O_S$ is the change from present in oxygen production-weighted source-water $\delta^{18}O$ (having removed the influence of changes in seawater $\delta^{18}O$) and $\Delta\varepsilon_{ET}$ is the change from present in oxygen production-weighted evapotranspiration enrichment of leaf water $\delta^{18}O$.

Many studies of Dole effect variability over the last glacial cycle (e.g. Bender et al., 1994; Severinghaus et al., 2009; Landais et al., 2010) have identified low-latitude precipitation as a key driver, based on coherence with orbital precession and atmospheric methane as well as high correlation with Chinese stalagmite δ^{18}O. A recent quantitative, earth system model-based analysis of Dole effect variations over a simulated HS corroborates the hypothesized influence of low-latitude precipitation and finds that the increase in $\delta^{18}O_{atm}$ over a HS can be explained almost entirely by changes in terrestrial oxygen production-weighted $\delta^{18}O_{precip}$ (Reutenauer et al., 2015). Reutenauer et al. (2015) find that oxygen production-weighted relative humidity stays effectively constant between HS and background glacial conditions. Because relative humidity governs leaf water fractionation due to evapotranspiration (Craig and Gordon, 1965), this suggests negligible change in $\Delta\varepsilon_{ET}$ and implies (in terms of equation 6.6) that $\Delta\varepsilon_L \approx \Delta\delta^{18}O_S$

The latitude dependence of global GPP-weighted $\delta^{18}O_{precip}$ over the modern seasonal cycle implies that $\Delta\varepsilon_{LAND}$ should be sensitive to the position of the TOE over a HE. At present, however, it is impossible to determine the exact TOE sensitivity of $\Delta\varepsilon_{LAND}$ because it is modulated by changes in the underlying spatial distribution of $\delta^{18}O_{precip}$. For instance, Chinese speleothem calcite records (Cheng et al., 2016; Wang et al., 2001; Wang et al., 2008) as well as isotope-enabled climate model simulations (Battisti et al., 2014; Liu et al., 2014) demonstrate that $\delta^{18}O_{precip}$ in southeastern China changes with EASM (East Asian Summer Monsoon) strength, such that local $\delta^{18}O_{precip}$ decreases during periods of an intense monsoon and increases with a weaker monsoon. Since this region is important for global oxygen production, it follows that a decrease in EASM intensity after a HE would act to increase $\Delta\varepsilon_{LAND}$. However, concurrent, smaller-amplitude decreases in southern tropical rainfall $\delta^{18}O_{precip}$ during a HS (Kanner et al., 2012), particularly in the productive Amazon lowlands (Wang et al., 2017), may somewhat offset this increase in

$\Delta\varepsilon_{LAND}$. Reutenauer et al. (2015) find that decreased southern tropical $\delta^{18}O_{precip}$ does not fully compensate for increased Northern Hemisphere $\delta^{18}O_{precip}$, and conclude that spatial changes in $\delta^{18}O_{precip}$ over the terrestrial biosphere impart a net increase on $\delta^{18}O_{atm}$ over a simulated HS.

Clearly, to understand $\Delta\delta^{18}O_S$ one must consider both 1) changes in regional $\delta^{18}O_{precip}$ ($\Delta\delta^{18}O_{precip}$), and 2) changes in the distribution of oxygen production (the TOE, to first order). We suggest that $\Delta\delta^{18}O_S$ is driven by the superposition of these two components, both of which likely operate in the same direction. For a northward migration of the thermal equator and tropical rainfall belts, rainfall over productive northern regions like Southeast Asia becomes more isotopically depleted (Battisti et al., 2014; Cheng et al., 2016; Liu et al., 2014; Wang et al., 2001; Wang et al., 2008). Assuming Northern Hemisphere $\Delta\delta^{18}O_{precip}$ outweighs Southern Hemisphere $\Delta\delta^{18}O_{precip}$, a northward migration of the tropical rainfall belts imparts a negative signature on $\Delta\delta^{18}O_S$. Similarly, a northward shift of the thermal equator and therefore a warmer and wetter northern hemisphere (and cooler, drier southern hemisphere) shifts the TOE northward as well. By increasing the relative contribution of the low-$\delta^{18}O_{precip}$ Northern tropics and mid-latitudes to global terrestrial O_2, global $\Delta\delta^{18}O_S$ will also decrease. Each of these effects on 1) and 2) – and especially their combination – would lead to a decrease in $\Delta\delta^{18}O_S$ and thus a decrease in $\Delta\varepsilon_{LAND}$ for an abrupt northern hemisphere warming (e.g. a D-O warming). In the opposite scenario (southward shift of thermal equator) during a HE, for example, the superposition of 1) and 2) would act to increase $\Delta\delta^{18}O_S$ because of a strong increase in Northern Hemisphere $\delta^{18}O_{precip}$ and a southward shift of the TOE. Therefore, we suggest that the sign of a $\Delta\varepsilon_{LAND}$ change faithfully reflects the direction of meridional shifts in the thermal equator and tropical rainfall belts.

While changes in respiratory fractionation, $\Delta\varepsilon_{RL}$, are poorly known, two leading suggestions for the response of $\Delta\varepsilon_{RL}$ to large-scale hydroclimate change each reinforce the notion that the sign of $\Delta\varepsilon_{LAND}$ change is a robust indicator of meridional shifts in tropical rainfall. First, Reutenauer et al. (2015) find that changes in terrestrial respiration over a modeled HS are uncertain but small, one order of magnitude less important than GPP-weighted $\delta^{18}O_{precip}$ in explaining the modeled change in $\delta^{18}O_{atm}$. If true, this is consistent with the notion that $\Delta\varepsilon_{LAND}$ is largely controlled by $\Delta\varepsilon_{L}$, which mostly reflects $\Delta\delta^{18}O_{S}$. Second, if instead global $\Delta\varepsilon_{RL}$ does appreciably vary with shifts in tropical rainfall, a candidate mechanism is the "monsoon rectifier effect" which proposes that changes in $\Delta\varepsilon_{RL}$ may oppose and partially conteract changes in $\Delta\delta^{18}O_{S}$ at high latitudes but amplify changes in $\Delta\delta^{18}O_{S}$ in monsoon regions (Luz & Barkan, 2011; Severinghaus et al., 2009). This notion hinges on the close coupling between local photosynthesis and respiration, along with the temperature dependence of soil respiration fractionation, which is stronger (i.e. increased discrimination of ^{18}O) in cold high-latitude soils (Angert et al., 2012). If, for example, northern high-latitude GPP were to increase (e.g. for a northward shift of the thermal equator during a D-O warming), so too would northern high-latitude soil respiration. In terms of equation 6.1, then, the lowering of $\Delta\varepsilon_{L}$ (due to contribution of the isotopically light high-latitude source water) would be somewhat offset by a more negative $\Delta\varepsilon_{RL}$ (stronger fractionation), leading to attenuation of any change in $\Delta\varepsilon_{LAND}$. In monsoon regions, however, a stronger monsoon accompanying a northward shift of the thermal equator would result in both lower $\delta^{18}O_{precip}$ and weaker (less negative) soil respiration fractionation due to slow diffusion of oxygen in wet soils (Angert et al., 2001). In these regions, a lowering of $\Delta\varepsilon_{L}$ would be accompanied by less negative $\Delta\varepsilon_{RL}$, both of which act to lower $\Delta\varepsilon_{LAND}$. Therefore, in either case – whether $\Delta\varepsilon_{RL}$ is negligible or amplifies monsoon $\delta^{18}O_{precip}$ signals – one would still expect a net decrease (increase) in $\Delta\varepsilon_{LAND}$ for a northward (southward) shift of the thermal equator and tropical rain belts.

The TOE-latitude dependence of past changes in $\Delta\varepsilon_{LAND}$ makes the composite SD-WD $\Delta\varepsilon_{LAND}$ record a useful complement to other records of past tropical hydroclimate change. A recent analysis of the high-resolution WD CH_4 record suggests that abrupt peaks in CH_4 during Hudson-strait HS (HS 1, 2, 4 and 5) are imprints of HE (Rhodes et al., 2015). Because past changes in tropical wetland CH_4 emissions are thought to be a bimodal function of the latitude of the thermal equator (Rhodes et al., 2015), an abrupt northern hemisphere cooling and southward shift of the thermal equator and land-extension of the intertropical convergence zone (ITCZ) would intensify southern tropical precipitation and thus enhance CH_4 emissions. However, because northern hemisphere warming (e.g. D-O events) also increases atmospheric CH_4 emissions by stimulating northern wetland emissions, CH_4 measurements alone cannot definitively reveal the direction of meridional shifts in tropical rainfall. $\Delta\varepsilon_{LAND}$, which increases during and after CH_4 peaks representing HE (Figure 6.4), implies a southward shift of the TOE and therefore provides strong evidence supporting the interpretation that these CH_4 peaks have a Southern Hemisphere source.

Future higher-resolution measurements of $\delta^{18}O_{atm}$ from WD alone may yield further insight into large-scale hydroclimate changes. A WD-only record would remove any uncertainty in $\Delta\varepsilon_{LAND}$ induced by the WD-SD synchronization process and allow for direct comparison with WD CH_4. Centennial-scale WD CH_4 variability may indicate important tropical dynamics (Rhodes et al., 2017) that could be elucidated by a companion high-resolution $\Delta\varepsilon_{LAND}$ record. For instance, the centennial-scale oscillations in $\Delta\varepsilon_{LAND}$ following HE 1, which appear independently in both the SD and WD records, possibly hint that $\Delta\varepsilon_{LAND}$ may have spectral power in the centennial band.

Finally, we caution against over-interpretation of small changes in $\Delta\varepsilon_{LAND}$ as clear indications of shifts in TOE latitude. Although global GPP-weighted mean $\delta^{18}O_{precip}$ is a first-order control on $\Delta\varepsilon_{LAND}$, small, under-constrained changes over time in respiratory fractionation, evapotranspiration fractionation, the marine Dole effect, the terrestrial fraction of global oxygen production, and the slope of the TOE-$\delta^{18}O_{precip}$ relationship preclude meaningful analysis of 0.01‰-order $\Delta\varepsilon_{LAND}$ variability.

6.5. Conclusions

We analyzed a composite record of $\delta^{18}O_{atm}$ from the Siple Dome and WAIS Divide ice cores to compare synchronous instantaneous changes in the terrestrial fractionation of $\delta^{18}O_{atm}$ to records of Chinese speleothem $\delta^{18}O$ and WAIS Divide atmospheric methane. Based on an analysis of the modern seasonal cycles of terrestrial oxygen production and production-weighted $\delta^{18}O_{precip}$, we propose a simple relationship between spatial shifts in terrestrial oxygenesis and $\delta^{18}O_{atm}$. Specifically, we identify a strong negative correlation between the centroid latitude of terrestrial oxygenesis and GPP-weighted mean $\delta^{18}O_{precip}$. This relationship suggests that positive $\delta^{18}O_{atm}$ (or $\Delta\varepsilon_{LAND}$) anomalies should accompany southward shifts of terrestrial oxygen production. Because productivity has strong hydroclimate controls, we propose that this mechanism may explain much of the shared variability between past changes in the Dole Effect and proxies for low-latitude hydrological changes. Finally, positive excursions in $\Delta\varepsilon_{LAND}$ during HS 1, 2, 4 and 5 culminate in local $\Delta\varepsilon_{LAND}$ maxima which shortly follow abrupt increases in atmospheric CH_4 (of several tens of ppb) that occurred within these stadial periods (times of otherwise low CH_4 concentrations). These changes in $\Delta\varepsilon_{LAND}$ imply southward shifts of terrestrial rainfall and therefore strongly support that interpretation that the near-contemporaneous spikes in methane – proposed to be evidence of a rapid atmospheric teleconnection during HE 1, 2, 4 and 5 – had a Southern Hemisphere source.

Appendix 6.A: Gas-loss correction and curve fitting

Following Severinghaus et al. (2009), WD $\delta^{18}O$ measurements were corrected for enrichment due to gravitational settling and fractionation during gas loss. Gravitational settling leads to an increase in heavy to light gases, scaling nearly linearly with their mass difference (Craig et al., 1988). Gravitational corrections were made to each measurement ($\delta^{18}O$, $\delta O_2/N_2$, $\delta^{15}N$, $\delta Ar/N_2$) as follows:

$$\delta_{gravcorr} = \delta_{meas} - \Delta m \cdot \delta^{15}N \tag{6.A1}$$

where δ_{meas} is a raw measured gas ratio, $\delta_{gravcorr}$ is its gravitationally corrected value, and Δm is the mass difference between heavy and light gases in amu (4 for $\delta O_2/N_2$, 12 for $\delta Ar/N_2$, and 2 for $\delta^{18}O$).

To determine $\delta^{18}O_{atm,}$ $\delta_{gravcorr}$ was corrected empirically for fractionation due to gas loss. Slow loss of gases from the lattice to microcracks causes mass-independent fractionation which affects $\delta O_2/N_2$ and $\delta Ar/N_2$, due to their different diameters, but does not affect isotopes (Bender et al., 1995). Mass-dependent fractionation, which affects elemental and isotopic ratios, occurs due to diffusive loss of gases through the microcracks (Kobashi et al., 2008). Following Severinghaus et al. (2009) we find a plane of best fit (Figure 6.S3) by regressing gravitationally corrected $\delta^{18}O$ replicate pair differences ($\Delta\delta^{18}O_{gravcorr}$) against gravitationally corrected $\delta O_2/N_2$ and $\delta Ar/N_2$ pair differences ($\Delta\delta O_2/N_{2,gravcorr}$ and $\Delta\delta Ar/N_{2,gravcorr}$):

$$\Delta\delta^{18}O_{gravcorr} = A \cdot \Delta\delta O_2/N_{2,gravcorr} + B \cdot \Delta\delta Ar/N_{2,gravcorr} \tag{6.A2}$$

The regression coefficients governing this plane of best fit (R^2=0.31), *A* and *B*, are nearly equal and opposite in sign (A=-0.00454; B=0.00447) similar to the finding of Severinghaus et al (2009) in SD samples, implying that fractionation of $\delta^{18}O_{gravcorr}$ is indeed due to mass-dependent fractionation process (proportional to: $\delta Ar/N_{2,gravcorr}$ - $\delta O_2/N_{2,gravcorr}$), as the mass-independent fractionation process equally fractionates $\delta Ar/N_2$ and $\delta O_2/N_2$. Finally, $\delta^{18}O_{atm}$ is calculated by removing this empirically determined mass-dependent fractionation and fixing the mean $\delta^{18}O_{atm}$ value over the last 1000 years to 0‰ by choosing *C* (below) to be 1.357:

$$\delta^{18}O_{atm} = \delta^{18}O_{gravcor} - A\cdot(\delta O_2/N_{2,gravcorr} + C) - B\cdot\delta Ar/N_{2,gravcorr} \tag{6.A3}$$

In order to reduce the influence of noise in calculating time derivatives of $\delta^{18}O_{atm}$ from SD, WD and the composite record, each record was fit to a Fourier series by weighted linear least squares. Following Severinghaus et al. (2009), Fourier amplitudes were assumed to be inversely proportional to their squared frequency (i.e. red spectrum). A Fourier series with frequencies ranging from 1/697 to 3.2 cycles ka^{-1} with spacing of 1/697 cycles ka^{-1} was used for curve fitting. $\delta^{18}O_{atm}$ data were weighted according to measurement uncertainties (pooled standard deviations of 0.0095‰ and 0.0085‰ for SD and WD, respectively). SD outliers with anomalous $\delta^{15}N$ were downweighted as in Severinghaus et al. (2009). After determining Fourier amplitudes, continuous fitted curves and analytical derivatives were evaluated at 10-year resolution.

Appendix 6.B: Details of Synchronization Method

The gas timescale synchronization method implemented in this study (ALT, Fudge et al., 2014) optimizes error-weighted tie point agreement and smoothness of the annual layer thickness profile. Note that because this study only concerns gas ages, annual layer thicknesses are defined as vertical distances between two ice layers containing gas bubbles differing in age by one year. Here we present: 1) the formally defined linear least squares problem and its uncertainty estimate, 2) methods for tie point selection and uncertainty analysis, 3) an evaluation of the WD2014-synchronized SD gas age timescale, and 4) the results of a sensitivity test using an alternate initial SD timescale for tie-point selection.

The generalized ALT cost function (equation 6.3) is given here in the full form used in our analysis (bold, capitalized and lower-case letters denote matrices and vectors, respectively, while unbolded letters denote scalars):

$$\mathrm{C} = \mathbf{m}^{\mathbf{T}}\mathbf{G}^{\mathbf{T}}\mathbf{W}\mathbf{G}\mathbf{m} - \mathbf{2}\mathbf{m}^{\mathbf{T}}\mathbf{G}^{\mathbf{T}}\mathbf{W}\mathbf{d} + \mathbf{d}^{\mathbf{T}}\mathbf{W}\mathbf{d} + \alpha\mathbf{m}^{\mathbf{T}}\mathbf{L}^{\mathbf{T}}\mathbf{L}\mathbf{m} \tag{6.B1}$$

where (as in equation 6.3) **G** maps annual layer thicknesses, $\mathbf{m}$, to a depth-gas age relationship evaluated at tie point depths, **d**. **L** is a second derivative operator, α is a trade-off parameter between smoothness and tie-point agreement, and **W** is a weighting matrix with inverse tie point depth uncertainties ($1/\boldsymbol{\sigma}^2$) along its diagonal. The time series of annual layer thicknesses that minimizes equation 6.B1, $\hat{\mathbf{m}}$, found at the zero crossing of $\frac{\partial \mathrm{C}}{\partial \mathbf{m}}$:

$$\hat{\mathbf{m}} = \mathbf{G}^{\#}\mathbf{d} \tag{6.B2}$$

Equation B2 follows the common notation of Lundin et al. (2012) and Aster et al. (2013), such that $\mathbf{G}^{\#}$ is defined as:

$$\mathbf{G}^{\#} = (\mathbf{G}^{\mathbf{T}}\mathbf{W}\mathbf{G} + \alpha\mathbf{L}^{\mathbf{T}}\mathbf{L})^{-\mathbf{1}}\,\mathbf{G}^{\mathbf{T}}\mathbf{W} \tag{6.B3}$$

We note that an alternate formulation of $\mathbf{G}^{\#}$ is possible by using generalized singular value decomposition (Aster et al., 2013; Lundin, 2012). We solved for $\hat{\mathbf{m}}$ via singular value decomposition and found that the maximum absolute disagreement of the resulting annual layer thickness profile with the one calculated using B2 and B3 was negligible (order 10^{-8} meters).

The 1σ uncertainty of $\hat{\mathbf{m}}$ (for a fixed value of α) is initially estimated by taking the square root of the diagonal values on the covariance matrix, $\mathbf{V}_{\mathbf{m}}$:

$$\mathbf{V}_{\mathbf{m}} = \mathbf{G}^{\#}\mathbf{G}^{\#\mathbf{T}} \tag{6.B4}$$

However, uncertainty in α also contributes to uncertainty in $\hat{\mathbf{m}}$. We account for this additional source of uncertainty by determining two candidate optimal values of α and evaluating resulting timescales using each value. These two candidate values of α minimize root mean square deviations between WD fitted-curve and SD discrete 1) $\delta^{18}O_{atm}$ values, or 2) CH_4 values, with SD gas ages shifted in each case to a new estimate of the WD2014-synchronized timescale. We evaluate $\hat{\mathbf{m}}$ separately for each value of α and take the absolute difference between these two time series of $\hat{\mathbf{m}}$ as an estimate of the 1σ uncertainty in our $\hat{\mathbf{m}}$ due to uncertainty in α. The final estimate of 1σ uncertainty in $\hat{\mathbf{m}}$ is then given by the quadrature sum of the covariance-matrix (fixed α) estimate (equation 6.B3) and the estimated uncertainty due to α described above.

Tie points were estimated by matching abrupt transitions in $d\delta^{18}O_{atm}/dt$ and CH_4 in the WD and SD records. To find $d\delta^{18}O_{atm}/dt$-based tie points, continuous time derivatives of the fitted $\delta^{18}O_{atm}$ curves were first evaluated as described in Appendix 6.A. All local minima and maxima in $d\delta^{18}O_{atm}/dt$ were then identified and 36 abrupt transitions identifiable in each record were selected (each one between an identified local minimum and maximum). The midpoint time of a transition was found by determining when $d\delta^{18}O_{atm}/dt$ was halfway between the bounding extrema. The times at which $d\delta^{18}O_{atm}/dt$ was 25% and 75% between bounding extrema were taken as ±1σ uncertainty estimates. Figure 6.B1 shows abrupt $d\delta^{18}O_{atm}/dt$ transition midpoints, bounding extrema, and 25-75% markers identified in the SD (original timescale) and WD records. For each $d\delta^{18}O_{atm}/dt$ midpoint, corresponding SD depths and WD gas ages were used as tie points for the synchronization method.

A similar approach was employed to determine CH_4-based tie points using CH_4 records at SD and WD. Since WD CH_4 records (Rhodes et al., 2015; Sowers, 2012) are far higher resolution than SD CH_4 records (Ahn et al., 2012, 2014; Ahn and Brook, 2014; Brook et al., 2005; Ahn and Yang, unpublished), discrete SD CH_4 values were selected during abrupt transitions for which the magnitude of SD and WD CH_4 values were in good agreement. 20 of these discrete mid-transition values were identified and used as tie-points. To find a WD gas age matching the SD depth of a discrete CH_4 measurement, the gas age of the nearest value in the 2-yr resolution WD record was determined. The 1σ uncertainty range for CH_4 tie points was estimated from the range of gas ages corresponding to all nearby WD CH_4 values that agreed with the selected SD CH_4 value to within ±15 ppb. Figure 6.B2 illustrates this CH_4 tie point value matching and uncertainty process.

We also tested the sensitivity of the resulting timescale to the chosen CH_4 matching value range (±15 ppb) by varying it from ±5 to ±25 ppb to construct alternate timescales. Figure 6.S5 shows deviations of these alternate timescales from the final timescale used in this study. The results of this test suggest that the choice of ±15 ppb for the final timescale is reasonable, because alternate timescales constructed with ranges of ±10 and ±20 ppb agree with the ±15 ppb-based timescale within ±1σ uncertainty at all times, with a maximum absolute deviation of ~58 years.

Together, $d\delta^{18}O_{atm}/dt$ and CH_4 tie points were used to constrain equation 6.B2 via the weighting matrix $\mathbf{W}$ to produce a best estimate of SD annual layer thicknesses at 10-year resolution from 50.12-0 ka BP (before 1950). Integrating this annual layer thickness time series yields a depth-gas age relationship. Figure 6.2 shows the annual layer thickness estimate, its uncertainty, and a comparison between our new ALT-based and the original Brook et al. (2005) SD timescales. To assess the validity of the new SD gas timescale estimate, we calculated root mean squared deviations (RMSDs) between WD (fitted curve or interpolated) and SD (discrete) $\delta^{18}O_{atm}$ and CH_4 on the original and new timescales. Although a non-ideal evaluation metric for relatively flat portions of these records, RMSDs penalize timescale errors during transitions. The substantial RMSD reductions between the original and new timescale add confidence to the synchronization method. CH_4 RMSDs decrease from 33.7 to 18.3 ppb on the original and new timescales, respectively. $\delta^{18}O_{atm}$ RMSDs decrease from 0.029 to 0.022‰ on the original and new timescales, respectively. Figures S5 and B3 show fitted and interpolated WD $\delta^{18}O_{atm}$ and CH_4 curves, respectively, alongside discrete SD $\delta^{18}O_{atm}$ and CH_4 measurements on the original and new timescales.

To investigate the sensitivity of our SD depth-gas age to the initial SD timescale, we repeated the SD tie point selection procedure and least squares minimization using an alternate SD timescale. This sensitivity test was motivated by concern that error in the original timescale would lead to error in the magnitude of the time derivative of $\delta^{18}O_{atm}$. The tie point method implemented in this study (aligning the midpoints of $d\delta^{18}O_{atm}/dt$ transitions rather than value-matching) partially alleviates this concern. Nonetheless, for completeness, we carried out a sensitivity test using an alternate initial SD timescale for curve fitting, differentiation, and tie point determination to constrain synchronization method (equation 6.3). Because the Brook et al. (2005) timescale was constructed by tying SD gas measurements to the Meese/Sowers GISP2 (Greenland) ice core timescale (Meese, 1999), we added the difference in gas ages between the Meese/Sowers and more recent GICC05 timescales (Rasmussen et al., 2014) to the Brook et al. (2005) SD timescale. This resulting alternate timescale differs from the original Brook et al. (2005) timescale by up to ~2 ka in the interval from ~50 ka to present. This alternate timescale is notable older before ~45 ka, as shown clearly by comparison of SD $d\delta^{18}O_{atm}/dt$ records on the original and alternate GISP2-tied timescales (Figure 6.S6). The close similarities in the magnitude of SD $d\delta^{18}O_{atm}/dt$ on the original and alternate timescales strongly indicates that the small dating errors are not significant enough to substantially affect the magnitude of the $\delta^{18}O_{atm}$ derivative. Each of the 36 transitions associated with $d\delta^{18}O_{atm}/dt$ tie points was identifiable on this alternate timescale (Figure 6.S7). After determining the depths corresponding to these midpoints on the alternate timescale (in order to determine tie point array **d** for equation 6.B2) midpoint depths were compared between the original and alternate timescales and found to agree within the 25-75% transition value derived 2σ

uncertainty range for 35 of 36 tie points. The same CH_4 tie point method was implemented and the resulting set of 46 depth-gas age tie points was used to estimate an alternate annual layer thickness profile via the ALT method (equation 6.3). This alternate estimate was found to agree the original estimate within 2σ uncertainty throughout the entire time range considered (Figure 6.S8). We therefore conclude that given these relatively small dating errors of below ~2 ka, the $\delta^{18}O_{atm}$ derivative-based tie point determination method is justified.

Acknowledgements

We thank Bruce Cornuelle for helpful discussions about curve fitting and linear optimization, Ross Beaudette for ice core measurements, and the WAIS Divide and Siple Dome project members for making this work possible. WAIS Divide atmospheric oxygen isotope measurements were made at Scripps Institution of Oceanography's Noble Gas Isotope Laboratory and were supported by National Science Foundation grant 0538657.

This chapter, in full, is a reproduction of material as it appears in Seltzer, A., Buizert, C., Baggenstos, D., Brook, E., Ahn, J., Woong, J.-W., and Severinghaus, J. Does $\delta^{18}O$ of O_2 record meridional shifts in tropical rainfall? *Climate of the Past*, 2017. The dissertation author was the primary investigator and author of this work.

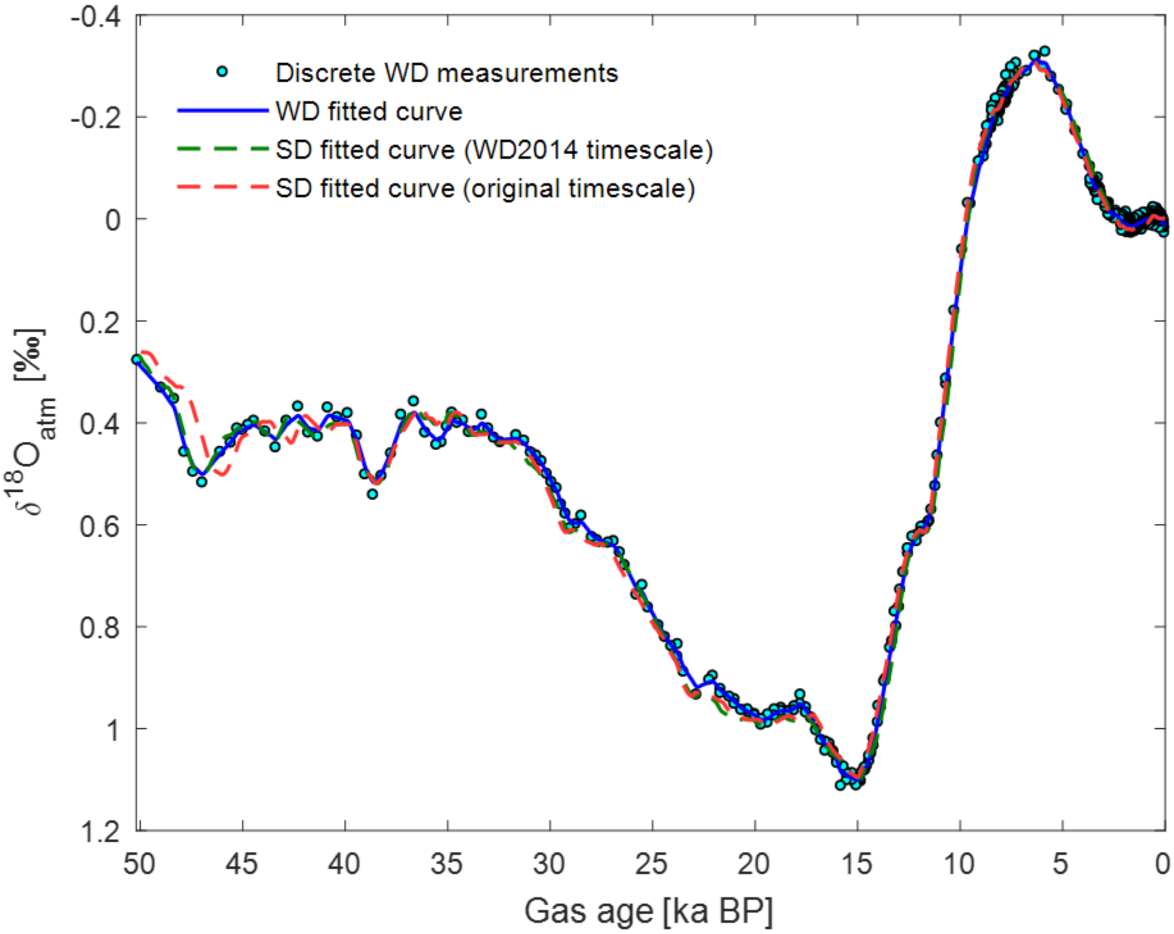

Figure 6.1: Discrete measurements from WAIS Divide (light blue markers) and fitted curves of $\delta^{18}O_{atm}$ from WAIS Divide (solid blue line) and Siple Dome on its original gas timescale (red dashed line, Brook et al., 2005) and WD2014-synchronized gas timescale (green dashed line, this study).

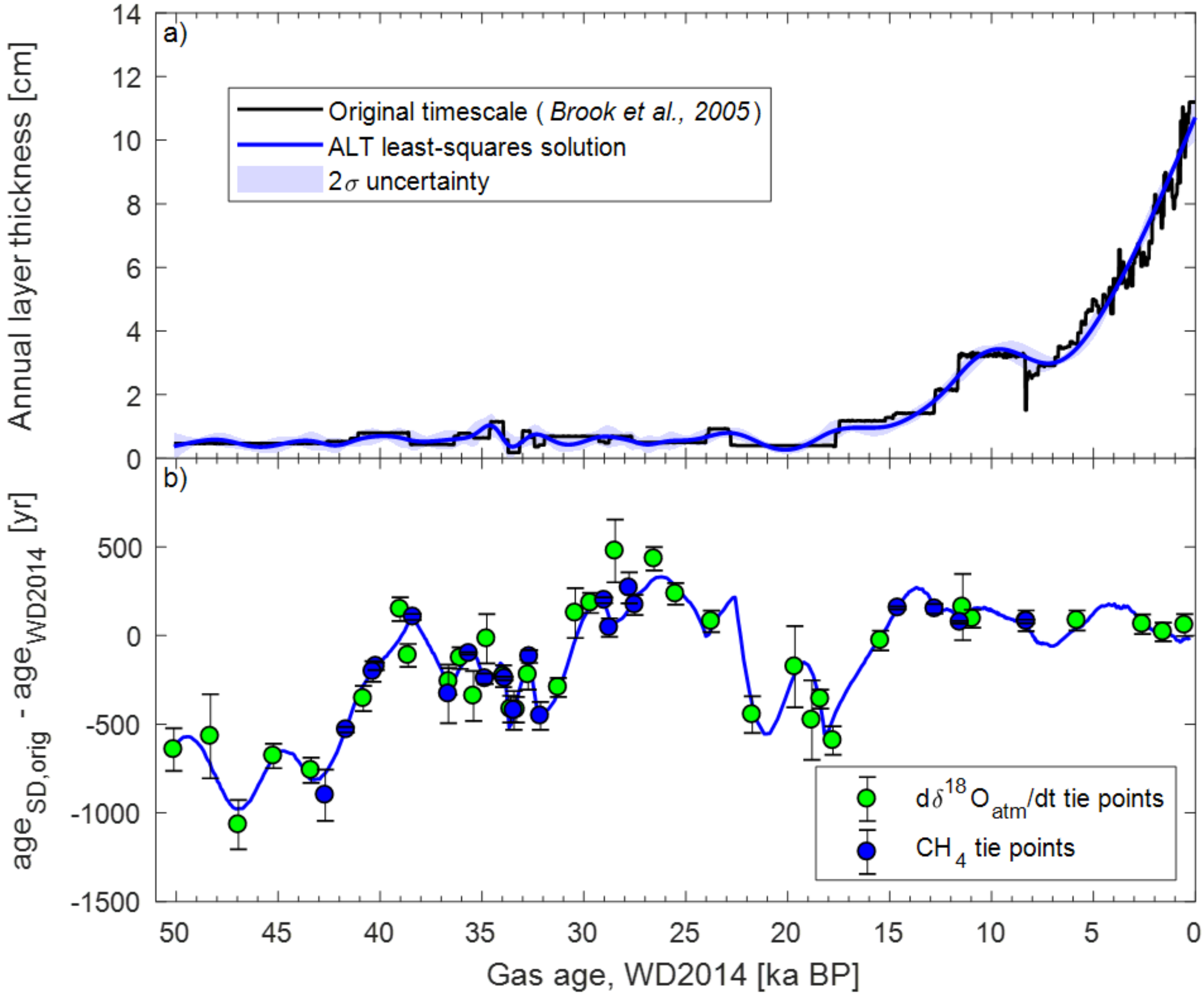

Figure 6.2: Annual layer thickness **(a)** from the original Siple Dome gas timescale (Brook et al., 2005) and WD2014-synchronized timescale (this study), and gas age differences between the original and WD2014-synchronized Siple Dome gas timescales **(b)** constrained by tie points selected from abrupt transitions in the CH_4 and $d\delta^{18}O_{atm}/dt$ records at SD and WD.

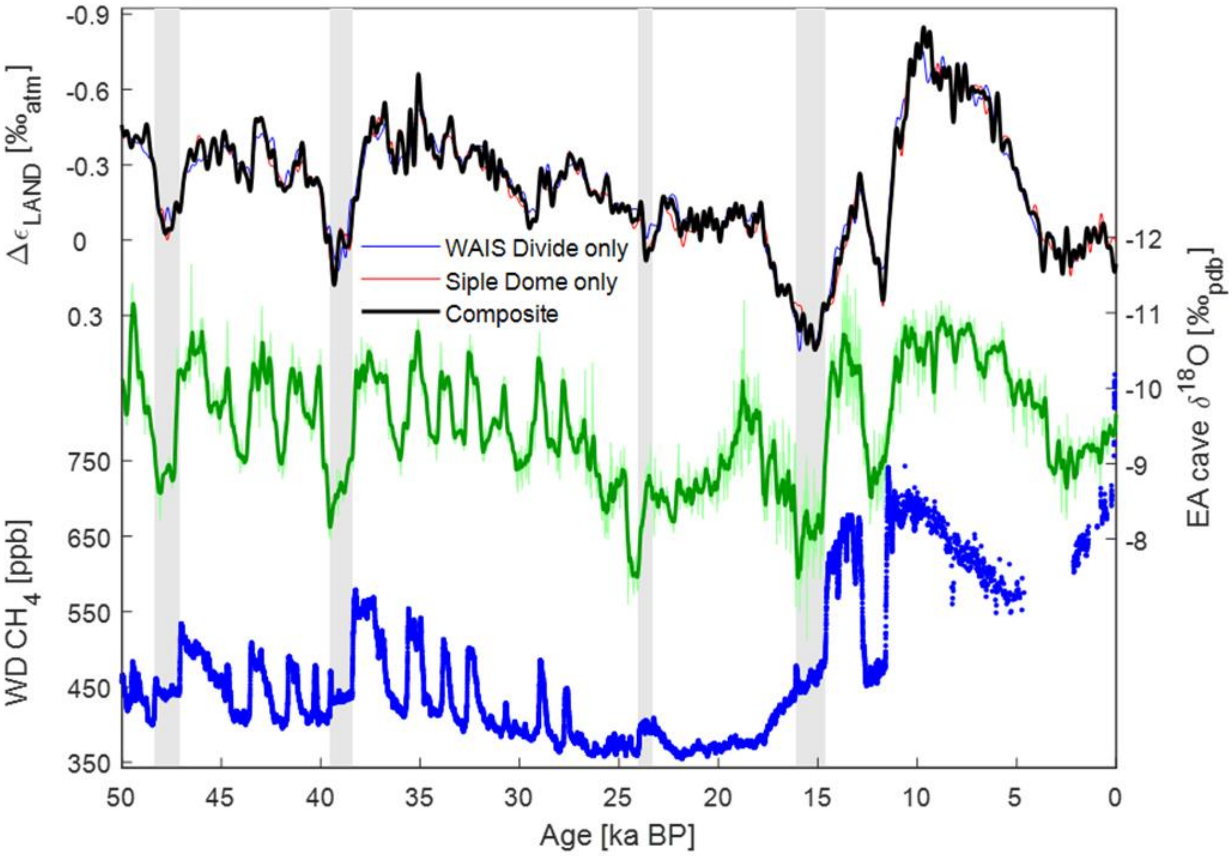

Figure 6.3: Top: $\Delta\varepsilon_{LAND}$ (estimate of change in terrestrial fractionation of $\delta^{18}O_{atm}$ from modern value) calculated independently based on the fitted $\delta^{18}O_{atm}$ curves from WAIS Divide (blue) and Siple Dome (red, on WD2014-synchronized timescale) as well as the composite WD-SD record (black); Middle: unsmoothed and smoothed (200-yr boxcar) records of composite calcite $\delta^{18}O$ from Southeast Asian speleothems (Cheng et al., 2016) corrected for changes in seawater $\delta^{18}O$ (Waelbroeck et al., 2002); Bottom: WAIS Divide CH_4 measurements (Rhodes et al., 2015; Sowers, 2012). Shaded regions indicate periods of climate impact due to Heinrich Events 1, 2, 4, and 5 identified by Rhodes et al. (2015), coincident with the highest observed glacial values of $\Delta\varepsilon_{LAND}$.

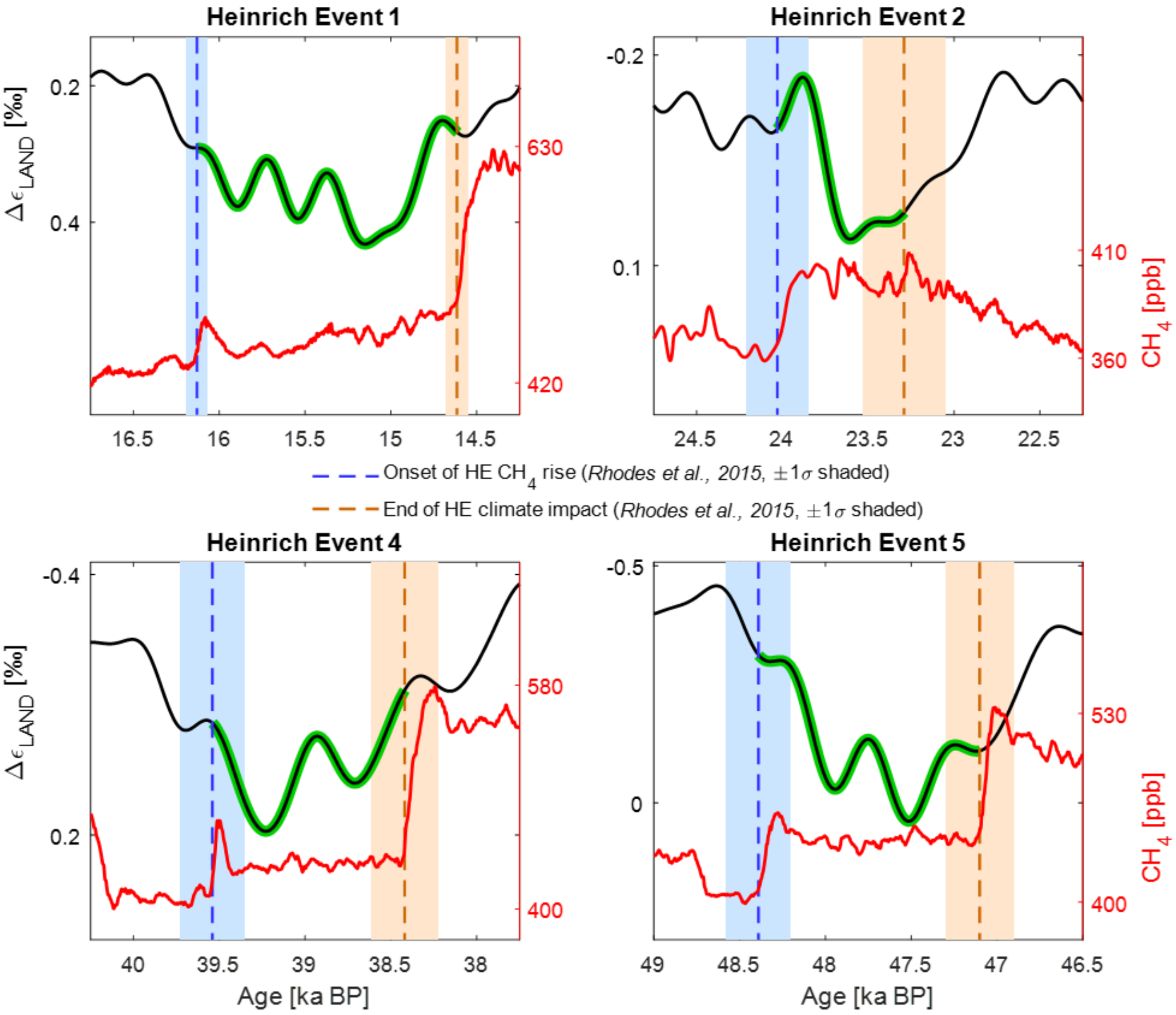

Figure 6.4: Atmospheric CH_4 measured at WAIS Divide and composite WD-SD $\Delta\varepsilon_{LAND}$ throughout and following Heinrich Events 1, 2, 4 and 5. $\Delta\varepsilon_{LAND}$ is highlighted green during periods of climate impact from Heinrich Events 1, 2, 4, and 5 proposed by Rhodes et al. (2015), beginning with an abrupt CH_4 rise (blue dashed line with shaded ±1σ dating uncertainty) and ending with another CH_4 rise of a presumed northern source (red dashed line with shaded ±1σ dating uncertainty).

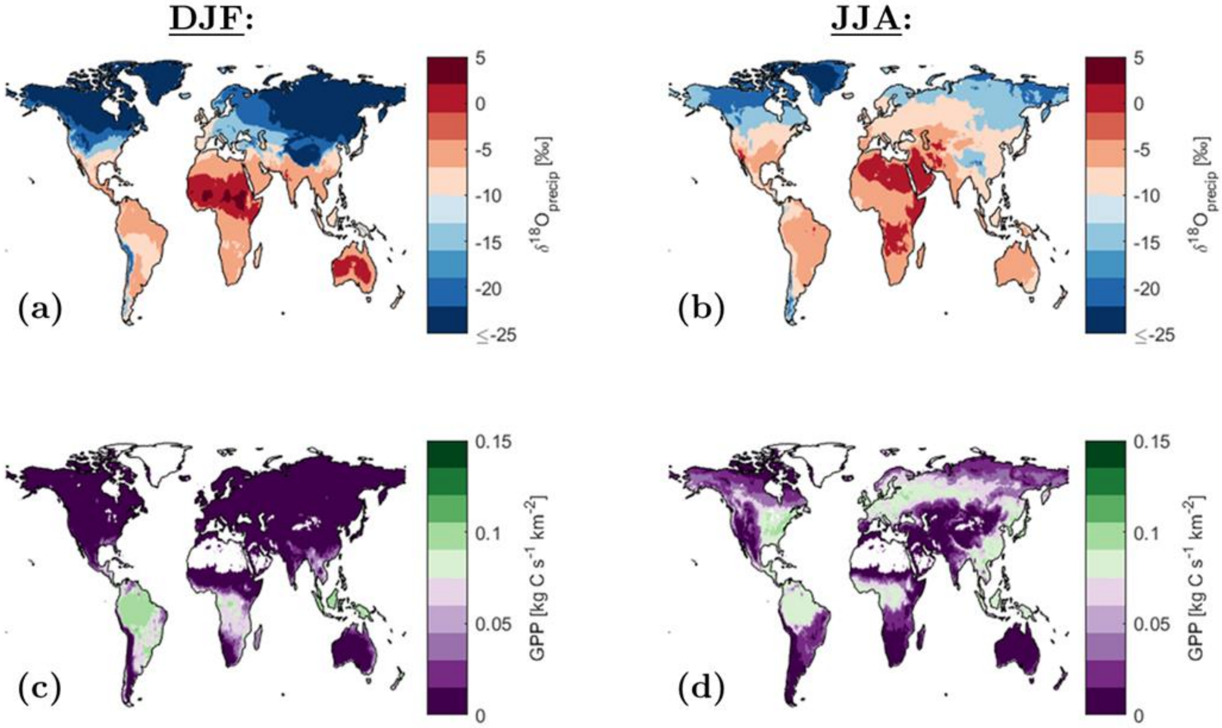

Figure 6.5: Mean terrestrial December-January-February (**a, c**) and June-July-August (**b, d**) $\delta^{18}O_{precip}$ (**a, b**) and GPP (**c, d**). GPP data used in this study are monthly values averaged across a 30-year (1982-2011) dataset of upscaled eddy covariance observations (Jung et al., 2011). Monthly $\delta^{18}O_{precip}$ isoscapes are derived from long-term (1960-2009) monthly GNIP (Global Network of Isotopes in Precipitation) data (Terzer et al., 2013). Data gaps (e.g. over oceans, Greenland, Sahara Desert) are left unfilled in this plot.

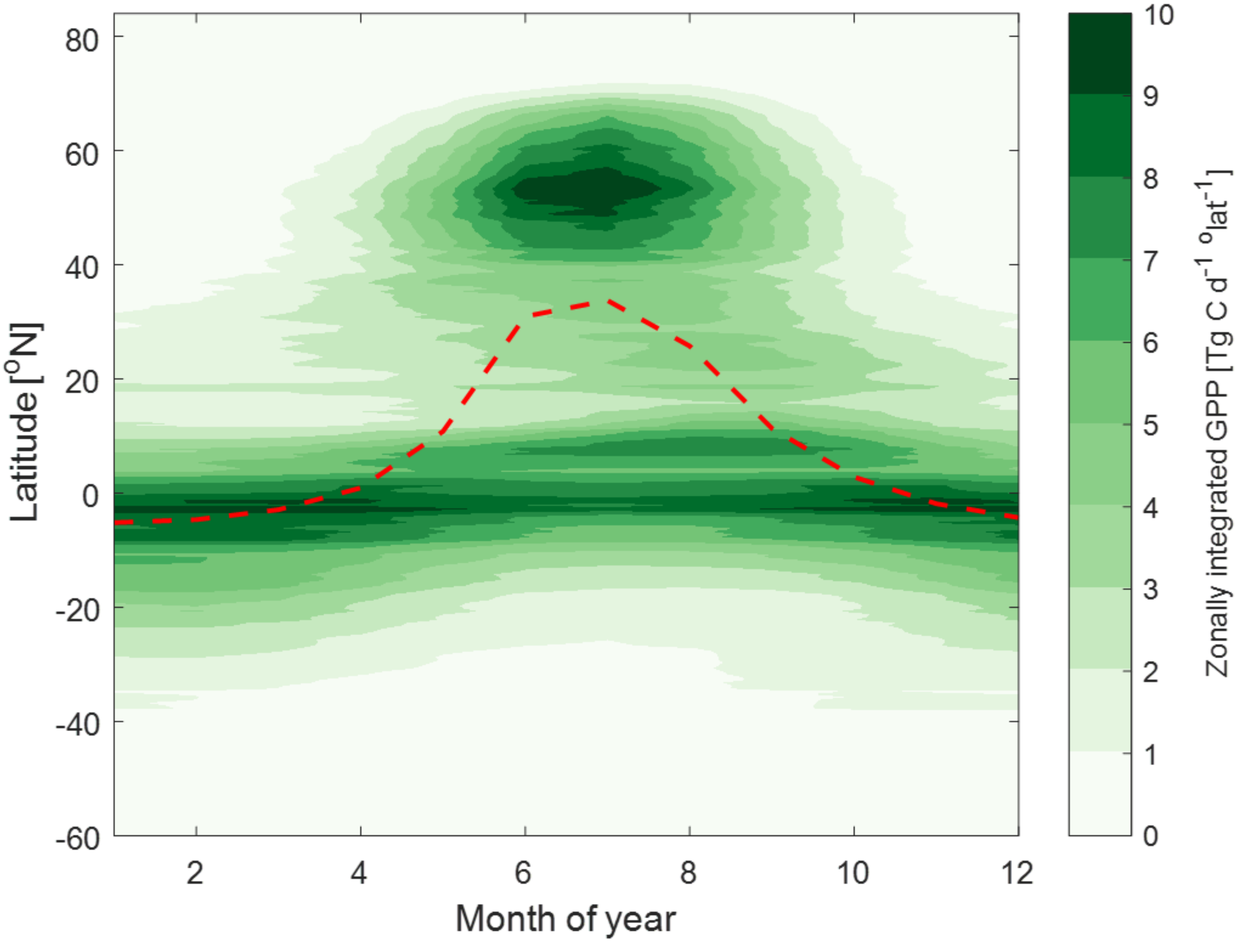

Figure 6.6: Zonally integrated terrestrial gross primary productivity as a function of latitude for monthly-mean data averaged over years from 1982 to 2011 (Jung et al., 2011). The dashed red line shows monthly-mean TOE latitude.

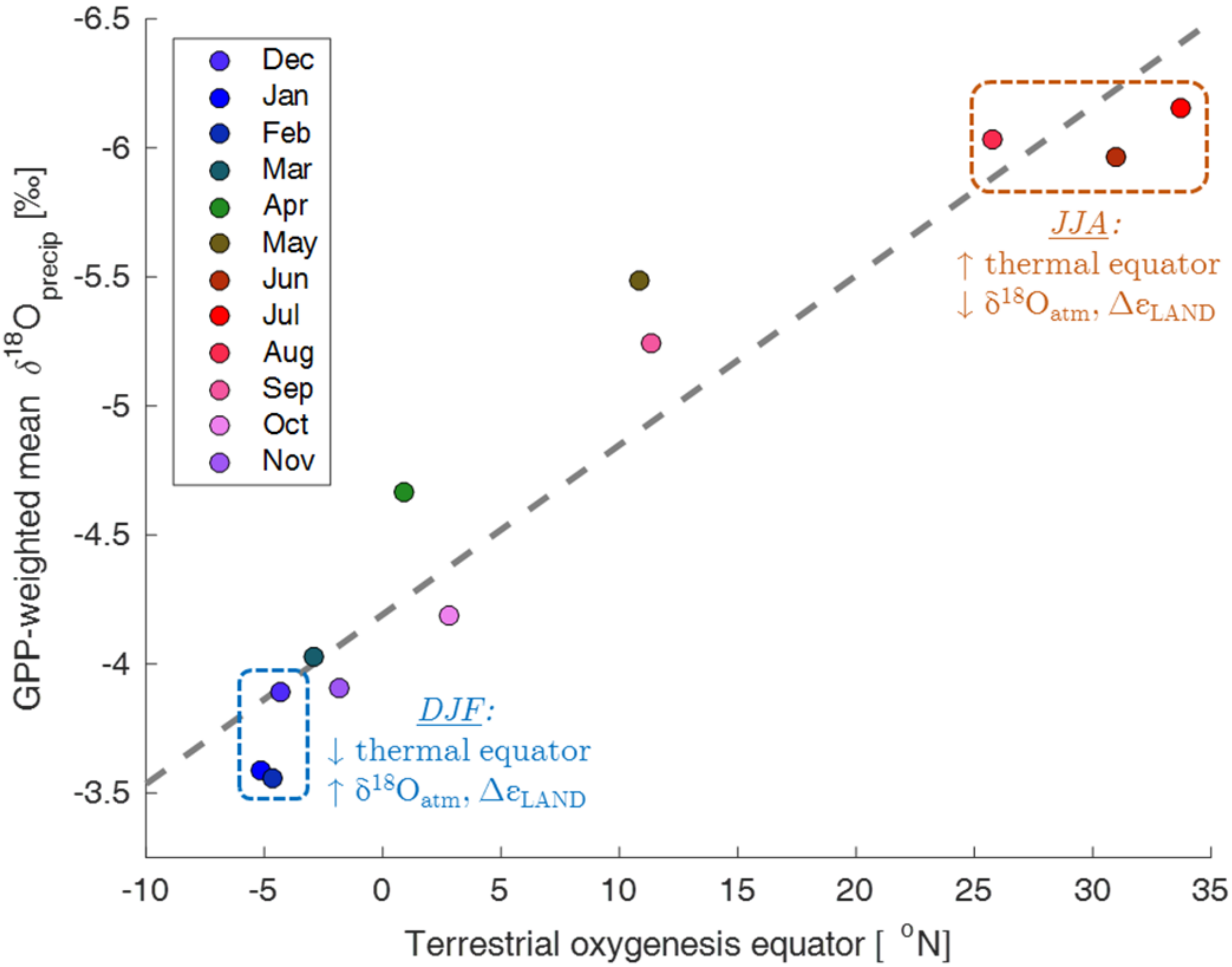

Figure 6.7: Mean monthly terrestrial $\delta^{18}O_{precip}$, weighted by oxygen production (GPP), is significantly correlated to the latitude of terrestrial oxygenesis equator ($r = 0.95$, $p < 0.0001$). Green (June-July-August) and red (December-January-February) boxes highlight extreme seasonal shifts in TOE latitude and terrestrial GPP-weighted $\delta^{18}O_{precip}$. Associated text describes the simple mechanism suggested by this study in which meridional shifts in the thermal equator affect $\delta^{18}O_{atm}$ and $\Delta\varepsilon_{LAND}$ by shifting terrestrial oxygenesis to latitudes of higher or lower $\delta^{18}O_{precip}$.

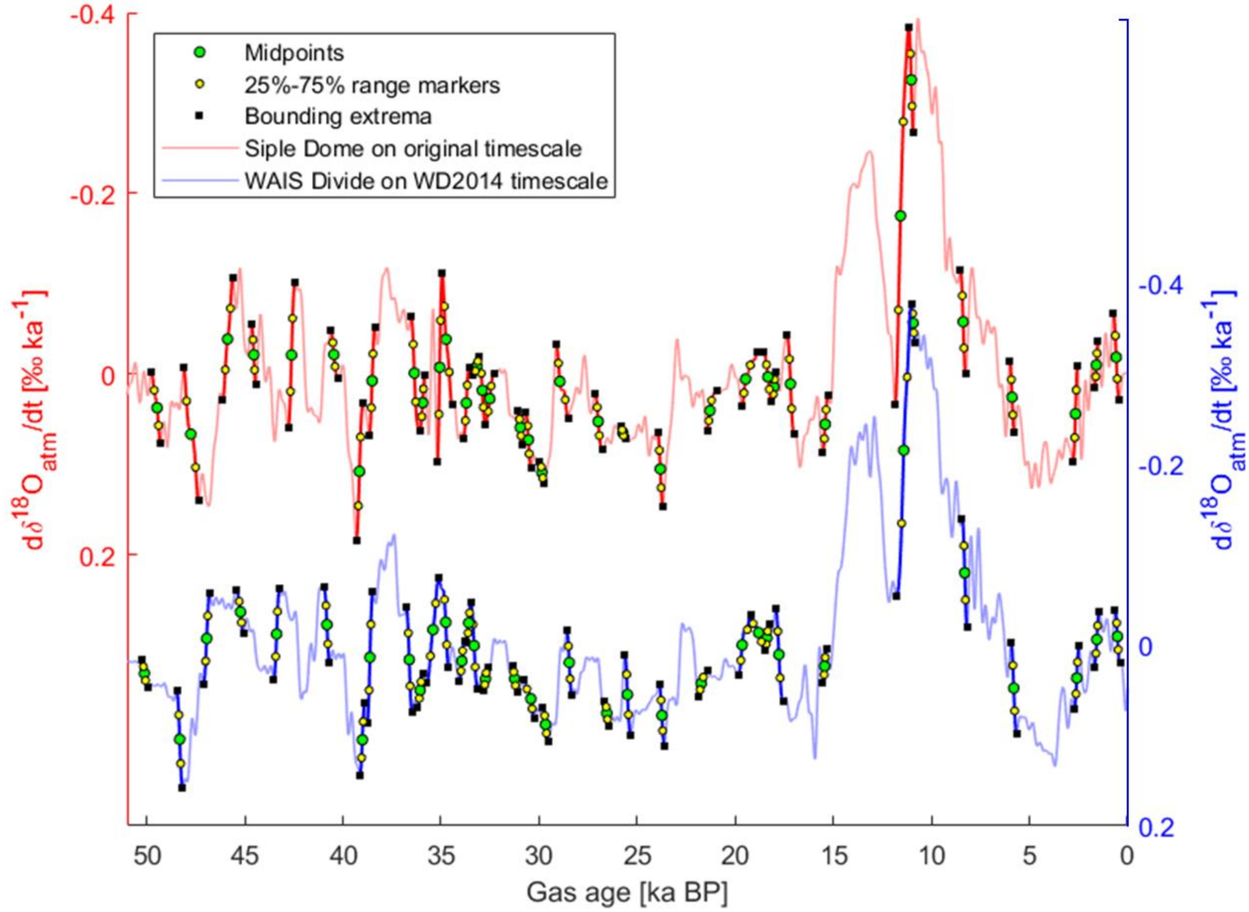

Figure 6.B1: Overview of tie point selection process from $d\delta^{18}O_{atm}/dt$ records at WD (blue) and SD (red, on original *Brook et al.*, 2005 gas timescale). Green circles (N=36) indicate midpoints of abrupt $d\delta^{18}O_{atm}/dt$ transitions recorded in both records. Smaller yellow markers indicate 25% and 75% values between local extrema (black dots) bounding each abrupt transition. ±1σ tie point uncertainty was taken from the range of 25-75% markers.

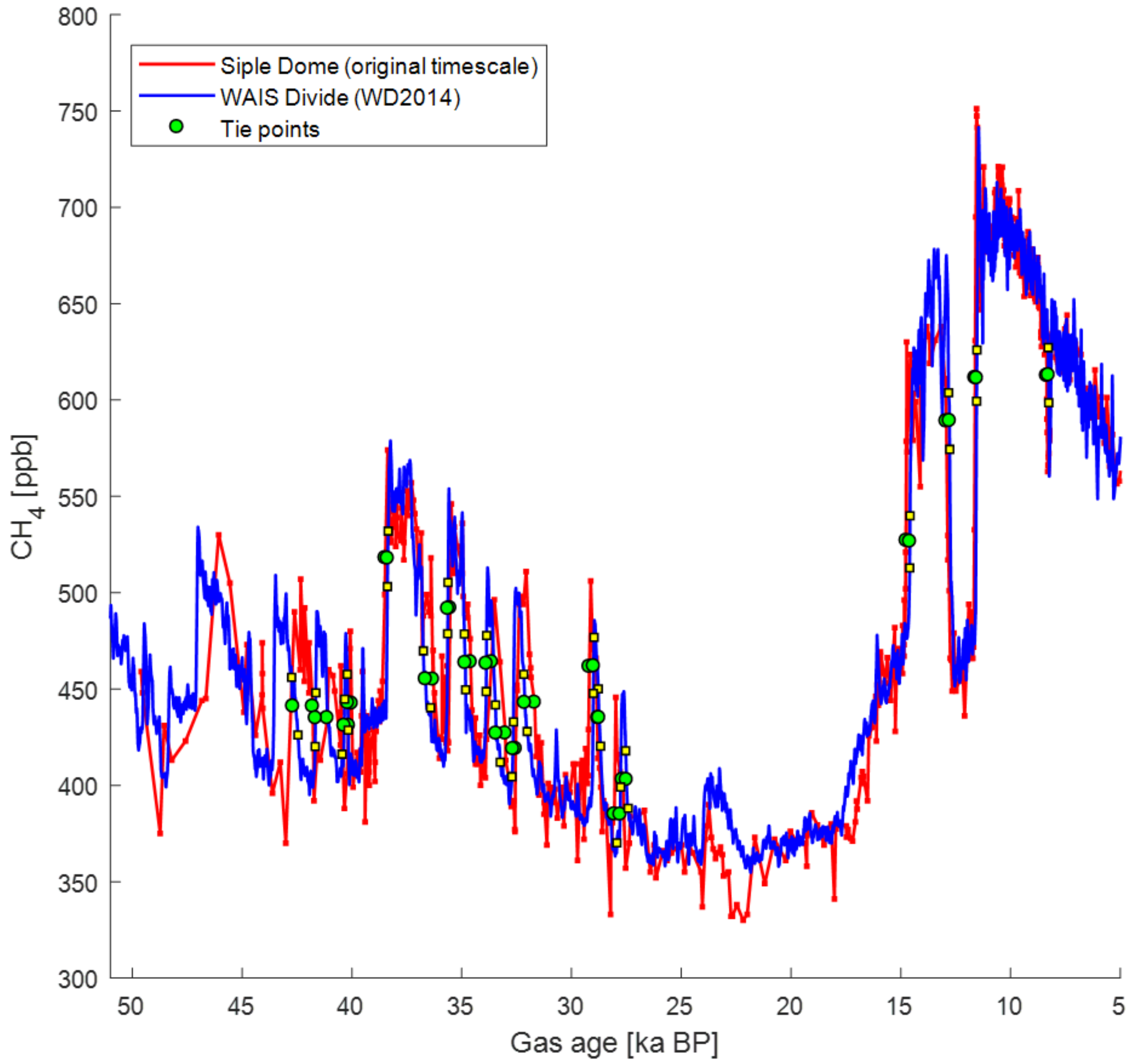

Figure 6.B2: Overview of tie point selection process from CH_4 records at WD (blue) and SD (red, on original *Brook et al*., 2005 gas timescale). Green circles (N=20) indicate selected discrete SD CH_4 values and nearest matching WD values. Smaller yellow markers indicate range of WD values agreeing with each selected SD CH_4 value within ±15ppb, taken as an estimate of ±1σ tie point uncertainty.

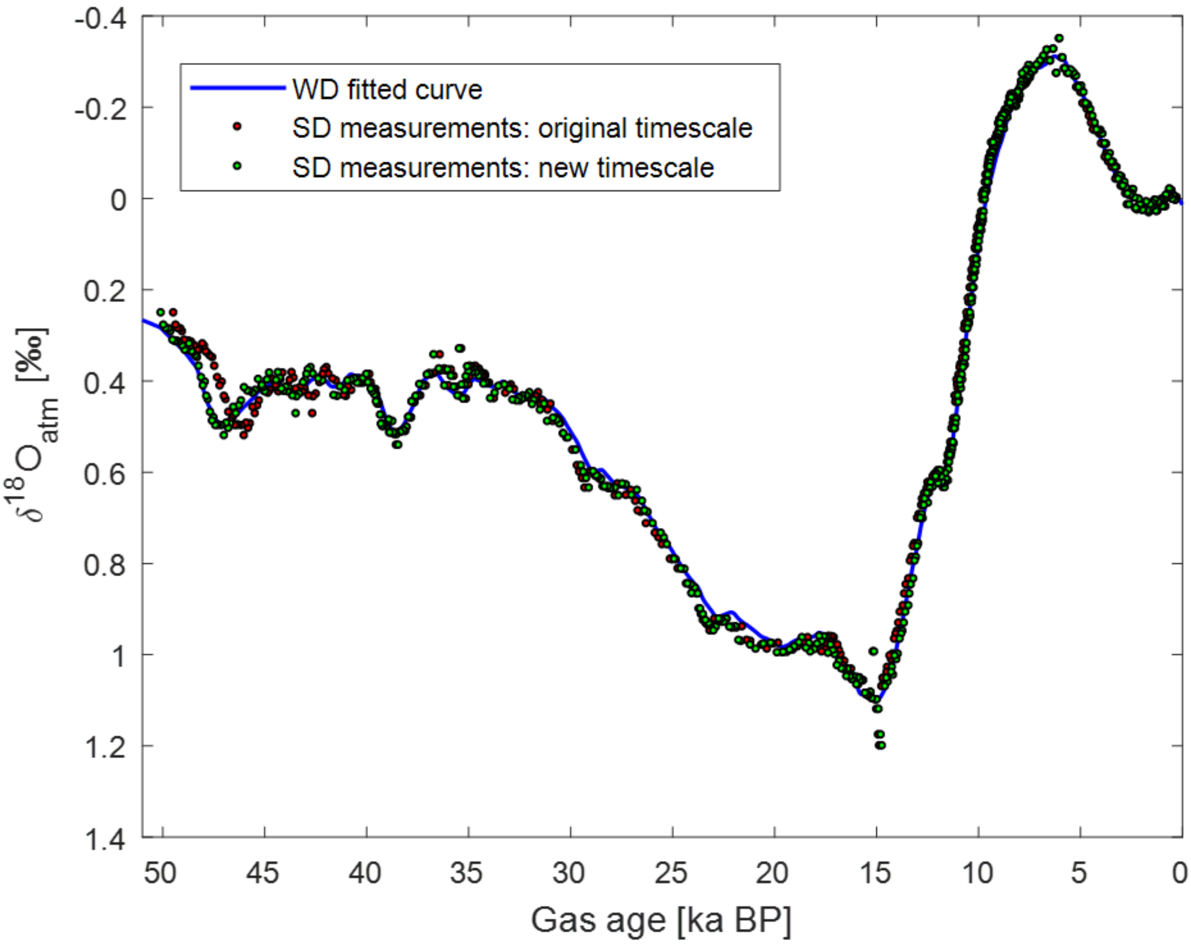

Figure 6.B3: $\delta^{18}O_{atm}$ in SD and WD: discrete SD measurements on original gas timescale (blue markers, Brook et al., 2005) and on new gas timescale (green markers, this study) are superimposed on WD fitted curve (blue line) on WD2014 gas timescale (C. Buizert et al., 2015). Root mean squared deviations between WD fitted curve and SD discrete measurements are 0.029‰ on the original timescale and 0.022‰ on the new timescale.

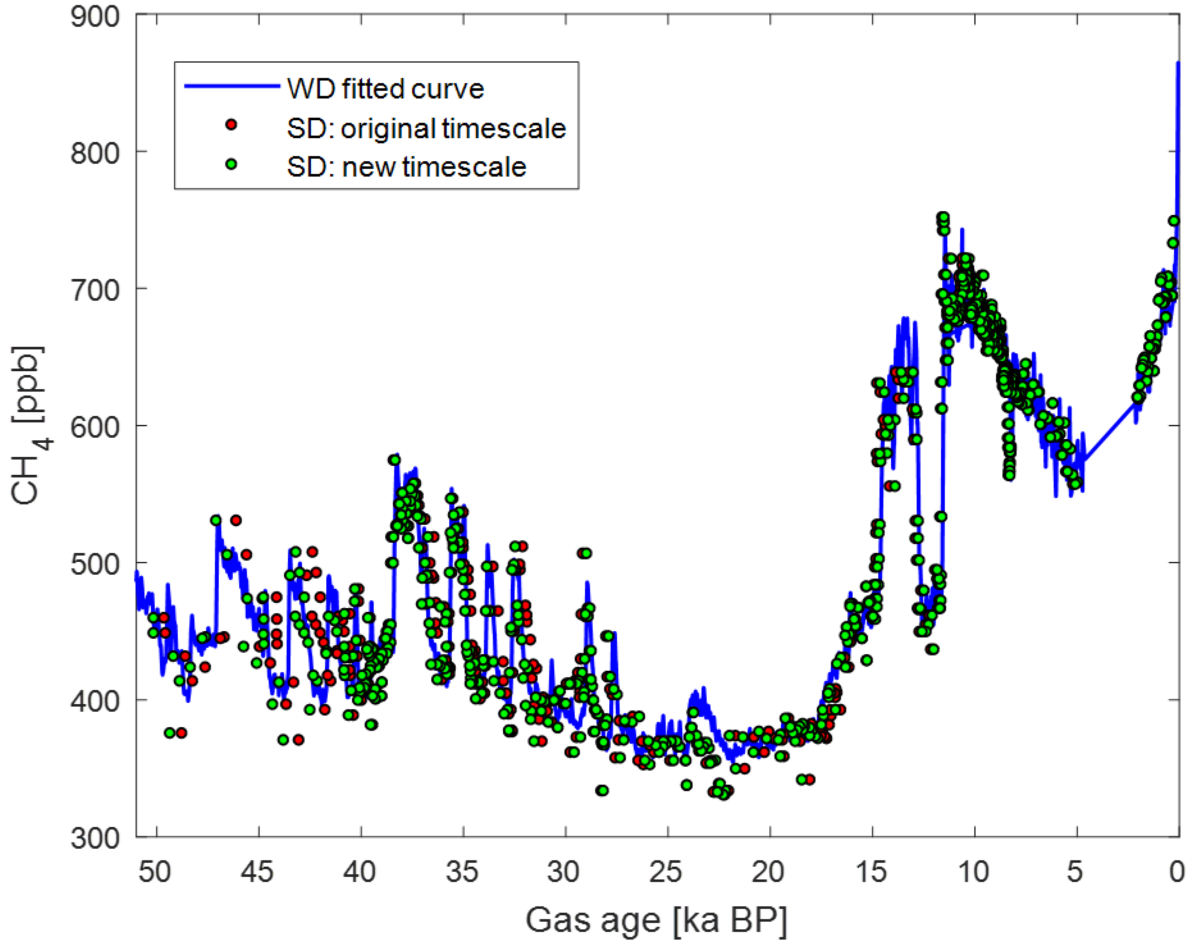

Figure 6.B4: CH_4 in SD (Ahn et al., 2012, 2014; Ahn and Brook, 2014; Brook et al., 2005; Ahn and Yang, unpublished) and WD (Rhodes et al., 2015; Sowers, 2012): discrete SD measurements on original gas timescale (blue markers, Brook et al., 2005) and on new gas timescale (green markers, this study) are superimposed on WD interpolated curve (blue line) on WD2014 gas timescale (C. Buizert et al., 2015). Root mean squared deviations between WD fitted curve and SD discrete measurements are 33.7 ppb on the original timescale and 18.3 ppb on the new timescale.

References

Ahn, J., & Brook, E. J. (2014). Siple Dome ice reveals two modes of millennial CO2 change during the last ice age. *Nature Communications, 5*, 3723. https://doi.org/10.1038/ncomms4723

Ahn, J., Brook, E. J., Schmittner, A., & Kreutz, K. (2012). Abrupt change in atmospheric CO 2 during the last ice age. *Geophysical Research Letters, 39*(17), 1–5. https://doi.org/10.1029/2012GL053018

Ahn, J., Brook, E. J., & Buizert, C. (2014). Response of atmospheric CO2 to the abrupt cooling event 8200 years ago. *Geophysical Research Letters*, *41*(2), 604–609. https://doi.org/10.1002/2013GL058177

Andersen, K. K., Azuma, N., Barnola, J.-M., Bigler, M., Biscaye, P., Caillon, N., et al. (2004). High-resolution record of Northern Hemisphere climate extending into the last interglacial period. *Nature*, *431*(7005), 147–151. https://doi.org/10.1038/nature02805

Angert, A., Luz, B., & Yakir, D. (2001). Fractionation of oxygen isotopes by respiration and diffusion in soils and its implications for the isotopic composition of atmospheric O $_2$. *Global Biogeochemical Cycles, 15*(4), 871–880. https://doi.org/10.1029/2000GB001371

Angert, A., Rodeghiero, M., & Griffin, K. (2012). High alternative oxidase activity in cold soils and its implication to the Dole Effect. *Geophysical Research Letters*, *39*(16), n/a-n/a. https://doi.org/10.1029/2012GL052719

Argus, D. F., Peltier, W. R., Drummond, R., & Moore, A. W. (2014). The Antarctica component of postglacial rebound model ICE-6G_C (VM5a) based on GPS positioning, exposure age dating of ice thicknesses, and relative sea level histories. *Geophysical Journal International*, *198*(1), 537–563. https://doi.org/10.1093/gji/ggu140

Aster, R. C., Borchers, B., & Thurber, C. H. (2013). Tikhonov Regularization. In *Parameter Estimation and Inverse Problems* (2nd ed., pp. 93–127). Waltham, MA: Elsevier Academic Press. https://doi.org/10.1016/B978-0-12-385048-5.00004-5

Banta, J. R., McConnell, J. R., Frey, M. M., Bales, R. C., & Taylor, K. (2008). Spatial and temporal variability in snow accumulation at the West Antarctic Ice Sheet Divide over recent centuries. *Journal of Geophysical Research*, *113*(D23), D23102. https://doi.org/10.1029/2008JD010235

Barkan, E., & Luz, B. (2005). High precision measurements of17O/16O and18O/16O ratios in H2O. *Rapid Communications in Mass Spectrometry, 19*(24), 3737–3742. https://doi.org/10.1002/rcm.2250

Battisti, D. S., Ding, Q., & Roe, G. H. (2014). Coherent pan-Asian climatic and isotopic response to orbital forcing of tropical insolation. *Journal of Geophysical Research: Atmospheres*, *119*(21), 11,997-12,020. https://doi.org/10.1002/2014JD021960

Bender, M., Sowers, T., & Labeyrie, L. (1994). The Dole Effect and its variations during the last 130,000 years as measured in the Vostok Ice Core. *Global Biogeochemical Cycles*, *8*(3), 363–376. https://doi.org/10.1029/94GB00724

Bender, M., Sowers, T., & Lipenkov, V. (1995). On the concentrations of O 2 , N 2, and Ar in trapped gases from ice cores. *Journal of Geophysical Research*, *100*(D9), 18651. https://doi.org/10.1029/94JD02212

Broccoli, A. J., Dahl, K. A., & Stouffer, R. J. (2006). Response of the ITCZ to Northern Hemisphere cooling. *Geophysical Research Letters*, *33*(1), n/a-n/a. https://doi.org/10.1029/2005GL024546

Brook, E. J., White, J. W. C., Schilla, A. S. M., Bender, M. L., Barnett, B., Severinghaus, J. P., et al. (2005). Timing of millennial-scale climate change at Siple Dome, West Antarctica, during the last glacial period. *Quaternary Science Reviews*, *24*(12–13), 1333–1343. https://doi.org/10.1016/j.quascirev.2005.02.002

Buizert, C., Adrian, B., Ahn, J., Albert, M., Alley, R. B., Baggenstos, D., et al. (2015). Precise interpolar phasing of abrupt climate change during the last ice age. *Nature*, *520*(7549), 661–665. https://doi.org/10.1038/nature14401

Buizert, C., Cuffey, K. M., Severinghaus, J. P., Baggenstos, D., Fudge, T. J., Steig, E. J., et al. (2015). The WAIS Divide deep ice core WD2014 chronology Part 1: Methane synchronization (68–31 ka BP) and the gas age–ice age difference. *Climate of the Past*, *11*(2), 153–173. https://doi.org/10.5194/cp-11-153-2015

Cheng, H., Edwards, R. L., Sinha, A., Spötl, C., Yi, L., Chen, S., et al. (2016). The Asian monsoon over the past 640,000 years and ice age terminations. *Nature*, *534*(7609), 640–646. https://doi.org/10.1038/nature18591

Chiang, J. C. H., & Bitz, C. M. (2005). Influence of high latitude ice cover on the marine Intertropical Convergence Zone. *Climate Dynamics*, *25*(5), 477–496. https://doi.org/10.1007/s00382-005-0040-5

Craig, H., Horibe, Y., & Sowers, T. (1988). Gravitational separation of gases and isotopes in polar ice caps. *Science*, *242*(4886), 1675–8. https://doi.org/10.1126/science.242.4886.1675

Cvijanovic, I., Langen, P. L., Kaas, E., Ditlevsen, P. D., Cvijanovic, I., Langen, P. L., et al. (2013). Southward Intertropical Convergence Zone Shifts and Implications for an Atmospheric Bipolar Seesaw. *Journal of Climate*, *26*(12), 4121–4137. https://doi.org/10.1175/JCLI-D-12-00279.1

Dansgaard, W., Johnsen, S. J., Clausen, H. B., Dahl-Jensen, D., Gundestrup, N. S., Hammer, C. U., et al. (1993). Evidence for general instability of past climate from a 250-kyr ice-core record. *Nature*, *364*(6434), 218–220. https://doi.org/10.1038/364218a0

Dole, M. (1935). THE RELATIVE ATOMIC WEIGHT OF OXYGEN IN WATER AND IN AIR. *Journal of the American Chemical Society*, *57*(12), 2731–2731. https://doi.org/10.1021/ja01315a511

Fudge, T. J., Waddington, E. D., Conway, H., Lundin, J. M. D., & Taylor, K. (2014). Interpolation methods for Antarctic ice-core timescales: Application to Byrd, Siple Dome and Law Dome ice cores. *Climate of the Past*, *10*(3), 1195–1209. https://doi.org/10.5194/cp-10-1195-2014

Goldsmith, Y., Broecker, W. S., Xu, H., Polissar, P. J., deMenocal, P. B., Porat, N., et al. (2017). Northward extent of East Asian monsoon covaries with intensity on orbital and millennial timescales. *Proceedings of the National Academy of Sciences of the United States of America*, *114*(8), 1817–1821. https://doi.org/10.1073/pnas.1616708114

Helman, Y., Barkan, E., Eisenstadt, D., Luz, B., & Kaplan, A. (2005). Fractionation of the three stable oxygen isotopes by oxygen-producing and oxygen-consuming reactions in photosynthetic organisms. *Plant Physiology*, *138*(4), 2292–8. https://doi.org/10.1104/pp.105.063768

Hemming, S. R. (2004). Heinrich events: Massive late Pleistocene detritus layers of the North Atlantic and their global climate imprint. *Reviews of Geophysics*, *42*(1), RG1005. https://doi.org/10.1029/2003RG000128

IAEA/WMO. (2017). *Global Network of Isotopes in Precipitation. The GNIP Database*. Retrieved from http://www.iaea.org/water

IAEA. (2017). *International Atomic Energy Agency: RCWIP (Regionalized Cluster-Based Water Isotope Prediction) Model – gridded precipitation δ18O|δ2H| δ18O and δ2H isoscape data.* Vienna, Austria. Retrieved from http://www.iaea.org/water

Jung, M., Reichstein, M., Margolis, H. A., Cescatti, A., Richardson, A. D., Arain, M. A., et al. (2011). Global patterns of land-atmosphere fluxes of carbon dioxide, latent heat, and sensible heat derived from eddy covariance, satellite, and meteorological observations. *Journal of Geophysical Research*, *116*(G3), G00J07. https://doi.org/10.1029/2010JG001566

Kanner, L. C., Burns, S. J., Cheng, H., & Edwards, R. L. (2012). High-Latitude Forcing of the South American Summer Monsoon During the Last Glacial. *Science*, *335*(6068), 570–573. https://doi.org/10.1126/science.1213397

Kobashi, T., Severinghaus, J. P., & Kawamura, K. (2008). Argon and nitrogen isotopes of trapped air in the GISP2 ice core during the Holocene epoch (0–11,500 B.P.):

Methodology and implications for gas loss processes. *Geochimica et Cosmochimica Acta*, *72*(19), 4675–4686. https://doi.org/10.1016/j.gca.2008.07.006

Landais, A., Dreyfus, G., Capron, E., Masson-Delmotte, V., Sanchez-Goñi, M. F., Desprat, S., et al. (2010). What drives the millennial and orbital variations of δ18Oatm? *Quaternary Science Reviews*, *29*(1), 235–246. https://doi.org/10.1016/j.quascirev.2009.07.005

Liu, Z., Wen, X., Brady, E. C., Otto-Bliesner, B., Yu, G., Lu, H., et al. (2014). Chinese cave records and the East Asia Summer Monsoon. *Quaternary Science Reviews*, *83*, 115–128. https://doi.org/10.1016/j.quascirev.2013.10.021

Lundin, J. M. (2012). *Self-consistent modeling of ice-sheet evolution and paleoclimate*. Retrieved from https://digital.lib.washington.edu/researchworks/bitstream/handle/1773/20276/Lundin_washington_0250E_10164.pdf?sequence=1

Luz, B., & Barkan, E. (2011). The isotopic composition of atmospheric oxygen. *Global Biogeochemical Cycles*, *25*(3), n/a-n/a. https://doi.org/10.1029/2010GB003883

Lynch-Stieglitz, J. (2017). The Atlantic Meridional Overturning Circulation and Abrupt Climate Change. *Annual Review of Marine Science*, *9*(1), 83–104. https://doi.org/10.1146/annurev-marine-010816-060415

Meese, D. A. (1999). *GISP2 Meese/Sowers Timescale*. https://doi.org/doi:10.1594/PANGAEA.56083

Morita, N. (1935). The increased density of air oxygen relative to water oxygen. *J. Chem. Soc. Japan*, *56*(1291).

Morse, D. L., Blankenship, D. D., Waddington, E. D., & Neumann, T. A. (2002). A site for deep ice coring in West Antarctica: results from aerogeophysical surveys and thermo-kinematic modeling. *Annals of Glaciology*, *35*(1), 36–44. https://doi.org/10.3189/172756402781816636

Peterson, L. C., Haug, G. H., & Hughen, K. A. (2000). Tropical Atlantic During the Last Glacial Rapid Changes in the Hydrologic Cycle of the Tropical Atlantic During the Last Glacial. *Science*, *290*(5498), 1947–1951. https://doi.org/10.1126/science.290.5498.1947

Petrenko, V. V., Severinghaus, J. P., Brook, E. J., Reeh, N., & Schaefer, H. (2006). Gas records from the West Greenland ice margin covering the Last Glacial Termination: a horizontal ice core. *Quaternary Science Reviews*, *25*(9–10), 865–875. https://doi.org/10.1016/j.quascirev.2005.09.005

Rasmussen, S. O., Bigler, M., Blockley, S. P., Blunier, T., Buchardt, S. L., Clausen, H. B., et al. (2014). A stratigraphic framework for abrupt climatic changes during the Last Glacial period based on three synchronized Greenland ice-core records: refining and extending the INTIMATE event stratigraphy. *Quaternary Science Reviews*, *106*, 14–28. https://doi.org/10.1016/j.quascirev.2014.09.007

Reutenauer, C., Landais, A., Blunier, T., Bréant, C., Kageyama, M., Woillez, M.-N., et al. (2015). Quantifying molecular oxygen isotope variations during a Heinrich stadial. *Climate of the Past*, *11*(11), 1527–1551. https://doi.org/10.5194/cp-11-1527-2015

Rhodes, R. H., Brook, E. J., Chiang, J. C. H., Blunier, T., Maselli, O. J., McConnell, J. R., et al. (2015). Enhanced tropical methane production in response to iceberg discharge in the North Atlantic. *Science (New York, N.Y.)*, *348*(6238), 1016–9. https://doi.org/10.1126/science.1262005

Rhodes, R. H., Brook, E. J., McConnell, J. R., Blunier, T., Sime, L. C., Faïn, X., & Mulvaney, R. (2017). Atmospheric methane variability: Centennial-scale signals in the Last Glacial Period. *Global Biogeochemical Cycles*, *31*(3), 575–590. https://doi.org/10.1002/2016GB005570

Severinghaus, J. P., Beaudette, R., Headly, M. A., Taylor, K., & Brook, E. J. (2009). Oxygen-18 of O2 records the impact of abrupt climate change on the terrestrial biosphere. *Science (New York, N.Y.)*, *324*, 1431–1434. https://doi.org/10.1126/science.1169473

Sigl, M., Fudge, T. J., Winstrup, M., Cole-Dai, J., Ferris, D., McConnell, J. R., et al. (2016). The WAIS Divide deep ice core WD2014 chronology - Part 2: Annual-layer counting (0-31 ka BP). *Climate of the Past*, *12*(3), 769–786. https://doi.org/10.5194/cp-12-769-2016

Sowers, T. (2012). *Methane Concentrations from the WAIS Divide Ice Core (WDC06A), 60 to 11,300 ybp, Version 1*. Boulder, Colorado USA. https://doi.org/http://dx.doi.org/10.7265/N5J1013R

Taylor, K. C., White, J. W. C., Severinghaus, J. P., Brook, E. J., Mayewski, P. A., Alley, R. B., et al. (2004). Abrupt climate change around 22 ka on the Siple Coast of Antarctica. *Quaternary Science Reviews*, *23*(1–2), 7–15. https://doi.org/10.1016/j.quascirev.2003.09.004

Terzer, S., Wassenaar, L. I., Araguás-Araguás, L. J., & Aggarwal, P. K. (2013). Global isoscapes for δ H in precipitation: improved prediction using regionalized climatic regression models. *Hydrol. Earth Syst. Sci*, *17*, 1–16. https://doi.org/10.5194/hess-17-1-2013

Waelbroeck, C., Labeyrie, L., Michel, E., Duplessy, J. C., McManus, J. F., Lambeck, K., et al. (2002). Sea-level and deep water temperature changes derived from benthic foraminifera isotopic records. *Quaternary Science Reviews*, *21*(1–3), 295–305. https://doi.org/10.1016/S0277-3791(01)00101-9

Wang, X., Edwards, R. L., Auler, A. S., Cheng, H., Kong, X., Wang, Y., et al. (2017). Hydroclimate changes across the Amazon lowlands over the past 45,000 years. *Nature*, *541*(7636), 204–207. https://doi.org/10.1038/nature20787

Wang, Y., Cheng, H., Edwards, R. L., He, Y., Kong, X., An, Z., et al. (2005). The Holocene Asian Monsoon: Links to Solar Changes and North Atlantic Climate. *Science*, *308*(5723), 854–857. https://doi.org/10.1126/science.1106296

Wang, Y., Cheng, H., Edwards, R. L., Kong, X., Shao, X., Chen, S., et al. (2008). Millennial- and orbital-scale changes in the East Asian monsoon over the past 224,000 years. *Nature*, *451*(7182), 1090–3. https://doi.org/10.1038/nature06692

Wang, Y.., Cheng, H., Edwards, R. L., An, Z. S., Wu, J. Y., Shen, C. C., & Dorale, J. A. (2001). A high-resolution absolute-dated late Pleistocene Monsoon record from Hulu Cave, China. *Science (New York, N.Y.)*, *294*(5550), 2345–8. https://doi.org/10.1126/science.1064618

Yu, G., Xue, B., & Li, Y. (2013). Lake level changes in Asia. In *Encyclopedia of Quaternary Science (Second Edition)* (pp. 506–523). https://doi.org/http://dx.doi.org/10.1016/B978-0-444-53643-3.00369-1

Chapter 7

Conclusions

Quantitative records of past terrestrial climate are scarce but essential for understanding the drivers of regional change in a warming world. The principle motivation for this work was to develop a new tool to precisely reconstruct past terrestrial hydroclimate information, with specific application to the arid southwestern United States during the late Pleistocene. This tool makes use of a physical prediction that depth-dependent gravitational settling fractionation should dominate other sources of isotopic fractionation of Kr and Xe in unsaturated-zone air (Schwander, 1989; Seltzer et al., 2017; Severinghaus et al., 1996). Because gas exchange between unsaturated-zone air and groundwater occurs at the water table over long spatial and temporal scales, and dispersive intra-aquifer mixing acts to low-pass filter geochemical signals, one would expect long-term regional-scale gravitational signals from past climate periods to be preserved in the dissolved Kr and Xe isotope ratios of ancient groundwater. By measuring these isotope ratios at high precision, the goal was to inversely model past water-table depth to gain insight into past shifts in terrestrial hydroclimate. Here I will briefly summarize the progress made toward this goal and outline the future direction of this new paleoclimate tool.

In Chapter 2, air samples from a deep unsaturated zone in the Amargosa Desert were collected and analyzed for their noble gas isotopic composition. This work served as a test of the underlying physical assumption that gravitational settling fractionation should overwhelm any other sources of fractionation for the isotopes of Kr and Xe in unsaturated-zone air.

In Chapter 3, a method was developed to quantitively extract gases from two-liter water samples for high-precision noble gas isotopic analysis. In laboratory experiments, the solubility and kinetic fractionation factors of these isotope ratios were determined, enabling for the first time the extension of groundwater excess air models to noble gas isotope ratios. In addition to the development of an analytical method, the key finding of this chapter was that the influence of excess air on dissolved Kr and Xe isotope ratios is negligible.

In Chapter 4, 58 groundwater samples were collected in two-liter flasks from 36 wells across three separate study areas in California: Fresno, the Mojave Desert, and San Diego. Kr and Xe isotope ratio analyses in these samples generally followed the expected 1:1 mass-normalized gravitational fractionation expectation, offset by amounts in close agreement with the solubility fractionation values determined in Chapter 3. Using these gravitational signals, water-table depths were reconstructed in the Fresno and San Diego regions (some Mojave Desert samples indicated sensitivity to another physical process, which we suggest may be steady-state O_2 consumption). Reconstructed water-table depths were found to closely agree with historical observations in Fresno, and measurements from wells in San Diego revealed a pronounced ~20-m drop in mean regional water-table depth during the last deglaciation. This finding is consistent with considerably wetter conditions during the latter portion of the last glacial period (LLGP), shifting toward more arid conditions as the Laurentide Ice Sheet waned throughout the deglaciation. Analysis of noble gas concentrations in these samples indicated 6-6.5 ºC cooler-than-present temperatures during the LLGP.

Chapter 5 and 6 are not related to the groundwater noble gas-based water-table depth tool. Instead, they focus on isotopic tracers of large-scale atmospheric and oceanic processes.

In Chapter 5, a pilot study was carried out to measure Ar, Kr, and Xe isotope ratios in the deep North Pacific to test for isotopic disequilibrium associated with the well-established undersaturation of heavy noble gases in the deep ocean. To compare measured values to solubility equilibrium, isothermal seawater equilibration experiments were carried out using filtered water from the Scripps pier. In the deep North Pacific, Ar and Kr heavy-to-light isotope ratios were found to fall significantly below solubility equilibrium, while Xe isotope ratios were not found to be significantly different, within analytical uncertainty. Comparison of the isotopic disequilibrium signals of Ar and Kr to model predictions offers preliminary support for the notion these signals reflect kinetic fractionation associated with incomplete, cooling-driven, diffusive air-to-sea gas transfer during deep-water formation.

In Chapter 6, records of oxygen isotopes of O_2 from the West Antarctic Ice Sheet (WAIS) Divide ice core were merged with the Siple Dome ice core to generate a composite, 50,000-year record of atmospheric $\delta^{18}O$. Analysis of the modern seasonal cycles of precipitation $\delta^{18}O$ and terrestrial primary productivity indicated that shifts in the median latitude of oxygen production change the weighting of precipitation $\delta^{18}O$ supplied to the terrestrial biosphere in a nearly linear fashion. This trend, in which productivity-weighted mean precipitation $\delta^{18}O$ is lowest when oxygen production is furthest north and highest when it is furthest south, persists across the equator. Therefore, observations of rapid increases in $\delta^{18}O$ of O_2 from the composite ice-core record were suggested to indicate southward shifts of oxygen production driven by concomitant shifts in the latitude of tropical rainfall.

While this thesis represents an important first step, considerable work remains to properly develop the noble gas isotope-based water-table depth tool and better understand its limitations. For instance, several Mojave Desert groundwater samples from locations of deep present-day water-table depth displayed characteristic departures from gravitational settling that may indicate fractionation due to diffusion against steady-state vertical gradients in O_2. A means of testing this hypothesis and more generally understanding past unsaturated-zone air fractionation is the measurement of ^{22}Ne/^{20}Ne ratios in groundwater, which should be highly sensitive to kinetic fractionation. Recent analytical advances in the Scripps Noble Gas Isotope laboratory make this a realistic possibility in the near future.

With modest gains in analytical precision, dissolved Kr and Xe isotope ratios can become more useful tools to detect <1-m equivalent gravitational signals and better quantify small disequilibrium signals in seawater associated with deep-water formation. One immediate step toward this goal is the ongoing development of a five-liter sampling and extraction system in the Scripps Noble Gas Isotope Laboratory. This will in principle enable 2-3 per meg amu^{-1} precision analyses of dissolved Kr and Xe isotope ratios. A longer-term consideration to achieve even higher precision and test for <1 per meg amu^{-1} signals in seawater is to develop a field-based extraction system for large ~250-L seawater samples. The challenge will be to quantitatively extract all gases, thereby preventing kinetic fractionation. However, with a robust and quantitative field-based extraction system, a future order-of-magnitude improvement in dissolved Kr and Xe isotopic analysis may be achievable. With higher-precision measurements and additional constraints (such as neon isotopes), it may ultimately be possible to quantify anthropogenic water-level drawdown signals at < 1-m accuracy, which could aid policymakers in sustainable groundwater resource management.

Finally, additional analysis of water-table depth in the context of groundwater and earth system models may provide more useful constraints on past hydrological parameters to better understand regional hydroclimate sensitivity. While the noble gas isotope technique provides a quantitative estimate of water-table depth, this value is only qualitatively useful at present to interpret past hydroclimate. In other words, our interpretation of changes in water-table depth is presently limited to generally relating shallower water-table depths to wetter conditions, for example. Additional work is needed to formally relate water-table depth changes to changes in precipitation minus evaporation rates (P-E), a variable of more fundamental importance to climate. Because equilibrium water-table depth reflects a complex balance of surface hydrology as well as P-E, high-resolution groundwater models (e.g. Fan et al., 2013) forced under various P-E boundary conditions may allow for the determinations of regional-scale relationships between water-table depth and P-E. Knowledge of past regional P-E changes would provide an important benchmark for earth system model simulations of last glacial maximum hydroclimate.

References

Fan, Y., Li, H., & Miguez-Macho, G. (2013). Global Patterns of Groundwater Table Depth. *Science*, *339*(6122), 940–943. https://doi.org/10.1126/science.1229881

Schwander, J. (1989). The transformation of snow to ice and the occlusion of gases. In H. Oeschger & C. C. Langway (Eds.), *The Environmental Record in Glaciers and Ice Sheets* (pp. 53–67). New York: Wiley.

Seltzer, A. M., Severinghaus, J. P., Andraski, B. J., & Stonestrom, D. A. (2017). Steady state fractionation of heavy noble gas isotopes in a deep unsaturated zone. *Water Resources Research*, *53*(4), 2716–2732. https://doi.org/10.1002/2016WR019655

Severinghaus, J. P., Bender, M. L., Keeling, R. F., & Broecker, W. S. (1996). Fractionation of soil gases by diffusion of water vapor, gravitational settling, and thermal diffusion. *Geochimica et Cosmochimica Acta*, *60*(6), 1005–1018. https://doi.org/10.1016/0016-7037(96)00011-7